Research Frontiers 2020

SPring-8
SACLA

ISSN 2433-5126
SPring-8 Document D2021-010

SPring-8/SACLA Research Frontiers 2020

CONTENTS

Chemical Science

Earth & Planetary Science

Industrial Applications

Note: The principal publication(s) concerning each article is indicated with all author's names in italics in the list of references.

Preface

It is my great pleasure to publish SPring-8/SACLA Research Frontiers 2020. JASRI has stewardship responsibility for SPring-8 and SACLA, whereas RIKEN has ownership. SPring-8 and SACLA are located on the same campus; thus, their synergy produces groundbreaking results.

In FY2020, COVID-19 affected the activities of SPring-8 and SACLA in many ways. Most directly, all users, except those with proposals for work related to COVID-19, were prohibited from visiting the campus from April 11 to June 15. In addition, many precautionary measures were taken on site, including limiting staff attendance for some months. Moreover, the number of users from abroad was severely reduced owing to travel restrictions. Nevertheless, SPring-8 welcomed about 9,200 users who came to perform 1,321 experiments in FY2020. To date, SPring-8 and SACLA users have published more than 1,000 and about 80 research papers, respectively, in FY2020.

Two SPring-8 and SACLA users were awarded prestigious prizes in 2020 for their achievements in science and technology. Professor Jian-Ren Shen (Okayama University) was awarded the Medal with Purple Ribbon for his structural analyses of the photosystem II protein complex, for which his X-ray crystallography experiments at SPring-8/SACLA contributed significantly. Professor Makoto Fujita (The University of Tokyo) was awarded the Citation Laureate of Clarivate for his advances in supramolecular chemistry through self-assembly strategies that take inspiration from natural processes.

This volume includes two comprehensive review articles. In one article, Professor Yasuhiro Iwasawa (The University of Electro-Communications) describes recent progress in the advanced SR characterization of fuel cells at SPring-8. In the other article, Professor Kouichi Hayashi (Nagoya Institute of Technology) describes recent achievements in experiments using X-ray fluorescence holography and photoelectron holography.

In the main part of this volume, active users of SPring-8 describe the essence of their findings in various fields that include Life Science, Physical Science, Chemical Science, Earth & Planetary Science, and Industrial Applications. In addition, the principal activity reports on SPring-8/SACLA facilities are included in the sections of Accelerators & Beamlines Frontiers and Facility Status.

I am very grateful to the many authors and experts who contributed their papers to this volume. Special thanks are due to Dr. Naoto Yagi, Ms. Marcia Obuti-Daté, and the members of the editorial board for their continuous efforts.

Yoshiyuki Amemiya
President
Japan Synchrotron Radiation Research Institute (JASRI)

Editor's Note

This is the 2020 issue of SPring-8/SACLA Research Frontiers that covers outstanding scientific outcomes of SPring-8 and SACLA in 2019 and 2020, in the so-called pre-COVID-19 era. The best scientific achievements are collected from more than 1,000 papers published using SPring-8 or SACLA each year. At the moment we are not sure how COVID-19 will affect scientific output of SPring-8 and SACLA. Although our facilities are operating normally and users are making experiments, scientific activities particularly at universities have been severely restricted. This situation is expected to improve gradually and we all hope we can go back to the pre-COVID-19 state as soon as possible.

There are two reviews in this issue. One is written by Professor Yasuhiro Iwasawa of The University of Electro-Communications. Because of the serious energy crisis and concerns on carbon dioxide emission, research on batteries is very actively carried out at SPring-8. Among several different types of batteries, Professor Iwasawa is specialized in fuel cells. His group has built BL36XU which is dedicated to this research and utilized different experimental techniques to reveal chemical reactions in fuel cells. This review summarizes their more than ten years' efforts and outcomes. The second review was jointly contributed by Professor Kouichi Hayashi of Nagoya Institute of Technology and Professor Tomohiro Matsushita of Nara Institute of Science and Technology. Although they work in different X-ray disciplines, hard X-ray fluorescence and photoelectrons, their holography approaches are similar to each other as scientific tools, particularly in studies on dopants. They polished up the techniques for further refined measurements at SPring-8.

SPring-8/SACLA Research Frontiers is made of two parts. The first is scientific results (Scientific Frontiers) and the second is additional information on hard and soft infrastructures that support scientific research. Although some important numbers such as the operation time are given in the second part, other information and more complete statistical numbers on the operation of SPring-8 and SACLA are available on the website so that more updated information can be accessed (http://www.spring8.or.jp/en/about_us/spring8data/).

The full text of SPring-8/SACLA Research Frontiers is also available on the SPring-8 website (http://www.spring8.or.jp/en). For the list of publications produced by SPring-8 users and staff, please visit the publication database at http://www.spring8.or.jp/en/science/publication_database/.

On behalf of all the editors, I would like to thank those who helped us by recommending excellent research results suitable for publication in this issue, and the users and staff of SPring-8 who contributed their reports to this issue despite this pandemic.

Naoto Yagi
Japan Synchrotron Radiation Research Institute (JASRI)

Editorial Board

Scientific Frontiers

Review Article

Recent progress in advanced SR characterization of fuel cells at SPring-8

1. Introduction—a central base for SR research on fuel cell science and technology

The recent progress in the advanced SR characterization of new materials and functions, particularly the dynamic catalysis and degradation of polymer electrolyte fuel cells (PEFCs) at SPring-8, promises well for the rational development of next-generation PEFCs with high performance and remarkable long-term durability. This can bring about their commercialization for a wide range of fuel cell vehicles (FCVs) such as automobiles, taxis, buses, trucks, and forklifts. Recent reports of cars powered by hydrogen fuel cells have captured the world's imagination with the hope of a clean energy source to mitigate environmental issues. The FCV is itself a clean power generator, making it entirely different from electric cars that need great amounts of external electric power. A hydrogen and fuel cell society is a major and long-term challenge requiring close academia–industry–government cooperation.

The synchrotron facility, which has various beamlines for frontier, interdisciplinary, and emerging area research involving diverse, multi-axial and cross-disciplinary views, is a scientific base resembling a planetary projector which provides stellar achievements in modern science and technology for the Future Earth, Society 5.0, and SDGs. This review summarizes the recent progress in advanced SR analysis techniques for PEFCs and the findings and discoveries achieved mainly at beamline BL36XU with the world's only *in situ* and *operando* simultaneous and sequential multi-analysis systems, which have been constituted from high-performance time-, space- and energy-resolved techniques such as XAFS, high-energy resolution fluorescence detected (HERFD)-XANES, resonant inelastic X-ray scattering (RIXS), nano-focused XAFS, three-dimensional (3D) computed tomography (CT)-XAFS imaging, XRD, and ambient pressure (AP)-HAXPES under PEFC working conditions.

Before the *in situ* time-resolved XAFS study on a Pt/C cathode catalyst in a PEFC under operating conditions conducted by Tada *et al*. at BL01B1 in 2007 [1], there had been no reports on the full exploration and determination of the elementary reaction steps or the kinetics of both structural changes of the metal catalysts and electrochemical reactions on the electrode surfaces in PEFCs. Tada *et al*. in collaboration with Toyota Motor Corporation and Toyota Central R&D Labs. Inc. reported a major breakthrough in fuel cell research with their development of a novel time-gating quick XAFS technique with a high time resolution. They found evidence of dynamic surface events and a significant time lag among those events at the Pt/C cathode in a PEFC under *operando* fuel-cell conditions for the first time. We also collaborated with Honda Motor Co., Ltd. in 2008–2010 to study the potential-dependent chemical bonding and electronic states at the surfaces of different types of core-shell cathode by *operando* time-resolved XAFS and found potential-dependent restructuring and hysteresis due to the adsorbed oxygen in PEFCs [2]. Such novel molecular-level information, which is difficult to obtain by other analysis techniques, may have contributed to the realization of the world's first commercialization of FCVs from Japan; MIRAI from Toyota and CLARITY FUEL CELL from Honda. *In situ* and *operando* XAFS techniques are very powerful for the *in situ*/*operando* and element-selective investigation of electronic states and local coordination structures as well as the fluctuations of cathode electrocatalysts in PEFCs, which are regarded to be relevant to the oxygen reduction reaction (ORR) performance and durability of PEFC electrocatalysts [3].

Following these achievements in the *in situ* and *operando* characterization of operating PEFCs by synchrotron XAFS,

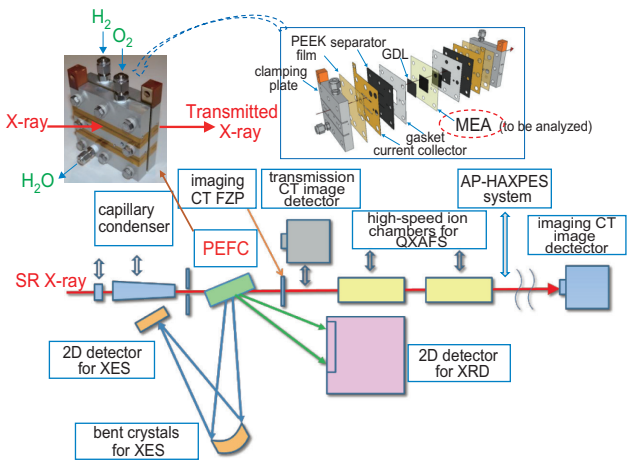

Fig. 1. Schematic of simultaneous and sequential *in situ*/*operando* multi-analytical measurement system for PEFC [6].

NEDO initiated a PEFC program (2010–2014 FY) to construct the world's only and highest performance beamline BL36XU for *in situ* and *operando* PEFC characterization by XAFS and related X-ray analysis techniques for understanding the dynamic electrocatalysis and severe degradation of the membrane-electrode assembly (MEA), which is a power generation part inside a PEFC, and to enable the rational and efficient development of next-generation PEFCs. In the subsequent NEDO program (2015-2019 FY) at BL36XU, we constructed several *in situ* and *operando* simultaneous and time-series multi-analysis systems by combining two to three X-ray techniques, for example, XAFS, HERFD-XANES, RIXS, 3D CT–XAFS imaging, nano-focused XAFS, and XRD. HAXPES at BL36XU is applicable to measuring time-resolved XPS and AP-XPS spectra of MEA electrocatalysts [4]. A new PEFC analysis platform project under NEDO has been ongoing since July 2020.

A schematic layout of the main components of BL36XU is illustrated in Fig. 1 [5,6]. In general, each beamline in synchrotron facilities has been optimized for each particular analysis technique separately, and different techniques at different beamlines have often given rise to contradictory results and conclusions regarding complex heterogeneous catalytic systems such as PEFC systems. An effective way of overcoming such a problem of contradiction may be to conduct simultaneous or sequential multi-analysis experiments under working conditions at the same beamline and beamtime on the same sample.

The NEDO and FC communities were in need of such a high-performance beamline as BL36XU because there were no public beamlines capable of enabling XAFS measurements with the high time and spatial resolutions required for dynamic PEFC analysis under operating conditions. BL36XU was designed and built on a definite concept and with high-performance specifications by The University of Electro-Communications (T. Uruga and Y. Iwasawa) in close collaboration with Nagoya University (M. Tada; moved from Institute for Molecular Science in 2013) and Institute for Molecular Science (Y. Takagi and T. Yokoyama) with the invaluable assistance of JASRI and RIKEN in 2010–2012. From 2013, it was operated by the three-university team. In 2015–2016, BL36XU was advanced and upgraded to conduct the *in situ* and *operando* simultaneous and sequential multi-analysis of an identical area of the same PEFC sample by the X-ray techniques described above; it became the world's only and highest performance multi-analysis beamline for FC research (Fig. 1) [5,6]. From 2016, it was operated by the three-university team and was also opened to six other university groups involved in the NEDO PEFC program. After the NEDO program, BL36XU was transferred to RIKEN in March 2020, where it is now positioned as a key beamline for a new NEDO PEFC program.

In 2010–2012 after the start of the NEDO program but before the start of BL36XU operation, 23 articles on PEFCs and solid oxide fuel cells (SOFCs) were published at SPring-8. From 2013 to Feb. 2021, 103 articles were reported at SPring-8, and among them 53 articles on PEFCs were reported by the three-university team using beamline BL36XU. After the construction of BL36XU, the number of users and that of publications concerning the PEFC research area at SPring-8 increased as a result of increased attention from people who had previously never used SR X-ray-based techniques. SPring-8 is now a central base for the SR research of fuel cells not only in Japan but also in the world.

2. *Operando* simultaneous XAFS–XRD at high time resolution

Sekizawa *et al.* [7] investigated the mechanism behind the electrochemical processes involved in rapid voltage control processes of Pt/C in PEFC at BL36XU. The simultaneous observation of time-resolved quick XAFS (20 ms acquisition) and XRD (20 ms acquisition) at a time resolution of 60 ms in the transient response process against the voltage jumps 0.4→1.4 V and 1.4→0.4 V (vs RHE) was conducted to directly monitor the chemical bonding and electronic states and the lattice parameters and crystalline phase transformation, respectively, in the Pt nanoparticles. The reaction mechanism and structural kinetics for Pt surface events and crystalline core events of the Pt/C electrocatalyst in the MEA under the transient voltage cyclic process were revealed by the simultaneous *operando* XAFS–XRD technique, as shown in Fig. 2. Under the voltage operation 0.4→1.4 V, the first fast surface Pt–O bond formation event (rate constant k_1) was followed by the second slow events of Pt–O formation, Pt charging, Pt–Pt dissociation, and Pt size decrease

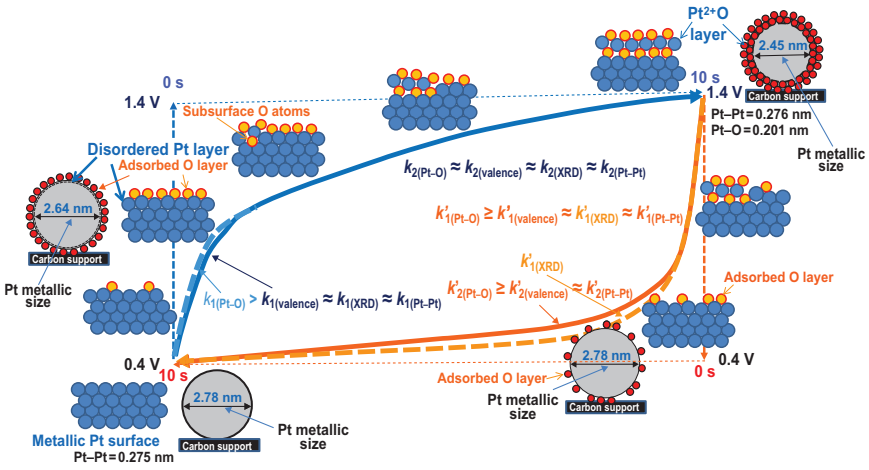

Fig. 2. *Operando* time-resolved Pt L_{III}-edge XANES, EXAFS, and XRD profiles of an MEA Pt/C cathode electrocatalyst and reaction mechanism for Pt nanoparticles under transient voltage cyclic operations [7].

(rate constant k_2). The surface Pt–O formation induces the partial disordering of the outermost Pt layer, resulting in a decrease in metallic phase size from 0.278 to 0.264 nm. The slow events occur concertedly to ultimately produce the tetragonal Pt^{2+}–O layer (Pt–O = 0.201 nm) at the Pt surface. At the transient voltage operation 1.4→0.4 V, the first fast steps of Pt–O dissociation, Pt valence decrease, Pt–Pt reformation, and Pt size increase proceed concertedly at rates similar to the rate constants k'_1. The second slow steps of Pt–O dissociation, Pt valence decrease, and Pt–Pt reformation also occur concertedly (rate constants k'_2). The change in metallic phase size is completed at the fast step, and the changes in Pt valence, Pt–O dissociation, and Pt–Pt reformation at the surface proceed further at the lower rates (Fig. 2). It was found that the rate constants for the 15 elementary steps are related to the PEFC performance and durability [8,9].

3. *Operando* XAFS–CT imaging and unsupervised machine learning

Current PEFC systems suffer from critical problems, particularly the low ORR activity and poor durability of Pt/C cathode electrocatalysts during practical PEFC operation [3,10]. A Pt_3Co/C cathode catalyst shows higher activity and durability than standard Pt/C catalysts, but still degrades to an unacceptable degree under PEFC operating conditions. Although the dissolution and aggregation of Pt nanoparticles in Pt_3Co/C are more suppressed than in Pt/C, Co gradually dissolves from the bimetallic catalyst, and hence the alloy benefit gradually disappears [11]. Tada and colleagues, for the first time, successfully visualized 3D images of the morphology, Pt and Co distributions, Co/Pt atomic ratio, and Pt valence of a Pt_3Co/C cathode electrocatalyst in an MEA before and after an accelerated durability test (ADT) by combining the *operando* XANES–CT and unsupervised machine learning of the 3D images, revealing a catalyst degradation mechanism for Pt and Co with different degradation and migration behaviors in the 3D catalyst layer depending on the structure of the carbon support [11].

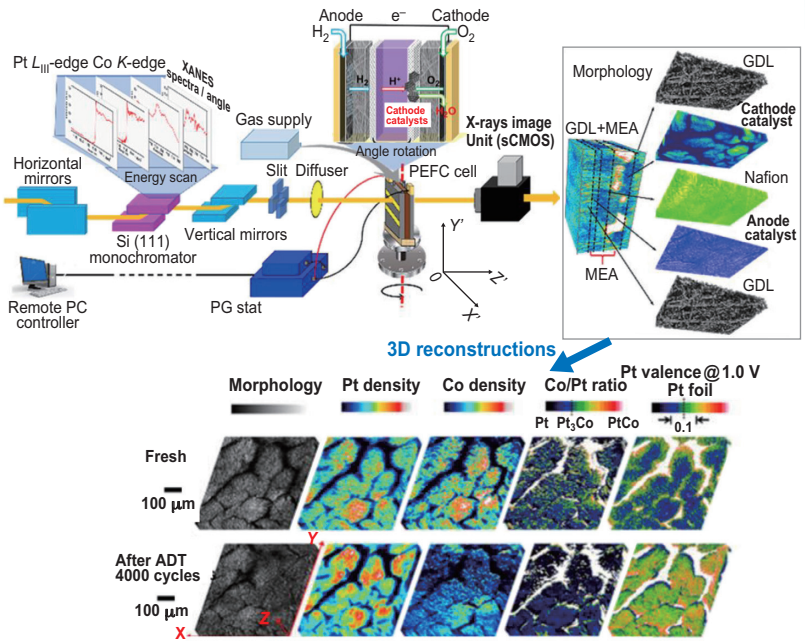

Fig. 3. Schematic of *operando* XANES–CT imaging for MEA Pt_3Co/C under PEFC operating conditions and reconstructed 3D images of the cathode catalyst layer in an MEA [11].

Figure 3 shows a schematic of *operando* XANES–CT imaging under PEFC operating conditions at BL36XU and reconstructed 3D images of the cathode catalyst layer in an MEA [11]. The effective viewing area of the image was 666×666 μm^2 with a pixel resolution of 325 nm. However, the actual spatial resolution was around 1 μm because of blurring on the scintillator crystal. The PEFC cell was mounted on a rotation stage and rotated perpendicularly with respect to the incident X-ray beam. At each particular angle, the Pt L_{III}-edge (11.386–11.697 keV, merged to 375 points) or Co *K*-edge XANES (7.517–7.849 keV, merged to 374 points) spectrum was recorded by quick scanning using an X-ray image unit for 25 or 18 s, respectively. Then, the rotation angle θ was changed in steps of 1° and the quick XANES scanning was repeated over a range of θ from –80° to 80° to obtain 161 data sets of quick XANES spectra. The imaging data were reconstructed into a 3D (x, y, z) matrix in real space using the angle-limited CT calculation of the ordered-subset expectation maximization (OS-EM) method [10,11].

The 3D XANES–CT imaging indicated the occurrence of intrinsic heterogeneous degradation of the Pt_3Co/C electrocatalyst in the MEA. Each reconstructed 3D image contained 18, 620, 250 structural parameter data points. Hence, unsupervised machine learning was conducted to find correlations between the structural parameters in the observed 3D imaging data [11]. The data mining of the difference in Pt or Co density between the ADT states suggested that the regulation of the 3D morphology inside the cathode layer is one of the key parameters to consider in order to control the degradation of the MEA Pt_3Co/C electrocatalyst. Here, further explanation of the results on *operando* XANES–CT imaging and unsupervised learning is omitted owing to the page limitation of this review. Their infographic approach of combining the 3D chemical imaging and unsupervised learning may be a promising way to reveal intrinsic events of PEFCs as well as of practical materials and devices [11].

4. Same-view nano-XAFS–STEM/EDS combined technique

A visualization analysis of Pt and Co species of Pt_3Co/C in an MEA following aging and degradation processes has been performed by the same-view nano-XAFS–STEM/EDS technique using a membrane cell under humid N_2 atmosphere. Figure 4 shows the results of the same-view nano-XAFS/STEM-EDS visualization analysis for the Pt_3Co/C cathode layer in the MEA after 5,000 cycles of 0.6–1.0 V rectangular ADT [12]. The same-view nano-XAFS/STEM-EDS measurements were carried out in areas of 3 μm × 3 μm at two typical locations with different degrees of degradation, e1 and m1 in Fig. 4(a). Results are shown in images labeled e1, $E1_{-1}$, $E1_{-2}$, v_e, and V_e, and in m1, $M1_{-1}$, $M1_{-2}$, v_m, and V_m, respectively. In the area of the cathode about ~400 nm from the electrolyte edge, the Co content decreased ($E1_{-2}$), where Co dissolved in electrolytes as Co^{2+} ions (V_e). Moreover, there was little change in Pt content ($E1_{-1}$), and the Pt valence remained at zero (v_e), unlike the MEA Pt/C. In contrast, Co was oxidized and dissolved over a wide range of the cathode layer (~70% of the initial Co amount) (Figs. 4(c) and 4(f)). It was shown in Figs. 4(e) and 4(h) that Co dissolved in the electrolyte region had an octahedral Co^{2+}–O_6 structure by 150 nm × 150 nm nano-XAFS analysis. It was also shown that the existence of Co suppressed the oxidation and dissolution of Pt. From CN_{Pt-Pt} and CN_{Pt-Co} and from CN_{Co-Co} and CN_{Co-Pt}, the number of Pt shell layers of the core-shell nanoparticles near the cathode edge and near the center of the cathode was estimated to be 7 and 4, respectively. The MEA Pt_3Co/C after 10,000 ADT-rec cycles had many cracks and pores in the cathode electrocatalyst layer, and about 90% of Co was dissolved and removed from the cathode layer. We discovered square planar Pt^{2+}–O_4 and octahedral Co^{2+}–O_6 species in the area between the cathode edge and the Pt–Co band. Pt and Co chemical species in the Pt_3Co/C cathode electrocatalyst in the MEA during the deterioration process and a fuel cell deterioration suppression process by Co were visualized for the first time at the nanoscale using the same-view nano-XAFS–STEM/EDS combination technique while maintaining the working environment of PEFCs.

5. Conclusion and prospect

Humanity alone has created scientists throughout the long process of evolution of species. Scientists should have a definite mission and responsibility to make a happy, prosperous, and sustainable society for humans as well as all other species by discovering and developing modern science and technology. We have great expectations for fuel cell science and technology at the SR facility in a sustainable society and in our future life. However, we cannot simply apply the fruits of the current SR research to achieve this objective nor can we continue to develop the present technology in the present form to achieve this objective unless we have a new advanced-class SR facility.

Yasuhiro Iwasawa

Innovation Research Center for
Fuel Cells and Graduate School of
Informatics and Engineering,
The Univ. of Electro-Communications

Email: iwasawa@g.ecc.u-tokyo.ac.jp

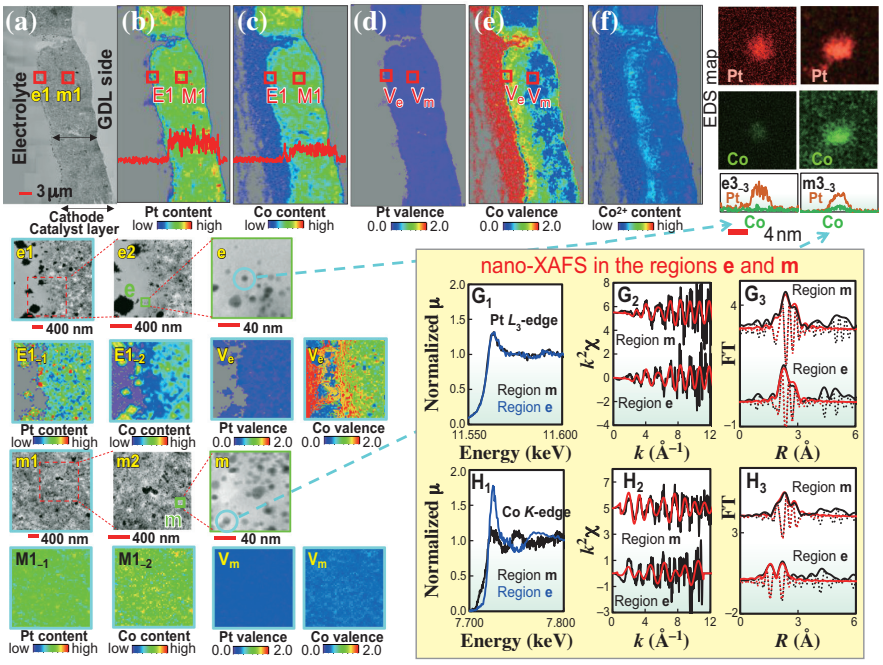

Fig. 4. Results of the same-view nano-XAFS and STEM/EDS measurements of the MEA Pt_3Co/C cathode electrocatalyst layer after 5,000 ADT cycles. See the details of each nano-XAFS map, nano-XANES, and nano-EXAFS analysis in [12].

References

[1] M. Tada *et al.*: Angew. Chem. Int. Ed. **46** (2007) 4310.
[2] S. Nagamatsu *et al.*: J. Phys. Chem. C **117** (2013) 13094.
[3] Y. Iwasawa, K. Asakura, and M. Tada (Eds), "XAFS Techniques for Catalysts, Nanomaterials, and Surfaces", Springer, Switzerland (2016/2017).
[4] Y. Takagi *et al.*: Acc. Chem. Res. **51** (2018) 719.
[5] O. Sekizawa *et al.*: J. Phys: Conf. Series **430** (2013) 012020; ibid. **712** (2016) 012142.
[6] T. Uruga *et al.*: Chem. Rec. **19** (2019) 1444.
[7] O. Sekizawa *et al.*: ACS Sus. Chem. Eng. **5** (2017) 3631; Topics Catal. **61** (2018) 889.
[8] N. Ishiguro *et al.*: ACS Catal. **2** (2012) 1319.
[9] T. Kaneko *et al.*: J. Phys. Chem. C **120** (2016) 24250.
[10] H. Matsui *et al.*: Angew. Chem. Int. Ed. **56** (2017) 9371.
[11] Y. Tan *et al.*: J. Phys. Chem. C **123** (2019) 18844.
[12] S. Takao *et al.*: Angew. Chem. Int. Ed. **53** (2014) 14110; ACS Appl. Mater. Interfaces **12** (2020) 2299.

Review Article

Recent achievements using X-ray fluorescence holography and photoelectron holography

Atomic-resolution holography is a method of 3D atomic structure determination based on Gabor's original concept of holography. We are leading research on atomic-resolution holography with X-rays, electrons and neutrons. Among several types of atomic-resolution holography, X-ray fluorescence holography (XFH) [1, 2] and photoelectron holography (PH) have been conducted mostly at SPring-8, and many important achievements have been produced thus far. We show some recent results of XFH and PH in the present article.

In both XFH and PH, there are "normal" and "inverse" modes [2], as shown in Figs. 1(a) and 2(b), respectively. In the normal mode (Fig. 1(a)), fluorescent X-rays or photoelectrons from atoms in a sample, with and without being scattered by surrounding atoms, serve as the object and reference waves, respectively. A holographic pattern is recorded by scanning a detector around the sample. In the inverse mode (Fig. 1(b)), fluorescence (or characteristic X-rays) is used to detect an interference field originating from incident and scattered X-rays or electrons. The holographic pattern is obtained by detecting the fluorescence (or characteristic X-rays) while the sample's orientation is varied relative to the incident beam. XFH and PH are expected to be used for medium-range local structural analysis, which cannot be performed by X-ray diffraction or x-ray absorption fine structure analysis.

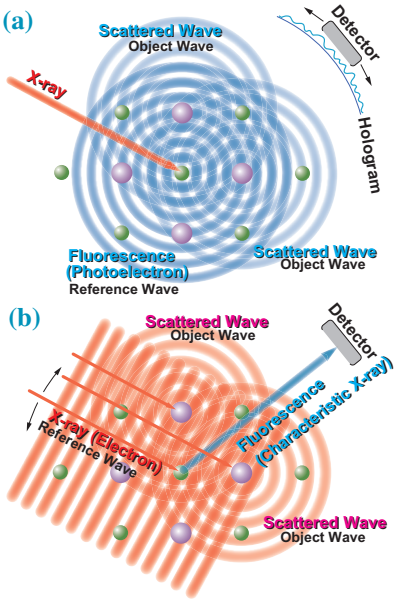

Fig. 1. Principle of atomic resolution holography. **(a)** Normal mode. **(b)** Inverse mode.

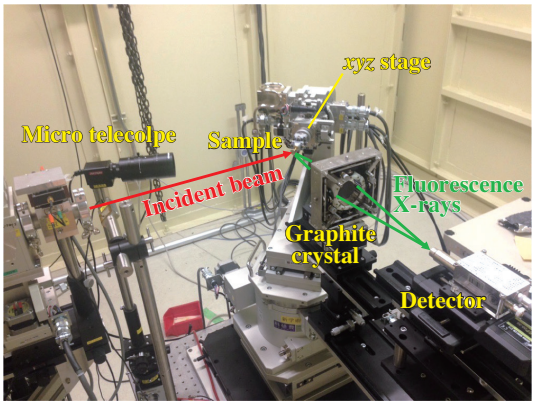

Fig. 2. Photograph of X-ray fluorescence holography apparatus.

X-ray fluorescence holography

Figure 2 shows the XFH apparatus installed at SPring-8 BL13XU [3]. In the measurements of holograms in the inverse mode, the intensity variation of the X-ray fluorescence is measured as a function of the direction of the incident X-ray beam. Fluorescent photons from the sample should be detected as much as possible within the large solid angle of the detector. To accept and choose the wanted X-ray fluorescence lines with large solid angles, we have used cylindrical or toroidal graphite analyzers. The energy-analyzed fluorescent photons are focused on an avalanche photodiode (APD), which is a typical fast X-ray detector with a maximum count rate of as high as 10^8 cps. On the other hand, a silicon drift detector, which is an energy-dispersive detector, has been recently used for dilute systems instead of avalanche photodiodes. In dilute systems, even when using the analyzing crystals, unwanted radiation is still detected at a non-negligible intensity ratio. Thus, further analysis of the incoming X-rays using the silicon drift detector is effective for measuring pure holograms. Typical scan ranges of azimuthal ϕ and incident θ angles are $0° \leq \phi \leq 360°$ in steps of 0.25° and $0° \leq \theta \leq 75°$ in steps of 1°, respectively. Regarding X-ray fluorescence holography, we describe here two applications to state-of-the-art metallic materials.

Mg alloys have attracted considerable attention owing to their lightness because we must reduce the energy

consumption of vehicles, such as cars, trains and airplanes. However, pure Mg is disadvantageous for its poor workability and low fire resistance. The Mg alloy with a synchronized long-period stacking ordered (LPSO) structure would be one of the solutions; it is a long-period stacking derivative of the hcp Mg structure, where the hcp structure is modified by a periodical insertion of stacking faults. The stacking fault is related to the concentration of heavier impurity elements, which form specific cluster structures, as shown in Fig. 3(a). Since the excellent mechanical properties of these Mg alloys are believed to originate from the synchronized LPSO structure, details of the LPSO structure have been investigated using various characterization methods. Here, we studied the local structure around Zn in the 10H-type long-period stacking ordered $Mg_{75}Zn_{10}Y_{15}$ alloy by XFH [4,5].

XFH measurements were performed at SPring-8 BL39XU. Using a focusing mirror and a slit, we obtained a small beam size of 20 × 20 μm^2, which serves to record fluorescent X-rays from a small single-crystal region of about 0.3 × 1.0 mm^2. In addition, the polycrystalline region of the sample was masked with Ag paste to suppress the emission of the fluorescent X-rays from the polycrystalline parts. We set the energies of the incident X-rays from 10.0 to 13.5 keV in steps of 0.25 keV and measured Zn Kα holograms. We can observe clear standing wave lines in the measured holograms, confirming that the measurements were successful.

As shown in Fig. 3(b), atomic images were clearly observed at 4.2 Å from the central Zn atom and correspond to Zn atoms inside the $L1_2$ cluster. On the other hand, the atomic images at the positions indicated by dashed circles are hardly observable, which correspond to those in the adjacent clusters. Figure 3(c) shows the reconstruction obtained from the calculated holograms using the structure model depicted in Fig. 3(a), and the dashed circles are superposed experimental results. This result indicates weak intercluster positional correlations. To evaluate the magnitude of the fluctuations, we calculated the atomic image including the positional fluctuation between the $L1_2$ clusters. A simulation including intercluster positional fluctuations with a magnitude of 0.33 Å well reproduced the experimental results. Because the degree of order is strongly related to the mechanical properties, the quantitative information of the intercluster fluctuation will be useful for understanding the origin of the excellent mechanical properties of LPSO alloys.

Fe_2VAl Heusler-type alloy is a promising thermoelectric material consisting only of abundant elements. The performance of thermoelectric materials is expressed by the dimensionless figure of merit, $ZT = (S^2/\rho\kappa)T$, where T is the temperature, S is the Seebeck coefficient, ρ is the electrical resistivity, and κ is the thermal conductivity. The S value of this material is as high as that of the bismuth chalcogenide system, which is used in commercially available thermoelectric material, but, the κ value is larger than that of the bismuth chalcogenides by one order of magnitude. Therefore, reducing the thermal conductivity is an urgent issue that must be resolved to enable practical use. One solution is the doping of a heavy element, which scatters phonons, to reduce the thermal conductivity. On the basis of this idea, Nishino and his coworkers doped Ta into the V site and observed a significant effect on the thermal conductivity. To gain details on the local structure around Ta, we measured Ta *K*-edge X-ray fluorescence holograms of a Ta-doped Fe_2VAl single crystal [6].

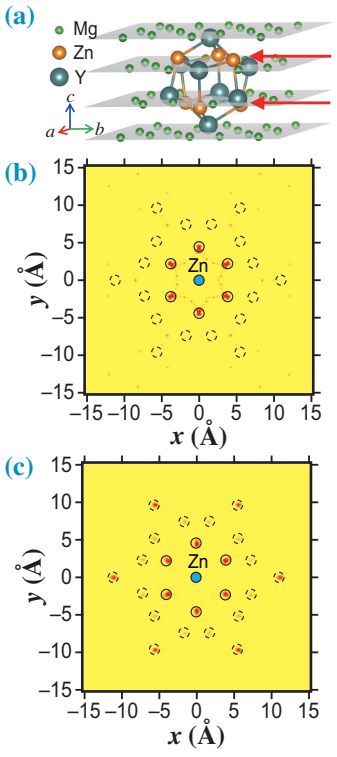

Fig. 3. Atomic images of (0001) planes around Zn in $Mg_{75}Zn_{10}Y_{15}$ alloy. **(a)** Atomic configuration of Zn_6Y_8 cluster. **(b)** Experimental data. **(c)** Calculated data. (b) and (c) show superpositions of neighbor Zr images on the same (0001) planes indicated by the coordinates in (a).

A $Fe_2(V_{0.95}Ta_{0.05})Al$ single crystal was prepared by the Czochralski method in a triarc furnace. XFH measurements were performed at SPring-8 BL13XU and BL6C at Photon Factory in Japan. We measured Ta Lα and V Kα holograms with the same incident X-ray energy range (11.9–14.4 keV in steps of 0.5 keV). The measured holograms of V Kα and Ta Lα show clear standing wave lines, indicating that the experiments were successfully performed. We also measured the X-ray absorption fine structure (XAFS) of $Fe_2(V_{0.95}Ta_{0.05})Al$ to determine more precisely the features of the local structure. Moreover, inelastic X-ray scattering (IXS) was applied to this material to understand the relationship between the doped Ta and the atomic dynamics.

The reconstructed atomic image of the Fe plane around V is shown in Fig. 4(a). Circles indicate the expected positions of Fe atoms around V, derived from the crystal structure of Fe_2VAl. Clear atomic images are observable within the circles. Figure 4(b) shows the corresponding atomic image around Ta. The positions of the spots agree well with those around V. On the other hand, the intensity of the atomic images is higher around Ta than around V. Such a feature was also observed

in the radial distribution functions (RDFs) around V and Ta obtained from XAFS measurement. This behavior is in contrast to the observation that atomic images around dopants exhibit a lower intensity than those around matrix elements. In addition, higher intensities around Ta were observed in a wide spatial range of more than 10 Å. These results show that the positional correlation between Ta and surrounding Fe atoms is much more rigid than that between V and Fe atoms. In the IXS results, we observed a broad dispersionless mode cross to the acoustic phonons, called the "resonant mode". It disturbs the coherency of phonons and thus will enhance the thermal insulation.

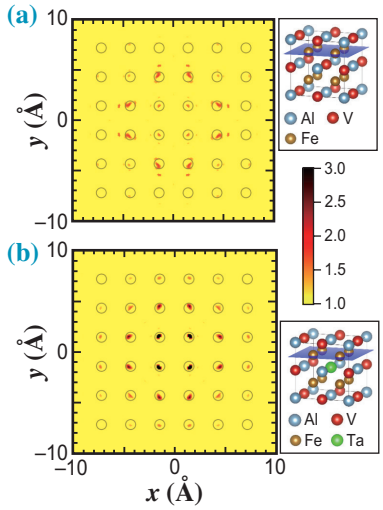

Fig. 4. Atomic images of Fe plane in Ta-doped Fe_2VAl Heusler-type alloy. **(a)** Image around V. **(b)** Image around Ta. The right figures show Fe_2VAl and Ta-doped Fe_2Val structures, respectively. We sliced the images at the blue planes. The color bar indicates the image intensities.

Photoelectron holography

Photoelectron holography is an advanced technology of core-level X-ray photoelectron spectroscopy (XPS). The atomic arrangement of the dopant can be determined, which is one of advantages of XPS measurement. The core-level XPS can identify the elements contained in the material. In addition, the valence state of the element can be directly observed because the binding energy shifts with the valence state (chemical shift). This feature enables us to distinguish holograms from different dopant sites even with the same element, which cannot be performed by other ordinary techniques. In addition, it is sensitive to surfaces and is useful for observing the chemical state of semiconductor circuits that are created on the surface and for tracking changes in the chemical state of catalysts that react on the surface. The principle of photoelectron holography can be explained using Fig. 1(a). Since the scattering power of electrons is larger than that of X-rays by two orders of magnitude, the holographic pattern of PH is more observable than that of XFH.

At SPring-8, some types of apparatus for photoelectron measurement have been installed, as shown in Fig. 5. The display-type spherical mirror analyzer (DIANA) shown in Fig. 5(a) has been in place since 1997. Since it can display the photoelectron angular distribution two-dimensionally in real time, it has supported the development of many photoelectron diffraction and holography techniques. Some examples are given below.

- Principle of photoelectron holography and demonstration of atomic image reconstruction theory [7]. This work mainly theoretically clarified the physics factors of the geometric patterns that appear in high-resolution photoelectron holograms.
- X-ray absorption and magnetic circular dichroism measurements of magnetic thin film, as shown in Fig. 6(a) [8]. It was shown that it is possible to perform layer-by-layer X-ray absorption and magnetic circular dichroism measurements on Ni thin films on a Cu substrate.
- Layered material such as graphene, as shown in Figs. 6(b,c) [9,10]. These studies revealed the atomic arrangement of graphene and buffer layers that can be obtained by heating SiC, and that of graphite showing superconductivity when doped with Ca and K.

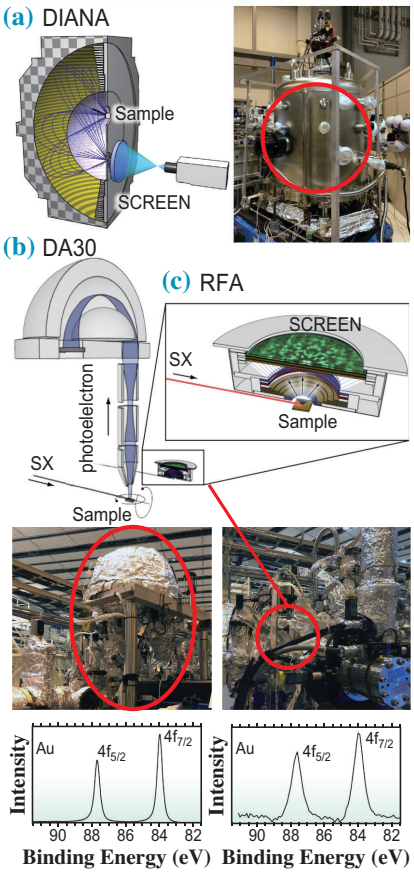

Fig. 5. Electron analyzers for photoelectron holography. **(a)** Display-type analyzer. **(b)** DA30. **(c)** RFA [12].

- Measurement of the reaction structure of the gas-sensing material W-doped ZnO as shown in Fig. 6(d) [11]. The atomic sites of the dopant W were clarified, and it was found that the W atoms migrate to the surface side by heat treatment.

The energy resolution used to be a bottleneck for the precise photoelectron holography measurement and the chemical shift could not be measured. Recently, the apparatus using the DA30 electron energy analyzer (Scienta Omicron) shown in Fig. 5(b) and the retarding field analyzer (RFA) [12] shown in Fig. 5(c) have been developed, and these have markedly improved the energy resolution. The RFA is a display-type electron energy analyzer like DIANA. As shown in Fig. 5(c), the energy resolution of the

RFA is slightly lower than that of the DA30 electron analyzer, but chemical shifts can be sufficiently separated. DA30, on the other hand, has a high energy resolution and can measure fine chemical shifts, as well as relatively low concentrations of dopants. However, the measurement time is long because the sample is measured while being rotated. The RFA is good choice for dopants at concentrations of a few at%, and DA30 is useful for more dilute dopants. Currently, there is a report of a measurement down to 0.06 at% obtained using DA30. As a result of measurements using DA30, the structure of the As dopant in Si crystal [13] and the structure of the P dopant in diamond [14] have been determined. With the improved energy resolution, it is now possible to separate the arrangement of each kind of atom in accordance with the chemical state of the dopant. In As in Si, a substitutional structure and an As_2V structure (Fig. 6(e)) were observed. In P in diamond, a substitutional structure and a PV split vacancy were observed (Fig. 6(f)). In addition, the structural anisotropy attributed to crystal growth was also observed. This information will be important in material fabrication. Photoelectron holography is expected to make great progress in the future.

In the XFH part, we showed the results for the LPSO Mg alloy and Heisler-type thermoelectric material. In the PH part, first we introduced the position-sensitive detectors of photoelectrons used in the experiments and then we showed PH applications to several materials. Both holography techniques have provided valuable information on local structures around dopants that help to understand the material functions. We look forward to welcoming new users reading this review to our community.

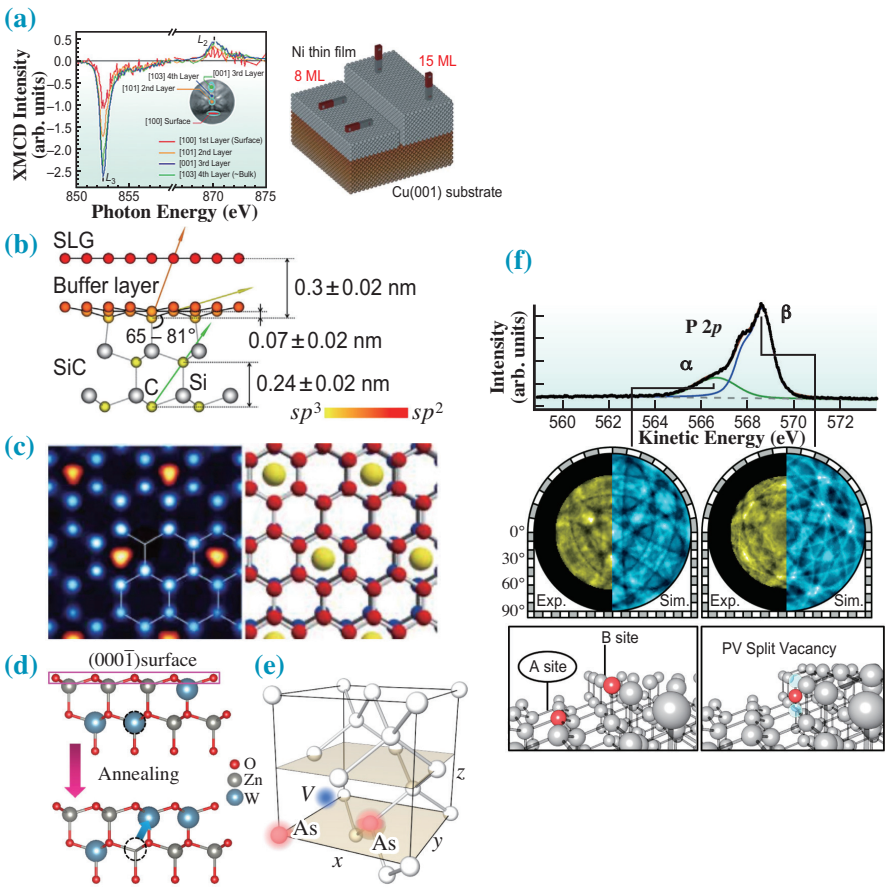

Fig. 6. Experimental results of photoelectron holography (diffraction). **(a)** Measurement of each atomic layer of Ni thin film [8]. The image on the left shows the MCD spectrum of each Ni atomic layer. The image on the right shows the direction of the magnetization in a Ni film. **(b)** Atomic structure of graphene grown on SiC [9] obtained from photoelectron hologram (diffraction). A buffer layer is formed under the graphene layer. **(c)** Atomic arrangement of intercalated K atoms in a layer of graphite [10] obtained from photoelectron hologram. The intercalant metal atom layer was found between two AA-stacked graphenes. The K atomic image revealed 2 × 2 periodicity. **(d)** W structure of the gas sensing material W-doped ZnO [11]. The dopant W atoms were found to occupy the Zn atom sites. Heat treatment caused W atoms to move to the surface side. **(e)** As dopant in Si crystal [13]. Not only substitution sites but also As_2V structures with vacancies were observed, as shown in the figure. **(f)** P dopant in diamond crystal [14]. From the X-ray photoemission results, two components were found, and their photoelectron holograms (Exp.) were obtained. They were determined to be substitutional and PV split vacancy structures. Sim. are the results of photoelectron hologram simulations based on the atomic structures.

Kouichi Hayashi[a,*]
and Tomohiro Matsushita[b]

[a] Nagoya Institute of Technology
[b] Nara Institute of Science and Technology

*Email: hayashi.koichi@nitech.ac.jp

References

[1] K. Hayashi and P. Korecki: J. Phys. Soc. Jpn. **87** (2018) 061003.
[2] K. Hayashi *et al.*: J. Phys. Condens. Matter. **24** (2012) 093201.
[3] N. Happo *et al.*: Jpn. J. Appl. Phys. **57** (2018) 058006.
[4] K. Kimura *et al.*: Mater. Trans. **58** (2017) 539.
[5] T. Nishioka *et al.*: Materialia **3** (2018) 256.
[6] K. Kimura *et al.*: Phys. Rev. B **101** (2020) 024302.
[7] T. Matsushita *et al.*: Phys. Status Solidi B **257** (2020) 2000117.
[8] F. Matsui *et al.*: Phys. Rev. Lett. **100** (2008) 207201.
[9] H. Matsui *et al.*: Surf. Sci. **635** (2015) 1.
[10] F. Matsui *et al.*: Sci, Rep. **6** (2016) 36258.
[11] S. Fukami *et al.*: Phys. Rev. App. **7** (2017) 064029.
[12] T. Muro *et al.*: Rev. Sci. Instrum. **88** (2017) 123106.
[13] K. Tsutsui *et al.*: Nano Lett. **17** (2017) 7533.
[14] T. Yokoya *et al.*: Nano Lett. **19** (2019) 5915.

Crystal structure of the first orphan GPCR

G-protein-coupled receptors (GPCRs) are membrane proteins with seven-transmembrane (7TM) structural features. Of the over 800 members in the human genome, there are more than 100 are orphan receptors whose endogenous ligands are yet to be identified. GPR52 is a Class-A orphan GPCR highly expressed in the brain, particularly in the striatum. The psychiatric diseases in which it plays a role include hyperactivity, schizophrenia [1], psychiatric disorders, brain malformation [2], and cognitive symptoms. Therefore, GPR52 is a promising target for a variety of neurological disorders. Moreover, it was recently reported as a potential therapeutic target for Huntington's disease [3]. However, tool ligand and drug discovery have been largely hampered by a lack of structural understanding due largely to the low homology (< 20%) of GPR52 to any known GPCR structure. Orphan GPCR structures are highly demanded and we decided to solve the first one by focusing efforts on GPR52.

To obtain a stable GPR52 protein for structural determination, we generated and screened over 600 constructs, tried different purification procedures, and did crystallization trials for more than 100 constructs. Finally, we obtained multiple types of crystals for GPR52 and collected diffraction data at SPring-8 **BL41XU** and **BL45XU** with kind help of beamline scientists. Guided by the feedback of data collection at SPring-8 from the initial crystal hits, we immediately optimized the crystals following the right direction which allowed us to obtain the high-quality diffraction data for structural determination within a few months. Finally, we were able to collect three complete data sets at SPring-8 BL41XU and BL45XU beamlines and solved high-resolution structures for GPR52: one in complex with agonist c17 (at 2.2 Å) and two in ligand-free (apo) forms (at 2.8 Å, 2.9 Å) [4].

The two apo structures in the ligand-free state (GPR52-Rub-apo and GPR52-Fla-apo) were engineered with different ICL3 fusion partners and were crystallized in different space groups. Comparison of the two structures reveal that the overall conformations at the transmembrane region were essentially identical (root-mean-square deviation (RMSD) of helix bundle Cα is 1.1 Å), confirming that receptor conformation was not altered by crystal packing (Fig. 1(a)). we will not distinguish the two structures and named them GPR2-apo unless otherwise noted.

With close examination of the GPR52-apo structure, a 22-residue ECL2 caught our attention as it folds into a special configuration and occupies the orthosteric binding pocket of the receptor. To maintain this unique configuration, the side chain of $Y185^{ECL2}$ packs tightly into a local aromatic environment formed by the residues $Y281^{6.51}$, $Y284^{6.54}$ and $F285^{6.55}$ of TM6. In addition, $K182^{ECL2}$ forms a salt bridge with $D188^{ECL2}$, $C193^{ECL2}$ forms a disulfide bond with $C114^{3.25}$ in TM3, both interactions strongly hold the ECL2 in its registry (Fig. 1(b)). Alignment of the ECL2 with canonical ligand binding pocket in other GPCRs suggests that this motif may behave as an agonist intrinsically contributing to the high basal activity of GPR52. To test this hypothesis, mutagenesis

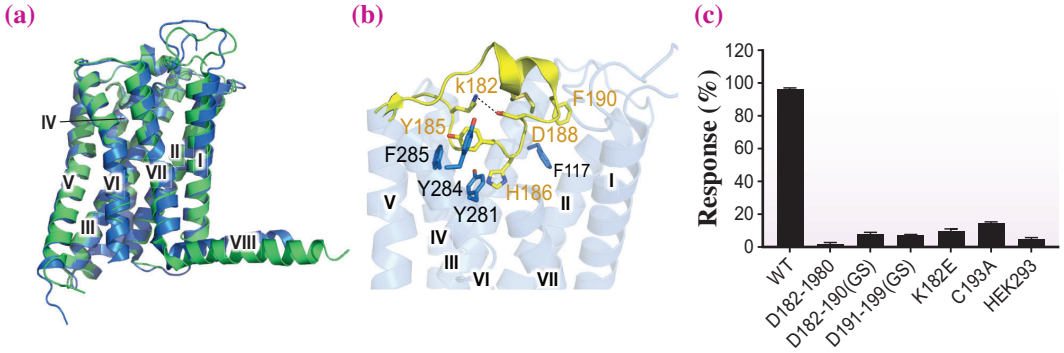

Fig. 1. **(a)** Overall structure of GPR52-rub-apo (green) and GPR52-Fla-apo (blue). **(b)** The close view of the ECL2 in the orthosteric binding pocket. Key residues are shown as sticks. **(c)** Mutations that interfere with the conformation of the ECL2 reduced downstream signaling in the cellular cAMP assay.

and cellular functional assays showed that deleting residues 182–198, replacing residues 182–190 or 191–199 with a 6-residue linker (GGSGGS), breaking the disulfide bond between $C193^{ECL2}$ and $C114^{3.25}$ or mutating the single key residue $K182^{ECL2}$ all markedly reduced the basal activity of GPR52 (Fig. 1(c)).

Next, we were curious where the tool ligand binds if the orthosteric pocket is already occupied by the ECL2. We therefore set out to investigate the binding mode of a GPR52 agonist by co-crystallizing GPR52 with the surrogate ligand c17. The overall conformation of GPR52-c17 is highly consistent with GPR52-apo and the C_α RMSD of the two structures at the helix bundle is 1.7 Å. The most remarkable difference occurs at the N-terminal loop. In the GPR52-c17 structure, it is well-folded and engaged in the coordination with the c17 ligand. In particular, the conformation of the ECL2 region is highly conserved in GPR52-apo and GPR52-c17 structures, suggesting that c17 may play a positive allosteric modulating role to further enhance the receptor activity without disturbing the intrinsic conformation of ECL2. In the GPR52–c17 complex, the N-terminal loop and ECL2 push the ligand towards one side and contribute to the formation of a new ligand pocket—side pocket (Fig. 2(a)).

We compared the side pocket of GPR52 to that of Class-A representative peptide receptors, non-lipid small-molecule receptors and lipid-activated receptors. We found that c17 in GPR52 is located closer to TM1, TM2 and TM7 while other ligands are closer to TM4–TM6—a ligand-binding mode that is commonly seen in other Class-A receptors (Fig. 2(b)). The GPR52 unique ligand-binding side pocket we have revealed can be targeted by rational structure-based ligand design and holds promise for selective drug screening owing to its allosteric-like features.

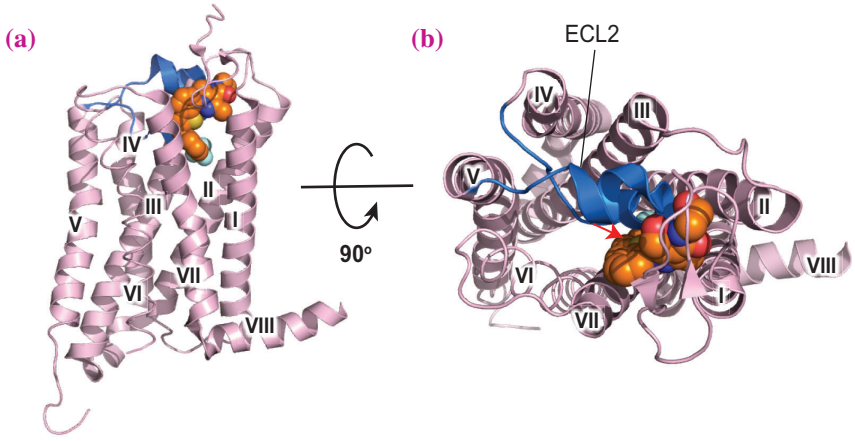

Fig. 2. Side view **(a)** and top view **(b)** of GPR52-c17 (pink-orange) complex, ECL2 is colored in blue.

Xi Lin and Fei Xu*

iHuman Institute, ShanghaiTech University

*Email: xufei@shanghaitech.edu.cn

References

[1] K. Nishiyama *et al.*: J. Pharmacol. Exp. Ther. **363** (2017) 253.
[2] S. K. Krutzke *et al.*: Birth Defects Res. A Clin. Mol. Teratol. **106** (2016) 16.
[3] H. Song *et al.*: Brain **141** (2018) 1782.
[4] *X. Lin, M. Li, N. Wang, Y. Wu, Z. Luo, S. Guo, G.W. Han, S. Li, Y. Yue, X. Wei, X. Xie, Y. Chen, S. Zhao, J. Wu, M. Lei, F. Xu: Nature* ***579*** *(2020) 152.*

Crystal structure of an antagonist-bound ghrelin receptor

Ghrelin, a peptide hormone consisting of 28 amino acids, was originally discovered in the stomach as an endogenous ligand for the growth hormone secretagogue receptor (GHSR, now called the ghrelin receptor), which belong to class A G protein-coupled receptors (GPCRs) [1]. The name "ghrelin" comes from the root word "ghre" in Proto-Indo-European languages meaning "grow", since ghrelin exhibits a potent growth hormone releasing activity. Moreover, ghrelin has a wide range of physiological functions that play roles in appetite stimulation, adiposity, energy homeostasis, memory formation, and hippocampal neurogenesis (Fig. 1) [2]. A salient feature of ghrelin is the *O*-acyl modification at Ser3, which is essential for its activity; des-acyl ghrelin (i.e., ghrelin lacking the acyl modification) is inactive. No other peptide hormone is known to require such an acyl modification for its activity. Despite such an interesting feature, because of the lack of structural information about the ghrelin receptor, it is unclear how the ghrelin receptor recognizes the acyl modification of ghrelin.

To facilitate crystallization, 28 and 20 residues were removed from the N- and C-termini of the ghrelin receptor, respectively, and the thermostabilized apocytochrome b_{562}RIL (bRIL) protein from *Escherichia coli* was fused to the deleted N-terminus. In addition, two mutations have been introduced: Thr130$^{3.39}$Lys (superscripts are the standard residue numbers for GPCRs in accordance with the Ballesteros-Weinstein nomenclature) to improve thermostability and Asn188Gln in the second extracellular loop (ECL2) to avoid glycosylation. Moreover, a Fab antibody fragment specific for the ghrelin receptor (Fab7881) was generated to increase thermostability and to promote the crystallization of the bRIL-conjugated truncated ghrelin receptor. We obtained microcrystals of the ghrelin receptor in a complex with Fab7881 and the antagonist Compound21 [3]. The structure of this complex was determined at 3.3 Å resolution using SPring-8 **BL32XU**.

Like other class A GPCRs, the ghrelin receptor has a canonical seven-transmembrane helical architecture and an intracellular amphipathic helix 8 (Fig. 2(a)). Similarly to other peptide hormone receptors, ECL2 forms antiparallel β-strands with a short hairpin and is stabilized by a highly conserved disulfide bond between Cys116$^{3.28}$ and Cys198^{ECL2}. Fab7881 binds to the third intracellular loop (ICL3) and seems to stabilize ICL3 and improve the thermostability of the ghrelin receptor, allowing its crystal formation.

An antagonist-bound ghrelin receptor has two main characteristics (Fig. 2(b)). There are a bifurcated ligand-binding pocket and the hydrophobic wide gap of transmembrane helices (TM) 6 and 7 (Fig. 2(b)). The binding pocket is separated into two cavities by a salt bridge between Glu124$^{3.33}$ and Arg283$^{6.55}$. Mutations of residues in the salt bridge, Glu124$^{3.33}$Ala and Arg283$^{6.55}$Ala, completely abolished the ghrelin-induced receptor function, whereas after replacement with the cognate amino acid mutants Glu124$^{3.33}$Asp and Arg283$^{6.55}$Lys, the receptor remains functional, although its activity is significantly reduced. Recent NMR and modeling studies suggest that the N-terminus of ghrelin extends down into the bottom of the ligand-binding pocket of the receptor, where it interacts with Glu124$^{3.33}$. Furthermore, the alanine mutation of two other polar amino acids in the ligand-binding pocket, Asp99$^{2.60}$ and Arg102$^{2.63}$, abolishes the receptor activity. Polar amino acids in the ligand-binding pocket are also important in other peptide hormone GPCRs, such as NTSR1 (PDB code; 4grv), ET_B (PDB code; 5glh), and AT2 (PDB code; 5xjm). These polar amino acids likely interact with the peptide main-chain and side-chain atoms in the binding pockets. Four polar amino acids in the ligand-binding pocket of the ghrelin receptor likely play a similar function.

Another characteristic feature of the ghrelin receptor is the gap between TM6 and TM7. We call this gap "the crevasse". Such a wide gap is often found in lipid GPCRs, such as EP4 (PDB code; 5yhl), GPR40 (PDB code; 4phu), and $S1P_1$ (PDB code; 3v2y). On the other hand, no peptide GPCRs with a gap structure have yet been reported. The crevasse of the ghrelin receptor

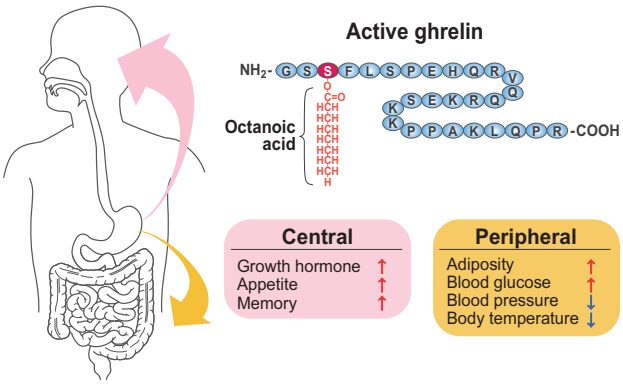

Fig. 1. Structure of human ghrelin and its physiological functions. Ghrelin secreted from the stomach is modified by octanoic acid to the active form, which exhibits various central and peripheral effects.

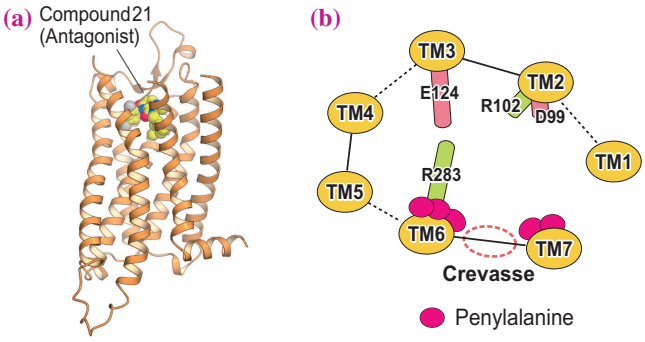

Fig. 2. Structure of the antagonist-bound ghrelin receptor. **(a)** Overall structure of the ghrelin receptor and **(b)** schematic model of the ligand-binding pocket of ghrelin receptor. The ghrelin receptor is shown in cartoon representation and colored in orange. Compound21 (antagonist) is shown as spheres and sticks with carbon atoms in yellow, oxygen in red, and nitrogen in blue. The crevasse is shown as a red dashed line. The five phenylalanine residues are shown as red circles.

contains five phenylalanine residues (Phe279$^{6.51}$, Phe286$^{6.58}$, Phe290$^{6.62}$, Phe309$^{7.39}$, and Phe312$^{7.42}$), indicating that the hydrophobic environment of the crevasse is suitable for receiving the acyl-modified moiety of ghrelin. Results of mutagenesis analyses of the phenylalanine cluster in the crevasse suggest that the cluster is important to the receptor activity. When phenylalanine residues, which are located at the bottom of the crevasse (Phe279$^{6.51}$, Phe309$^{7.39}$, and Phe312$^{7.42}$), are individually mutated to alanine, ghrelin-induced receptor activities are significantly reduced. By contrast, receptor activities of alanine mutants of Phe286$^{6.58}$ or Phe290$^{6.62}$, located near the extracellular surface of the receptor, were only slightly lower than that of the wild-type ghrelin receptor. These results may suggest that the role of phenylalanine residues at the upper part of the crevasse is different from that of the lower part. Some lipid GPCRs accommodate the hydrophobic moieties of their lipid ligands at positions corresponding to the bottom of the crevasse of the ghrelin receptor. For example, the acyl tail of ML056, an antagonist of the $S1P_1$ receptor, and both the tricyclic tetrahydrocannabinol ring and alkyl chain of AM11542, an antagonist of the CB_1 receptor, are placed in this position (Figs. 3(a,b)). These facts suggest that the acyl moiety of ghrelin could be located at the bottom of the ligand-binding pocket where it interacts with phenylalanine residues essential for receptor activation.

This study provides insights into the interactions between ghrelin and its receptor, and our findings may explain why the acyl modification of the ghrelin peptide is necessary for ghrelin receptor activation. Several ghrelin mimetics are under development for the treatment of cancer cachexia or metabolism-linked disorders, and our results may promote the design of more potent and effective ghrelin mimetics.

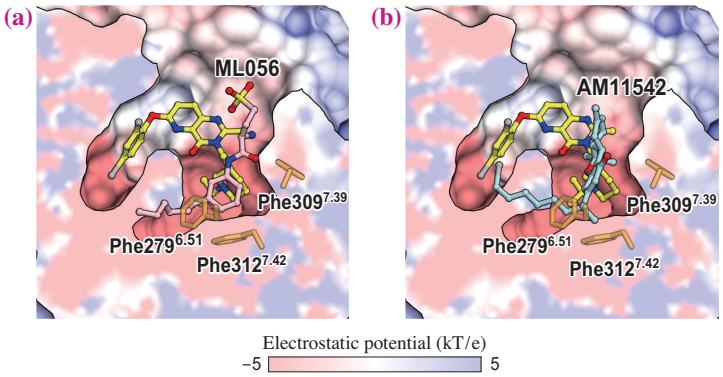

Fig. 3. Ligand binding modes of the ghrelin receptor, $S1P_1$ receptor, and CB_1 receptor. The ghrelin receptor surface and its cross section were colored with respect to electrostatic potential from red (negative) to blue (positive) using APBS tools. **(a)** $S1P_1$ receptor (PDB code; 3v2y) and **(b)** the CB_1 receptor (PDB cord; 5xra) are superposed onto the ghrelin receptor. Phe279$^{6.51}$, Phe309$^{7.39}$, and Phe312$^{7.42}$ of the ghrelin receptor and Compound21 are depicted as orange and yellow sticks, respectively. The sphingolipid mimic $S1P_1$ antagonist (ML056) and the CB_1 antagonist (AM11542) are depicted as pink and cyan sticks, respectively.

Yuki Shiimura[a,b,†,*], So Iwata[b] and Masayasu Kojima[a]

[a] Division of Molecular Genetics, Kurume University
[b] Department of Cell Biology, Kyoto University

[†] Present address: Kurume University

*Email: shiimura_yuuki@kurume-u.ac.jp

References

[1] M. Kojima *et al.*: Nature **402** (1999) 656.
[2] S. Yanagi *et al.*: Cell Metab. **27** (2018) 786.
[3] *Y. Shiimura, S. Horita, A. Hamamoto, H. Asada, K. Hirata, M. Tanaka, K. Mori, T. Uemura, T. Kobayashi, S. Iwata and M. Kojima: Nat. Commun.* ***11*** *(2020) 4160.*

Structural basis for the inhibition of *Plasmodium falciparum* hexose transporter

Malaria remains one of most devastating disease in tropic and subtropic regions around the world, leading approximately 409,000 mortalities during 2019. Five parasites of *Plasmodium spp.* cause human malaria, of which *Plasmodium falciparum* is the deadliest form and is responsible for more than half of total malaria cases. Administration of effective antimalarials, like chloroquine and artemisinin-based combination therapies (ACTs), has markedly decreased malaria-related toll in the past decades. However, the commence and rapid spread of drug-resistance parasites raise increasing concerns to malarial eradication, which results in urgent needs for novel antimalarial chemotherapies [1].

The blood-stage malaria parasites primarily uptake glucose from host erythrocyte as energy source. In particular, *P. falciparum* levers the hexose transporter PfHT1, a single-copy gene without close paralogues, to achieve this goal, which makes it possible to cut off energy supply of asexual stage parasite by inhibiting the transport activity of PfHT1 (Fig. 1(A)). Previous investigation on substrate specificity of PfHT1 yielded a glucose analog, Compound 3361 (C3361), that can moderately and selectively inhibit PfHT1 rather than its human homologue hGLUT1 [2]. However, efforts for chemotherapeutic development based on C3361 has long been hampered due to lack of structural information of PfHT1. Here, we elucidated the molecular model of PfHT1 by solving a 2.6 Å resolution crystal structure of PfHT1 bound with D-glucose. We also successfully revealed a novel ligand-binding-induced allosteric pocket through a 3.7 Å crystal structure of PfHT1-C3361 complex, followed by rational design on the basis of C3361. We succeeded in obtaining a high potent and selective PfHT1 inhibitor, **HTI-1**, which simultaneously targets the orthosteric and allosteric sites of PfHT1 [3] (Fig. 1(B)).

To elucidate the structure of PfHT1 in complex with D-glucose, codon-optimized cDNA of PfHT1 was expressed in Sf9 insect cell. Recombinant PfHT1 was purified through combined biochemical approaches, followed by crystallization using hanging-drop vapor diffusion method. Crystals of PfHT1-glucose complex were screened at SSRF BL18U and diffraction data was collected at SPring-8 **BL32XU**. The structure of PfHT1-glucose complex was solved by molecular replacement, using modified initial model of hGLUT3, at a final resolution 2.6 Å. Similar to other sugar porter (SP) family members, PfHT1 exhibits a canonical major facilitator superfamily (MFS) fold with 12 transmembrane segments (TMs) form two six-helical bundles. The intervening sequence between N and C domains, together with C-terminal segment, constitutes an intracellular helical (ICH) domain (Fig. 2(A)).

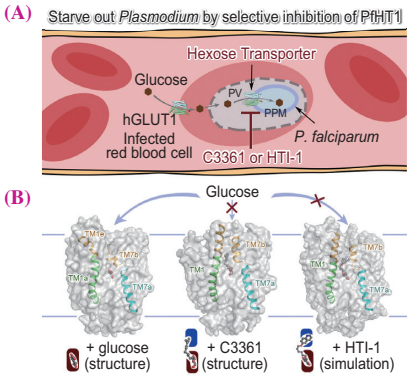

Fig. 1. Schematic diagram of inhibition of PfHT1. **(A)** Cutting off the glucose uptake of *P. falciparum* by selectively inhibiting PfHT1. **(B)** Structural models for C3361 and HTI-1 inhibition.

Analysis of central pocket revealed a highly conserved glucose binding pattern; the sequence and acting mode of glucose binding residues are almost identical to hGLUT1 and hGLUT3 (Fig. 2(B)).

On the other hand, PfHT1 possesses unique features in several aspects. The second half of TM7, designated TM7b, bends to a larger degree toward substrate binding site, which seals the entrance tunnel from extracellular side. Together with the closed intracellular tunnel, PfHT1-glucose complex presents a novel occluded state (Fig. 2(C)). Despite the extracellular half of TM1 also forms a membrane-parallel helix, the TM1e of PfHT1 is much shorter than it in hGLUTs. Two long extracellular loops, L1-2 between TM1 and TM2 and L5-6 between TM5 and TM6, coordinate with each other through H-bonds between Arg67 of L1-2 and Glu196 and Lys191 of L5-6. In addition, TM1 and TM2 is linked by a disulfide bound between Cys61 and Cys70, which is important for the transport activity of PfHT1 (Fig. 2(D)).

The structure determination of PfHT1 in complex with C3361 was unexpectedly challenging. Using the aforementioned vapor diffusion method, we could only obtain tiny crystals without an acceptable diffraction. We turned to Lipid cubic phase (LCP) method and screened thousands of micro-crystals manually or with the help of ZOO system at BL32XU using micro-focus beam. Finally, a 3.7 Å PfHT1-C3361 complex structure was resolved by merging 172 data sets with wedges of 10 degree for each LCP crystals. Structure of PfHT1 bound to C3361 retained occluded state; However, an unprecedented conformational shift was induced by C3361 binding (Fig. 2(E)). Compared to D-glucose bound PfHT1, TM1e and TM7b straighten up upon C3361 association. TM2 and TM4 slightly swap away from center pocket (Fig. 2(F)). Consequently, the

aliphatic tail of C3361 accommodated to a hydrophobic tunnel and a novel allosteric pocket formed at the end of the tail (Fig. 2(G)). Nevertheless, the coordination between PfHT1 and glucose moiety of C3361 is largely unchanged comparing to PfHT1-glucose complex.

Targeting the C3361-induced allosteric pocket, we designed dozens of compounds with modifications on sugar moiety, aliphatic linker, and functional group at the end of its tail. Three compounds, designated **1a**, **1b**, and **1c** (also named as **HTI-1** for its highest potency), stood out for their high efficiency to inhibit the transport activity of PfHT1 (Fig. 3(A)). Among these compounds, an aromatic group (**1a**, phenyl; **1b**, 2-naphthyl) or a heteroaromatic group (**1c**, 6-quinolyl) is attached to the C8 alkyl chain through an ether linker to substitute the vinyl group in C3361. The IC50 decreases in order of C3361, **1a**, **1b**, and **1c**, referring the substitution gradually fits into allosteric site. In addition, all three compounds retain selectivity of PfHT1 over hGLUT1 (Fig. 3(B)), which makes it possible to apply these compounds to selectively kill parasites with minimal effect on human cells. As expected, all rational-designed compounds demonstrate high potency to multi-drug-resistant strain (Dd2) of *P. falciparum* while moderate cytotoxicity is observed on HEK293T/17 cell line (Fig. 3(C)). Besides, an excellent correlation between IC50 and EC50 values of rational-designed C3361 derivatives indicates the suppression of parasites growth is caused by inhibition of PfHT1 activity (Fig. 3(D)).

Taken together, the emergence of multi-drug-resistant malaria necessitates development of next-generation antimalarials that act with alternative molecular target. PfHT1, the unique hexose transporter mediates glucose uptake of *P. falciparum*, was characterized as potential drug target to "starve out the malaria parasites" through cutting off their energy supply. Previous lead optimization was hindered by enigmatic structure of PfHT1. Our insights into PfHT1 in complex with D-glucose or C3361 illuminate the mechanism of C3361 inhibition and reveal a novel ligand-induced allosteric pocket, which establishes a foundation for structural-guided drug discovery. Given the molecular model of central cavity and allosteric pocket, we rational-designed and obtained a high potency and low cytotoxicity lead, **HTI-1**, which effectively suppressed the growth of parasites by blocking their glucose uptake. Our results serve as proof of principle for an orthosteric-allosteric dual inhibition of PfHT1 and pave the way to next-generation antimalarials targeting PfHT1.

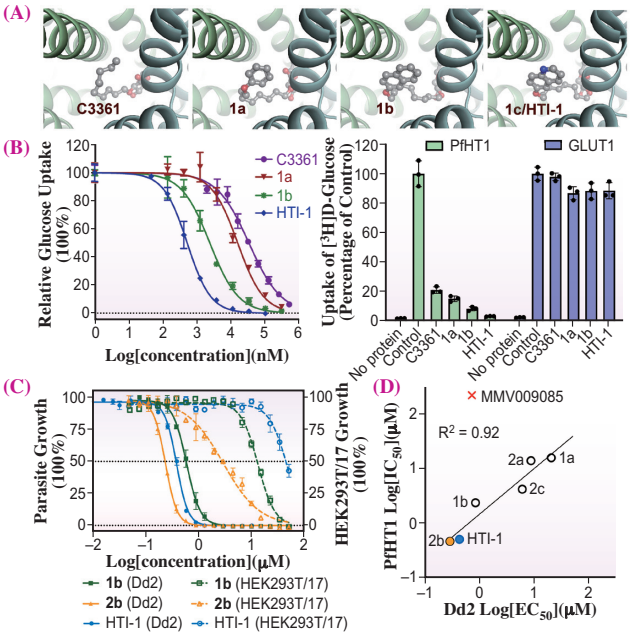

Fig. 3. Rational design and characterization of PfHT1 selective inhibitors. **(A)** Representative of docking results of C3361 and designed inhibitors. **(B)** Proteoliposome based inhibition assay to measure the potency of PfHT1 inhibitors. **(C)** Antiparasitic effect and cytotoxicity of represent PfHT1 inhibitors. **(D)** Correlation between PfHT1 inhibition and parasites growth suppression reveal an on-target effect.

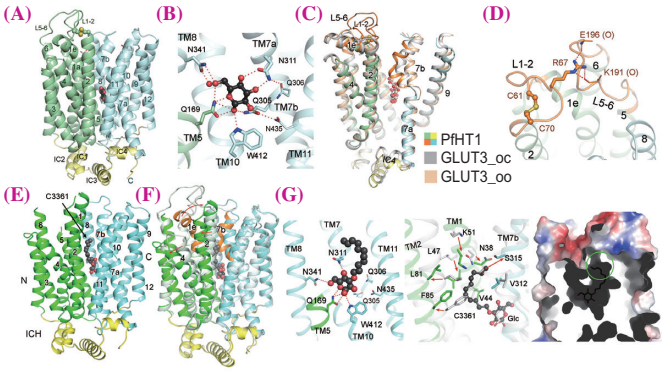

Fig. 2. Crystal structures of PfHT1 bound with D-glucose or C3361. **(A)** Overall structure of PfHT1-glucose complex. **(B)** Coordination of D-glucose in PfHT1. **(C)** Structural comparison between PfHT1 and hGLUT3. **(D)** Unique extracellular loops and disulfide bound of PfHT1. **(E)** Occluded state of PfHT1 in complex with C3361. **(F)** Conformational shift of PfHT1 upon C3361 binding. **(G)** Coordination of C3361 and ligand-induced-allosteric pocket.

Xin Jiang and Nieng Yan[†,*]

State Key Lab. of Membrane Biology, Beijing Advanced Innovation Center for Structural Biology, China
Joint Center for Life Sciences, Tsinghua University, China

[†] Present address: Department of Molecular Biology, Princeton University, USA

*Email: nyan@princeton.edu

References

[1] K. Haldar *et al.*: Nat. Rev. Microbiol. **16** (2018) 156.
[2] T. Joet *et al.*: Proc. Natl. Acad. Sci. USA **100** (2003) 7476.
[3] *X. Jiang, Y. Yuan, J. Huang, S. Zhang, S. Luo, N. Wang, D. Pu, N. Zhao, Q. Tang, K. Hirata, X. Yang, Y Jiao, T. Sakata-Kato, J.-W. Wu, C. Yan, N. Kato, H. Yin, N. Yan: Cell* ***183*** *(2020) 258. e12.*

Structural insights into isoform-selective regulators of mammalian Cryptochromes

The circadian clock is a biological timekeeper that regulates sleep-wake behavior, hormone secretion, body temperature, and metabolism with ~24-hour periodicity. The transcription factors CLOCK and BMAL1 activate transcription of their own inhibitors, encoded by *Period* (*Per*) and *Cryptochrome* (*Cry1* and *Cry2*) genes. Cryptochromes (CRYs) are light-responsive flavoproteins related to DNA repair enzymes, photolyases. In mammals, however, CRYs typically do not bind a flavin cofactor, FAD, and function as light-independent transcriptional repressors of the circadian clock by forming complexes with PER proteins, and translocating to the nucleus where they inhibit CLOCK-BMAL1 to close the negative feedback loop. Dysfunction of CRY proteins affects circadian period, and has been associated with sleep disorders, metabolic disease, and cancer, thus making them attractive therapeutic targets. The first CRY-targeting compound KL001 was found to stabilize CRY proteins and lengthen the circadian period, but KL001 binds to both CRY1 and CRY2 without preference [1]. Since CRY1 and CRY2 have overlapping and distinct cellular functions, the development of isoform-selective modulators is important for the elucidation of unique regulatory mechanisms between CRYs. Crystal structures of the photolyase homology regions (PHRs) of CRY1 [2] and CRY2 [3] provided a foundation for the understanding of compound interactions. However, very high sequence identity in the FAD-binding pockets of CRY1 and CRY2 (where compounds bind) has hampered isoform-selective compound design.

By conducting phenotypic screens of circadian period modulators, we identified first-in-class compounds KL101, TH301, and KL201 that stabilize CRY1 and CRY2 in an isoform-selective manner (Fig. 1) [4,5]. To understand the mechanisms of action of these unique compounds, we determined X-ray crystal structures in complex with CRY1- and CRY2-PHR proteins. Crystals were initially screened at SPring-8 **BL32XU** using ZOO automated data collection, and the final diffraction data were subsequently collected manually at SPring-8 **BL44XU**. We determined the structures of CRY1-apo and CRY1-KL101 at a resolution of 2.0 Å, and CRY1-TH301 and CRY1-KL201 at 2.1 Å [4,5]. All structures formed canonical photolyase folds comprising N-terminal α/β and C-terminal α-helical domains, connected by an extended linker region (Fig. 2). The FAD-binding pocket is located within the α-helical domain and is composed of 17 residues, with only one variant residue between CRY1 and CRY2 (Fig. 3). We divided the FAD-binding pocket into three regions: Hydrophobic region 1, hydrophobic region 2, and the affinity region, due to interactions formed with various compound moieties (Fig. 3).

The compounds KL101 (CRY1-selective) and TH301 (CRY2-selective) consisted of a phenylpyrazole moiety (Fig. 1) which formed multiple hydrophobic interactions with residues in hydrophobic region 2, and an H-bond with R358 (Fig. 3). A methoxy group in TH301 engaged in an H-bond with W397. Amide groups in KL101 and TH301 formed an H-bond to S396, and TH301 formed a unique compound-induced interaction between the amide oxygen and Q289 (a typically disordered residue). A *meta*, *para*-dimethylphenyl (KL101) and a cyclopentyl (TH301) group bound at hydrophobic region 1, with a notable difference in the conformation of W399: "Out" in CRY1-KL101, and "in" in CRY1-TH301. The steric bulk of the *meta*, *para*-dimethylphenyl group (KL101) appeared to preclude an "in" conformation of W399, and revealed a potential CRY1-selective mechanism in KL101 binding. The smaller steric bulk of the cyclopentyl induced a stacking interaction with W399, which rotated to an "in" conformation that was significantly different to the "out" conformation in CRY1-apo. We analyzed structural activity relationships (SARs) of KL101 and TH301 derivatives to help characterize their interactions observed in the crystal structures. The *para*-methyl group of KL101 (Fig. 1, blue) and the *meta*-methyl (Fig. 1, red) were important for compound activity. Removal or substitution of these groups resulted in severely reduced activity. Regarding TH301 derivatives, removal or substitution of the methoxy group caused inactivity and reduced activity, respectively, and the cyclopentyl and chlorophenyl

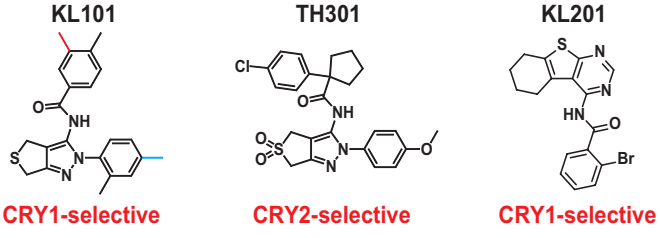

Fig. 1. CRY1 and CRY2 isoform-selective compounds. Important KL101 *para*- and *meta*-methyl groups are colored blue and red, respectively.

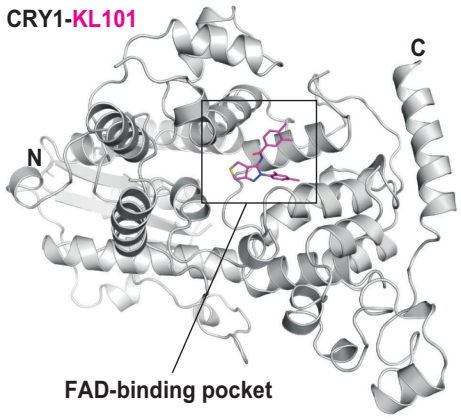

Fig. 2. Overall crystal structure of CRY1 in complex with KL101.

were essential for activity. The CRY1-selective compound KL201 contains a small bromophenyl group that occupied hydrophobic region 2, with the bromine atom facilitating a π-stacking interaction between the phenyl group and W397 (Fig. 3). A heterocyclic thienopyrimidine and cyclohexyl moiety occupied hydrophobic region 1, forming hydrophobic and stacking interactions with aromatic residues. W399 adopted an "out" conformation perhaps due to increased steric bulk compared to TH301. The KL201 amide formed a canonical H-bond with S396, as well as an H-bond with R358. SAR analyses of KL201 derivatives identified an essential role of the bromophenyl in compound activity, whereas the steric bulk of the cyclohexyl (connected to the thienopyrimidine) had a size-dependent effect.

The subsequent determination of the CRY2-TH301 structure (PDB: 6KX8) revealed very similar binding mechanisms to CRY1-TH301 [4]. Comparison of KL101, KL201 and TH301 structures, showed differential organization of two core FAD-binding pocket residues: H355 and W399 in CRY1 (corresponding to H373 and W417 in CRY2). Equivalent residues in *Drosophila* CRY have been implicated in the binding of a CRY C-terminal tail (CCT). We tested the response of compounds on mutant CRY1 and CRY2 proteins and found the CCT to play an important role in isoform selectivity, perhaps by forming interactions with differentially arranged FAD-binding pocket residues. The results of our studies provide a basis to understand how isoform-selective compounds interact with CRYs, and a rationale into the design of compounds with potentially improved selectivity.

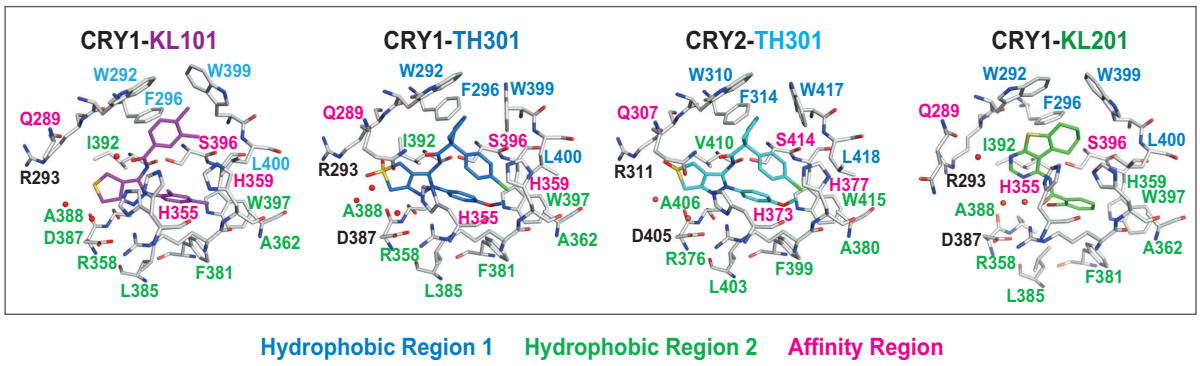

Fig. 3. Interactions of KL101, TH301, and KL201 with CRY1, and TH301 with CRY2. CRY1 H355 and W399 (corresponding to CRY2 H373 and W417) were differentially organized by compounds.

Simon Miller and Tsuyoshi Hirota*

Institute of Transformative Bio-Molecules, Nagoya University

*Email: thirota@itbm.nagoya-u.ac.jp

References

[1] T. Hirota *et al.*: Science **337** (2012) 1094.
[2] A. Czarna *et al.*: Cell **153** (2013) 1394.
[3] W. Xing *et al.*: Nature **496** (2013) 64.
[4] *S. Miller, Y.L. Son, Y. Aikawa, E. Makino, Y. Nagai, A. Srivastava, T. Oshima, A. Sugiyama, A. Hara, K. Abe, K. Hirata, S. Oishi, S. Hagihara, A. Sato, F. Tama, K. Itami, S.A. Kay, M. Hatori and T. Hirota: Nat. Chem. Biol.* ***16*** *(2020) 676.*
[5] *S. Miller, Y. Aikawa, A. Sugiyama, Y. Nagai, A. Hara, T. Oshima, K. Amaike, S.A. Kay, K. Itami, T. Hirota: Cell Chem. Biol.* ***27*** *(2020) 1192.*

Structural basis of the intracellular interaction between type IIa receptor protein tyrosine phosphatases and Liprin-α

In a mammalian brain, billions of neurons are connected and form circuits for brain functions. Neurons are composed of three parts: an axon, dendrites, and a cell body (Fig. 1(a)). The axon terminal of one neuron is connected to the dendrites or cell bodies of another neuron. Neuronal signals are transmitted from the axon terminal to the attached dendrites or cell bodies. The connection between neurons is mediated by a cell-cell adhesion termed a synapse, which is specialized for neuronal signal transmission (Fig. 1(b)). The axon terminal side of the synapse is termed a presynapse, while the dendritic or cell-body side is termed a postsynapse. The pre- and postsynapses face each other across a synaptic cleft. At the presynapse, synaptic vesicles (SV) containing neurotransmitters are pooled, and the neurotransmitters are released to the synaptic cleft upon action potential-evoked Ca^{2+} influx. At the postsynapse, ion-channel-type neurotransmitter receptors generate action potentials upon binding to the neurotransmitters released to the synaptic cleft. Dense molecular assemblies or condensates are formed at both pre- and postsynapses, which are termed an active zone (AZ) and postsynaptic synaptic density (PSD), respectively. The AZ is an ultrastructure for Ca^{2+}-dependent neurotransmitter release, while the PSD is an ultrastructure for the neurotransmitter-dependent generation of action potentials. Understanding the molecular mechanisms underlying the formation of the AZ and PSD will help to understand how synapses are formed to establish a neural circuit.

Synaptic organizers are a family of cell adhesion molecules that can induce synapse formation through extracellular interaction across the synaptic cleft (Fig. 1(b)). Pre- and postsynaptic organizers interact with each other and stimulate the accumulation of pre- and postsynaptic proteins to induce the formation of the AZ and SV pools at the presynapse and the PSD at the postsynapse, respectively. Type IIa receptor protein tyrosine phosphatases (IIa RPTPs) function as presynaptic organizers. Mammalian IIa RPTPs consist of three members, LAR, PTPσ, and PTPδ. The large extracellular domain (ECD) of IIa RPTPs interacts with the ECD of various partner postsynaptic organizers. Functional defects in synaptic organizers have been reported to be associated with neurodevelopmental disorders such as autism and intellectual disability. We and other research groups have extensively studied the mechanism of the extracellular interaction between IIa RPTPs and their postsynaptic partners by crystallography and other biophysical techniques in combination with structure-based mutational analyses *in vitro* and *in cellulo* (see our latest review [1]). On the other hand, the structural basis of the intracellular interaction with downstream effectors of IIa RPTPs remained unknown.

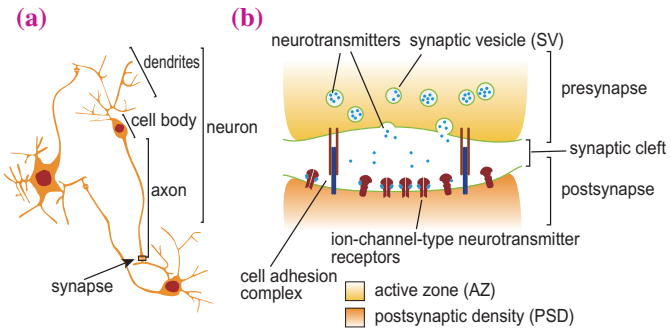

Fig. 1. Schematic of neurons **(a)** and a synapse **(b)**.

The ECD of IIa RPTPs is followed by a single transmembrane helix and a cytoplasmic domain, which is composed of two protein tyrosine phosphatase domains (Fig. 2(a)). The membrane-proximal domain (D1) is catalytically active, whereas the membrane-distal one (D2) is inactive. The D2 domain of IIa RPTPs has been reported to directly interact with several synaptic proteins including Liprin-α. The intracellular interactions of IIa RPTPs with synaptic proteins via the D2 domain are critical to the synaptogenic activity. Liprin-α is the first protein identified as an intracellular binding partner of IIa RPTPs and is localized in the AZ. Among four mammalian Liprin-α isoforms (Liprin-α1–Liprin-α4), Liprin-α2 and -α3 are predominant in the brain. All isoforms share a similar domain organization and contain an N-terminal coiled-coil domain and three tandem sterile alpha motifs (SAM1–SAM3; tSAM; Fig. 2(a)). The N-terminal coiled-coil domain binds to other AZ proteins including CAST/ELKS and RIM, whereas the tSAM domain interacts with IIa RPTPs, CASK, and Liprin-β. Liprin-α may serve as a hub for synaptic function.

To elucidate the mechanism of the interaction between IIa RPTPs and Liprin-α, we determined the crystal structure of the complex between the D2 domain of mouse PTPδ and the tSAM domain of mouse Liprin-α3 at 1.91 Å resolution (Fig. 2(b)) [2]. X-ray diffraction data were collected at 100 K at SPring-8 **BL41XU**. The D2 domain of PTPδ adopts an α/β structure similar to the reported D1 and D2 structures of IIa RPTPs [3,4]. The tSAM domain of Liprin-α3 has

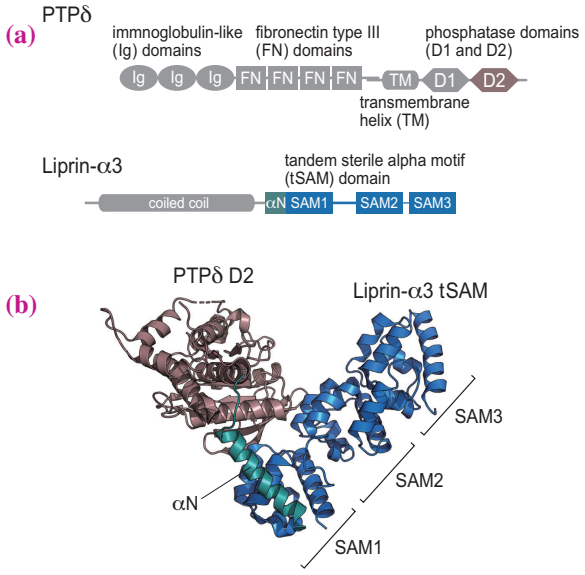

Fig. 2. **(a)** Domain organizations of PTPδ and Liprin-α3. The regions analyzed in this study are colored in brown (PTPδ D2), green (Liprin-α3 tSAM αN), and blue (Liprin-α3 tSAM SAM1–SAM3). **(b)** Overall structure of the complex between PTPδ D2 and Liprin-α3 tSAM. The coloring scheme is the same as that in (a).

an additional helix located at the N-terminal end of SAM1 (αN). The individual SAM structures and their relative configurations of the PTPδ D2-bound Liprin-α3 are similar to those of the previously reported CASK-bound Liprin-α2 [5]. Three SAMs in the tSAM domain of Liprin-α seem to function as a single structural unit.

The D2 domain of PTPδ interacts with αN, SAM1, and SAM2 of Liprin-α3 but not with SAM3. Further intermolecular interaction analysis using surface plasmon resonance (SPR) spectroscopy of site-directed mutants of PTPδ D2 or Liprin-α3 showed that the interfaces with SAM1 and SAM2 are critical to the binding between PTPδ D2 and Liprin-α3 tSAM. Tyr1373, Leu1380, Phe1399, and Phe1430 of PTPδ form a hydrophobic pocket that accommodates Trp856 of Liprin-α3 at the interface with SAM1 (Fig. 3(a)). Phe1430 of PTPδ hydrophobically interacts with Leu978 of Liprin-α3, and Arg1397 and Asp1433 of PTPδ form hydrogen bonds with Glu976 and Arg971 of Liprin-α3, respectively, at the interface with SAM2. These structural features well explain the specificity between the D2 domain of IIa RPTPs and the tSAM domain of Liprin-α proteins. The effects of the PTPδ mutations that impair the interaction with either or both SAM1 and SAM2 domains of Liprin-α on presynaptic differentiation were further examined by artificial synaptogenic assays. Briefly, single point mutations of PTPδ at the interface with Liprin-α SAM1 (Y1373A) or with SAM1/SAM2 (F1430A) disturbed the synaptogenic activity, which was observed in wild-type PTPδ and a triple mutant of PTPδ at the interface with Liprin-α αN (F1503A D1504A Y1506A). The docking analyses using other Liprin-α-binding proteins and *in vitro* binding assay suggested the tripartite assembly of IIa RPTPs, Liprin-α, and CASK (Fig. 3(b)). The predicted geometry of the tripartite complex raises the possibility that this complex can form a larger complex by binding to other AZ proteins and may function as a platform of the AZ. Further studies on this molecular assembly may help us gain a deeper understanding of the molecular mechanism of synapse formation.

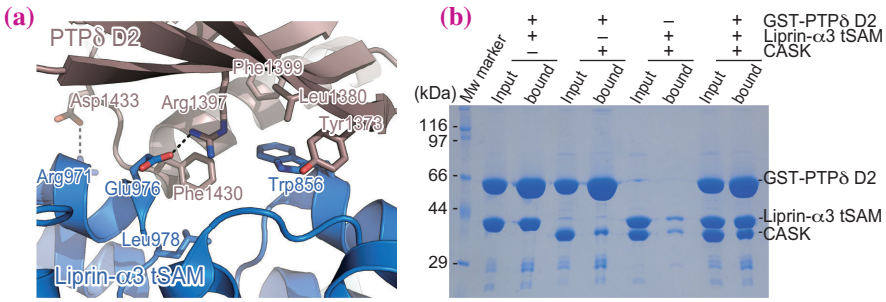

Fig. 3. **(a)** Close-up view of the interaction between PTPδ D2 and Liprin-α3 tSAM. The interacting residues are shown as sticks. Dotted lines indicate hydrogen bonding. The coloring scheme is the same as that in Fig. 2. **(b)** GST pulldown assays to test the tripartite assembly of PTPδ, Liprin-α3, and CASK. Samples were analyzed by SDS-PAGE with Coomassie Brilliant Blue staining.

Shuya Fukai

Department of Chemistry, Kyoto University

Email: fukai@kuchem.kyoto-u.ac.jp

References

[1] S. Fukai and T. Yoshida: FEBS J. (2020) DOI: 10.1111/febs.15666 - in press.
[2] *M. Wakita, A. Yamagata, T. Shiroshima, H. Izumi, A. Maeda, M. Sendo, A. Imai, K. Kubota, S. Goto-Ito, Y. Sato, H. Mori, T. Yoshida, S. Fukai: Nat. Commun.* ***11*** *(2020) 649.*
[3] S.C. Almo *et al.*: J. Struct. Funct. Genomics **8** (2007) 121.
[4] H.J. Nam *et al.*: Cell **97** (1999) 449.
[5] Z. Wei *et al.*: Mol. Cell **43** (2011) 586.

A new powerful research tool for GPCR structure determination

G-protein-coupled receptors (GPCRs) are the largest transmembrane receptor family in humans and consist of approximately 800 genes. They are involved in several physiological functions, such as immune response, blood pressure regulation, nerve stimulation, vision, and smell (Fig. 1) [1]. Hence, drugs that target GPCRs have been developed to treat multiple human diseases, such as central nervous system disorders, inflammatory diseases, metabolic imbalances, cardiac diseases, and cancer [2]. All GPCRs have conserved seven-pass transmembrane helices (TM1-7) that are connected by three extracellular loops (ECL1-3) and three intracellular loops (ICL1-3) (Fig. 1). The third intracellular loop (ICL3) is very flexible and interacts with G proteins, which are necessary for intracellular signal transduction [3].

During small molecule drug development, knowledge of the three-dimensional structure of the target protein with the candidate compound is very useful for refining the compound to improve its binding capacity. This method—structure-based drug design (SBDD)—has been widely used since the 1990s. By the SBDD approach, rational drug design is possible, which greatly improves the success rates of drug development. However, the structure determination of GPCRs is very difficult owing to their poor protein expression in native tissues or heterologous expression systems, low protein stability, and the presence of several receptor conformational states. Over the last ten years, several technologies for protein expression, purification, crystallization, and X-ray diffraction data collection have been developed [4]. To improve the stability of GPCRs for crystallization, ICLs are often replaced with soluble proteins, such as T4 lysozyme, thermostabilized apocytochrome b562 from *Escherichia coli* M7W/H102I/R106L (BRIL), or rubredoxin [4]. Such soluble proteins could also be attached to the N-terminus of GPCRs. In cases where the target GPCR cannot be successfully crystallized even after its fusion to soluble proteins, additional approaches are needed to enhance crystallizability, and antibodies that specifically bind to target GPCRs are often used for this purpose (Fig. 2(a)). Although this approach is useful to expand the soluble regions of the target for crystal packing [4], antibodies must be screened for each target GPCR to identify those with high binding affinity; this is very difficult and laborious. Another common approach to increase the thermal stabilities of GPCRs is to mutate the transmembrane helices [4]. In this method, the mutation sites are originally specified using the extensive knowledge of the active and inactive forms of the adenosine A_{2a} receptor. However, the screening of the mutation sites within the target GPCR is still necessary to determine those

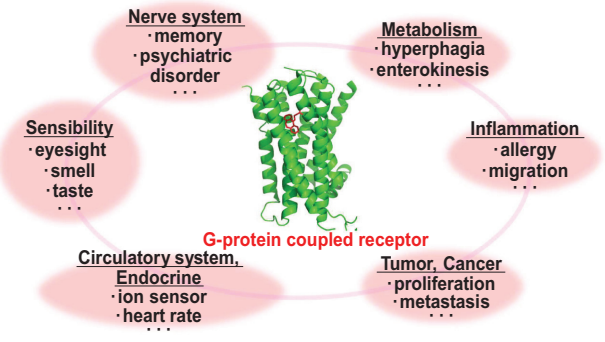

Fig. 1. GPCRs are involved in several physiological functions, such as immune response, blood pressure regulation, nerve stimulation, vision, and smell. The molecule at the center is a model of GPCR with seven-pass transmembrane helices.

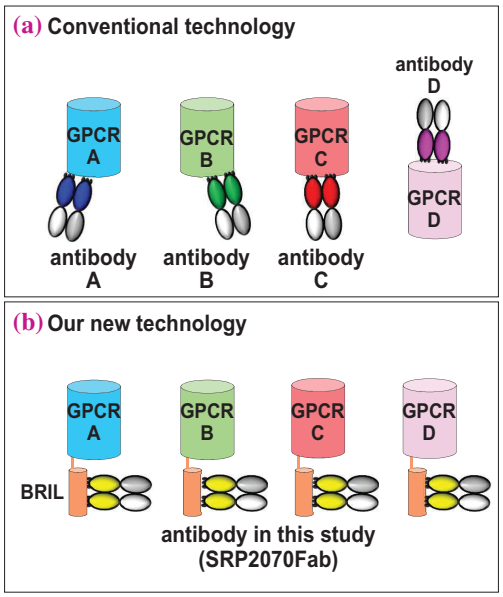

Fig. 2. Advantage of our new technology. **(a)** The conventional technology requires the preparation of antibodies for every GPCR. Producing antibodies that are useful for crystallization is very laborious work. **(b)** Our new antibody (SRP2070Fab) recognizes BRIL. Hence, once BRIL is attached to GPCRs, SRP2070Fab can be used for all GPCRs.

that stabilize the active or inactive state before the construct can be used for crystallization experiments. As this approach is also very strenuous and time-consuming, there is an urgent need for optimization methods that are more efficient and can be widely applied to various GPCR targets for crystallography.

To solve this problem, we produced a new antibody (SRP2070) targeting BRIL [5]. We found that a fragment of this antibody (SRP2070Fab) facilitated the crystallization of the BRIL-tagged, ligand-bound GPCRs (Fig. 2(b)) and determined the structures of 5-hydroxytryptamine receptor 1B ($5HT_{1B}$) with ergotamine (PDB:6JXB) and a Type-2 angiotensin II receptor (AT_2R) with [Sar1, Ile8]-angiotensin II (s-Ang II) (PDB:6JXO) (Fig. 3) [5]. These diffraction data were collected at SPring-8 **BL32XU**. To use SRP2070Fab for SBDD, it is very important to confirm that SRP2070Fab does not adversely affect the conformation of the ligand. We compared the ligand electron density maps with and without SRP2070Fab for both $5HT_{1B}$/ergotamine and AT_2R/s-Ang II [5]. There was no difference for either $5HT_{1B}$/ergotamine or AT_2R/s-Ang II. In short, although SRP2070Fab does not affect GPCR structures, it can improve the crystal packing. Considering these results, SRP2070Fab might be a universal chaperone for the crystallization of BRIL-fused GPCRs.

In addition, we anticipate that SRP2070Fab may also be used for cryo-EM analyses. In recent years, the resolution of cryo-electron microscopy has improved, and several structures of GPCRs have been determined by this technique [6]. By attaching SRP2070Fab to BRIL-fused GPCRs, the molecular weight is increased and the SRP2070Fab shape may be useful as a fiducial marker. Hence, we are convinced that this new tool (SRP2070Fab) will significantly accelerate structure determination and the design of small molecular drugs targeting proteins.

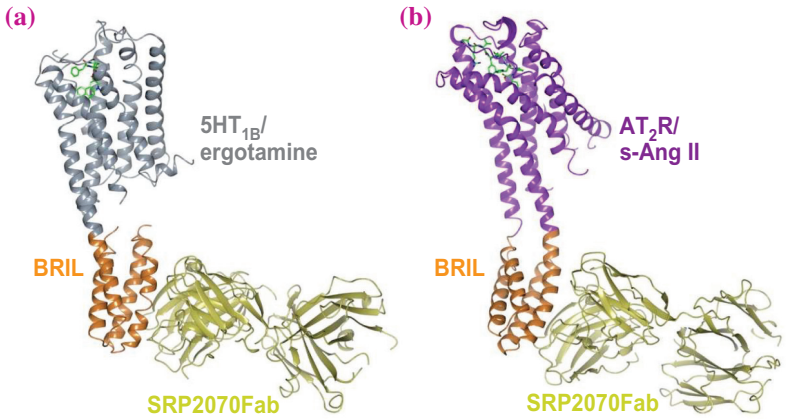

Fig. 3. Overall structures of 5HT1B-BRIL/ergotamine/SRP2070Fab and AT2R-BRIL/s-Ang II/SRP2070Fab. **(a)** Overall structure of 5HT1B -BRIL/ergotamine/SRP2070Fab. Ergotamine is shown as sticks. Each molecule is colored as follows: 5HT1B (light purple), BRIL (light brown), and SRP2070Fab (yellow). **(b)** Overall structure of AT2R-BRIL/s-Ang II/SRP2070Fab. s-Ang II is shown as sticks. Each molecule is colored as follows: AT2R (purple), BRIL (light brown), and SRP2070Fab (yellow).

Hikaru Miyagi[a], So Iwata[b,c] and Jun-ichi Saito[d,*]

[a] R&D Division/Tokyo, Kyowa Kirin Co., Ltd.
[b] Department of Cell Biology, Kyoto University
[c] RIKEN SPring-8 Center
[d] R&D Division/Shizuoka, Kyowa Kirin Co., Ltd.

*Email: jun.saito.su@kyowakirin.com

References

[1] P.M. Conn *et al.*: Pharmacol. Rev. **59** (2007) 225.
[2] W. Thomsen *et al.*: Curr. Opin. Biotechnol. **16** (2005) 655.
[3] Y. Lee *et al.*: J. Med. Chem. **61** (2018) 1.
[4] J. Xiang *et al.*: Trends Pharmacol. Sci. **37** (2016) 1055.
[5] *H. Miyagi, H. Asada, M. Suzuki, Y. Takahashi, M. Yasunaga, C. Suno, S. Iwata and J. Saito: Sci. Rep.* ***10*** *(2020) 11669.*
[6] H.A. Safdari *et al.*: Trends Cell Biol. **28** (2018) 591.

Characterizing DDS nanoparticles containing therapeutic DNAs or RNAs

The FDA approved the first therapeutic drug based on RNA interference, Onpattro, in 2018. Loaded siRNA is delivered into the cytoplasm of hepatocytes by means of a lipid nanoparticle (LNP). This LNP–siRNA complex (i.e., lipoplex) consists of its cargo siRNA and several lipids, including cationic ones. The chemical structure of the cationic lipid has been optimized for RNA encapsulation and intracellular delivery. The success of Onpattro has enhanced enthusiasm in related research areas. A large number of nanomedicines have been reported, but only a few of them are clinically approved. The leading cause of the failure may be a lack of preclinical characterization [1]. To attain marketing approval, it is desirable to clarify physicochemical properties such as average particle size, dispersibility, particle shape, surface charge, drug loading and release, and surface coating. It is believed that these physicochemical properties affect the therapeutic effects such as pharmacokinetics, biodistribution, and toxicity.

We have been investigating the relationship between the structural properties of nanomedicines and their biological properties by scattering techniques. We showed, for example, that the structure of drug carriers and the amount of drug loading are closely related [2], and a biocompatible polymer behavior on the surface of drug carriers affects the biocompatibility [3]. In this paper, we introduce the structural characterizations of transfection carriers using SAXS at SPring-8 **BL40B2**.

To achieve efficient transfection, lipid nanoparticles such as cationic liposomes, consisting of cationic lipids, co-lipids, and stealth lipids, are often used. The major roles of cationic lipids are complexation with anionically charged nucleic acids and interaction with the anionic cell. Our group has developed aromatic amine (BA) compounds as gene delivery reagents with a higher efficiency and a lower toxicity than commercial products [4]. We evaluated the transfection efficiency for a BA system containing two phospholipids, L-α-phosphatidyl ethanolamine dioleoyl (DOPE) and 1,2-dilauroyl-sn-glycero-3-phosphocholine (DLPC) and pGL3 cording luciferase. The luciferase gene expression, calculated as a relative light unit (RLU) per mg of total cellular protein, strongly depends on the composition. We compared the supramolecular structures between BA: DOPE: DLPC = 1:0:1 (composition A) with the lowest transfection efficiency (11.6 RLU/ug protein, i.e., almost zero) and 1:2:1 (composition B) with the highest transfection efficiency (2.5×10^5 RLU / ug protein).

The results of SAXS measurement at composition A showed that a spherical micelle was formed before adding DNA, and the structural transition occurred from a micelle to a cylinder at $26.4 > N/P > 4.4$. Here, the N/P ratio generally means the molar ratio of the nitrogen in the lipid to the phosphate in nucleic acids. The fitting analysis of these profiles suggests that once DNA forms an ion pair with BA, the DNA must be included inside the cylinder, and the cylinder surface is covered with the rest of the free lipids. Moreover, we found that further addition of DNA ($N/P > 3.3$) induced the structural transition from cylindrical to lamellar. At composition B, a hexagonally packed cylinder was formed before adding DNA (Fig. 1). The addition of DNA did not induce structural transitions but enhanced the hexagonal ordering and reduced the distance between cylinders from 7.16 nm to 6.85 nm. This indicates that DNA plays a role in adhesion. We conclude that DNA is incorporated into the hydrophobic domain at composition A and the hydrophilic domain at composition B and that the difference in the DNA location in the complex is related to the transfection efficiency.

A recent trend is to use cationic lipids mainly to encapsulate nucleic acids and to cover particle surfaces with a biocompatible polymer, such as PEG or a polysaccharide, because most cationic lipids

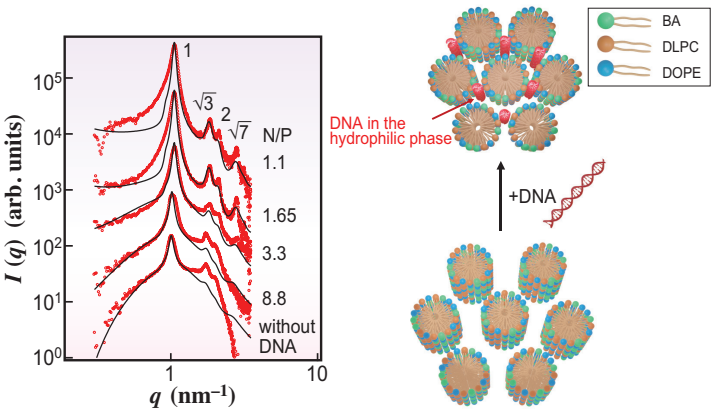

Fig. 1. N/P ratio dependence of SAXS profiles at composition B and schematic illustration of structural transition of the complex by adding DNA. Red dots and black lines show experimental data and theoretical curves, respectively.

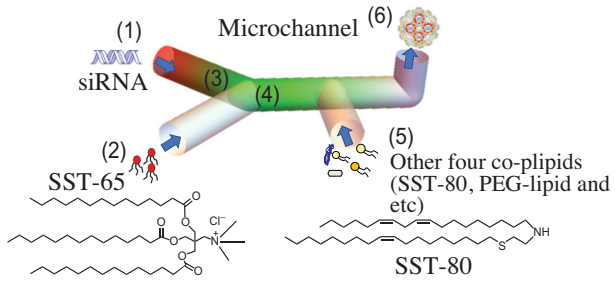

Fig. 2. Schematic illustration of the two-step mixing microchannel and chemical structures of SST-65 and SST-80. The numbers in parentheses show the lipoplex components (and mixing process).

have a high toxicity. Kyowa Kirin Co. designed a new cationic lipid denoted SST-65 with three alkyl tails and a new ionizable cationic one, SST-80 [5]. The cationic lipid/siRNA complex was prepared by two-step mixing using a microfluidic technique (Fig. 2). In the first step, siRNA (1) was mixed with SST-65 in EtOH-rich solution (2) and then mixed with a solution of other lipids (5), followed by solvent exchange with water. We changed the concentration of the co-lipids (5). First, the structure of the siRNA/SST-65 complex prepared in the first step was investigated using SAXS. The result showed that siRNA was coated by cationic SST-65, judging from the increased diameter and length in comparison with siRNA alone [compare scattering profiles (1)–(4) in Fig. 3(a)]. Then, the structures of the final products (6) were evaluated. Cryo-TEM images showed a spherical shape with a 20–50 nm radius packed with some filling (Fig. 3(b)). The inside patterns of the sample without siRNA (Ref. 2) and the complex containing a small amount of siRNA at N/P = 9.5 appeared to be patchy or spotty rather than circular. In contrast, the complex at N/P = 3.5 and 2 showed onion-like patterns (see Fig. 3(b)). These findings indicate the importance of the presence of siRNA. To determine the detailed structures of the complexes, SAXS analysis was carried out by changing the ratio of (5). Figure 3(b) shows the SAXS profiles for samples with different N/P ratios and the sample without siRNA as well as TEM images. The profile of the sample without siRNA showed no peaks but a small shoulder in the range of $q = 1.8–2.5$ nm^{-1}, indicating the thickness of the bilayer structures. The shoulder became obvious at N/P = 9.5, and a diffraction peak appeared at N/P = 6.5. This diffraction peak increased with the concentration of siRNA. According to the analysis using the Caillé theory, the layer spacing is consistent with the length of the adjacent onion patterns in cryo-TEM images, and siRNA leads to more ordering of lamellar structures. Judging from these results, we conclude that the complex forms a core–shell sphere; the densely packed core mainly consists of SST-65 and siRNA, and PEG chains cover the particle surface (Fig. 3(c)).

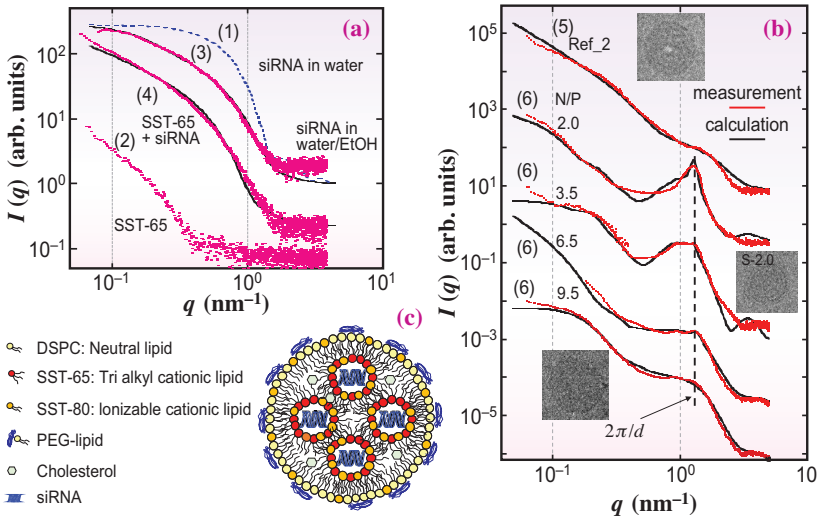

Fig.3. **(a)** SAXS profile changes on adding SST-65 to siRNA, **(b)** SAXS profiles at different N/P samples as well as TEM images. Red dots and black lines show experimental data and theoretical curves, respectively. The numbers in parentheses in (a) and (b) show the corresponding scattering profiles with the lipoplex components shown in Fig. 2. **(c)** Schematic illustration of the lipoplex. [5]

Mina Sakuragi[a] and Kazuo Sakurai[b,*]

[a] Department of Nanoscience, Sojo University
[b] Department of Chemistry and Biochemistry, University of Kitakyushu

*Email: sakurai@kitakyu-u.ac.jp

References

[1] S.R. D'Mello *et al.*: Nat. Nanotechnol. **12** (2017) 523.
[2] *M. Sakuragi, T. Zushi, R. Seguchi, T. Arai, K. Taguchi and K. Kusake: Chem. Lett.* ***46*** *(2017) 185.*
[3] S. Fujii *et al.*: ACS Symposium Series **1271** (2017) Chapter 5, 115.
[4] M. Sakuragi *et al.*: J. Phys. Conf. Ser. **184** (2009) 012008.
[5] *K. Aburai, K. Hatanaka, S. Takano, S. Fujii and K. Sakurai: Langmuir* ***36*** *(2020) 12545.*

Exercise regulates microRNAs to preserve coronary and cardiac function in the diabetic heart

Diabetes is associated with numerous long-term health complications, in particular cardiovascular disease. The onset of heart disease in diabetes begins at an early stage with impaired coronary blood flow as a precursor for heart failure [1]. Unfortunately, patients in the early stages of diabetes remain asymptomatic to any cardiac dysfunction till the later stage of the disease, thereby restricting its effective therapeutic management. An effective method for the early diagnosis of diabetic heart disease is critical for implementing effective therapeutic strategies [2].

MicroRNAs (miRNAs) are key players in various cardiovascular events through the regulation of cardiac gene expression. Indeed, circulating miRNA's serve as potential diagnostic biomarkers for cardiovascular disease [2]. Their potential role as biomarkers for the early onset of diabetic heart disease has not yet been addressed.

Exercise is generally viewed as an effective prophylactic strategy for combating diabetes because of the benefits on weight management and insulin sensitivity [3]. Studies have shown '*high intensity*' exercise as an effective means of reversing diabetic heart disease, because exercise ameliorates vascular dysfunction. However, once heart disease is well established, this high intensity of exercise required to impede the progression of heart disease is often unsustainable for most patients.

This study [4] proposed that initiation of a '*moderate*' and sustainable exercise regime in the early stages of diabetes, *before* cardiac dysfunction begins, could prevent diabetic coronary artery and heart disease. Yet, only '*high intensity*' exercise could ameliorate cardiac dysfunction in diabetes if the exercise was started *after* the cardiac dysfunction had already become established. Finally, we used miRNA's as a non-invasive biomarker to predict and identify changes in coronary function during the progression of diabetic heart disease.

All experiments were performed at SPring-8 **BL28B2**. We used the *db/db* mouse model, which progressively develop diabetic heart disease. Subgroups of '*Early cardiac dysfunction* (Early CD)' and '*Late cardiac dysfunction* (Late CD)' diabetic mice (DM) (n = 8/group) were subjected to either no exercise, moderate intensity (MIE) or high intensity exercise (HIE) for 1-hour per day over eight weeks. Blood samples were extracted every two weeks to measure miRNA-126. Echocardiography was used for repeated measurements of cardiac structure and function. Age matched nondiabetic mice (ND) served as controls.

At the end of the exercise regimes, we imaged and assessed the functional capacity of the coronary vessels using Synchrotron Radiation (SR) microangiography, as previously described [5]. Coronary angiograms were imaged at baseline and then in response to i) acetylcholine (ACh - endothelial-dependent vasodilation) and ii) sodium nitroprusside (SNP – endothelial-independent vasodilation).

Diabetes: Microangiography data revealed that diabetes caused coronary vessel rarefaction (loss of coronary vessels) (Fig. 1). Diabetes impaired the magnitude of endothelial-dependent vasodilatory response to ACh of small coronary microvessels (Fig. 1). Moreover, echocardiographic evidence revealed that both Early-CD and Late-CD DM mice had clear hallmarks of cardiac damage and dysfunction (Fig. 2).

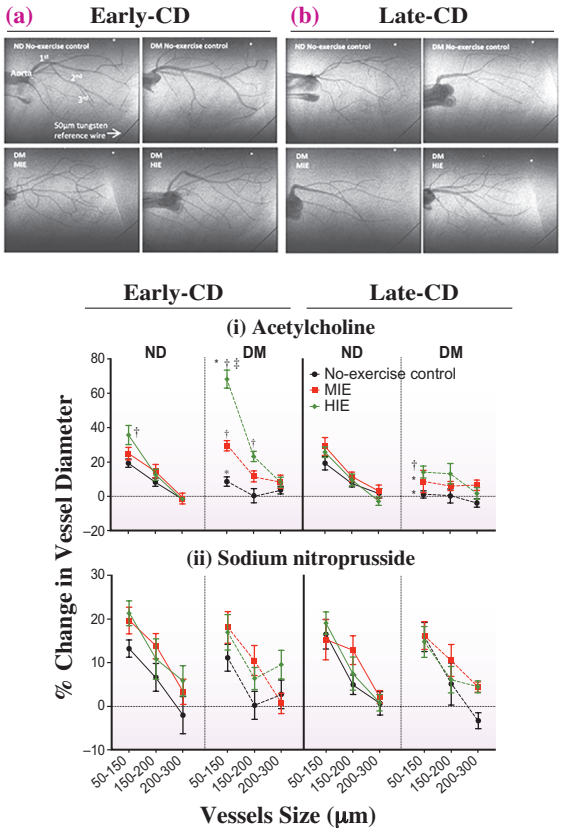

Fig. 1. Representative angiograms and quantitative line graphs showing the change in vessel diameter in response to (i) acetylcholine and (ii) sodium nitroprusside in a) Early-CD and b) Late-CD nondiabetic (ND) and diabetic (DM) mice, after eight weeks of no exercise, moderate intensity exercise (MIE) or high intensity exercise (HIE). *Significantly different to the ND, $p < 0.05$; †Significantly different to the no-exercise, $p < 0.05$.

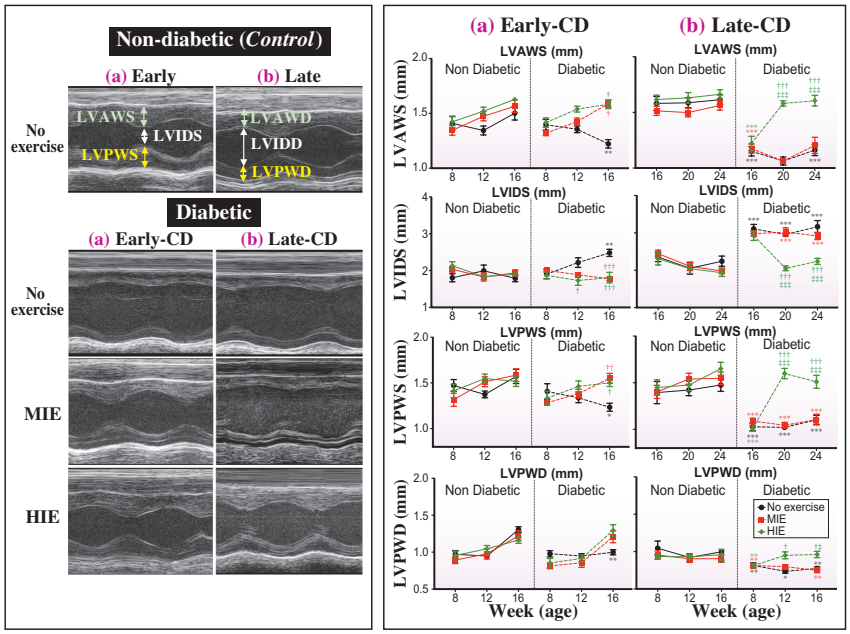

Fig. 2. Effect of exercise (MIE and HIE) on left ventricular (LV) structure in nondiabetic (ND) or diabetic (DM) mice. **Left panel**: Representative M-mode echocardiographic images. LVAWS & LVAWD - left ventricular anterior wall thickness at end systole and diastole; LVIDS & LVIDD – LV internal diameter at end systole and diastole; LVPWS & LVPWD – LV posterior wall thickness at end systole and diastole. **Right panel:** Line graphs showing the effect of exercise on left ventricular structure. *Significantly different from ND. †Significantly different from the no-exercise.

Diabetes + Exercise: Exercise, regardless of intensity (both MIE and HIE), prevented the diabetes-induced onset of coronary and cardiac damage and dysfunction when initiated from 8 weeks of age (Early-CD; Figs. 1 and 2). If, however, exercise was not initiated until 16 weeks of age, after cardiac dysfunction had already become well-established (i.e., Late-CD), then only HIE and not MIE could improve coronary vessel and heart function (Figs. 1 and 2).

Correlation with miRNA-126: Alterations in the circulating levels of pro-angiogenic miR-126 that were associated with diabetes, age and/or both MIE and HIE exercise regimes (Figs. 3(a,b)) were significantly and positively correlated with changes in coronary arteriole density (Fig. 3(d)) and capillary density (Fig. 3(c)).

Preventing the decline in coronary perfusion and myocardial remodeling that exacerbates cardiac dysfunction in advanced stages of diabetes remains a challenge. Our findings provide the first experimental evidence for the critical importance of early exercise intervention in ameliorating diabetic heart disease. Our results also suggest that the beneficial effects of exercise are mediated through the normalization of cardiovascular-enriched miRNA-126, which becomes dysregulated in diabetes.

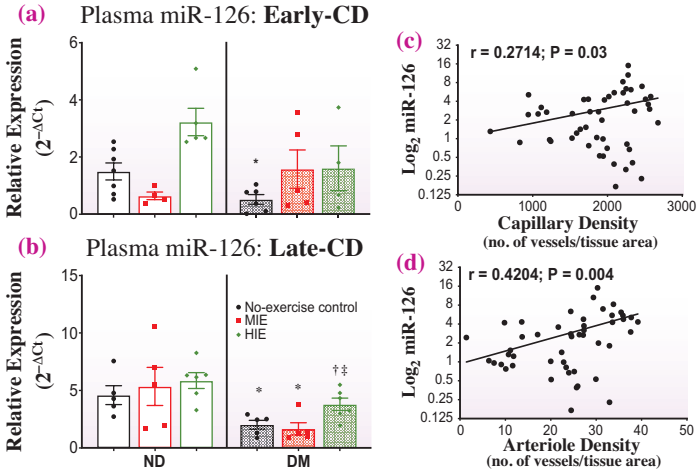

Fig. 3. Correlation between plasma miR-126 and coronary perfusion. Quantitative bar graphs showing plasma miR-126 following exercise in **(a)** Early-CD group and **(b)** Late-CD group. Right panel shows the correlation between plasma miR-126 expression and **(c)** total capillary density and **(d)** arteriole density.

Daryl O. Schwenke[a,*], Keiji Umetani[b] and James T. Pearson[b,c]

[a] Department of Physiology, University of Otago, New Zealand
[b] Japan Synchrotron Radiation Research Institute (JASRI)
[c] Department of Cardiac Physiology, National Cerebral and Cardiovascular Research Institute

*Email: daryl.schwenke@otago.ac.nz

References

[1] J.T. Pearson *et al.*: Cardiovasc Diabetol. **12** (2013) 111.
[2] S. Rawal *et al.*: Cardiovasc Diabetol. **13** (2014) 44.
[3] J. Sennott *et al.*: Pathophysiol. **15** (2008) 173.
[4] *J.K. Lew, J.T. Pearson, E. Saw, H. Tsuchimochi, M. Wei, N. Ghosh, C.K. Du, D.Y. Zhan, M. Jin, K. Umetani, M. Shirai, R. Katare, D.O. Schwenke: Circ. Res. **127** (2020) 1384.*
[5] R. Katare *et al.*: Front Physiol. **9** (2018) 696.

Visualization of platinum accumulation by synchrotron radiation X-ray fluorescence in cancer tumor of patients treated with oxaliplatin-based chemotherapy

Oxaliplatin (trans-(±)-diaminocyclohexane oxalatoplatinum; L-OHP), a platinum-based drug, is a key chemotherapeutic agent for colorectal cancer (CRC). Oxaliplatin is a third-generation platinum agent that forms cross-linking adducts, thus blocking DNA replication and transcription [1], similarly to cisplatin and carboplatin. However, there are major problems regarding oxaliplatin-related toxic effects, particularly, peripheral sensory neuropathy being the important dose-limiting toxicity of oxaliplatin-based therapy. Therefore, a prediction of the efficacy and toxicity of oxaliplatin-based chemotherapy may possibly improve its efficacy and safety in patients with CRC.

Synchrotron radiation X-ray fluorescence spectrometry (SR-XRF) traces both the chemical elements originally present in human tissues, such as potassium, calcium, zinc, copper, and iron, and the elements contained in drugs, such as noble metals. However, because of the extremely low concentration of such elements in human tissues, the *in situ* visualization of the distribution of the elements has not been possible using conventional imaging techniques. We applied SR-XRF to visualize the distribution of platinum and other elements in rectal cancer specimens resected from patients who received oxaliplatin-based preoperative chemotherapy. We also evaluated the correlations of Pt levels with therapeutic effects and clinicopathologic factors.

Our study subjects consisted of 30 patients who underwent surgical resection of rectal cancer at the Department of Surgery and Oncology, Kyushu University Hospital (Fukuoka, Japan) between January 2005 and December 2014. All patients received oxaliplatin-based chemotherapy without radiotherapy. Primary tumor response was assessed by physicians on the basis of their comprehensive interpretation of CT, MRI, and colonoscopy findings and reported in accordance with the Response Evaluation Criteria in Solid Tumors (RECIST) guidelines [2]. Neurologic toxicity was assessed in accordance with the Neurotoxicity Criteria of Debiopharm (DEB-NTC) [3] and toxic effects other than neurotoxicity were evaluated referring to the National Cancer Institute-Common Toxicity Criteria (NCI-CTC), version 4.0.

All resected specimens were fixed in formalin and embedded in paraffin, and all tissues adjacent to the specimens were evaluated histologically using the World Health Organization criteria. Consecutive 5-μm formalin-fixed, paraffin-embedded sections were cut and placed onto glass slides. The paraffin-embedded slices were stained with hematoxylin and eosin (H&E) and exfoliated from the slide glass using a cell transfer technique with Malinol mounting medium (Muto Pure Chemical, Tokyo, Japan) [4]. Then, this peeled slice was used for XRF analysis. The remaining paraffin-embedded slices were subjected to immunohistochemical analyses to identify the tumor region (stained for E-cadherin), the stromal region (stained for α-SMA), and tissue degeneration after chemotherapy (stained for CC-3).

SR-XRF measurements of rectal cancer specimens were performed at SPring-8 **BL37XU**. The monochromatic X-ray beam at 14.5 keV was focused into a 0.5 μm diameter using a Kirkpatrick-Baez type X-ray focusing system. The spatial resolution in our measurement was 0.5 μm, and 1.5 h was required to obtain the 2-mm-square tumor image for a sample mounted on an XY-scanning stage (excitation time of 0.1 s, 10 μm steps) [5].

Standard solutions were used to create the calibration curves for Pt, Cu, Zn, and Fe. The elemental concentration was calculated from the integrated elemental intensity using the calibration curve. The detection limit (DL) of each element was defined as the concentration at which the detected peak intensity could be statistically distinguished from the random fluctuations of the corresponding background at a confidence level of 3 standard deviations (SD). As a result, the DLs of Pt, Cu, Zn, and Fe were estimated to be 1.848, 0.380, 1.331, and 3.403 ppm, respectively. In our study, five areas in sections of SR-XRF images, each 50 μm square, were randomly selected, and the average concentrations of the elements were calculated.

As shown in Fig. 1, the Pt concentration in rectal cancer tissue could be estimated to be in the range of 2.85 to 11.44 ppm. In the tumor epithelium, the Pt concentration was significantly higher in areas of degeneration caused by chemotherapy than in the nondegenerated area ($p < 0.001$). Conversely, in the tumor stroma, the Pt concentration was significantly higher in patients with limited therapeutic responses than in those with strong therapeutic responses ($p < 0.001$). In our study, the Pt accumulation in the tumor stroma significantly correlated with histological chemoresistance to oxaliplatin-based chemotherapy. Therefore, our study suggests that drug accumulation in the tumor stroma possibly inhibits oxaliplatin delivery to the tumor cells.

In conclusion, we used SR-XRF to visualize and quantify, for the first time, the distribution of Pt and trace elements in resected rectal cancer tumor specimens from patients treated with oxaliplatin-based chemotherapy. Our novel results indicated that the Pt concentration in tumor stroma is significantly associated with therapeutic response in rectal cancer, suggesting that drug accumulation in the tumor stroma is one possible cause of platinum resistance. The examination of Pt accumulation in the biopsy specimen of rectal cancer during Pt-containing chemotherapy might be useful to predict the histological response and to avoid further administration of this agent to patients with poor-response tumors.

This study was approved by the Kyushu University Hospital Human Research Ethics Committee and conducted in accordance with the Ethical Guidelines for Human Genome/Gene Research enacted by the Japanese Government and the Declaration of Helsinki. Informed consent to harvest tissue for the studies was obtained from all patients.

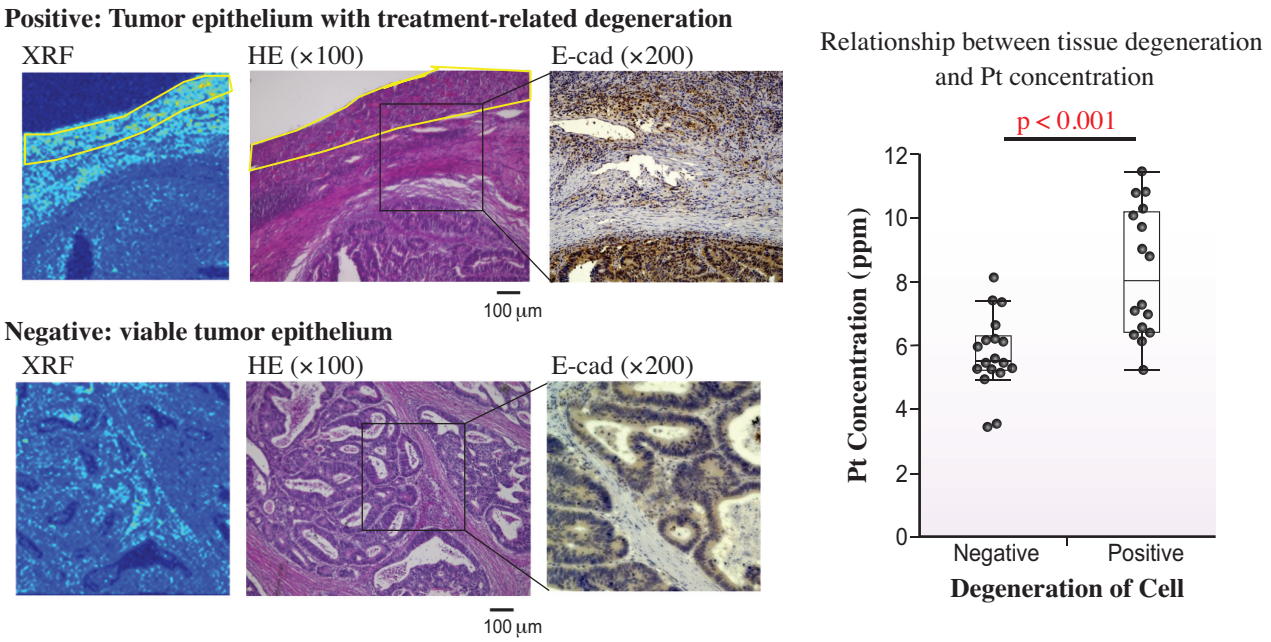

Fig. 1. Tumor epithelial tissue degeneration and platinum concentration. There is a high concentration of platinum in the therapeutically effective part of the tumor epithelium.

Maiko Nishibori[a,*] and Ryo Koba[b]

[a] Faculty of Engineering Sciences, Kyushu University
[b] Department of Surgery and Oncology, Kyushu University

*Email: nishibori.maiko.511@m.kyushu-u.ac.jp

References

[1] J.M. Woynarowski *et al.*: Mol. Pharmacol. **54** (1998) 770.
[2] E.A. Eisenhauer *et al.*: Eur J Cancer **45** (2009) 228.
[3] K. Shirao *et al.*: Jpn. J. Clin. Oncol. **36** (2006) 295.
[4] G.G. Brown, L.C. Tao: Acta Cytol **36** (1992) 259.
[5] *R. Koba, H. Fujita, M. Nishibori, K. Saeki, K. Nagayoshi, Y. Sadakari, S. Nagai, O. Sekizawa, K. Nitta, T. Manabe, T. Ueki, T. Ishida, Y. Oda, M. Nakamura: Int. J. Cancer* ***146*** *(2020) 2498.*

Direct determination of 3*d* orbital state in perovskite-titanate by synchrotron X-ray diffraction

The functions and physical properties of solid materials, such as magnetic order and unconventional superconductivity, are greatly affected by the orbital state of the outermost electrons (valence electrons) of the constituent atoms [1]. In other words, the minimal unit that determines the physical properties of a solid material is the orbital occupied by the valence electrons. Because the orbital state is responsible for the spatial anisotropy of physical properties, the orbital can also be regarded as the smallest unit of "shape." The orbital states in elements are basic knowledge that can be found in quantum mechanics or quantum chemistry textbooks. For example, it is known that the distribution of 3*d* electrons in transition elements have characteristic butterfly-type shapes (Fig. 1(c)). However, until now, it has been extremely difficult to observe the real-space distribution of such electron orbitals directly.

Using X-ray diffraction measurement, a complete electron density distribution can, in principle, be reproduced by performing the inverse Fourier transform on the 'infinite' number of diffraction intensities. However, in reality, because the number of reflections obtained by the X-ray diffraction experiment is 'finite', it is impossible to reproduce the complete electron density distribution owing to the mathematical truncation effects of the Fourier synthesis. We have found that this truncation effect can be minimized by focusing only on the valence electron term in the atomic scattering factor. Using SPring-8 **BL02B1**, which enables us to collect high-intensity and high-resolution diffraction data, we succeeded in observing the butterfly-shaped spatial distribution of single-valence 3*d* electrons in the center of titanium in perovskite-type titanium oxide $YTiO_3$ (Fig. 1(a)).

To extract only valence electron information, it should be noted that the atomic scattering factor is formed by the sum of inner-shell and valence electrons. Although the contribution of the inner-shell electrons extends to the high-angle region, that of the valence electrons exists only in the low-angle region. We developed a new Fourier synthesis method in which data from each titanium ion's inner-shell electrons — which do not contribute to the compound's physical properties — are subtracted from the total electron distribution of each ion. The method is called core differential Fourier synthesis (CDFS) [2,3]. By CDFS, we succeeded in extracting the butterfly-shaped valence electron density distribution around a titanium ion with almost no truncation effect (Fig. 1(b)) and in determining the quantum parameters of the 3*d* orbital experimentally in $YTiO_3$.

Notably, a closer look at the butterfly-shaped electron density revealed that a high density remained in the central region (inset of Fig. 1(b)), in contrast to free titanium atom in which electrons do not exist at the center because of the node of the 3*d* orbital (Fig. 1(c)). First-principles calculations confirmed this nontrivial orbital picture and reproduced the results of the CDFS analysis very well (Fig. 2(b)). It was found that the electron density at the center consists of the

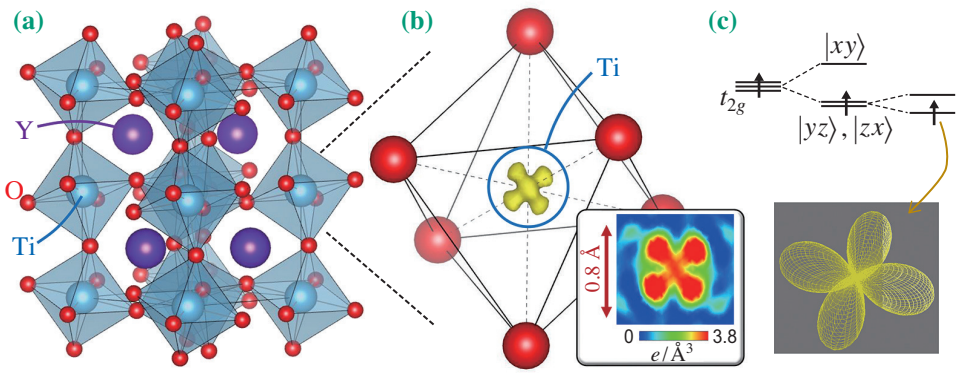

Fig. 1. **(a)** Crystal structure of $YTiO_3$ at 25 K. **(b)** Valence electron density distribution around Ti with internal coordinates (1/2, 1/2, 1/2) obtained by CDFS analysis (isosurface level: 3.2 e/Å^3). (Inset) Sectional view of the plane ($\bar{1}21$). **(c)** Schematic illustration of the Ti^{3+}-$3d^1$ orbital-ordered state in $YTiO_3$ system and the typical valence electron density distribution of a t_{2g} electron.

valence electrons occupying the hybridized orbitals, which are mainly formed by the Ti-4*s* and O-2*s*/2*p* orbitals, generated by the bond between titanium and oxygen (Figs. 2(a,c)).

CDFS reveals the orbital states in materials regardless of the physical properties and can be applied to almost all elements without the need for difficult experiments or analytical techniques. The method requires neither quantum-mechanical nor informatic models, so bias introduced by analysts is minimized. The CDFS based on the high-quality data obtained by short-wavelength synchrotron X-ray is extremely effective for observing not only atomic orbitals localized in one atom but also spatially extended molecular orbitals [2,4]. The results may signal a breakthrough in the study of orbital states in materials. The CDFS analysis will provide a touchstone for a complete description of the electronic state by first-principles or other theoretical calculations.

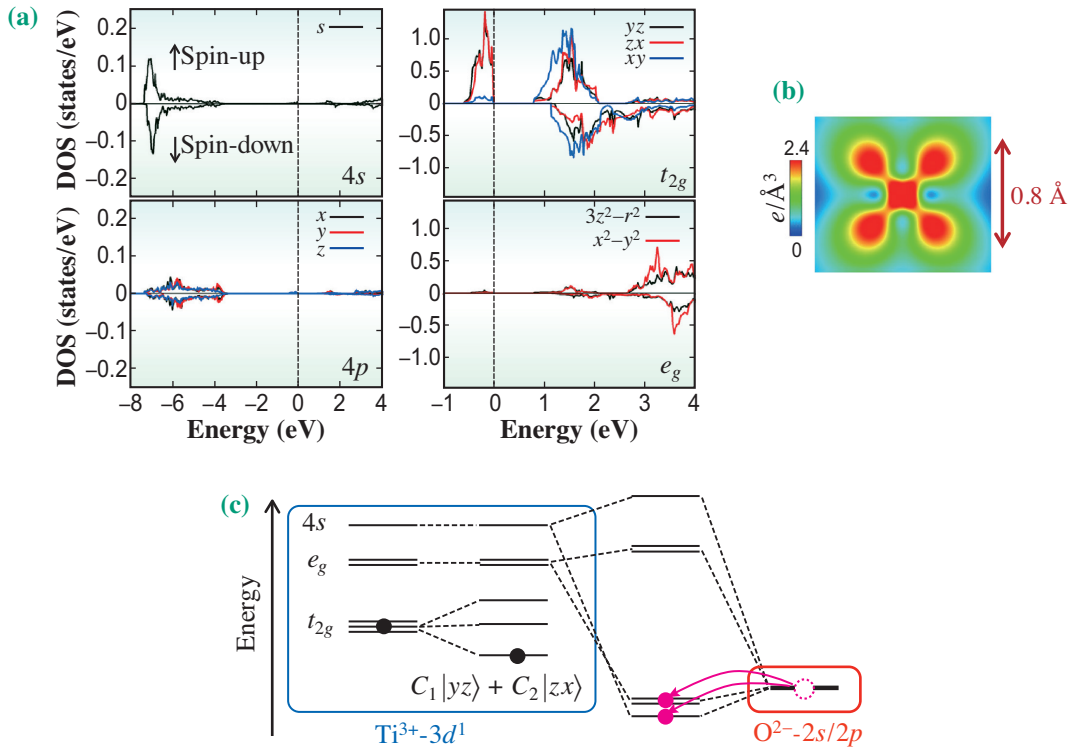

Fig. 2. **(a)** Density of states of the 4*s*, 4*p*, and 3*d* (t_{2g} and e_g) orbitals of Ti in $YTiO_3$. The zero-energy corresponds to the highest occupied level. **(b)** Valence electron density distribution around Ti, which corresponds to valence electrons occupying the orbitals below the Fermi level, obtained from the density-functional-theory calculation. **(c)** Schematic illustration of the orbital state including the Ti–O hybridization.

Shunsuke Kitou and Hiroshi Sawa*

Department of Applied Physics, Nagoya University

*Email: z47827a@cc.nagoya-u.ac.jp

References

[1] Y. Tokura and N. Nagaosa: Science **288** (2000) 462.
[2] *S. Kitou, T. Manjo, N. Katayama, T. Shishidou, T. Arima, Y. Taguchi, Y. Tokura, T. Nakamura, T. Yokoyama, K. Sugimoto and H. Sawa: Phys. Rev. Res. **2** (2020) 033503.*
[3] S. Kitou *et al.*: Phys. Rev. Lett. **119** (2017) 065701.
[4] S. Kitou *et al.*: Crystals **10** (2020) 998.

Time-resolved *in situ* X-ray powder diffraction measurements to clarify the kinetic nature of adsorption-induced structural transition on metal-organic frameworks

For a dozen years, metal-organic frameworks (MOFs) that consist of metal ions and organic ligands have been extensively studied as promising porous materials. Some flexible MOFs have attracted significant attention owing to their unique 'gate adsorption' behavior, a structural transition phenomenon induced by guest adsorption (Fig. 1). The gate adsorption leads to a stepwise change in the amount adsorbed at a specific gas pressure, which provides larger working capacities and higher selectivities than do conventional adsorbents. Therefore, flexible MOFs have the potential to be breakthrough materials for high-throughput separation processes and may help to ensure a sustainable future. In this study, we focused on the kinetic nature of CO_2 gate adsorption on ELM-11 ($[Cu(BF_4)_2(4,4'\text{-bipyridine})_2]_n$) [1] and revealed that time-resolved *in situ* X-ray powder diffraction (XRPD) measurements indicate CO_2 gate adsorption on ELM-11 to be significantly fast in response to the change in CO_2 pressure.

Time-resolved *in situ* XRPD measurements of ELM-11 during CO_2 gate adsorption were conducted using a large Debye–Scherrer-type diffractometer with a multimodular system constructed with six MYTHEN detectors at SPring-8 **BL02B2** [2]. The ELM-11 sample was placed at the end of a 0.3-mm-diameter borosilicate glass capillary attached to a stainless-steel tube with an epoxy adhesive. The sample was evacuated for 10 h at 373 K, and the sample temperature was then controlled at 273 K using a nitrogen gas blower. The *in situ* XRPD patterns were continuously obtained by exposing the sample for 1 s at intervals of 50 ms. After 4.15 s from starting the XRPD measurements, CO_2 gas in a gas manifold of a gas-handling system was introduced into the glass capillary in which the ELM-11 sample was maintained in a vacuum.

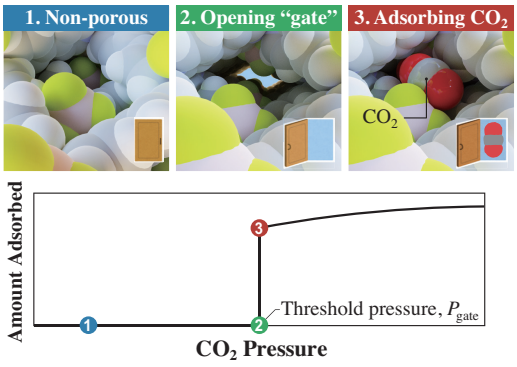

Fig. 1. Schematic illustration of the gate adsorption behavior on ELM-11. ELM-11 has no pores when the ambient CO_2 pressure is low (closed state). When the CO_2 pressure reaches the threshold pressure P_{gate}, the framework structure of ELM-11 and CO_2 molecules are adsorbed into the pores generated (open state).

Figure 2 shows time-resolved *in situ* XRPD patterns of ELM-11 during CO_2 gate adsorption together with the crystal structures of ELM-11 in closed and open states [3]. The color map showing the time development of peak intensities indicates that the structural transition of ELM-11 started immediately after the introduction of CO_2 at 40.8 kPa and was accomplished in approximately 10 s. Peak intensities of the 002 reflection at 6.1° for the open phase of ELM-11 were then obtained by the nonlinear least-squares fitting of the pseudo-Voigt function. The fractions of phases transformed as a function of time were determined by normalizing the peak intensities by that after the completion of the transition for the open phase. Figure 3(a) shows the time development of the fraction of the open phase by introducing approximately 41 kPa of CO_2 at 273, 264, and 241 K. It can be seen that the rate of phase transition increases as the temperature decreases under the same CO_2 pressure. We also investigated the dependence of the rate of phase transition on the pressure at 227 K. As shown in Fig. 3(b), the rate of structural transition increased with CO_2 pressure, and the phase transition was completed within a few seconds at the highest gas pressure. Furthermore, as drawn with solid lines in Figs. 3(a) and 3(b), these data were found to obey the following Kolmogorov–Johnson–Mehl–Avrami (KJMA) equation [4],

$$\alpha = 1 - \exp(-kt^n), \qquad (1)$$

where α is the fraction transformed at time t, k is the rate constant, and n is the number of dimensions at which the transition occurs. Figure 3(c) shows the relationship between the rate constant of the KJMA equation and the pressure difference $P–P_{gate}$, where P is the CO_2 pressure introduced into the glass capillary with ELM-11 and P_{gate} is the gate-opening pressure. We found that, as shown by the solid line in Fig. 3(c), the following characteristic curve could be drawn for all the rate constants of the open phase investigated:

$$k(P,T) = k_0\{P - P_{gate}(T)\}, \qquad (2)$$

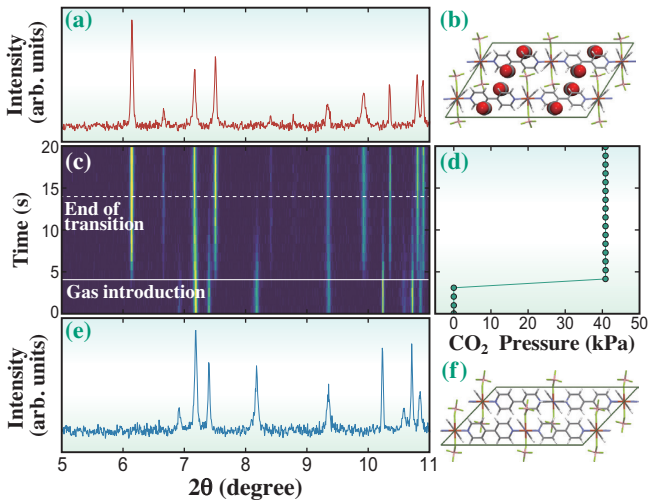

Fig. 2. **(a)** XRPD pattern and **(b)** crystal structure of ELM-11 in the open state. **(c)** Color map of time-resolved *in situ* XRPD patterns of ELM-11 at 273 K corresponding to **(d)** stepwise CO_2 pressure change from 0 to 40.8 kPa. **(e)** XRPD pattern and **(f)** crystal structure of ELM-11 in the closed state. The wavelength of the incident X-rays was 0.099899 nm.

where k_0 is a constant, which was determined to be 12.0 ± 0.5 $s^{-1/n}$ MPa^{-1} by least-squares fitting of Eq. (2). Note that the gate opening pressure at the corresponding temperature T is evaluated using the relationship obtained from the experimental adsorption isotherms over a wide temperature range of 195–298 K [3]:

$$\ln P_{gate}\,[\mathrm{kPa}] = -3064.5/T\,[\mathrm{K}] + 14.683 \qquad (3).$$

This suggests that the rate constant only depends on the CO_2 gas pressure and temperature, which controls the gate-opening pressure, and that the gate-opening rate is amplified by the CO_2 pressure exerted on ELM-11. Equation (3) tells us that it takes only 1.5 s for ELM-11 to achieve 95% structural transition when CO_2 gas of 250 kPa is introduced at 298 K, which corresponds to a model case of the gas separation process for landfill gas (500 kPa of an equimolar mixture of CO_2 and CH_4). Note that the exponent of the KJMA equation, n, obtained from all the data for the open phase was 1.2–1.3, which indicates the quasi-one-dimensional growth of the open phase of ELM-11 [4]. This is indeed consistent with the mechanism of gate opening predicted in the previous study [3]: one-dimensional channels composed of stacked two-dimensional square grid layers are formed in ELM-11 once the interlayer distance is increased, and simultaneously, CO_2 molecules penetrate through one-dimensional channels, i.e., the formation of the open phase encapsulating CO_2 proceeds along the one-dimensional direction.

This fast gating of ELM-11 is a desirable feature for high-throughput separation processes, particularly for pressure swing adsorption processes with a short cycle time (rapid PSA), to increase the flow rate of the gas without increasing the system size. We therefore evaluated the separation performance of a rapid PSA system using ELM-11 for landfill gas separation and demonstrated that the proposed system can produce the same amount of production with a 69% smaller column size and a 62% lower feed than a system using a conventional adsorbent [5].

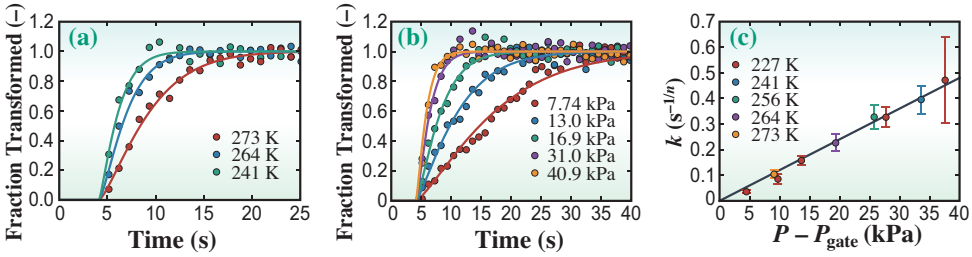

Fig. 3. **(a)** Normalized peak intensities (fractions of the phase transformed) from the 002 reflection ($2\theta = 6.1°$) of the open phase at CO_2 pressure of 41 kPa as a function of temperature and **(b)** normalized peak intensities from the 002 reflection for the open phase at 227 K as a function of CO_2 pressure. The solid lines were obtained by fitting the KJMA equation. **(c)** Relationship between the rate coefficient k and the pressure difference between the CO_2 gas pressure P and the gate-opening pressure P_{gate}.

Shotaro Hiraide[a,*], Minoru T. Miyahara[a] and Hideki Tanaka[b]

[a] Department of Chemical Engineering, Kyoto University
[b] Research Initiative for Supra-Materials (RISM), Shinshu University

*Email: hiraide@cheme.kyoto-u.ac.jp

References

[1] A. Kondo *et al.*: Nano Lett. **6** (2006) 2581.
[2] S. Kawaguchi *et al.*: J. Synchrotron Rad. **27** (2020) 616.
[3] S. Hiraide *et al.*: Dalton Trans. **45** (2016) 4193.
[4] T.J.W. De Bruijn *et al.*: Thermochim. Acta **45** (1981) 315.
[5] *S. Hiraide, Y. Sakanaka, H. Kajiro, S. Kawaguchi, M. T. Miyahara and H. Tanaka: Nat. Commun.* ***11*** *(2020) 3867.*

Early stages of iron passivation: defective growth of oxide layer observed by quick X-ray reflectometry

Chemical reactions at solid-liquid interfaces are, although quite common in chemistry, one of the most challenging phenomena in condensed matter physics. Usually, chemical reactions are explained in terms of thermodynamic potential. To gain physical insight into such phenomena, the atomistic visualization of a reaction process is highly desirable. Passivation is one of the chemical reactions that can be controlled by applying external electric voltage. Here, we take iron passivation as a typical example of a chemical reaction at solid-liquid interfaces in our microscopic study.

A passive layer of iron is known to have a defective spinel structure. The typical time scale of iron passivation at the interface between iron and an aqueous solution is twofold: a few seconds and a few years. The slow process is well explained by the point defect model (PDM) [1,2], where the time evolution of the oxide layer thickness is $dL/dt = A\exp(-BL)$, with L, t, and A and B denoting the thickness, time, and two constants, respectively. In contrast, the fast process is not understood well, partially because of the difficulty in experimental observation as well as the variety of sources of time evolution. We performed time-resolved X-ray reflectivity measurements to elucidate the time evolution of the iron oxide film growing in a pH 8.4 borate buffer solution.

The typical time scale of X-ray reflectometry is a few minutes [2], which is very slow for the fast time scale of iron passivation. In this study, we used the stationary photography method for imperfect surfaces [3]. An imperfect surface produces a broad signal in the reciprocal space having a finite range of overlap with the Ewald sphere, as shown in the inset of Fig. 1(b). This method allows us to measure reflectivity profiles without moving the diffractometer, and the time resolution of the measurement is only limited by the statistics. Using the strong undulator X-ray at SPring-8 **BL13XU** and the aid of Bayesian inference, we achieved a 20 ms time resolution [4] to obtain the reliable real space information of the iron oxide.

Iron single crystals were immersed in borate buffer solution. Their electric potential was controlled by a potentiostat using a Ag/AgCl reference electrode. The potential of –0.8 V versus Ag/AgCl makes the iron/buffer solution interface stable, while +0.3 to +0.7 V versus Ag/AgCl makes the passive surface stable. In reflectivity measurements, a 25 keV X-ray beam passes 10 mm into the solution. The absorption is less than half of the total intensity. The reflected beam was measured by a PILATUS detector with a 20 ms exposure time and a 5 ms interval. A typical signal obtained with 20 ms exposure is presented in Fig. 1(a). The blue curves show the 2000 samples obtained by Monte Carlo sampling for the Bayesian inference. Corresponding real-space electron densities ρ are presented in Fig. 1(b). The electron density shows four plateaus: iron, passive layer, outer layer, and buffer solution from left to right. The time evolution of the electron density and the thickness of the passive layer (ρ and L) was derived from a similar analysis of all the 20-ms-exposure photographs. The results are presented in Fig. 2. The dashed line for L shows the PDM prediction, and the experimental result deviates from it in the first 1 s of oxidation. The saturation value of ρ for the passive layer is close to the density of magnetite and greater than ρ at the

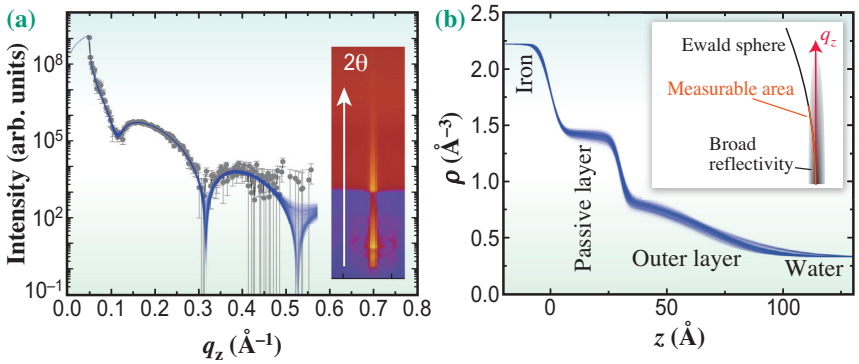

Fig. 1. **(a)** X-ray reflectivity profile measured with 20 ms exposure. Solid gray circles show the experimental result. The inset shows a PILATUS image. An attenuator was inserted in the low-scattering-angle region to improve the dynamic range. **(b)** Electron density profile around the iron surface derived from the reflectivity profile shown in **(a)**. The inset shows a schematic of the broad reflectivity profile in reciprocal space from an imperfect surface. The Ewald sphere overlaps a finite area of the reflectivity profile along q_z. The blue curves for both panels show the 2000 samples obtained by Monte Carlo sampling. [4]

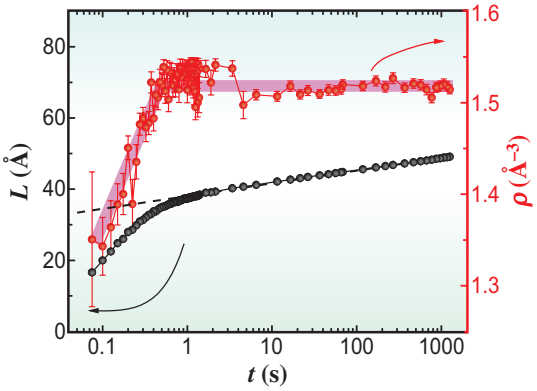

Fig. 2. Thickness L (black) and electron density ρ (red) of the passive layer grown at +0.7 V as a function of time t. Direct logarithmic law $L = \alpha \ln(t) + \beta$ (dashed line) is followed only when $t > 1$ s. The pink solid line is a guide for the eye. [4]

beginning of film growth, indicating that a passive film with many defects is formed at the first stage of passivation.

Different time evolutions of ρ and L in the first 1s of the passivation process indicate a change in the rate-limiting process. Let us discuss the film growth process using a schematic of the potential profile presented in Fig. 3. In the framework of the PDM, there is a constant electric field, i.e., a constant slope in electric potential, inside the oxide film. The potential of the bulk solution and that of bulk iron are connected by the potential step at the two electric double layers formed at the metal-film and film-liquid interfaces as well as the potential slope in the oxide film. When the film is thick, the potential discontinuities at the interfaces are small, as depicted in the inset of Fig. 3. This change causes an increase in potential barrier between the metal iron and oxide iron sites, as presented by the thick curves in Fig. 3. Therefore, when the film is very thin, the iron supply from the metal side to the oxide side should be rapid, and the rate limiting process should be the oxygen supply from the liquid-film interface. When the film becomes thicker, the barrier between the metal iron and the oxide iron sites is high, as depicted by the thick black curve. The rate-limiting process is then changed to the cation supply from the metal side to the oxide side.

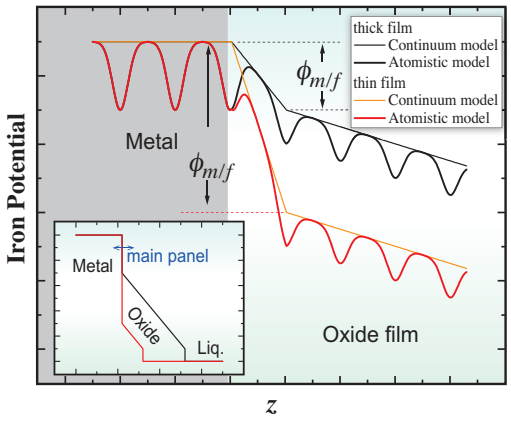

Fig. 3. Schematic of the iron potential profile around the metal-oxide interface. The thin curves show the profiles for the continuum approximation or ordinary PDM, and the thick curves show the profiles for the atomistic model. Black and red profiles are for thick and thin oxide films, respectively. $\phi_{m/f}$ denotes the potential difference between the metal and oxide regions. Inset: The potential curve for a wider z range. [4]

Yusuke Wakabayashi

Department of Physics, Tohoku University

Email: wakabayashi@tohoku.ac.jp

References

[1] D.D. MacDonald: Electrochim. Acta **56** (2011) 1761.
[2] D.H. Kim *et al.*: J. Phys. Chem. B **108** (2004) 20213.
[3] H. Fujii *et al.*: J. Electrochem. Soc. **166** (2019) E212.
[4] *H. Fujii, Y. Wakabayashi and T. Doi: Phys. Rev. Materials* ***4*** *(2020) 033401.*

Direct observation of molecular motions in soft materials: study of basic and applicational liquid crystal systems

The unique properties and functions of soft materials originate from the coexistence of microscopic structural ordering and molecular motions. Accordingly, understanding the relationships between microscopic structure and dynamics in soft matter provides crucial information on how macroscopic properties can be engineered from their microscopic origins. Liquid crystals are typical soft matter systems, and the nematic (*N*), cholesteric (*Ch*), and smectic (*Sm*) phases are the fundamental thermotropic liquid-crystal phases. In Fig. 1, we show the schematic figures of the molecular arrangements of these phases. In the *N* phase, the molecular symmetry axis is usually oriented along one direction. The *Ch* phase shows a similar orientational order locally. However, the average molecular direction in the *Ch* phase rotates continuously around a direction perpendicular to the director. These liquid crystals are widely used in liquid-crystal displays, e.g., twisted *N*-type displays. In the *Sm* phase, the molecular symmetry axis is usually oriented along one direction and the positions of the molecular center of gravity form a layered order. In the *Sm "A"* phase, the molecular direction is parallel to the layer normal. The translational molecular dynamics in these liquid-crystal phases has rarely been observed directly microscopically because of experimental limitations. Therefore, these microscopic dynamical images are virtually unknown despite their fundamental importance.

The synchrotron-radiation-based quasi-elastic gamma-ray scattering technique using multiline time-domain interferometry (TDI) allows us to study atomic/molecular-scale motions in soft matter [1-3]. The high energy resolution (4.7 neV) of the 14.4 keV Mössbauer gamma ray from the ^{57}Fe nucleus enables us to observe the density fluctuation on the atomic/molecular scale on the time scale of 100 ns. Regarding applications to soft-matter systems, we have thus far studied the diffusion motion of the polymer main chain and more local activation motions in pure polymer and model systems of tire by TDI [2,3].

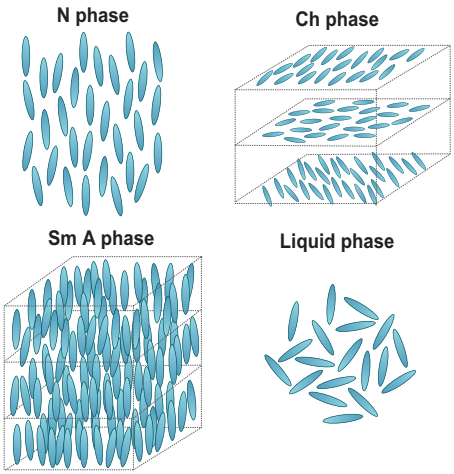

Fig. 1. Schematic figures of liquid crystal nematic (*N*), cholesteric (*Ch*), and smectic (*Sm*) phases and the liquid phase.

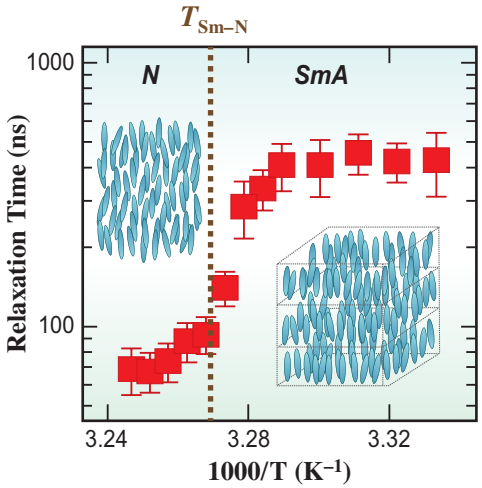

Fig. 2. Temperature dependence of relaxation times of 8CB in *N* and *Sm* phases. Schematic figures of *N* and *SmA* phases are also shown.

We studied microscopic molecular dynamics in various liquid-crystal phases. The experiments were conducted at the nuclear-resonance scattering beamline, SPring-8 **BL09XU**. First, we introduce a study of microscopic molecular motions in *N* and *SmA* phases of a typical liquid-crystal molecule, 4'-n-octyl-4-cyanobiphenyl (8CB), by TDI [4]. In Fig. 2, we show the temperature dependence of the microscopic relaxation times of intermolecular correlations in the direction of the molecular long axis. The relaxation time reflects the time scale of the translational motion across the layer. Such molecular translational motions in the *Sm* phase have been observed microscopically for the first time. We could observe a marked increase in relaxation time in the *SmA* phase after the *N*-*SmA* transition temperature T_{Sm-N}. This increase in relaxation time is caused by the ordering of the layer structure on cooling. By applying a theory predicting the relationship between the microscopic relaxation

time and the layer order, we could microscopically evaluate the *Sm*-layer order parameter, which had not been determined microscopically thus far. The methodology used to obtain the layer order parameter from the microscopic dynamics can be used for many layered systems.

Next, we introduce results on the *Ch* phase and the cholesteric blue phase (*ChBP*) for a mixture system of the nematic liquid crystal 4'-heptyloxy-4-biphenylcarbonitrile (7OCB) and the chiral dopant (S)-4'-(2-methylbutyl)-4-biphenylcarbonitrile (CB15) [5]. *ChBP* exhibits a double-twist orientational order that differs from the single-twist order of the *Ch* phase and also shows a self-assembled three-dimensional lattice structure of defect lines of the orientational order on the mesoscopic spatial scale. We show the schematic figure of the structure in Fig. 3. The helical structure of the molecular orientation in *ChBP* brings the structural color and photonic band gap into the wavelength range of visible light. Therefore, *ChBP* has been studied for application to photonic elements and fast-response displays. We measured the molecular translational dynamics along the long molecular axis in the *Ch* phase, *ChBP*, and liquid phase. We show the relaxation time for each phase in Fig. 3. It was found that the relaxation time of molecular translational motions in *ChBP* is of a similar time scale to that in *Ch* and liquid phases. Therefore, it was microscopically revealed that the molecular mobility in *ChBP* is as high as those in *Ch* and liquid phases even in the existence of mesoscopic lattice order. The mobility is interpreted to be one of the origins of its shorter response time for electro-optical switching, which is important for its application to fast display systems.

Our result demonstrates that the time scale of molecular motions in important liquid-crystal phases such as *N*, *Ch*, and *Sm* phases can be measured by quasi-elastic gamma-ray-scattering spectroscopy using TDI. We found that molecular translational motions in these liquid crystal phases occur on the time scale of nano- to microseconds. In addition, the microscopic molecular motion could be observed in the liquid-crystal phase *ChBP* with a complex structure. Our studies led to the expansion of the practicality of this spectroscopic technique to molecular-mobility studies of industrial materials, such as the study of the anchoring effect of molecular dynamics in liquid-crystal cells of display systems. Further studies on soft matter systems, e.g., lyotropic liquid crystal systems such as lipid bilayers, are in progress.

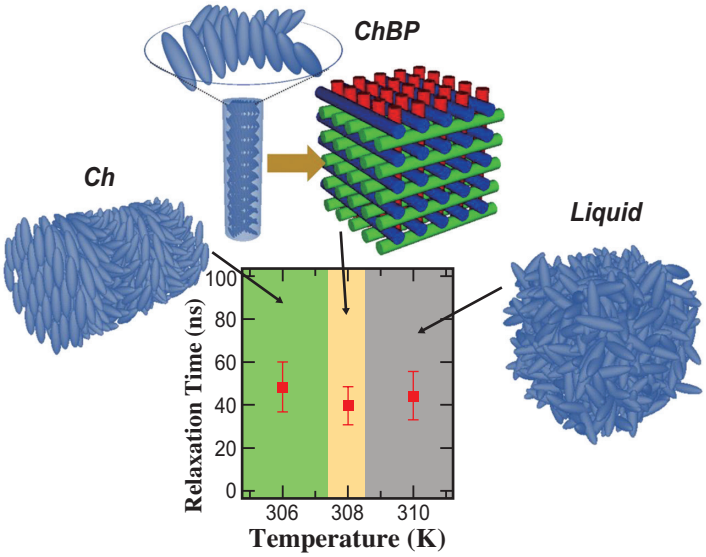

Fig. 3. Temperature dependence of relaxation times of the mixture system of 7OCB and CB15 in *Ch* phase, *ChBP*, and liquid phase. Schematic figures of *Ch* phase, *ChBP*, and liquid phase are also shown.

Makina Saito

Department of Physics, Graduate School of Science, Tohoku University

Email: makina.saito.d6@tohoku.ac.jp

References

[1] M. Saito *et al.*: Sci. Rep. **7** (2017) 12558.
[2] T. Kanaya *et al.*: J. Chem. Phys. **140** (2014) 144906.
[3] M. Saito *et al.*: Hyperfine Interact. **238** (2017) 99.
[4] *M. Saito, J. Yamamoto, R. Masuda, M. Kurokuzu, Y. Onodera, Y. Yoda and M. Seto: Phys. Rev. Res.* ***1*** *(2019) 012008(R).*
[5] *M. Saito, J. Yamamoto, R. Masuda, M. Kurokuzu, Y. Yoda and M. Seto: Hyperfine Interact.* ***241*** *(2020) 14.*

Extreme Fermi surface smearing in maximally disordered NiFeCoCr solid solution

Throughout history, advances in civilization have often been driven by advances in our mastery of materials. An alloy is a combination of at least two different elements. Alloy design has traditionally focused on there being one principal element (e.g., Cu) to which a small amount of something else is added, for example adding Sn to make bronze. In a class of materials known as "high entropy alloys", there are typically at least four different elements present at nearly equal concentrations [1,2]. This class of materials has shown unexpected and technologically important properties, such as their strength at low temperature. Further progress in exploiting their properties can be accelerated by understanding how the electrons behave in these complex alloys.

The Fermi surface of a metal is a surface of constant energy that separates the occupied and unoccupied electron momentum states, and its shape is crucial for determining the properties of the metal [3]. For most metals at low temperature, the Fermi surface is a sharp discontinuity between occupied and unoccupied states in momentum space, but the maximal disorder in these high entropy alloys smears this discontinuity across a significant fraction of the Brillouin zone. Using a simple argument based on Heisenberg's uncertainty principle, this smearing can be related to the distance the electrons can typically travel before being scattered (known as the mean-free-path). The electrons in most metals can travel unhindered over very long distances (even up to a cm), but it has been possible to show [4] that the electrons in the equiatomic NiFeCoCr alloy considered here would scarcely make it to the next atom before being scattered.

High-resolution X-ray Compton scattering experiments were performed at SPring-8 **BL08W**, allowing direct visualization of the impact of compositional disorder on the Fermi surface [4]. The nature of these alloys poses significant challenges to alternative techniques (such as quantum oscillatory methods or angle-resolved photoemission) since they are impossible to cleave and the electronic mean-free-path is extremely short. The Compton scattering technique is particularly powerful because the high-energy X-rays unambiguously probe the bulk electronic structure. Although the measured Compton profiles are actually projections of the electron momentum density in which two of the three momentum components have been integrated over, by measuring profiles down carefully chosen crystallographic directions (in this case it was 15 different directions) it is possible to tomographically reconstruct the full three-dimensional electron momentum density from this set of profiles. It is then straightforward to convert this electron momentum density into the occupation numbers within the first Brillouin zone, with the Fermi surface being associated with a change in the occupation number. First-principles electronic structure calculations were performed using the Korringa–Kohn–Rostoker (KKR) method within the Coherent Potential Approximation (CPA) and the Disordered Local Moment (DLM) state.

Figure 1 shows the calculated Bloch spectral function for the equiatomic NiFeCoCr alloy. For an ordered material, the spectral function would be an

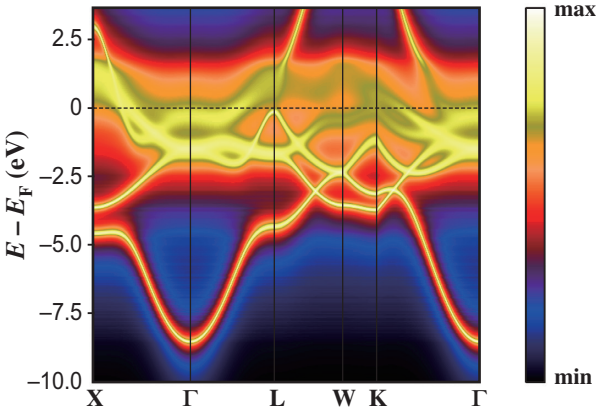

Fig. 1. The logarithm of the Bloch spectral function of NiFeCoCr from the KKR-CPA-DLM calculations.

image of the band structure of that material, showing sharply defined electronic energy bands. However, in a disordered alloy, the bands are smeared both in energy and crystal momentum, ***k***, due to the finite quasiparticle lifetime and mean-free-path, respectively. In Fig. 1 it can be seen that there is very significant smearing of the bands near the Fermi energy which implies that the Fermi surface is going to be substantially smeared.

Figure 2 shows a cut through the occupation number along the [110] direction, revealing a succession of three heavily smeared steps in occupation corresponding to three different Fermi surface sheets (the existence of which was also predicted by the first-principles calculations). By fitting a set of three smeared step functions to the ***k***-dependence of the occupation number, it was possible to extract the coherence length (which can be thought of as a ***k***-resolved mean-free-path).

This was the approach used to produce the colors on the Fermi surface sheet that is shown in Fig. 3. The colors indicate the effective coherence length for electrons located on that part of the Fermi surface (the average over all of the Fermi surfaces would be the mean-free-path of the alloy). It is important to note that the coherence length in this particular alloy is very close to the so-called Mott–Ioffe–Regel limit which describes the semi-classical upper bound for coherent electron transport.

Beyond their technological relevance, studies of these materials will also shed light on fundamental physics. Since the effects of chemical disorder are similar to those of strong electron-electron correlations on transport, these alloys may also be helpful in understanding the behavior of electrons in strongly correlated materials such as high-temperature superconductors. More recent work has probed the nature of the magnetism in these using magnetic Compton scattering at BL08W and XMCD at BL25SU [5].

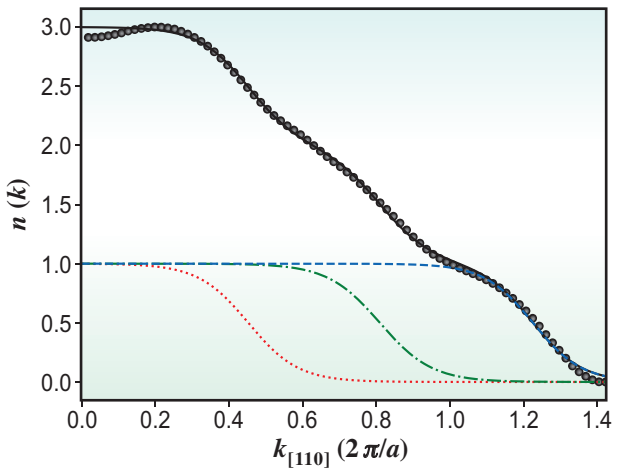

Fig. 2. Occupation number, $n(\boldsymbol{k})$, from the experiment along the [110] direction. $n(\boldsymbol{k})$ has been fitted with three *tanh* functions (one for each Fermi surface sheet) to represent smeared step functions from which the coherence length can be extracted.

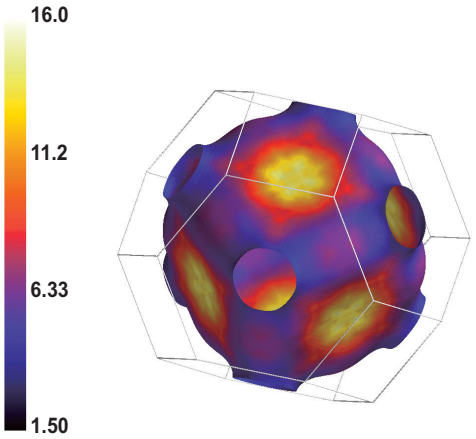

Fig. 3. One of the electron Fermi surface sheets obtained from the Compton experiment as an isodensity of the occupation number. The colors show how the coherence length (in angstrom) extracted from the experiment varies across the Fermi surface. The wireframe box shows the first Brillouin zone.

Stephen B. Dugdale

H.H. Wills Physics Laboratory, University of Bristol, United Kingdom

Email: S.B.Dugdale@bristol.ac.uk

References

[1] B. Cantor *et al.*: Mater. Sci. Eng. A **375-377** (2004) 213.
[2] J.-W. Yeh *et al.*: Adv. Eng. Mater. **6** (2004) 299.
[3] S.B. Dugdale: Phy. Scripta **91** (2016) 053009.
[4] *H.C. Robarts, T.E. Millichamp, D.A. Lagos, J. Laverock, D. Billington, J.A. Duffy, D. O'Neill, S.R. Giblin, J.W. Taylor, G. Kontrym-Sznajd, M. Samsel-Czekala, H. Bei, S. Mu, G.D. Samolyuk, G.M. Stocks and S.B. Dugdale: Phys. Rev. Lett.* ***124*** *(2020) 046402.*
[5] D. Billington *et al.*: Phy. Rev. B **102** (2020) 174405.

Understanding diffraction patterns of disordered materials

The absence of translational periodicity and symmetry, and the rich structural complexity make it difficult to understand the order within disorder [1] in the structure of glassy, liquid, and amorphous materials. Indeed, as noted by Egelstaff in his review article in 1983 [2], determining the structure of disordered materials can be frustrating; although the underlying concepts have been known for a while, appropriate measurement methods for obtaining diffraction data of sufficient quality are usually not available. However, the advent of advanced instrumentation and measurement protocols makes it feasible to use quantum beam diffraction (X-ray diffraction (XRD) and neutron diffraction (ND)) techniques to reveal the structure of disordered materials at synchrotron and neutron facilities [3]. Moreover, a combination of diffraction measurement, advanced computer simulation, and topological analysis techniques enables us to understand the structure of disordered materials. In our work, attempts are being made to understand and characterize diffraction patterns from disordered materials measured at SPring-8 **BL04B2** and other quantum beam facilities with the aid of topological analyses based on atomic configurations obtained from reverse Monte Carlo (RMC) and/or molecular dynamics (MD) simulations, which reproduce experimental diffraction data.

The ND $S(Q)$ for glassy (g)-SiO_2, a canonical network-forming glass, exhibits a three-peak structure: Q_1 (first sharp diffraction peak (FSDP)), Q_2 (principal peak (PP)), and Q_3 (Fig. 1(a), bottom). Note that scattering vector Q is scaled by the nearest-neighbor atomic distance observed in real space to eliminate the effect of atomic size. Amorphous (a-)Si, possessing a fully tetrahedral network, has Q_2 and Q_3 (Fig. 1(a), middle), whereas only Q_3 is observed in the $S(Q)$ for g-$Cu_{50}Zr_{50}$ (Fig. 1(a), top), which has a typical dense random packing (DRP) structure. It is well known that the short-range structural unit of g-SiO_2 is a SiO_4 tetrahedron with a corner-sharing motif, giving rise to a large fraction of cavity volume (Fig. 1(b)) owing to the chemical contrast between silicon (fourfold) and oxygen (twofold) atoms. This structural feature is manifested by the appearance of a FSDP (periodicity: $2\pi/Q_{FSDP}$~4.2 Å, correlation length: $2\pi/\Delta Q_{FSDP}$~9.9 Å). Such a contrast is not found in a-Si, whose short-range structural unit is a $SiSi_4$ tetrahedron that results in the absence of FSDP. The average coordination number in g-$Cu_{50}Zr_{50}$ is approximately 12, which is much larger than those of others, suggesting that the PP is the signature of chemical bonds, because g-$Cu_{50}Zr_{50}$ has no chemical bond in its DRP structure.

To understand the origin of FSDP, we introduced a novel topological analysis based on modern mathematics: persistent homology together with the conventional ring size distribution analysis. The Si–O ring size distribution of g-SiO_2 glass is compared with those of crystalline polymorphs in Fig. 2. It is well known that silica glass (d = 2.21 g·cm^{-3}) exhibits a broad ring size distribution, although the sixfold ring is dominant (Fig. 2(d)). In contrast, α-cristobalite (d = 2.33 g·cm^{-3}) shows only sixfold rings (Fig. 2(a)). A large fraction of eightfold rings is observed in α-quartz (d = 2.65 g·cm^{-3}) (Fig. 2(b)), and coesite (d = 2.91 g·cm^{-3}) shows a variety of different ring sizes, similarly to g-SiO_2 (Fig. 2(c)). The Si-centric persistence diagrams (PDs) shown in Figs. 2(e-h) provide us with information on the shape of rings (how rings are buckled). The profile observed at b_k = 2.2 Å^2 in the Si-centric PD for α-cristobalite shows a large d_k of 7.4 Å^2, demonstrating that sixfold rings are symmetrical. However, d_k decreases with increasing density from α-quartz (Fig. 2(f)) to coesite (Fig. 2(g)), suggesting that the rings are significantly buckled in the high-density phases. The Si-centric PD for g-SiO_2 exhibits a characteristic vertical profile along with the death axis at b_k = 2.2 Å^2, which is in line with the formation of the FSDP in the glass. Indeed, our recent studies on densified g-SiO_2 confirmed this point [1]. Moreover, it is implied that this profile stretching from α-cristobalite to coesite is a signature of a good glass former; in other words, glass does not have a profile, which is similar to one specific crystalline phase.

Uncovering the difference between amorphous and liquid phases on the basis of diffraction and topology provides us with crucial information to understand the nature of glass formation. In this section, we compare g-/l-SiO_2 and a-/l-Si. As mentioned in the previous section, g-SiO_2 exhibits a FSDP (Q_1) not only in the ND $S(Q)$ (Fig. 3(a), bottom) but also in the XRD $S(Q)$ (Fig. 3(a), top). However, the PP (Q_2) is visible only in the ND $S(Q)$ (Fig. 3(a)), because it reflects the packing fraction of oxygen atoms [3,4], since neutrons are sensitive to O–O correlation, while X-rays are more sensitive to Si–Si

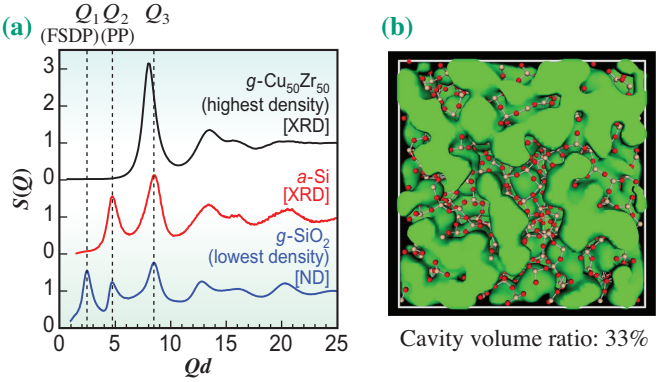

Fig. 1. Structure factors, $S(Q)$, for g-$Cu_{50}Zr_{50}$, a-Si, and g-SiO_2 [4] **(a)** and visualization of cavities (highlighted in green) in g-SiO_2 (b) [5].

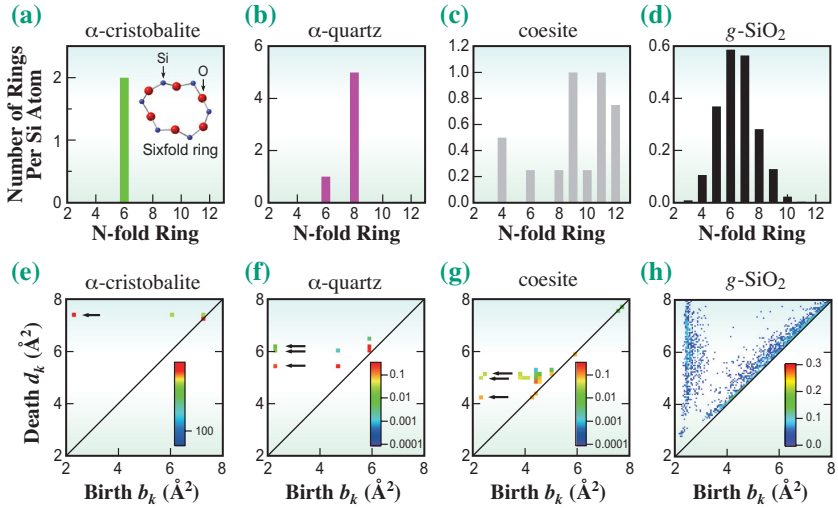

Fig. 2. Ring size distributions **(a–d)** and Si-centric PDs **(e–h)** of silica polymorphs [4].

correlations. The FSDP in the XRD $S(Q)$ is prominent in l-SiO_2, shown as a red curve in Fig. 3(a), suggesting that the Si–O covalent bond is strong even in liquid (2323 K) [4]. This behavior is consistent with the Si-centric PDs (Fig. 3(c)), in which the profile of the liquid phase is identical to that of the glassy phase, because density (glass: 2.21 g·cm^{-3}; liquid: 2.1 g·cm^{-3}) and Si–O coordination number differences (glass: 4.0; liquid: 3.9) are small between these two phases in SiO_2. On the other hand, both the XRD $S(Q)$ (Fig. 3(b)) and Si-centric PDs (Fig. 3(d)) for Si show significant differences between amorphous and liquid phases. The prominent Q_2 observed in the XRD $S(Q)$ of a-Si diminishes and overlaps with Q_3, suggesting that the density of the liquid phase is higher than that of the amorphous phase. This behavior is consistent with the Si-centric PDs for Si, because the characteristic vertical profile along with the death axis observed at $b_k \sim 1.5$ Å^2 in the amorphous phase is diminished in the liquid phase, suggesting that the liquid structure is highly densely packed. Indeed, density (amorphous: 2.3 g·cm^{-3}; liquid: 2.57 g·cm^{-3}) and Si–Si coordination number differences (amorphous: 4.0, liquid: 5.7) are large between the two phases in Si in comparison with SiO_2. This behavior is consistent with the fact that a-Si is a semiconductor and l-Si is a metal.

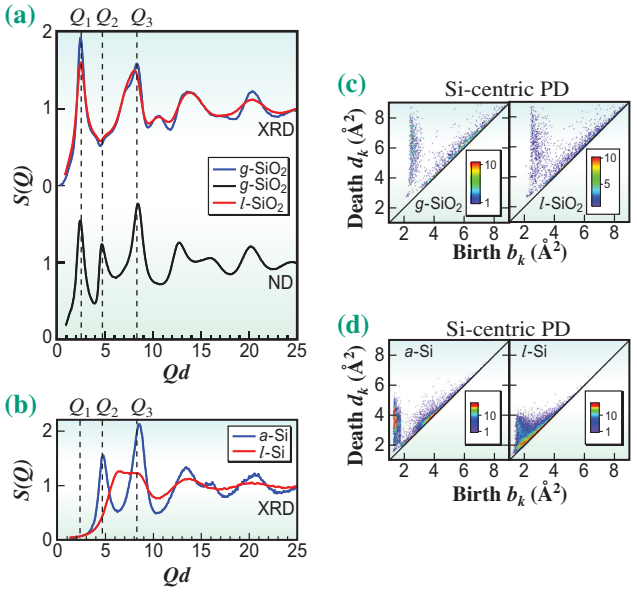

Fig. 3. Structure factors, $S(Q)$, for g- and l-SiO_2 (2323 K) **(a)**, and for a- and l-Si (1770 K) **(b)**, and Si-centric PDs for g- and l-SiO_2 **(c)**, and a- and l-Si **(d)**. [4]

In this article, we describe attempts to understand the origin of diffraction peaks from disordered materials with the aid of topological analyses based on structural models obtained by reverse Monte Carlo (RMC) modelling and/or molecular dynamics (MD) simulations. Combining quantum beam measurements and advanced simulations with topological analyses would be a very promising way to extract the hidden order in disordered materials. The results of advanced analysis will lead to the capability to forge a new path for designing novel functional disordered materials.

Shinji Kohara[a,*], Yohei Onodera[b,a] and Osami Sakata[a]

[a] Research Center for Advanced Measurement and Characterization, National Institute for Materials Science
[b] Institute for Integrated Radiation and Nuclear Science, Kyoto University

*Email: KOHARA.Shinji@nims.go.jp

References

[1] Y. Onodera *et al.*: NPG Asia Mater. **12** (2020) 85.
[2] P.A. Egelstaff: Adv. Chem. Phys. **53** (1983) 1.
[3] S. Kohara and P.S. Salmon: Adv. Phys. X **1** (2016) 640.
[4] *Y. Onodera, S. Kohara, S. Tahara, A. Masuno, H. Inoue, M. Shiga, A. Hiraha, K. Tsuchiya, Y. Hiraoka, I. Obayashi, K. Ohara, A. Mizuno and O. Sakata: J. Ceram. Soc. Jpn.* ***127*** *(2019) 853.*
[5] Y. Onodera *et al.*: NPG Asia Mater. **11** (2019) 75.

Very sharp diffraction peak in dense oxide liquid with the formation of distorted tetraclusters

Determining the liquid structure is the first step in understanding the nature of glass-liquid transitions, and high-quality diffraction and density data are very important in obtaining a reliable structure model by modeling or simulation. However, it is difficult to obtain the data of single-component oxides with high melting temperatures (T_m) in liquid states, because the liquids are easily contaminated with container materials or nucleated from the heterogeneous interface between the container and the liquid. To overcome such problems, we have developed levitation furnaces, which maintain high-temperature liquids without any contact [1,2].

Although liquid (*l*-) Er_2O_3 (T_m = 2686 K) is a representative non-glass-forming liquid (non-GFL), its structure has not been well understood. To elucidate the atomic structure [3], the density data were measured using an electrostatic levitation furnace (ELF) onboard the International Space Station (ISS) and the diffraction data were measured using an aerodynamic levitation furnace at the high-energy X-ray diffraction beamline, SPring-8 **BL04B2**. A combined molecular dynamics (MD) – reverse Monte Carlo (RMC) simulation was also performed to obtain an atomistic model that reproduces diffraction data. Persistence diagrams (PDs) were obtained on the basis of the structural model in a comparison with other non-GFLs and a typical GFL, *l*-SiO_2. The combination of an experiment and a simulation allows trends in single-component non-GFL oxides to be identified, with a special focus on atomic ordering and topology. Furthermore, we compared the features of single-component non-GFL oxide liquids with those of other systems.

The Faber–Ziman total structure factors, $S(Q)$, for *l*-Er_2O_3 [3], *l*-SiO_2 [4], *l*-Al_2O_3 [5], and *l*-ZrO_2 [1], together with the results of the MD–RMC simulation for *l*-Er_2O_3, are shown in Fig. 1. Note that the scattering vector Q is scaled by multiplying by r_{A-X} (distance between the center and corners of the polyhedron). The experimental $S(Q)$ of *l*-Er_2O_3 (solid cyan curve) is well reproduced by the MD–RMC simulation (dotted black curve) with the liquid density measured using the ISS–ELF. A well-defined first sharp diffraction peak (FSDP) is observed only for *l*-SiO_2 (GFL) at $Qr_{A-X} = 2.6$. The FSDP originates from the intermediate-range ordering [1,4] arising from the periodicity of boundaries between successive small cages in the network composed of connected polyhedra with shared oxygen atoms at the corners.

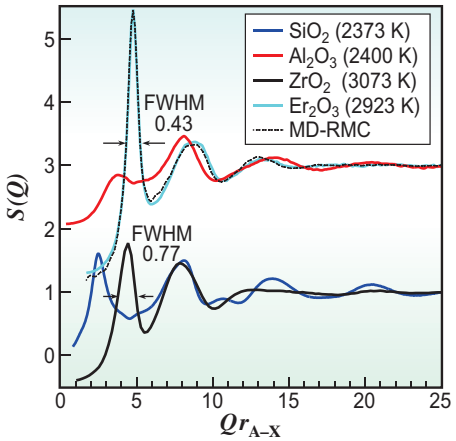

Fig. 1. Faber–Ziman X-ray total structure factors, $S(Q)$, for *l*-Er_2O_3 [3], *l*-SiO_2 [4], *l*-Al_2O_3 [5], and *l*-ZrO_2 [1] together with that of *l*-Er_2O_3 derived from the MD–RMC simulation. Scattering vector Q is scaled by multiplying by r_{A-X} (distance between the center and corners of the polyhedron).

l-Al_2O_3 gives rise to a small FSDP at Qr_{A-X} = 3.8, suggesting that the structure of *l*-Al_2O_3 is intermediate between those of *l*-SiO_2 and *l*-ZrO_2 /*l*-Er_2O_3. A very sharp principal peak (PP) is observed in both the *l*-ZrO_2 and *l*-Er_2O_3 data at $Qr_{A-X} \sim 4.5$. The PP originates from the packing of cations since X-rays are sensitive to heavy atoms.

The coordination number distributions, N_{A-X} and N_{X-A}, for *l*-Er_2O_3 [3] were obtained from the MD–RMC simulations. They show that the Er–O coordination number (up to 3.0 Å) is 6.1, which is rather close to that of the crystalline phase, and the O–Er coordination number can be estimated to be 4.1. These results suggest that cations are fourfold in *l*-SiO_2 (GFL)[4], whereas they are sixfold in *l*-ZrO_2 [1] and *l*-Er_2O_3 (non-GFLs), and the cation-oxygen coordination number in *l*-Al_2O_3 is intermediate [5] between those of GFL and *l*-ZrO_2/*l*-Er_2O_3, although *l*-Al_2O_3 is a non-GFL. This behavior is consistent with that of the first correlation peaks in experimental real-space functions [3] and with the fact that the viscosity of *l*-ZrO_2 is approximately one-tenth of that in *l*-Al_2O_3 [5]. Another interesting behavior is observed for the oxygen-cation coordination numbers. It is demonstrated that oxygen is twofold in *l*-SiO_2, which is a signature of the formation of a sparse network, while triclusters (XA_3) are dominant in *l*-Al_2O_3 and *l*-ZrO_2. The formation of tetraclusters (XA_4) is confirmed in *l*-Er_2O_3, suggesting that this behavior is a distinct feature of this liquid.

Moreover, it is implied that the behavior of the coordination numbers in a series of oxide liquids is affected by both the composition and the ionic radii between the constituent anions and cations. For instance, the ionic radii of Si and Al are small, which results in tetrahedral coordination, although the Al–O coordination number is greater than four on average. The tetracluster formation is governed by the ratio of Er to O in Er_2O_3.

As shown in Fig. 1, the PP of *l*-Er_2O_3 is much sharper than that of the extremely fragile *l*-ZrO_2 [1]. The FWHM of the PP in *l*-Er_2O_3 is 0.43 in comparison with 0.77 in *l*-ZrO_2. To reveal the origin of the very sharp PP in *l*-Er_2O_3, the bond angle distributions of the liquid and crystal were calculated. A pronounced difference was found between the liquid and crystal data for the O–Er–O and Er–O–Er distributions. The O–Er–O bond angle distribution exhibits two peaks at 80° and 140°, suggesting that ErO_6 polyhedra are highly distorted in the liquid. Another interesting feature is that the Er–O–Er bond angle distribution exhibits a peak at ~180°, which is not observed for the crystal or in *l*-ZrO_2, in addition to the peak at ~90° [1]. This two-peak structure in the Er–O–Er bond angle distribution indicates the formation of a distorted OEr_4 tetracluster network in the liquid phase (Fig. 2(a)), whereas tetraclusters are symmetric in the crystalline phase. This behavior suggests that the coordination of OEr_4 tetraclusters is more octahedral-like and hence is tolerant to disorder even in the liquid owing to the distortion, resulting in the very sharp PP in *l*-Er_2O_3 and a linear arrangement reflected by the prominent peak observed at 180° in the Er–O–Er bond angle distribution. This is clearly visible in Fig. 2(b), where linear atomic arrangements are highlighted by magenta lines.

To shed light on the similarity in topology between the crystal and liquid phases, the PDs for *l*-Er_2O_3 in both phases were calculated (Fig. 3). The figures show the similarity between the crystal and liquid phases. In particular, neither the Er-centric nor O-centric PD for *l*-Er_2O_3 shows a vertical profile along the death axis, which is a pronounced feature in a typical GFL such as *l*-SiO_2 [4]. The short lifetime of the profile as indicated by the small death value demonstrates that both the crystal and liquid phases exhibit a very densely packed structure associated with the formation of tetraclusters in both phases. We hypothesize that this similarity is a signature of non-GFL behavior and a factor hindering glass formation.

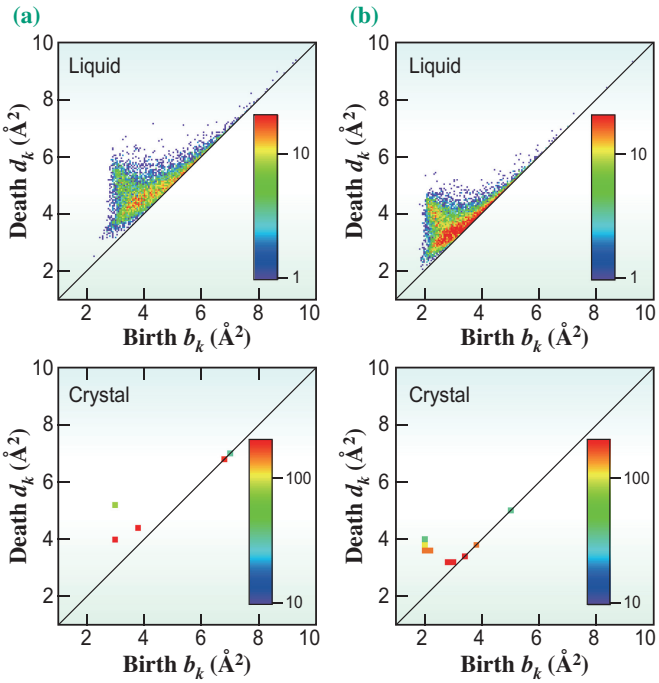

Fig. 3. Er-centric **(a)** and O-centric **(b)** persistence diagrams for Er_2O_3.

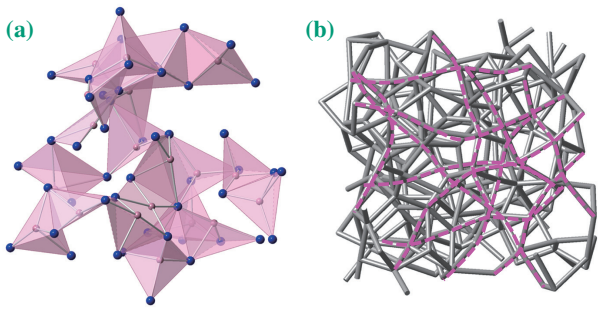

Fig. 2. **(a)** Visualization of the OEr_4 tetracluster network in *l*-Er_2O_3. Pink, oxygen; blue, erbium. **(b)** Visualization of the nearly linear arrangements of Er–O–E in *l*-Er_2O_3.

Chihiro Koyama[a,*], Shinji Kohara[b] and Takehiko Ishikawa[c]

[a] Human Spaceflight Technology Directorate, Japan Aerospace Exploration Agency
[b] Research Center for Advanced Measurement and Characterization, National Institute for Materials Science
[c] Institute of Space and Astronautical Science, Japan Aerospace Exploration Agency

*Email: koyama.chihiro@jaxa.jp

References

[1] S. Kohara *et al.*: Nat. Commun. **5** (2014) 5892.
[2] H. Tamaru *et al.*: Microgravity Sci. Technol. **30** (2018) 643.
[3] *C. Koyama, S. Tahara, S. Kohara, Y. Onodera, D.R. Småbråten, S.M. Selbach, J. Akola, T. Ishikawa, A. Masuno, A. Mizuno, J.T. Okada, Y. Watanabe, Y. Nakata, K. Ohara, H. Tamaru, H. Oda, I. Obayashi, Y. Hiraoka and O. Sakata: NPG Asia Mater.* ***12*** *(2020) 43.*
[4] Y. Onodera *et al.*: J. Ceram. Soc. Jpn. **127** (2019) 853.
[5] L.B. Skinner *et al.*: Phys. Rev. B **87** (2013) 024201.

Depth dependence of spin-specific magnetic hysteresis loop observed by magnetic Compton scattering

Since magnetic-field-dependent magnetization measurement is the most basic experimental technique for investigating magnetic materials, there are many magnetization measurement methods. The superconducting quantum interference device (SQUID) and vibrating sample magnetometer (VSM) are the most famous tools for observing the average magnetization curve of magnetic materials. X-ray magnetic circular dichroism (XMCD) is a useful method that has element selectivity and is extremely sensitive to surface magnetism. There are many methods for observing the magnetization curve, although magnetic Compton scattering (MCS) is the only method that has the potential to separate and investigate the magnetization curves of ferromagnets with sizes on the order of centimeters from the surface to the internal region.

MCS is one of the powerful methods of investigating the bulk magnetic properties of ferro- or ferrimagnets. MCS reflects only the spin magnetic moment. The magnetic field dependence of the magnetic effect of MCS represents the spin magnetization curve, in other words, the spin-specific magnetic hysteresis (SSMH) loop [1,2]. In this study, we present a novel application of MCS to measure the depth dependence of the SSMH loop [3]. This technique is realized by scanning X-rays with a vertical beam size of 10 μm. We demonstrate the depth dependence of coercivity in a neodymium magnet. The coercivity around the surface of the neodymium magnet degrades upon mechanical cutting and polishing.

The depth dependence of SSMH loops was measured on the high-energy inelastic scattering beamline of SPring-8 **BL08W**. The incident circularly polarized X-ray energy was monochromatized to 182.6 keV with a Si (620) monochromator. The degree of circular polarization was about 0.55. The X-ray beam size was determined to be 10 μm in the vertical direction and 1 mm in the horizontal direction using a four-quadrant slit. Scattered X-rays were detected using a 10-segmented Ge solid-state detector (Ge-SSD) with a scattering angle of 178°. The momentum resolution was 0.43 atomic units (a.u.). The sample was set in a quick reversible superconducting magnet with a magnetic field between –2.5 and 2.5 T. The reversal time from –2.5 to 2.5 was 7 s. The magnetization direction was taken to be parallel to the scattering vector. We can obtain the SSMH curve from the magnetic effect as a function of magnetic field. For example, to obtain the magnetic effect at H = X T, the sample was first saturated by applying the highest magnetic field (H = 2.5 T) and then the target magnetic field (X) was applied to the sample. Next, the lowest magnetic field (H = –2.5) was applied to saturate the sample and then the target magnetic field (–X) was applied to the sample. Then, the magnetic effect at H = X T was obtained as $(I_X - I_{-X})/(I_X + I_{-X})$, where I_T and I_{-X} are the integrated intensities of the magnetic Compton profile (MCP) at X T and –X T, respectively. The SSMH loops were measured in different regions from the surface to the inside by changing the vertical sample position where X-rays were irradiated. When the X-rays are at the edge of the sample, the SSMH loop represents the surface region. When the X-rays are at the center of the sample, the SSMH loop is dominated by the internal region. Note that the SSMH loop near the center position of the sample also includes the surface perpendicular to the incident X-rays. However, the effect is negligible because of the large penetration depth. Since MCS uses high-energy incident X-rays to enhance the magnetic effect of MCP, MCS has a large penetration depth. To demonstrate the depth dependence of the SSMH loop, a commercial neodymium magnet was used as a sample. The dimensions are 2×2×4 mm^3, and the long direction is parallel to the easy magnetization axis. All the measurements were carried out under vacuum at room temperature.

Figure 1 shows a schematic illustration of the depth dependence measurements of SSMH for the neodymium magnet. When the incident X-rays are at 1 or 3, the SSMH loop represents the surface region. When the X-rays are at 2, the loop is dominated by the internal region.

Figure 2 shows the depth dependence of SSMH loops, where 0.94 and –0.94 denote the surface regions and 0 is the center of the magnet. The vertical axis represents the magnetic effect, which is

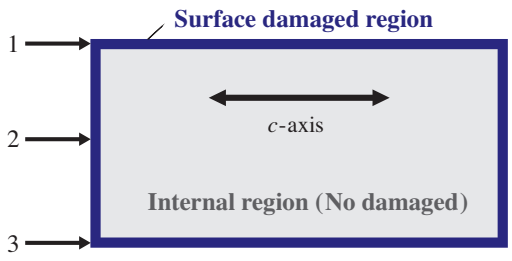

Fig. 1. Schematic illustration of the depth-dependent measurement of SSMH for the neodymium magnet.

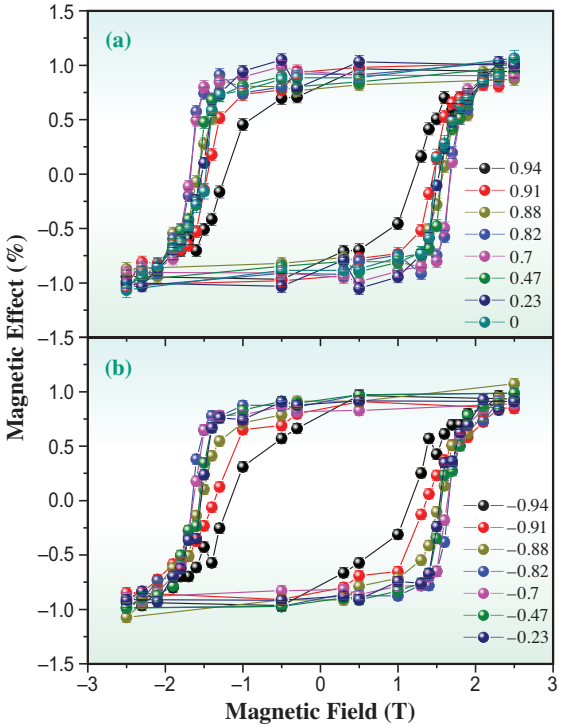

Fig. 2. Depth dependence of SSMH loops at **(a)** positive and **(b)** negative vertical sample positions.

proportional to the spin magnetization. The saturated spin magnetization is approximately constant, while the coercivity in the surface region decreases after surface treatment. To clarify the depth dependence of coercivity, we obtained the coercivity value by fitting a liner function to the SSMH data around its zero-cross point, as shown in Fig. 3. The demagnetization region extends to about 120 μm. Since the thickness of the surface damaged layer has been reported to be about 5 μm, this result shows that the effect of the narrow surface damaged layer extends to a deep region. The coercivity gradually decreases toward the center and is minimum at the center of the magnet. Kronmüller's equation is used to explain the coercivity of neodymium magnets and indicates that the coercivity is reduced by microstructural detects and/or the demagnetization field. Assuming that the microstructural defects are constant, we have concluded that the decrease in coercivity in the internal region may have been caused by the demagnetizing field. We expect that the present application of MCS will be a promising tool for magnetization measurement.

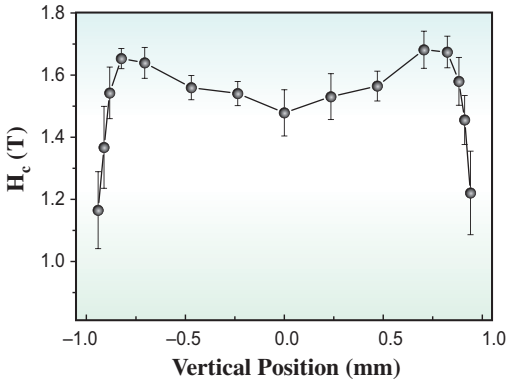

Fig. 3. Depth dependence of coercivity along the vertical sample position.

Naruki Tsuji

Japan Synchrotron Radiation Research Institute (JASRI)

Email: ntsuji@spring8.or.jp

References

[1] M. Itou *et al.*: Appl. Phys. Lett. **102** (2013) 082403.
[2] A. Agui *et al.*: J. Synchrotron Rad. **17** (2010) 321.
[3] *N. Tsuji, H. Sakurai and Y. Sakurai: Appl. Phys. Lett.* ***116*** *(2020) 182402.*

X-ray microscope for discriminating spiral orientation of structures inside materials

A number of creatures in our world have spiral structures, such as DNAs and α-helices in proteins in biology, and in modern industrial materials. It is an important scientific theme to clarify an origin of such structures and to conceive elaborate novel devices.

In the present research, the spiral staircase structures inside materials was transferred to form distinguished X-ray vortices by the transmission of X-rays. This new X-ray microscope is useful for discriminating the spiral orientations and for deriving the two-dimensional map of spiral structures inside materials (Fig. 1).

An optical vortex (OV) has a wave front in a spiral form that is smoothly connected to neighboring wave front displaced by integer multiples of wavelength (Fig. 2(a)). This integer number is the winding number, corresponding to the number of phase rotation in unit of 2π, and is proportional to the orbital angular momentum (OAM) around the central axis. Presence of strong novel dichroic effects is predicted to be induced by X-ray beams carrying OAM [2].

Such an optical vortex has a distinct intensity zero at the central spot and is one form of structured light, which has promoted various revolutionary applications in science and technology, especially in the visible wavelength. Structured light is formed by introducing defects in the wave fronts and is analogous to phase defects on other waves observed in physical phenomena over a wide range of length scales, from astrophysics, condensed matter physics to elementary particle physics.

Our novel X-ray microscope uses so-called radial-Hilbert transform (RHT) principle. The RHT is generalization of the Hilbert transform developed for signal processing of complex-valued data, such as calculation of the temporal derivative of radio signals. The RHT microscope visualizes the 2D distribution of the derivative of the "phase and amplitude" of a wave passing through a sample. Using this property, the RHT microscope is known to provide edge-enhanced image of the sample. Our research showed that the RHT microscope, further, has the high sensitivity to phase gradient along both radial and azimuthal angle and can be elaborately used to characterize OV for determining its winding number downstream of objects containing spiral structures.

The verification of our finding was performed at SPring-8 **BL29XU** using 7.71 keV X-rays. Our microscope used the Spiral Fresnel zone plate (SFZP) as the objective lens to modify the wave front downstream of objects and to add vorticity, l times 2π phase shift per one rotation around the optical axis, where l denotes the winding number [1] (Fig. 2(a)). The utilized SFZP is composed of two axially-symmetrical spiral zones with the depth of zones, the outermost zone width and the diameter of SFZP of 1.84 μm, 0.18 μm and 648 μm, respectively (Fig. 2(b)). The depth was chosen to give destructive interference for the two spiral zones for 7.71 keV X-rays. The distance between sample and SFZP and between SFZP and detector were chosen to be around twice the focal length of SFZP, 0.73 m, to satisfy the lens formula.

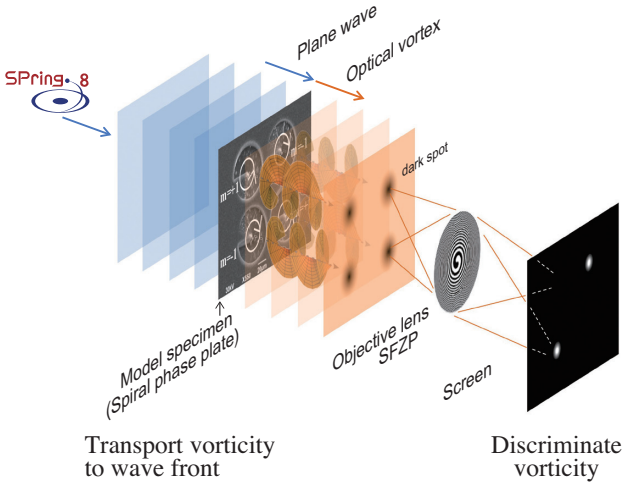

Fig.1. Schematics of the present research. Spiral staircase structure inside model specimen is transferred onto the X-ray wave front and form the distinguished X-ray vortex. Our new X-ray microscope using Spiral Fresnel Zone Plate (SFZP) as the objective lens is used to discriminate the spiral orientations and to derive the two-dimensional map of spiral structures in the model specimen.

We prepared a silicon demonstration specimen which contained multiple spiral phase plates (SPPs) with the thickness decrement in the clockwise and in the anti-clockwise orientations (Fig. 3(a)). The maximum depth of SPPs was set to 19.5 μm corresponding to the phase shift of 2π for 7.71 keV X-rays and the radii of SPPs were set to 34 μm. When X-ray transmitted through this specimen, X-ray vortices with reversed winding numbers, $m = -1$ and +1,were formed on its wave front. To prove our finding that the vorticity of the wave front will vanish when the vorticity given by the specimen and by the SFZP, objective lens, are canceled, we flipped SFZP to reverse the winding number l from $l = -1$ to +1. The observed microscope image manifested bright spots at the center of SPPs only when the winding numbers of OV formed by SPPs, m, and that of the SFZP, l, are canceled for $(l, m) = (-1, +1)$ or $(+1, -1)$, just as our theory predicted (Fig. 3(b) bottom panels). It is also important to note that the RHT microscope enables us to derive the two-dimensional map of spiral structures.

Our result manifested a high sensitivity of X-ray RHT microscope to detect X-ray vortices in the transmitted wave front downstream of spiral structures. We have already confirmed that X-ray vortices are formed by atomic spiral dislocations formed on crystals. X-ray RHT microscope will be a powerful tool for investigating such atomic spiral dislocations in Bragg reflection geometry. This method will be a new alternative to electron microscopes that need mapping of atoms to find such dislocations. Furthermore, our method will play a key role in investigating how the spiral and edge dislocations affect the quality of the functional materials, such as next-generation semiconductor power devices, light-emitting devices and high-rigidity metals. Special note is added here that the measured winding number or OAM is proportional to a quasi-magnetic field. Quasi-magnetic field represents the twist of the phase of the wave function and was the cause of another amazing effect, named the X-ray translation effect inside deformed crystal, which was first theoretically predicted [3] and was verified recently using SPring-8 [4,5].

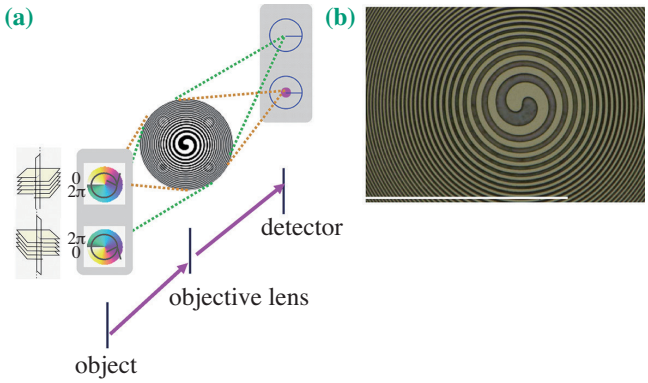

Fig.2. **(a)** Schematic diagram of experiment. At the object plane, spiral phase plates were set which gave the 2π phase jump to produce X-ray vortices with two inverse orientations as shown at the left. Due to the cancellation of vorticity, bright spots at the center of the spiral phase plates are observed in the microscope image plane only when the winding numbers of the spiral phase plates m and that of the SFZP l are canceled for $(l, m) = (-1, +1)$, or $(+1, -1)$ [see orange dotted lines]. Otherwise, dark spots are observed at the center [see green dotted lines]. **(b)** Visible light microscope image of SFZP. The scale bar is 100 μm.

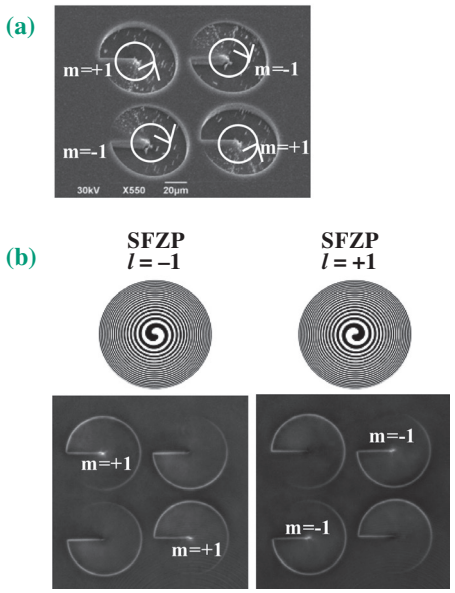

Fig.3. **(a)** Scanning electron microscope image of sample containing four spiral phase plates on silicon substrate with the thickness decrement in the clockwise and in the anti-clockwise orientations. The values of $m = -1, +1$ correspond to the winding number of the optical vortex when X-ray transmits through the spiral phase plates. **(b)** Middle panels show the orientations of the SFZP objective lens, which generates vorticity with the winding number $l = -1, +1$ to the wave front. The bottom panels show the X-ray radial-Hilbert transform microscope image of sample (a) with the corresponding settings of $l = -1, +1$. Bright spots were observed at the center of the spiral plates only for the cases of $(l, m) = (-1, +1)$, or $(+1, -1)$.

Yoshiki Kohmura

RIKEN SPring-8 Center

Email: kohmura@spring8.or.jp

References

[1] *Y. Kohmura, K. Sawada, M. Mizumaki, K. Ohwada, T. Watanuki and T. Ishikawa: Opt. Express* ***28*** *(2020) 24115.*
[2] M.V. Veenendaal and I. McNulty: Phys. Rev. Lett. **98** (2007) 157401.
[3] K. Sawada *et al.*: Phys. Rev. Lett. **96** (2006) 154802.
[4] Y. Kohmura *et al.*: Phys. Rev. Lett. **104** (2010) 244801.
[5] D. Takei *et al.*: Opt. Express **24** (2016) 24544.

Nematic correlation length in iron-based superconductors probed by inelastic X-ray scattering

Rod-shaped molecules in liquid crystals sometimes spontaneously align by "choosing" one of several equivalent orientations. This ordering is called nematic. Surprisingly, low temperature electronic nematic order was observed in iron (Fe)-based superconductors: Fluctuations of electronic spins and orbitals choose one of two equivalent orientations based on crystal symmetry. In many Fe-based superconductors, such as doped $BaFe_2As_2$, nematicity is believed to arise as a vestigial order of the stripe spin-density wave state that sets in at a lower temperature and selects one of two orthogonal wave-vectors related by a 90° rotation [1]. An exception may be FeSe, where nematic order sets in at 90 K, but magnetic order does not form at any temperature at ambient pressure [1], although antiferromagnetic (AFM) order appears under pressure. The origin of nematic order in FeSe remains a topic of intense debate.

The impact of the electron-phonon coupling on the nematic order in Fe-based superconductors has been investigated in different contexts.

Transverse acoustic (TA) phonons dispersing in the [100] direction exhibit the strongest experimentally observed electron-phonon coupling. They soften with temperature (T) on approaching the orthorhombic distortion at the structural transition temperature (T_S) of the atomic lattice in the nematic phase [2]. Quantitative analysis of this softening allows extracting the nematic correlation length ξ [2].

The new experiments [3] compared the T dependence of ξ in FeSe and underdoped $Ba_2(Fe_{1-x}Co_x)_2As_2$ (UD Ba-122), whose doping level (x = 0.03) was chosen such that its structural transition temperature T_S = 95 K was close to that of FeSe, which was T_S = 90 K. In addition, detailed measurements of an optimally doped $Ba(Fe_{0.94}Co_{0.06})_2As_2$ (OP Ba-122) sample with a superconducting transition temperature T_c = 25 K, reached larger wave vectors than in the previous study [3]. To achieve better wave vector resolution with larger scattering intensity, inelastic X-ray scattering instead of neutron scattering was used.

Measurements were carried out on the high-resolution inelastic X-ray scattering beamlines SPring-8 **BL43LXU** and APS Sector 30. The phonon softening is clearly seen in Fig. 1(a) as the separation between energy loss and energy gain peaks decreases and the intensity increases upon cooling toward T_S. The trend reverses upon further cooling. Figure 1(b), where the peaks are well separated, shows the individual contributions of the elastic peak plus the Stokes and anti- Stokes phonon peaks. The phonon energy at **Q** = (2, 0.05, 0) in FeSe as a function of temperature is similar to the expected behavior of the shear modulus C_{66} from mean-field theory (inset of Fig. 1(a)), which cannot otherwise be observed below T_S by three-point bending or resonant ultrasound experiments due to twinning in the sample.

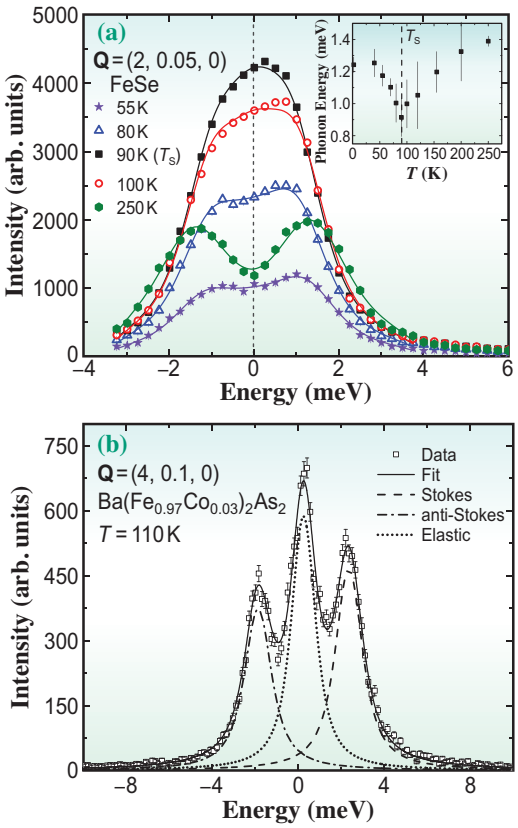

Fig. 1. Raw data with fits. **(a)** Energy scans on FeSe at **Q** = (2, 0.05, 0). Data taken at T_S = 90 K are represented by the black squares. Error bars are similar in size to the symbols. Inset: Phonon energy at **Q** = (2, 0.05, 0), with T_S marked by the dashed line. **(b)** An example fit for data on UD Ba-122 at **Q** = (4, 0.1, 0), T = 110 K. The raw data are represented by the empty symbols, the total fit by the solid black line, and then the elastic, Stokes, and anti-Stokes peaks by the dotted, dashed, and dash-dotted lines, respectively.

Figure 2 shows the phonon dispersion (solid lines) in (a) UD Ba-122 at 290 and 98K (T_S = 95 K) and (b) in FeSe at 300 and 95 K (T_S = 90 K) fitted with Eq. 1 in Ref. 4, where ξ is the only free parameter. The fits accurately described the phonon behavior at all recorded temperatures, including the phonon softening effect near the structural transition temperature.

There was a striking similarity in the behaviors of the nematic correlation lengths between all three compounds, despite their rather different ground states, demonstrated in Fig. 3. Most importantly, the T dependence of ξ in FeSe and underdoped and optimally doped $Ba_2(Fe_{1-x}Co_x)_2As_2$ is very well described by $(T - T_0)^{-1/2}$. Combined with the Curie-Weiss behavior observed in nematic susceptibility, these results point to a mean-field behavior with fluctuations extending to rather high temperatures above the structural transition temperature T_S. This mean-field behavior may originate from the coupling to the lattice, which is known theoretically to change the universality class of the nematic transition from Ising-like to mean field due to the long-range nematic interactions mediated by strain fluctuations.

These observations highlight the key role played by the nematoelastic coupling, which not only changes the character of the nematic transition, but also extends the impact of the nematic fluctuations to rather high temperatures above T_S. Such a coupling has been proposed to be detrimental to the enhancement of T_c by quantum critical nematic fluctuations. Whether this explains the observed behavior of T_c across the phase diagram of chemically substituted $FeSe_{1-x}S_x$, is an interesting topic for future investigation. Moreover, the similar behavior of the nematic correlation length in FeSe and Ba-122 raises important questions about the interplay between nematicity and magnetism. Although FeSe displays no long-range magnetic order, it has a strong fluctuating magnetic moment, comparable to that of Ba-122. Whether this is enough to explain the similar behavior of ξ in both compounds is an issue that deserves further studies.

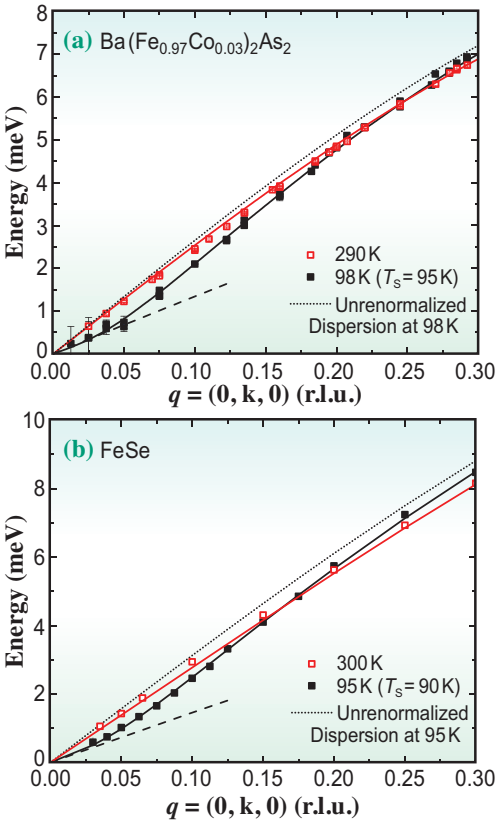

Fig. 2. Phonon dispersion fits for UD Ba-122 **(a)** and FeSe **(b)**. The dotted black line is the expected dispersion in the absence of nematic fluctuations. The data (solid black squares) and fit (solid black curve) show clearly visible softening that increases at low q. The dashed line shows the expected low q slope if the nematic correlation length was very small; it matches the phonon energies only at very low q. Hollow red squares (solid red line) show data (fit) at high temperature.

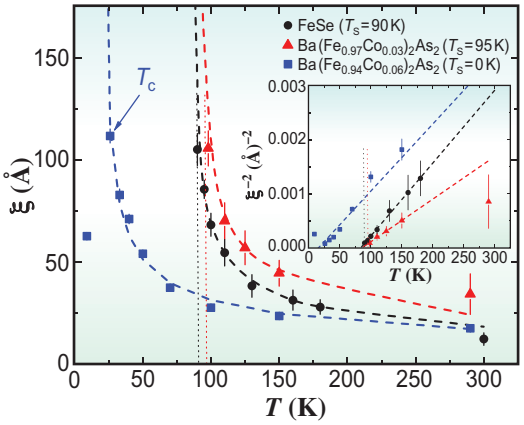

Fig. 3. Nematic correlation length as a function of temperature for FeSe (black circles), for UD Ba-122 (red triangles), and for OP Ba-122 (blue squares). The dashed lines are power-law fits of the form $\xi = \xi_0/(T - T_0)^{1/2}$. Note that only the data above T_c were fit for OP Ba-122, since the increase in nematic correlation length on cooling is reversed by superconductivity. Inset: ξ^{-2} for the materials as in the main panel, with linear fits (dashed lines). It demonstrates the universal power-law behavior with the x intercepts at 84 ± 1 K for FeSe, 86 ± 2 K for UD Ba-122, and 16 ± 4 K for OP Ba-122.

Adrian M. Merritt[a], Frank Weber[b] and Dmitry Reznik[a,*]

[a] Department of Physics, University of Colorado at Boulder, USA
[b] Institute for Quantum Materials and Technologies, Karlsruhe Institute of Technology, Germany

*Email: dmitry.reznik@colorado.edu

References

[1] R.M. Fernandes *et al.*: Nat. Phys. **10** (2014) 97.
[2] T.M. McQueen *et al.*: Phys. Rev. Lett. **103** (2009) 057002.
[3] J.L. Niedziela *et al.*: Phys. Rev. B **84** (2011) 224305.
[4] F. Weber *et al.*: Phys. Rev. B **98** (2018) 014516.
[5] *A.M. Merritt, F. Weber, J.-P. Castellan, Th. Wolf, D. Ishikawa, A.H. Said, A. Alatas, R.M. Fernandes, A.Q.R. Baron and D. Reznik: Phys. Rev. Lett.* ***124*** *(2020) 157001.*

Impact of massive-like ferrite to austenite transformation during and after solidification on microstructure evolution in steels

The peritectic reaction in the Fe–C system is taught as a fundamental transformation mode in undergraduate courses on solidification and casting of metallic alloys. During solidification in peritectic FeC systems with carbon contents of less than 0.5 mass% C, the primary solid phase (ferrite, body-centered cubic) grows as a high-temperature phase and the secondary solid phase (austenite, face-centered cubic) is produced through reaction between ferrite and the remaining liquid phase. As a result of the peritectic reaction, ferrite is covered with austenite. This multiphase solidification model has been accepted for many years.

In solidification and casting processes of steels, the peritectic solidification reaction is key to understanding formation of casting defects, such as unevenness of solidifying shells and hot tears (cracks). Volume change owing to the transformation from ferrite to austenite can contribute to formation of these defects. Thus, the previous studies focused on the mechanism of casting defect formation based on the peritectic transformation. Apart from solidification, the undesirable coarsening of austenite grains has been recognized during subsequent cooling. Until recently, rapid coarsening and peritectic solidification were considered as separate phenomena.

Time-resolved and *in situ* observations of solidification in steels, which were performed at SPring-8 **BL20B2** and **BL20XU**, proved that ferrite could transform massively to austenite in Fe–C peritectic systems (referred to as a massive-like transformation) [1]. The preliminary findings introduced some challenges for further understanding by X-ray imaging techniques: one question was whether the massive-like transformation influences the subsequent microstructure evolution; another is whether the massive-like transformation applies to industrial solidification and casting processes. Progress in understanding of this massive-like transformation was recently reviewed [2].

Figure 1(a) shows a typical setup for transmission imaging with X-ray diffraction (XRD). Transmission images were observed by a beam monitor (pixel size: 1 μm×1 μm to 5 μm×5 μm; frame rate: up to 100 fps). XRD images were observed by a panel-type detector to identify the crystal structure. XRD images help to detect a phase transformation, even though the Bragg condition is rarely satisfied because of the highly coherent and monochromatized X-rays of these beamlines. Figure 1(b) shows a time-resolved tomography (4D-CT) and XRD setup. Projected images for three-dimensional (3D) reconstruction were observed by a beam monitor (pixel size: 6.5 μm×6.5 μm; typical frame rate for steels: 100 fps). XRD spots were observed by a panel-type detector (pixel size: 100 μm×100 μm; frame rate: 30 fps). The crystallographic orientation was analyzed from the XRD spot positions and sample rotation angle. The typical temporal resolution was 4 s for steel solidification. This technique was also used to observe the distribution of crystallographic orientations before and after the massive-like transformation.

This transmission imaging showed the impact of the massive-like transformation from ferrite to austenite on subsequent microstructure evolution. Figure 2 shows dendrite arm fragmentation that was induced by the massive-like transformation in Fe–0.45% C–0.6% Mn–0.3% Si alloys [3]. The ferrite dendrites were maintained at approximately 20 K below the peritectic temperature (after 152 s), allowing austenite to thermodynamically nucleate and grow. The massive-like transformation from ferrite to austenite occurred at 346 s. Austenite with a perturbed interface grew rapidly into the liquid phase. Dark spots in the dendrite arms indicate that multiple austenite grains formed within the ferrite dendrite arms. Liquid film formation at austenite grain boundaries was also detected, as indicated by the blue arrows. In addition, the austenite boundaries (liquid film) migrated with a velocity as fast as 1 μm/s. As a result of the liquid film formation and austenite coarsening, the austenite

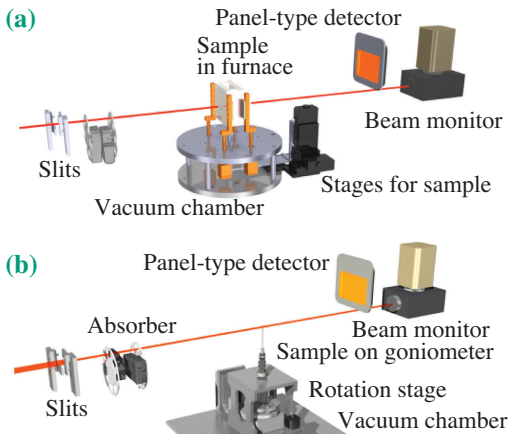

Fig. 1. Typical setups to observe steel solidification and transformation from ferrite to austenite. **(a)** Transmission imaging (2D observation) with X-ray diffraction and **(b)** time-resolved tomography (3D+time observation, 4D-CT) with X-ray diffraction.

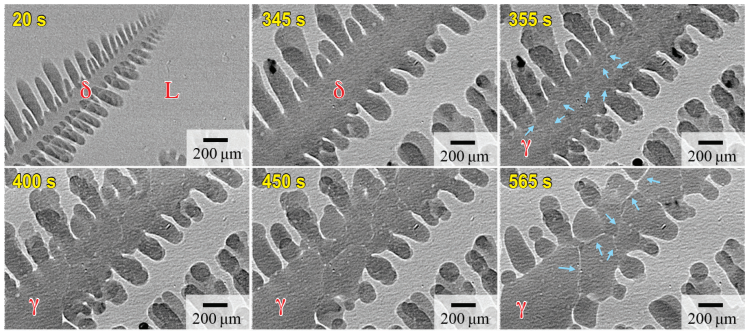

Fig. 2. Fragmentation of γ grains induced by massive-like δ–γ transformation in 0.45 C steel (0.45 C, 0.6 Mn, 0.3 Si in mass%) [3]. Transformation occurred at 20 K below the peritectic temperature after 152 s. Liquid film produced at γ grain boundaries indicated by blue arrows. The X-ray energy and exposure time were 21 keV and 50 ms, respectively.

grains were isolated by the liquid phase, as shown in the image at 565 s. These observations demonstrated that solidified dendrites could be remelted and fragmented by the massive-like transformation. The multiple austenite grains produced by the massive-like transformation consequently influence formation of the subsequent microstructure.

From industrial considerations, it was critical to confirm whether ferrite massively transformed into austenite or austenite grew in the diffusion-controlled mode. Time-resolved and *in situ* observation using transmission imaging was performed to observe the microstructure evolution during unidirectional solidification [4]. The massive-like transformation was selected at a growth rate of as low as 50 μm/s. The peritectic reaction, which was controlled by atomic diffusion, only occurred at growth velocities of less than 10 μm/s. Growth velocities in industrial processes exceed 10 μm/s, so the massive-like transformation is expected to be selected for conventional processes.

Time-resolved XRD measurements using the 4D-CT setup were performed to observe austenite coarsening [5]. Fine austenite grains, in which strains were induced, were produced in a ferrite grain through the massive-like transformation. After the transformation, the austenite grains coarsened and/or vanished. Simultaneously, the induced strains were released and new γ grains were even created. Grain formation during coarsening cannot be simply explained by typical coarsening controlled by the curvature effect: the massive-like transformation should be included to understand the coarsening kinetics in subsequent cooling after solidification.

Figure 3 shows a schematic illustration of possible transformation modes from ferrite to austenite in Fe–C alloys. As proved by recent studies [1–5], the massive-like transformation—rather than the peritectic reaction—occurs in conventional solidification processes. However, this transformation mode has not, to date, been explicitly included in modeling of solidification and casting defect formation. This will be critical for improving our understanding of the transformation and casting defect formation from an industrial perspective.

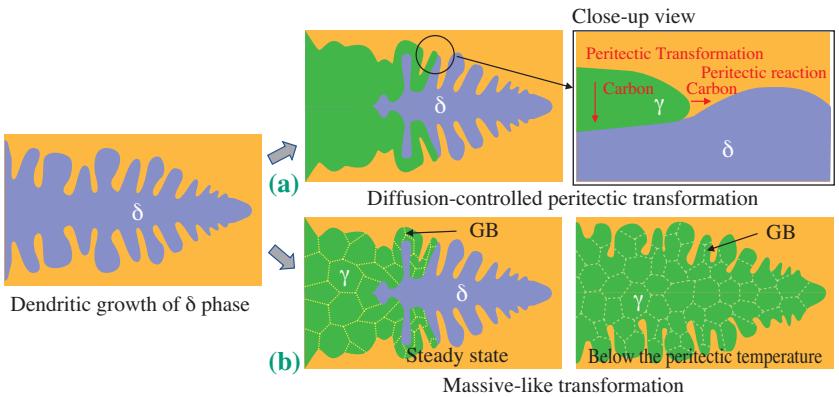

Fig. 3. Possible of transformation modes in peritectic Fe–C alloy systems [2]. **(a)** Diffusion-controlled peritectic transformation and **(b)** massive-like transformation. X-ray imaging studies in SPring-8 proved that the latter mode is selected in conventional processes.

Hideyuki Yasuda

Department of Materials Science and Engineering, Kyoto University

Email: yasuda.hideyuki.6s@kyoto-u.ac.jp

References

[1] H. Yasuda *et al.*: ISIJ Int. **51** (2011) 402.
[2] H. Yasuda, K. Morishita, M. Yoshiya, T. Narumi: ISIJ Int. **60** (2020) 2755.
[3] *H. Yasuda, K. Morishita, N. Nakatsuka, T. Nishimura, M. Yoshiya, A. Sugiyama, K. Uesugi, and A. Takeuchi: Nat. Commun. **10** (2019) 3183.*
[4] T. Nishimura *et al.*: ISIJ Int. **60** (2020) 930.
[5] H. Yasuda *et al.*: IOP Conf. Ser. Mater. Sci. Eng. **861** (2020) 12051.

Observation of magnetization reversal process for $(Sm,Ce)_2(Co, Fe, Cu, Zr)_{17}$ magnets by soft X-ray magnetic circular dichroism microscopy

Sm_2Co_{17} magnets, which have a higher saturation magnetization than $SmCo_5$, have been developed in Japan [1]. In the beginning of 1970s, the magnetic properties of Sm–Co magnets were markedly improved to more than 240 kJ/m^3 in $Sm_2(Co, Fe, Cu, Zr)_{17}$ magnets [2]. These magnets were used in small motors such as spindle motors for cassette tape players called "WALKMAN®", acoustic applications such as small speakers, microphones or pick-up sensors, and motors used in wristwatches. Sm–Co magnets contributed to the realization of unprecedent small size and light weight of electric appliances. At the beginning of 1980, Nd–Fe–B magnets were invented, replacing the Sm–Co magnets, and have been used in various applications of not only small devices but also high-power devices such as the traction motors of hybrid and electric vehicles or the compressor motors of air conditioners. However, as these markets grow, significant resource problems arise. A small portion of Nd in Nd–Fe–B was replaced with heavy rare-earth elements of dysprosium (Dy) and terbium (Tb) to achieve the high coercivity necessary to enable the use of these magnets in high-temperature and high-demagnetization-field applications. Among rare-earth elements, Dy and Tb belong to precious metals; they are mainly produced in China and their resources are limited. Even though the Sm resources are almost 1/10 of the Nd resources, Sm–Co magnets do not require Dy or Tb and have good magnetic properties at high temperature above 200°C.

It is well known that the coercivity of $Sm_2(Co, Fe, Cu, Zr)_{17}$ is determined by the magnetic domain wall motion. In the grain of this magnet, cellular structures of $Sm(Co,Cu)_5$ and $Sm_2(Co,Fe)_{17}$ phases exist, where almost 100 nm of $Sm_2(Co, Fe)_{17}$ phases is surrounded by $Sm(Co,Cu)_5$ thin platelet phases, and these $Sm_2(Co, Fe)_{17}$ phases are separated from each other. Magnetic domain walls are pinned at the phase boundary of the two phases or are in the $Sm(Co,Cu)_5$ phase. When the demagnetization field applied is greater than the pinning field, the magnetic domain wall jumps through this cellular structure and the coercivity can be determined. However, it was unclear where the initial reverse magnetic domain formed in the demagnetization process and why the rectangularity (H_k/H_{cJ}) of the demagnetization curve, where H_k is defined as the magnetic field corresponding to 90% of remanence and H_{cJ} is the coercivity, is lower than that of Nd–Fe–B sintered magnets.

We investigated the magnetization reversal process for highly aligned $Sm_{0.67}Ce_{0.33}(Co_{0.73}Fe_{0.2}Cu_{0.05}Zr_{0.02})_{7.2}$ by soft X-ray magnetic circular dichroism (XMCD) microscopy at SPring-8 **BL25SU** [3]. Figure 1(a) shows bulk demagnetization curves and Figs. 1(b–e) show the XMCD images obtained using the Co L_3 absorption edge in various magnetic fields indicated by circles in Fig. 1(a). In Figs. 1(b–e), the red (blue) region is where the magnetization is parallel (antiparallel) to the positive direction of the external magnetic field (H). White regions correspond to the neutral area in terms of magnetization or to nonmagnetic inclusions, which were identified as Sm oxide by energy dispersive X-ray spectroscopy (EDX). The magnetization saturated at +5.0 T. It was found that the initial magnetization reversal occurred at the grain boundary and in the vicinity of Sm oxide, as shown in Fig. 1(c). At –0.5 T, the reversal region extended into the grains(Fig. 1(d)), and reached the zero of magnetization i.e., coercivity (Fig. 1(e)).

Figure 2(a) is an enlargement of the area surrounded by the square in Fig. 1(d), where reversal extended into the grains at the grain boundary (Fig. 1(d)) and in the vicinity of Sm oxide (Fig. 1(e)). The local demagnetization curves for each position

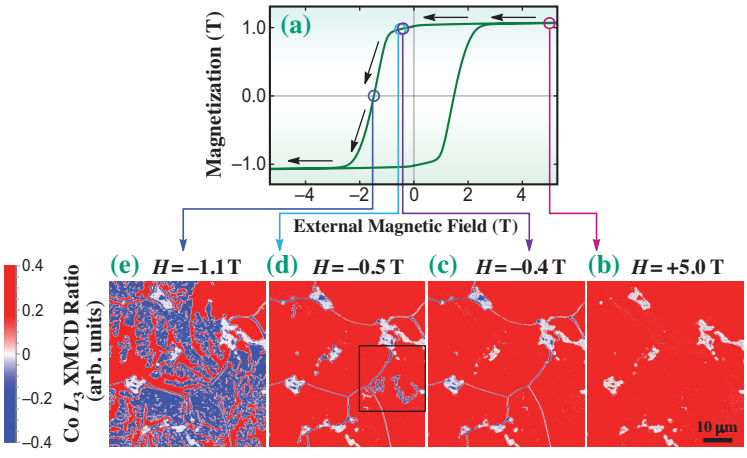

Fig. 1. Bulk demagnetization curve of anisotropic $(Sm, Ce)_2(Co, Fe, Cu, Zr)_{17}$ magnets **(a)** and XMCD images obtained using Co L_3 absorption edge under external magnetic fields of H=+5.0 T **(b)**, –0.4 T **(c)**, –0.5 T **(d)** and –1.1 T **(e)**. [3]

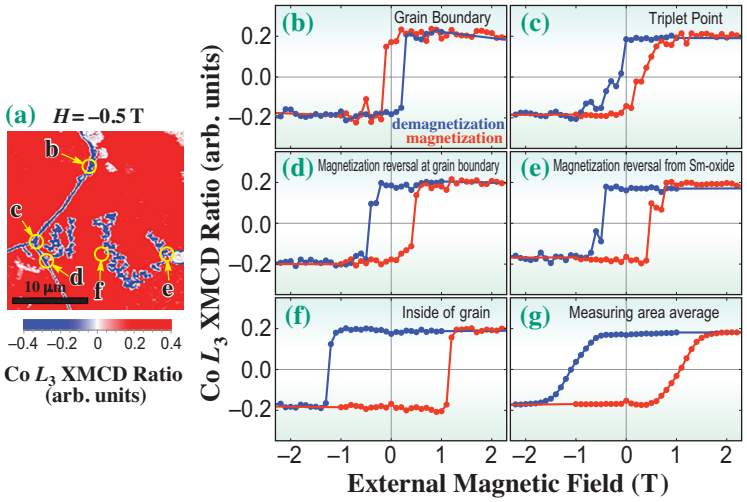

Fig. 2. Enlarged XMCD image **(a)** of the area surrounded by the square in Fig. 1(d), where initial magnetization occurred at grain boundary (b) and in the vicinity of Sm oxide, followed by magnetization reversal areas extending into grains from the grain boundary at (d) and the vicinity of Sm oxide at E in Fig. 2(a). **(b)–(f)** Local demagnetization curves at (b) to (f) marked in (a). **(g)** Average of local demagnetization curves of entire measurement area. [3]

marked by yellow circles in Fig. 2(a) are shown in Figs. 2(b–f); these were evaluated from the Co L_3-edge XMCD signal intensity. The average local demagnetization curve of the entire measurement area is shown in Fig. 2(g). It was found that the coercivity and rectangularity in local magnetic properties are different between those inside the grain (Fig. 2(f)), at the grain boundary (Fig. 2(b)), at a triplet point (Fig. 2(c)), at the starting point where a reversal domain extends into a grain (Fig. 2(d)), and in the vicinity of Sm oxide (Fig. 2(e)). It was verified that H (–0.5 T) in Fig. 2(d) agrees well with H where their magnetization starts to decrease in Fig. 2(g). To verify the composition differences between grains and the grain boundary and the vicinity of the Sm oxide, EDX line scanning was applied. Figure 3 shows the results of line scanning for Co, Fe, and Cu in the peripheral region of the grain boundary, and for Sm, Co, Fe and Cu in the vicinity of Sm oxide. At the grain boundary, it was confirmed that the amount of Fe increases and that of Cu decreases, and in the vicinity of Sm oxide, the amounts of Cu, Fe, and Co decrease and that of Sm increases.

Using the cutting-edge visualization technology of XMCD microscopy, the factors causing the deterioration of coercivity for Sm_2Co_{17} magnets were clarified and directly detected by the observation of the magnetization reversal process. The coercivities of these magnets could be increased by the improvement of the process of removing Sm oxide and by the improvement of the composition of the grain boundary.

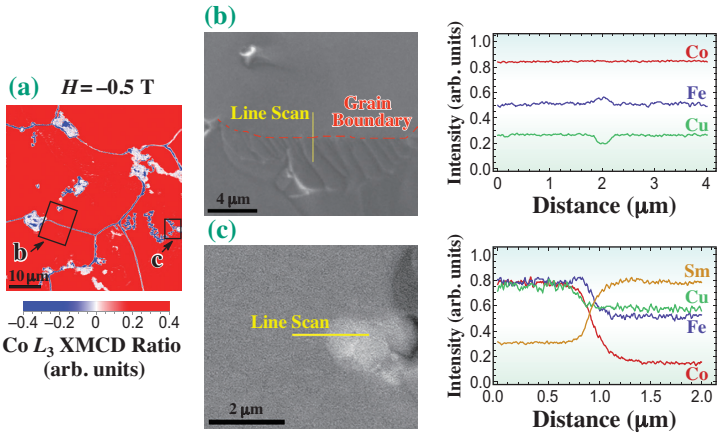

Fig.3. **(a)** Co L_3 XMCD image under external magnetic field of –0.5 T. Secondary electron microscopy images and results of line scanning at grain boundary **(b)** and in the vicinity of Sm oxide **(c)**. [3]

Y. Matsuura[a,*], R. Tamura[b], K. Ishigami[c] and T. Nakamura[c,d]

[a] Research Institute for Applied Sciences
[b] Dept. of Materials Science and Technology, Tokyo University of Science
[c] Japan Synchrotron Radiation Research Institute (JASRI)
[d] International Center for Synchrotron Rad. Innovation Smart, Tohoku University

*Email: yutaka.matsuura@rias.or.jp

References

[1] H. Senno, Y. Tawara: IEEE Trans. Magn. **10** (1974) 313.
[2] T. Ojima *et al.*: IEEE Trans. Magn. **13** (1977) 1317.
[3] *Y. Matsuura, R. Maruyama, R. Kato, R. Tamura, K. Ishigami, K. Sumitani, K. Kajiwara and T. Nakamura: Appl. Phys. Lett.* ***117*** *(2020) 022409.*

Skewing of electronic band along the direction of electric polarization in ferroelectrics

Ferroelectric materials have a spontaneous polarization due to the relative ionic displacement involving inversion symmetry breaking that plays an essential role in high dielectric capacitors, piezo-actuators, pyro-sensors, and nonlinear optics. In the research and industry fields, the majority treats ferroelectric material as a typical insulator owing to its high resistivity and wide optical band gap, and this is the fact that we learned in textbooks. Modern theoretical work has revealed an approach showing the electronic structure of ferroelectrics using the Berry phase formulation, which is a revolutionary breakthrough that opens the doors to new methodologies for developing novel functioning electronic devices using ferroelectric oxide materials, such as a nonvolatile random access memory and memristors, for realizing a future artificial neural network. The principle of the work for such ferroelectric devices is based on a characteristic electron tunneling. Electrons can be transferred in the heterostructure of a ferroelectric oxide thin film sandwiched by two different electrodes, e.g., Pt/$BaTiO_3$ (BTO)/Nb-$SrTiO_3$, the so-called ferroelectric tunneling junction (FTJ) [1]. In FTJs, electrons can move in the film along the potential slope depending on the polarization direction (Fig. 1). In the Schottky barrier formed at the interface near the doped semiconductor, its height and depletion regions can be switched by electric polarization reversal. This behavior originates from the skewed electronic structure of ferroelectrics. The depolarization field generated by electric polarization causes an electrostatic potential gradient along the polarization direction, forming a skewed band structure. Such a gradual potential affects the Schottky barrier and drives the rectification of electron transfer in FTJs. Thus, the ferroelectric band skewing (FEBS) structure is a crucial physical property for developing functional FTJs. The concept of the FEBS structure was predicted in 1973 [2]. The first-principles calculation is performed for FEBS in the ferroelectric BTO thin film [3]; however, the actual structure has not yet been demonstrated.

We have recently succeeded in showing experimental evidence for FEBS, which was obtained from the depth profiles of atomic orbitals of angle-resolved hard X-ray photoemission spectra of ferroelectric BTO thin films [4]. We prepared epitaxial BTO thin films of various thicknesses by pulsed laser deposition. We used the experimental equipment of angle-resolved hard X-ray photoemission

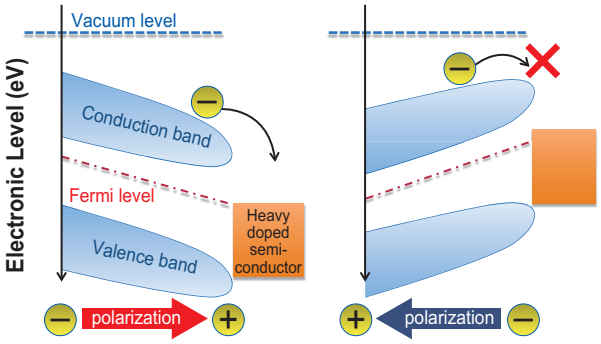

Fig. 1. The schematic figure of the FEBS structure. The electronic band is skewed along the direction of the electric polarization. This slope can be switched by the polarization reversal.

spectroscopy (AR-HAXPES) at SPring-8 **BL47XU**, which allows for the direct observation of the FEBS structure in ferroelectric materials. AR-HAXPES with synchrotron radiation has the advantage of providing a 20-nm-deep profile of photoelectron emission spectra. The AR-HAXPES unit installed at BL47XU is equipped with an objective lens with a wide acceptance angle of 64°, which is a significant advantage for our study. In a conventional AR-HAXPES unit without a wide-angle objective lens, the optical angle between the incident beam and the sample is often required to be mechanically adjusted, a feature that causes difficulty in achieving accurate angular resolution and beam positioning within the micrometer domain on samples. The emission angle of the photoelectron almost corresponds to the depth of the sample, but this estimation is theoretically invalid. We must consider the depth sensitivity, which is affected by the inelastic mean free path of photoelectrons, and the optical geometry between the sample surface and incident X-ray/irradiated photoelectrons. As a future task, we are developing an analytical technique for the accurate measurement of the depth profile.

Our results show that electronic core levels and the valence band shift to higher energy following electrical polarization orientation in BTO thin films. Figure 2 shows AR-HAXPES spectra of the valence band in 5-nm-thick BTO, observed at various depths. The valence band of BTO consists of three electronic states: one pure O–2*p* orbital and two O–2*p* and Ti–3*d* hybridized states. The position of the three states shifts to the high-energy side from the surface to a deeper region. Since the direction of electric

polarization of this sample points into the substrate, the binding energy of atomic orbitals increases along with the electric polarization. The energy shift depends on the magnitude of the electric polarization. We also demonstrated that the slope of FEBS could be changed by switching the polarization, as shown in Fig. 3. Our experimental result proves the ferroelectric origin of the band-skewed structure, which agrees with the theoretical prediction.

The electric polarization induces FEBS, which indicates a gradual change in electrostatic potential in a ferroelectric crystal. In our experiment, an electronic structure skewed by the electric polarization is revealed by the binding energy shift of atomic orbitals. All atomic orbitals show similar behaviors, but the magnitude of the energy shift derived from FEBS is different. We attributed the electric polarization in the ion crystal to the atomic contribution. It is well known that the amplitude of the polarization calculated from the relative ionic displacement is underestimated. Born effective charges, which are different from nominal ionic charges, are defined by the actual amplitude of the polarization divided by the ionic displacement [5]. We found that the magnitude of the energy shift of each atomic orbital has good correlation with the Born effective charge. We also estimated an effective screening length and a depolarizing field using the magnitudes of the binding energy shift and electric polarization at various thicknesses. The values are in good agreement with the results of first-principles calculation and depend on the film thickness. The direct observation of FEBS has been performed by AR-HAXPES, which proves to be a useful technique for observing the ferroelectric characteristic electronic structure and facilitates its understanding.

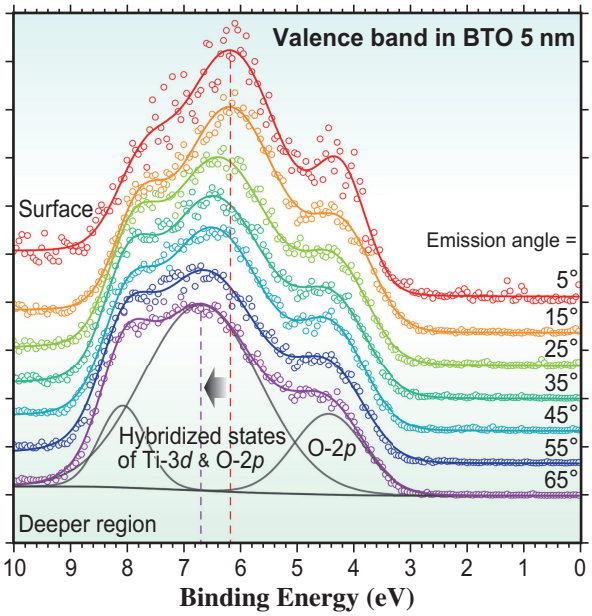

Fig. 2. AR-HAXPES spectra of the valence band in the 5-nm-thick BTO observed at each emission angle. The valence band consists of three densities of states. In the spectrum at emission angle = 65°, the fitted curves of background and Voigt function are drawn as gray lines. Binding energy is referenced to the energy of the Au Fermi edge.

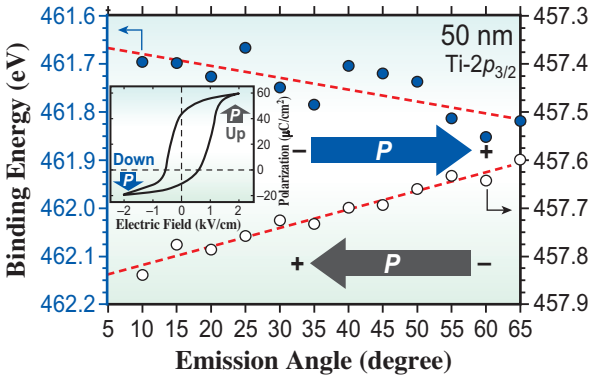

Fig. 3. Depth dependence of binding energies of Ti-$2p_{3/2}$ atomic orbital in 50-nm-thick BTO with different polarization directions. Open circles indicate the energy shift when the electric polarization points upward. Blue closed circles are for electric polarization the pointing downward. Black and blue arrows show the directions of electric polarization upon switching induced by applying an electric field. The inset shows the *P*–*E* hysteresis loop.

Jun Kano[a,*] and Norihiro Oshime[b]

[a] Graduate School of Natural Science and Technology, Okayama University
[b] Synchrotron Radiation Research Center, QST

*Email: kano-j@cc.okayama-u.ac.jp

References

[1] E.Y. Tsymbal and A. Gruverman: Nat. Mater. **12** (2013) 602.
[2] P. Wurfel and I.P. Batra: Phys. Rev. B **8** (1973) 5126.
[3] X. Liu *et al.*: Phys. Rev. Lett. **116** (2016) 197602.
[4] *N. Oshime, J. Kano, E. Ikenaga, S. Yasui, Y. Hamasaki, S. Yasuhara, S. Hinokuma, N. Ikeda, P.-E. Janolin, J.-M. Kiat, M. Itoh, T. Yokoya, T. Fujii, A. Yasui, H. Osawa: Sci. Rep.* ***10*** *(2020) 10702.*
[5] R. Resta *et al.*: Phys. Rev. Lett. **70** (1993) 1010.

Electronic structure of Yb compounds probed by hard X-ray photoemission spectroscopy

Yb compounds exhibit interesting physical properties originating from the hybridization between localized 4*f* electrons and itinerant conduction electrons (c–f hybridization). When the c–f hybridization is weak, the Ruderman-Kittel-Kasuya-Yosida interaction, where the 4*f* moments at different Yb sites interact indirectly mediated by the conduction electrons, is dominant and a magnetic order is realized at low temperatures. In contrast, when the c–f hybridization is strong, the Kondo effect becomes dominant and the 4*f* moments are screened with the conduction electrons, leading to a nonmagnetic ground state. The situation is summarized in the Doniach phase diagram [1]. The boundary point separating the magnetic and nonmagnetic ground state regions defines the quantum critical point (QCP). Unconventional physical phenomena such as superconductivity and a non-Fermi liquid state, where the electrical resistivity and specific heat, for example, show temperature dependences different from those in the normal metals, are observed near the QCP. In the study of 4*f* electron systems, one of the most important issues is to establish the electronic structure around the QCP.

$YbNi_3X_9$ and $Yb_2Pt_6X_{15}$ (X = Al, Ga) are suitable systems for investigating the change in electronic structure across the QCP. $YbNi_3Al_9$ exhibits magnetic order below 3.4 K, while $YbNi_3Ga_9$ shows no magnetic order. $YbNi_3Al_9$ and $YbNi_3Ga_9$ thus occupy the weak and strong c–f hybridization regions, respectively, across the QCP in the Doniach phase diagram, in spite of having the same crystal structure and similar conduction electronic states. Although $YbNi_3X_9$ and $Yb_2Pt_6X_{15}$ have similar crystal structures and are both located in the nonmagnetic region, magnetic susceptibility measurements indicate that $Yb_2Pt_6Al_{15}$ is closer to the QCP than $Yb_2Pt_6Ga_{15}$. Thus, $YbNi_3X_9$ and $Yb_2Pt_6X_{15}$ provide an opportunity to systematically investigate the change in electronic structure in moving from magnetic (weak c–f hybridization) to nonmagnetic (strong c–f hybridization) regions in the Doniach phase diagram across the QCP. In this study, we carried out hard X-ray photoemission spectroscopy (HAXPES) measurements at hν = 5.95 keV on $YbNi_3X_9$ and $Yb_2Pt_6X_{15}$ at SPring-8 **BL15XU** [2,3].

The Yb $3d_{5/2}$, Ni $2p_{3/2}$ ($YbNi_3X_9$) and Pt $4f_{7/2}$ ($Yb_2Pt_6X_{15}$) and valence-band HAXPES spectra of $YbNi_3X_9$ and $Yb_2Pt_6X_{15}$ measured at 20 K showed similar X-dependences (Fig. 1) as follows. The Yb $3d_{5/2}$ spectrum is split into the Yb^{2+} ($4f^{14}$) and Yb^{3+} ($4f^{13}$) parts. The Yb^{2+} peak is very tiny for X = Al and is enhanced for X = Ga, indicating that the Yb valence is shifted from almost trivalent toward divalent states. The Ni $2p_{3/2}$ and Pt $4f_{7/2}$ peaks for X = Ga are located at a lower binding energy (E_B) than those for X = Al. The same energy shift is observed for the Ni 3*d* and Pt 5*d* structures in the valence-band spectra. In contrast, the opposite energy shift is observed in the Yb^{3+} 4*f* multiplet.

The similar X-dependent spectra of $YbNi_3X_9$ and $Yb_2Pt_6X_{15}$ suggest some systematic changes in electronic structure in moving from weak (X = Al) to strong (X = Ga) c–f hybridization regions in the Doniach phase diagram. A simple electronic model (Fig. 2) qualitatively explains these experimental results. The

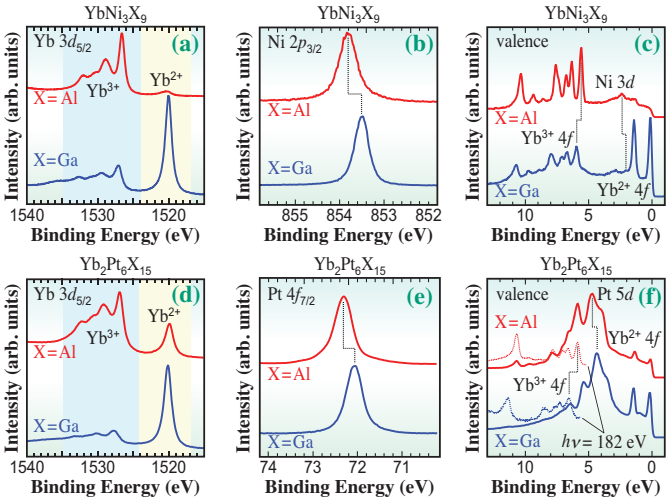

Fig. 1. **(a)** Yb $3d_{5/2}$, **(b)** Ni $2p_{3/2}$ and **(c)** valence-band HAXPES spectra of $YbNi_3X_9$ and **(d)** Yb $3d_{5/2}$, **(e)** Pt $4f_{7/2}$ and **(f)** valence-band HAXPES spectra of $Yb_2Pt_6X_{15}$ measured at 20 K. The spectra at $h\nu = 182$ eV obtained at BL-7 of HiSOR to enhance the Yb^{3+} 4*f* peak are also presented in (f).

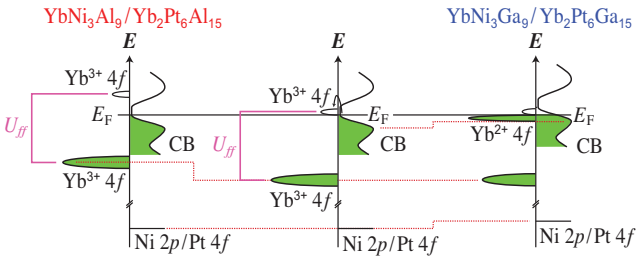

Fig. 2. Electronic model of $YbNi_3X_9$ and $Yb_2Pt_6X_{15}$ for X = Al (left) and X = Ga (right). The middle figure connects the left and right figures.

Yb 4*f* and conduction-band densities of states (DOS) are drawn at the left and right sides of the energy axis, respectively. The Yb^{3+} 4*f* level is split into the occupied and unoccupied levels at the energy distance of the Coulomb interaction energy between the 4*f* electrons (U_{ff}). The 4*f* hole level for X = Al is located far above the Fermi energy (E_F), and the Yb valence is close to 3. On going from X = Al to X = Ga, the 4*f* hole level becomes closer to E_F, and as a result, the occupied 4*f* level is shifted to higher E_B side, as observed in the experiments. The conduction electrons are easily transferred to the 4*f* hole just above E_F, and some Yb^{3+} ions change to Yb^{2+} ions and the Yb^{2+} $4f_{7/2}$ peak appears just below E_F. With the transfer of conduction electrons, E_F shifts to a smaller value in the conduction-band DOS. This E_F shift leads to the Ni $2p_{3/2}$ and Pt $4f_{7/2}$ shifts to lower E_B. Thus, the X-dependent HAXPES spectra of $YbNi_3X_9$ and $Yb_2Pt_6X_{15}$ are both understood in terms of the simple electronic model (Fig. 2).

Recently, a resonant HAXPES (rHAXPES) technique has been developed at SPring-8 **BL09XU** as a Partner User Proposal (PI: Prof. K. Mimura, Osaka Prefectural University). The Yb $3d_{5/2}$ HAXPES spectra (Figs. 1(a) and 1(d)) were obtained at a fixed photon energy. When an incident photon energy is tuned at the Yb L_3 edge (8.94 keV), a resonant behavior in the Yb^{2+} and Yb^{3+} peaks is expected. The detailed analysis of the resonant behavior provides the Coulomb interaction energy between the localized 4*f* and itinerant 5*d* electrons (U_{fd}), which is related to the Yb valence. Here, we present rHAXPES results for $YbInCu_4$ [4] with a valence transition at T_V = 42 K, where the Yb valence abruptly changes from 2.90 to 2.74 on cooling. The present results obtained at BL09XU are first reported for Yb L_3 rHAXPES. Figure 3(a) shows the Yb $3d_{5/2}$ rHAXPES spectra measured at 20 K with hν varied from 8915 to 8965 eV. Clear resonant enhancement is successfully detected both for the Yb^{2+} and Yb^{3+} peaks around the Yb L_3 edge. Figure 3(b) shows the Yb^{2+} and Yb^{3+} peak intensities as a function of hν, called constant initial state (CIS) spectra. The Yb^{2+} and Yb^{3+} CIS spectra exhibit similar behaviors. As hν increases from 8915 eV, the intensity gradually decreases. After reaching a minimum, the intensity rapidly attains a maximum and then again decreases. The CIS spectra are well fitted with the Fano profile given by $(E+q)^2/(E^2+1)$ with $E = (h\nu - E_0)/\Gamma$, where E_0, Γ and *q* are the resonant photon energy, the half-width of the resonance and the asymmetry parameter, respectively.

The Yb^{2+} CIS spectrum is shifted to a lower photon energy than the Yb^{3+} CIS spectrum. The amount of energy shift provides information on U_{fd}, which plays an important role in the valence transition. In the present experiment, no clear change between the CIS spectra measured at 20 and 70 K across the valence transition was detected. To enable further discussion, a theoretical calculation based on the single impurity Anderson model is in progress.

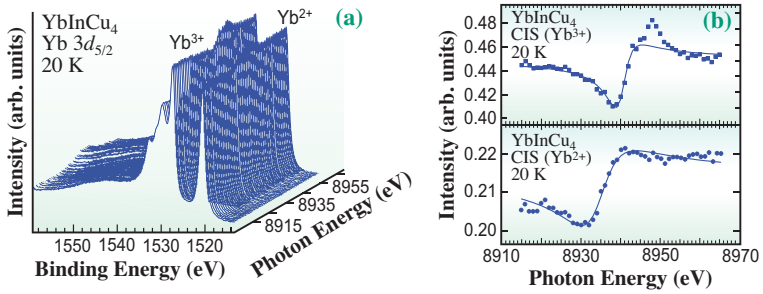

Fig. 3. **(a)** *hν* dependence of Yb $3d_{5/2}$ rHAXPES spectra around the Yb L_3 edge of $YbInCu_4$ measured at 20 K. **(b)** CIS spectra of Yb^{3+} (squares, upper panel) and Yb^{2+} (circles, lower panel) components in the Yb $3d_{5/2}$ rHAXPES spectra in (a). The Fano profiles are shown by line curves.

Hitoshi Sato

Hiroshima Synchrotron Radiation Center,
Hiroshima University

Email: jinjin@hioshima-u.ac.jp

References

[1] S. Doniach: Physica B+C **91** (1977) 231.
[2] Y. Utsumi *et al.*: Phys. Rev. B **86** (2012) 115114.
[3] A. Rousuli *et al.*: Phys. Rev. B **96** (2017) 045117.
[4] *K. Maeda, H. Sato, Y. Akedo, T. Kawabata, K. Abe, R. Shimokasa, A. Yasui, M. Mizumaki, N. Kawamura, E. Ikenaga, S. Tsutsui, K. Matsumoto, K. Hiraoka and K. Mimura: JPS Conf. Proc.* ***30*** *(2020) 011137.*

Evidence of Fermi level tuning in multiferroic $BiFeO_3$ thin films by Mn doping for high photovoltage generation

A bulk photovoltaic effect (BPVE) is a recently refocused mechanism for novel solar cells that are expected to have power conversion efficiencies exceeding those of conventional p-n junction solar cells. The BPVE is due to a quantum mechanical effect called shift current, which can generate a high open-circuit voltage (V_{OC}) exceeding the band gap (E_g) by irradiating light to noncentrosymmetric crystals. Among the noncentrosymmetric crystals, a ferroelectric material with a polar crystal structure shows the BPVE and a converse piezoelectric effect simultaneously, realizing optically induced strain. However, high electric field generation by the BPVE in the material itself is necessary for inducing optical strain. The multiferroic $BiFeO_3$ (BFO) is one of the best candidates for optical actuator application because of its excellent ferroelectric properties and environmentally friendly lead-free composition. In addition, the bandgap of BFO is in the visible wavelength region of 2.5–2.8 eV, realizing visible-light-driven devices. Indeed, the ultrafast response of the optical strain under femtosecond laser irradiation [1] and the magnetic field modulation [2] of the optical strain in bulk single crystals have already been reported. However, the optical strain is still small at *ca.* 0.0002% even in bulk BFO single crystals. To enhance the optical strain, the enhancement of the photovoltage is required; therefore, a highly insulating BFO thin film is necessary. We have generated 852 V generation in a multiferroic Mn 0.5-at% doped $BiFeO_3$ (BFMO) thin-film coplanar capacitor at 80 K under blue-violet laser (λ = 405 nm) irradiation, as shown in Figs. 1(a) and 1(b) [3]. The interelectrode distance was 260 μm, indicating that such a high voltage can generate an electric field of 32.7 kV/cm to the BFMO thin film itself, which is a sufficiently high electric field for inducing the converse piezoelectric effect. In addition, by investigating the dependence of V_{OC} in the BFMO thin films on the amount of doped Mn, the maximum V_{OC} of 280 V at RT was found to be obtained in the Mn 1-at% doped BFMO thin film, as shown in Fig. 1(c). This indicates electronic structural evolution upon Mn doping because high voltage generation can be induced in a highly insulating medium.

In the present work [3], we investigated the Fermi level tuning of BFO by Mn doping to clarify the electronic structure evolution. For the precise evaluation of Fermi level shift in ferroelectrics, the hard X-ray photoemission spectroscopy (HAXPES) of ultrathin metal-film-capped surfaces is suitable, because ferroelectrics are insulators with spontaneous polarization charges at the surface. The charged surface is partly terminated by adsorbed molecules, causing an unstable surface potential. Therefore, it is difficult to evaluate the chemical shifts of the charged surface by photoemission spectroscopy. On the other hand, at the ultrathin metal-film-capped ferroelectric surface, the spontaneous polarization charges are terminated by the capped metal layer, stabilizing the potential at the metal/ferroelectric interface. In other words, the Fermi level of the ferroelectric at the interface is pinned by the Fermi level of the metal layer; however, this means that band bending in the ferroelectric layer should be evaluated. HAXPES can be used to evaluate the ferroelectric layer through the ultrathin metal layer because of the deep penetration of high energy photoelectrons (>20 nm). Therefore, Au (9 nm)/BFMO (150 nm)/$SrRuO_3$ (SRO) (30 nm)/$SrTiO_3$(001) structures were used for the measurements. The

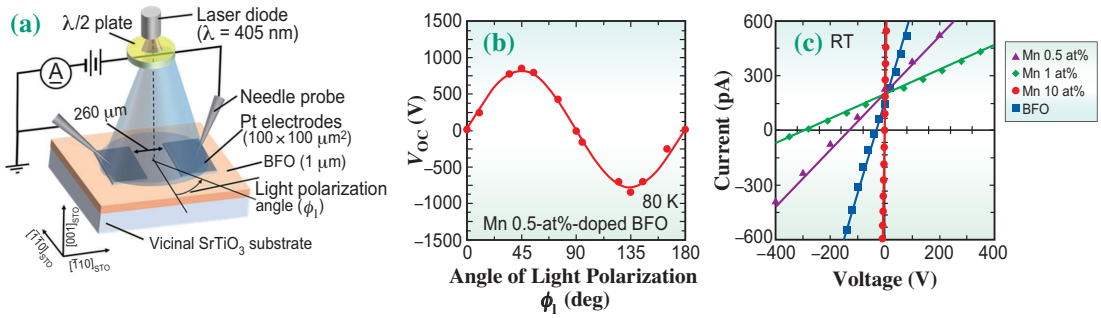

Fig. 1. **(a)** Schematic illustration of the sample structure and setup for photovoltaic property measurements. **(b)** Dependence of the light polarization angle (ϕ_l) on the open circuit voltage (V_{OC}) defined as the voltage at I = 0 A in Mn-0.5-at%-doped BFO thin film at 80 K. **(c)** I–V characteristics of BFMO thin films with various amounts of doped Mn measured at RT. The measurements were performed under blue violet laser (λ = 405 nm) irradiation with a power density of 17 W/cm^2. The light polarization angle (ϕ_l) was fixed at 45° in (c). The double sinusoidal dependence of V_{OC} in (b) means that the photovoltage is due to the BPVE, and the maximum V_{OC} of 852 V was confirmed at ϕ_l = 45°.

HAXPES measurements were performed at SPring-8 **BL47XU**. For exciting Bi 4*f*, Au 4*f* and valence band electrons in the samples, synchrotron X-rays with an energy of 7.94 keV were used. The measurements were performed at RT, and the excited photoelectrons were detected using the R4000 photoelectron analyzer (VG-Scienta Co.) equipped with a wide-acceptance-angle electrostatic lens with an acceptance angle of about ±32° [4,5]. During the measurements, both Au and SRO electrodes were grounded.

Figures 2(a) and 2(b) show Au 4*f* and Bi 4*f* HAXPES spectra, respectively, for the Au-capped Mn-1-at%-doped BFO/SRO/STO structure. For the measurements, photoelectron take-off angles (TOAs) are fixed at 85° (TOA85) and 5° (TOA5). The lower TOA corresponds to surface-sensitive conditions, whereby the electronic structures at the Au/BFMO interface might be evaluated. In contrast, the higher TOA corresponds to bulk sensitive conditions owing to the deep penetration of hard X-rays. From the Bi 4*f* spectra, slightly lower binding energies can be obtained at a TOA of 5° than at a TOA of 85°, revealing that the energy bands of BFMO were bent up near the Au/BFMO interface. In contrast, from the Au 4*f* spectra, almost the same binding energies can be detected under any TOA condition, confirming stable surface potentials. Thus, the Bi 4*f* spectral shifts are due not to the surface potential fluctuations but to the energy band bending in the BFMO. Figures 2(c) and 2(d) show the change of the Bi 4*f* and Au 4*f* binding energies of the Au/BFMO/SRO/STO structures as a function of amount of Mn doping. With increasing amount of Mn, the shift to lower binding energies were confirmed in the Bi 4*f* spectra. In contrast, the binding energies of Au 4*f* remained almost the same. These results reveal Fermi level lowering upon Mn doping into BFO, indicating that the doped Mn acts as acceptors. In addition, the difference between the binding energies of Bi 4*f* spectra obtained at TOAs of 85° and 5° also increased clearly with the amount of doped Mn despite an almost constant binding energy of the Au 4*f* spectra. These results indicate a larger energy band bending with a higher amount of doped Mn, in agreement with Fermi level lowering upon Mn doping.

In conclusion, we have demonstrated high voltage generation by the BPVE in Mn-doped BFO single crystal thin films. In addition, the evidence of Fermi level lowering in BFO upon Mn doping has been found through HAXPES spectral measurements, revealing that Mn doped into the BFO acts as acceptors. These indicate that the photoconductance of BFO can be modulated by Fermi level tuning by Mn doping, resulting in photovoltage enhancement. These results provide important information for ferroelectric material design by impurity doping for optical actuator applications.

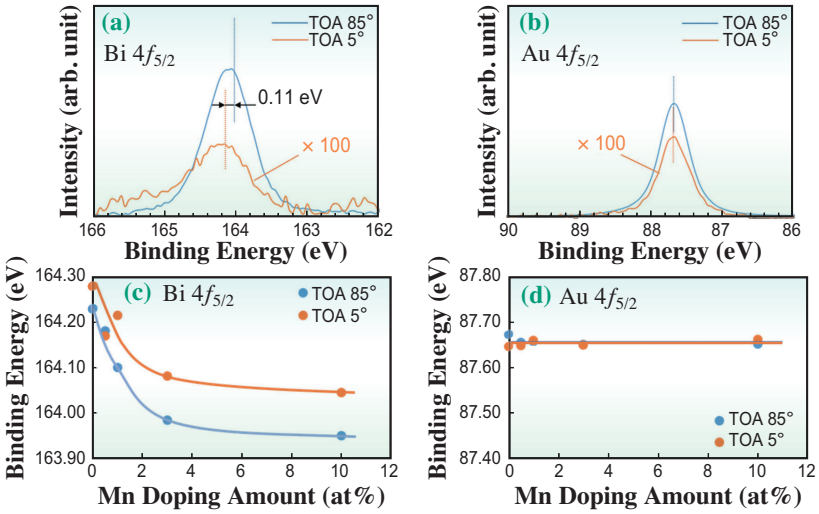

Fig. 2. **(a)** Bi $4f_{5/2}$ and **(b)** Au $4f_{5/2}$ HAXPES spectra at TOAs of 5° (orange line) and 85° (blue line) in the Au-capped Mn-1-at%-doped BFO thin film. Doped Mn amount dependence of **(c)** Bi $4f_{5/2}$ and **(d)** Au $4f_{5/2}$ binding energies measured at TOAs of 5° (orange line) and 85° (blue line) in the Au-capped BFMO thin films.

Seiji Nakashima* and Hironori Fujisawa

Department of Electronics and Computer Sciences, University of Hyogo

*Email: nakashima@eng.u-hyogo.ac.jp

References

[1] D. Schick *et al.*: Phys. Rev. Lett. **112** (2014) 097602.
[2] B. Kundys *et al.*: Nat. Mater. **9** (2009) 803.
[3] *S. Nakashima, T. Higuchi, A. Yasui, T. Kinoshita, M. Shimizu and H. Fujisawa: Sci. Rep.* ***10*** *15108 (2020).*
[4] E. Ikenaga *et al.*: J. Electron Spectrosc. Relat. Phenom. **190** (2013) 180.
[5] E. Ikenaga *et al.*: Synchrotron Rad. News **31** (2018) 10.

Time-resolved imaging of an operating hard-disk-drive write head using nanobeam X-ray magnetic circular dichroism

Hard disk drives (HDDs) are the principal storage device for digital technology, and thus, there is strong demand to increase the capacity to keep pace with the continuing growth of digital data. In a write operation of HDDs, a write head generates a localized magnetic field (recording field) on a magnetic recording medium and changes the magnetization direction. To generate a recording field in a small area, state-of-the-art HDDs have a main pole with a tip of sub-100-nm dimensions, and magnetization patterns written on the medium have a lateral size of ten to a few tens of nanometers, leading to an areal density exceeding 1 Tbit/inch^2. The write operation is completed in less than 1 ns. For the development of higher-capacity HDDs, elucidating the magnetization dynamics of the write head is of technological importance. However, experimental measurement has been difficult because of the small dimensions and high operation speed. In this research, we used the time-resolved nanobeam X-ray magnetic circular dichroism (XMCD) microscope installed at the soft X-ray beamline, SPring-8 **BL25SU** [1,2] and studied the dynamic behavior of an HDD write head under the operating condition [3]. XMCD has distinctive capacities such as nanometer-scale spatial resolution and sub-nanosecond time resolution. Because these resolutions are compatible with the dimensions and operation speed of the HDD write head, XMCD is suitable for studying its dynamic behavior.

Figure 1(a) shows a schematic image of the sample. The HDD write head used in this study was developed for perpendicular recording and is capable of recording at a density of 200 Gbit/inch^2 and writing at a speed of 700 Mbit/s. The HDD write head consists of a main pole, a shield, and a coil. The main pole and shield are composed of a magnetic material, and the tip of the main pole and part of the shield are exposed on the air-bearing surface (ABS). By introducing a write current to the coil, the magnetization of the main pole and shield is changed, generating a recording field localized around the main pole tip. In actual HDD operation, the ABS faces a recording medium with a very small flying height of approximately less than a few nanometers between them. As the recording medium moves in the direction depicted as the down-track direction, the recording field changes the medium magnetization, leaving recorded patterns. Figure 1(b) shows a scanning electron microscopy image of the ABS of the write head. Namely, the write head is seen from below in Fig. 1(a). The size of the main pole tip is approximately 250 nm×120 nm. Figure 1(c) shows the measurement setup. In A-mode operation, electron bunches circled the storage ring at intervals of 23.6 ns. Right or left circularly polarized soft X-ray pulse beams were selectively generated by twin helical undulators, focused down to approximately 100 nm by an order-sorting aperture (OSA) and a Fresnel zone plate (FZP), and scanned over the ABS of the write head. The incident angle was normal to the ABS. For detecting X-ray absorption, electrons emitted by X-ray absorption were collected by the voltage-biased OSA. Time-resolved measurements were realized by the synchronized timing control in which the write head was reversed at intervals of 2.36 ns (one-tenth of the cycle of the periodic X-ray pulses) by using an RF square-wave write current. The delay of the RF write current with respect to the X-ray pulses was varied to obtain snapshot magnetization images. XMCD images were generated by measuring two X-ray absorption (XA) images at right- and left-hand circular polarizations and calculating the subtraction of the signals from the two images normalized by their summation. The resulting XMCD signal represents the z-component magnetization of a selected element.

Figure 2 (a) shows the XA image obtained with the X-ray energy at the Fe L_3 absorption edge.

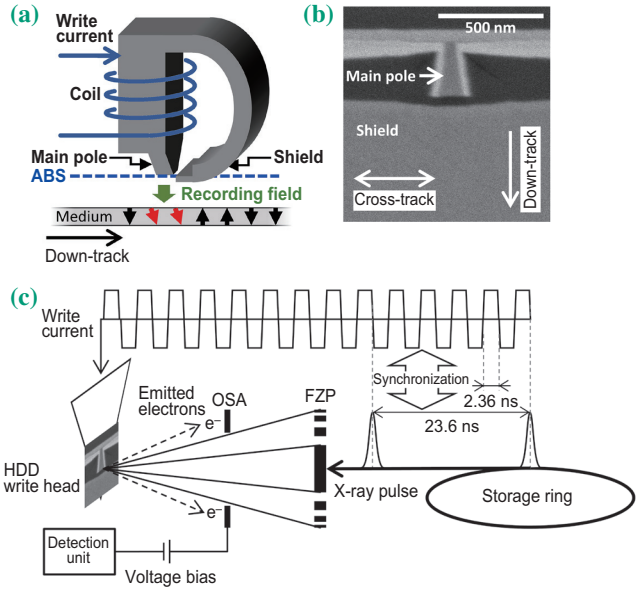

Fig. 1. **(a)** Schematic image of the HDD write head and its operation. The arrow of the down-track direction indicates the flying direction of the recording medium. **(b)** SEM image of the ABS of the write head. **(c)** XMCD measurement setup using the OSA collection method and timing control for time-resolved measurement.

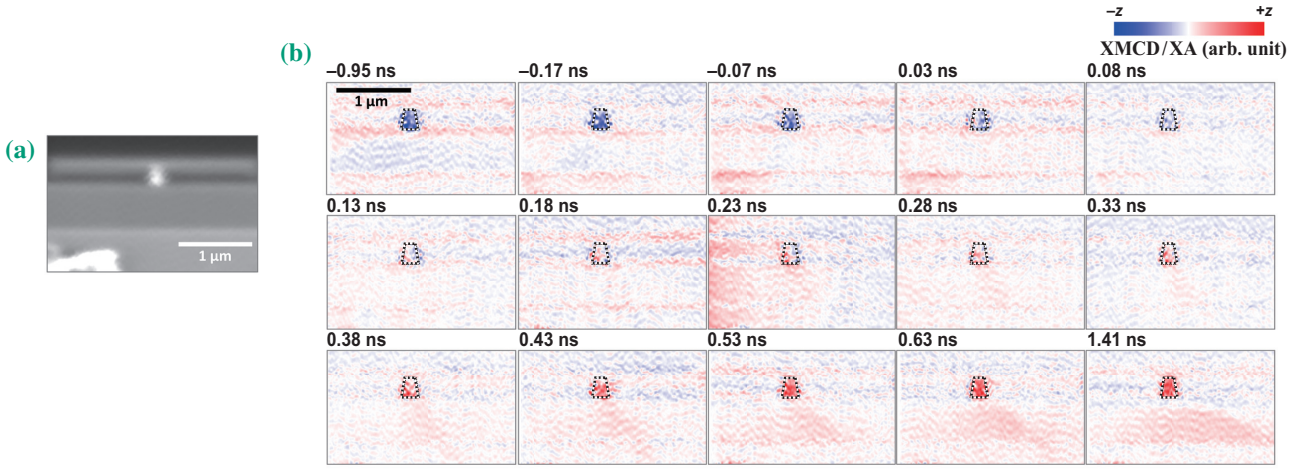

Fig. 2. **(a)** X-ray absorption image of the ABS of the write head obtained at the Fe L_3 absorption edge. **(b)**Time evolution of snapshot XMCD images. Dotted trapezoids show the positions of the main pole estimated from the XA image.

This image was taken at the same position as the SEM image in Fig. 1(b). The main pole exhibits a large signal because it is composed mainly of Fe. Figure 2(b) shows the time evolution of snapshot XMCD images obtained by changing the delay. Note that the time intervals between the images are not uniform and is as small as 50 ps around the transition. The dotted trapezoids show the position of the main pole estimated from the XA image. With time, the magnetization of the main pole decreases, and a demagnetized state appears. Then, the magnetization increases to the opposite polarity and the magnetization reversal is complete. The time interval between the first and last images is 2.36 ns, indicating that they were obtained at opposite phases of the RF write current. Figure 3(a) shows a waveform of the RF write current and Fig. 3(b) shows the intensity of the XMCD signal averaged over the main pole area as a function of time. The magnetization reversal of the main pole occurs from –0.17ns to 0.53ns, and the slope over time is nearly linear. The slope is more gradual than that of the write current, indicating that the main pole reversal is determined mostly by the response of the write head. These results show that the XMCD measurement setup developed in this study is a powerful tool for understanding the dynamic behavior of an HDD write head and contributes to the development of higher-capacity HDDs.

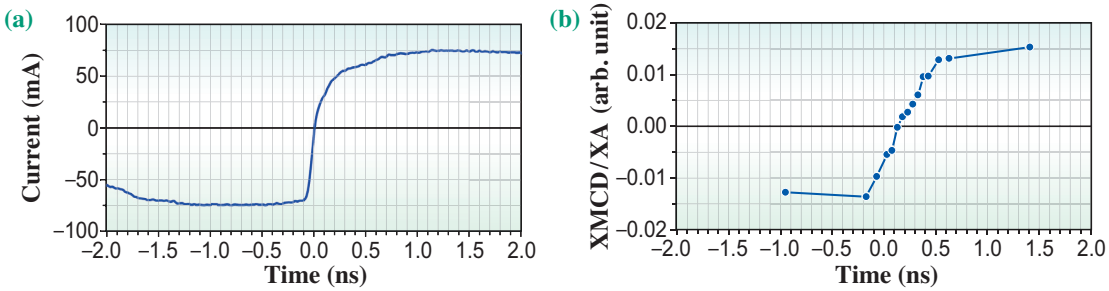

Fig. 3. **(a)** Waveform of the RF write current. **(b)** Average XMCD signal of the main pole area versus time, calculated from the data in Fig. 2(b). Note that the time axes in (a) and (b) are irrelevant because the absolute delay between the RF write current and the X-ray pulses is unknown.

Hirofumi Suto[a,b,*], Akira Kikitsu[a] and Yoshinori Kotani[c]

[a] Corporate Research and Development Center, Toshiba Corporation
[b] National Institute for Materials Science (NIMS)
[c] Japan Synchrotron Radiation Research Institute (JASRI)

*Email: suto.hirofumi@nims.go.jp

References

[1] Y. Senba *et al.*: AIP Conf. Proc. 1741 (2016) 030044.
[2] Y. Kotani *et al.*: J. Synchrotron Rad. **25** (2018) 1444.
[3] *H. Suto, A. Kikitsu, Y. Kotani, T. Maeda, K. Toyoki, H. Osawa, N. Kikuchi, S. Okamoto and T. Nakamura: J. Appl. Phys.* ***128*** *(2020) 133903.*

High-pressure X-ray diffraction studies of the supercritical fluid of hydrogen

Hydrogen has high potential as a next-generation clean energy source. One of the challenges facing the realization of a hydrogen society is the establishment of safe and efficient hydrogen transportation and storage technology. For this purpose, it is important to have information on the basic physical properties of high-pressure hydrogen (H_2) gas, such as its aggregation state and density.

Normal hydrogen (n-H_2) has a critical point at 32.97 K and 1.293 MPa and solidifies under a high pressure of 5.4 GPa at room temperature. Up to now, Mills *et al.* [1] have proposed an equation of state up to 2 GPa through volume compression and ultrasonic velocity measurements using a piston cylinder device. Pratesi *et al.* [2] have proposed a pressure dependence of density up to 5.4 GPa at room temperature on the basis of Brillouin scattering experiments.

In this study, synchrotron radiation X-ray diffraction experiments were performed to collect halo patterns within a wide pressure range (0.1 to 5 GPa) to obtain information on the density and structure of the supercritical fluid phase [3].

A diamond anvil cell (DAC) was used to generate high pressure. The sample was n-H_2 and high-pressure H_2 gas of 180 MPa (or 50 MPa) was loaded into the DAC using a high-pressure gas filling apparatus. High-pressure X-ray diffraction experiments were performed at room temperature at SPring-8 **BL10XU**. The incident X-ray energy was 30 keV and an image plate was used as a two-dimensional detector. In these one-dimensional data, the halo pattern from the fluid H_2 was overlaid by the relatively strong Compton scattered X-ray background from the diamond anvil. To subtract this background numerically, the background pattern of an empty cell containing no sample was measured.

During this X-ray diffraction experiment, we succeeded in observing the halo pattern of the hydrogen supercritical fluid phase within a wide pressure range from 0.12 to 5.1 GPa. Figure 1 shows the pressure change of a typical diffraction pattern. The first halo was observable, but the second was undetectable. A spectral analysis was performed to estimate the 2θ value and FWHM of the first halo peak. The d_H value was calculated from the 2θ value. The d_H value and FWHM decreased as the pressure increased (Fig. 2). The FWHM corresponds to a measure of the correlation of intermolecular distance in fluid.

We considered d_H to be the average nearest-neighbor intermolecular distance and assumed a packing of a hard sphere with diameter d_H. Herein, the molar volume was estimated using the equation of state proposed on the basis of the ultrasonic measurement by Mills *et al.* [1] That is, assuming that the cube of the d_H value at 2 GPa is proportional to the molar volume reported by Mills *et al.*, i.e., 11.593 cm^3/mol. At this pressure, the proportional constant A of the following formula was determined to estimate the molar volume V_m.

$$V_m(P) = A \cdot N_A \cdot [d_H(P)]^3$$

Here, N_A is Avogadro's number and A is 1.37, which corresponds to the reciprocal of the packing factor. If A was 1.0, it would correspond to the hexagonal coordinate of a simple cubic lattice. In our previous study on supercritical fluid phases of O_2 and N_2, A was 1.47, indicating that the filling rate of H_2 is higher than those of O_2 and N_2. Figure 3 shows the pressure dependence of the molar volume together with the results of previous studies.

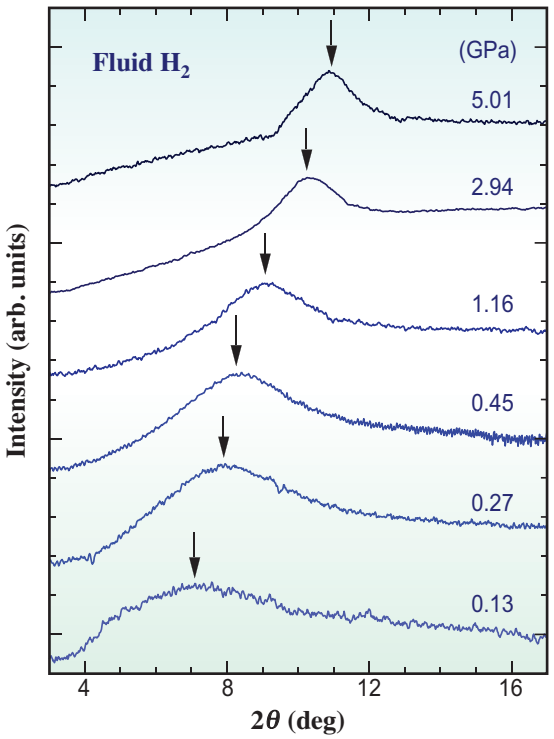

Fig. 1. Pressure evolution of the X-ray diffraction patterns for fluid H_2.

The pressure dependence in this study was in good agreement with the data of Mills *et al.* up to 2 GPa and the data of Pratesi *et al.* above 1 GPa. Therefore, the validity of the hard sphere model assumed in this study was demonstrated. That is, it was considered that the d_H value corresponded to the average intermolecular distance and that the average coordination number (packing factor: *A*) of the molecules was constant and did not change in the pressure range of 0.1 to 5 GPa. There was a change in compressibility at around 1 GPa, i.e., the dependence followed the relational expression of $P \sim V_m^{-3.11}$ above 1 GPa. Fluid O_2 and N_2, which are the same homonuclear diatomic molecules as H_2, followed the relational expression of $P \sim V_m^{-4.32}$ at a pressure higher than 0.2 GPa. The repulsive term of the Lennard–Jones potential, which is applied to molecular solids, became dominant for fluid O_2 and N_2. Therefore, it was found that fluid H_2 behaves differently from fluid O_2 and N_2 and is more easily compressed. The reason why H_2 and He are easily compressed is that the wave function of the 2*s* electrons occupying the outer orbital of O_2, N_2, and Ne molecules is required to be orthogonal to the wave function of the 1*s* electron, but the 1*s* electron cloud surrounding H_2 and He molecules does not have this orthogonality constraint.

However, in the pressure region lower than ~1 GPa, the pressure dependence of H_2 deviates from the relationship of $P \sim V^{-3.11}$. It seems that the repulsive term of the intermolecular potential becomes dominant in the pressure region higher than ~1 GPa. That is, the compressibility of the supercritical phase of hydrogen changes from gas-like to liquid- or solid-like at around 1 GPa.

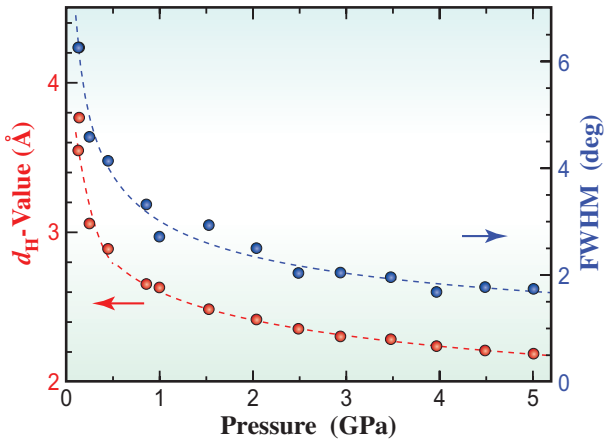

Fig. 2. Pressure dependence of the d_H value and FWHM of the first halo peak.

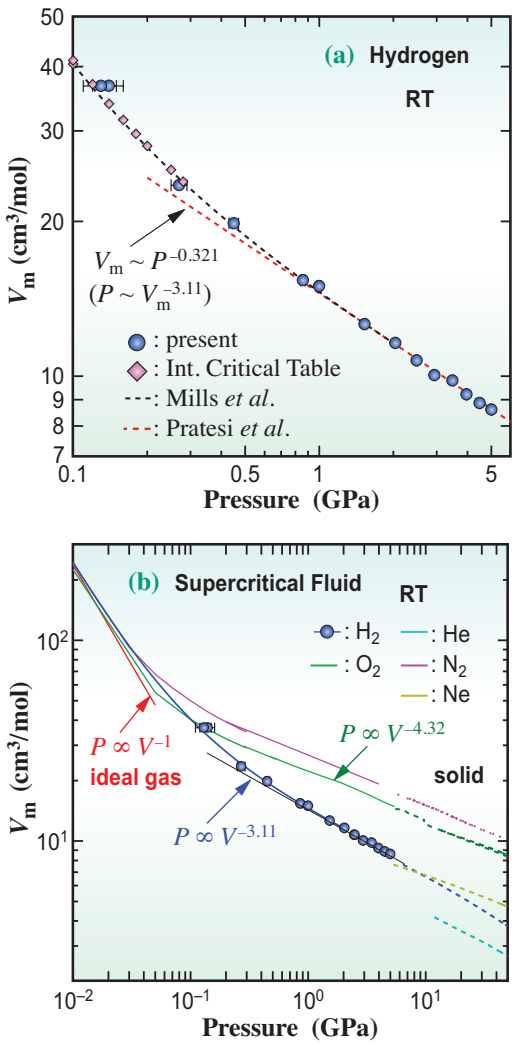

Fig. 3. Pressure dependence of V_m for the supercritical fluid of H_2 together with previous data **(a)** and for supercritical fluids (solid line) and solids (broken line) of H_2, He, Ne, N_2, and O_2 **(b).**

Yuichi Akahama

Graduate School of Material Science, University of Hyogo

Email: akahama@sci.u-hyogo.ac.jp

References

[1] R.L. Mills *et al.*: J. Chem. Phys. **66** (1977) 3076.
[2] G. Pratesi *et al.*: J. Phys.: Condens. Matter **9** (1997) 10059.
[3] *Y. Akahama, R. Miyamoto, S. Nakano, S. Kawaguchi, N. Hirao and Y. Ohishi: J. Appl. Phys.* ***128*** *(2020) 135901.*

Ultrafast structural dynamics of highly excited nanoparticles in intense laser fields

Recent developments of high-intensity femtosecond lasers generated by chirped pulse amplification have given us new opportunities to transform matter to novel states under extreme conditions. Intense and ultrashort infrared laser pulses deposit energy into matter with a femtosecond exposure time, thus triggering nonequilibrium dynamic processes such as the creation of a dense and transient electron-hole plasma. During the creation of the plasma, marked structural changes in the matter are expected to occur. Elucidating how and on what timescale structural changes proceed in the matter under the intense laser field leads to a deep understanding of the fundamental mechanisms of excitation and deexcitation in highly excited systems.

For the study of the fundamental aspects of laser-matter interaction, atomic clusters, especially noble-gas clusters, have been used as a testbed [1] owing to their characteristics such as ease of generation, size tunability, and an isolated system of bulk density. Numerous studies have revealed that a nanoscale atomic cluster exposed to an intense near-infrared (NIR) laser pulse becomes a nanoscale plasma (nanoplasma) [2]. Thus far, the properties and dynamics of laser-induced nanoplasmas have been studied by ion, electron, and fluorescence spectroscopies, by which one can only infer the structural changes in clusters.

The emergence of XFELs has changed the situation; the XFEL enables us to investigate the structural dynamics of nanoscale systems with an atomic-scale spatial resolution and a temporal resolution of several-ten-femtoseconds [3], using the diffraction-before-destruction scheme [4].

In this work, we investigated ultrafast structural dynamics in xenon (Xe) clusters irradiated by the NIR laser, employing the time-resolved wide-angle X-ray scattering (WAXS) technique. The experiments were carried out at experimental hutch 2 of SACLA **BL3** [5]. A schematic of the experiment is depicted in Fig. 1. A jet of Xe clusters (~1×10^7 atoms/cluster) was irradiated by a NIR laser pulse (1.55 eV, 30 fs FWHM, 4×10^{16} W/cm^2) followed by a single XFEL pulse (11 keV, 10 fs FWHM, 4×10^{17} W/cm^2) at a selected temporal delay. The temporal delay of the XFEL pulse relative to the NIR pulse was controlled by using the delay stages installed to the NIR laser system. The temporal jitter between the arrival time of the two laser pulses was measured using the arrival timing monitor [6]. Scattering signals from Xe clusters were collected by a short-work-distance multiport CCD detector for each XFEL shot. Xe ion signals were collected by an ion time-of-flight (TOF) spectrometer.

The experimental results are summarized in Fig. 2. We chose intense Bragg spots observed at each delay dataset for analysis to ensure the good exposure condition between XFEL pulses and clusters. Clear changes in the profiles of Bragg spots from the fcc (111) reflection of single Xe nanoparticles could be observed by applying this data filtering. As shown in Fig. 2(a), bright Bragg spots were observed before NIR irradiation and their intensity decreased after NIR irradiation. Figures 2(b) and 2(c) show the qualitative temporal development of the intensity and width (FWHM) of the Bragg spots with respect to the XFEL delay. The spot intensity decreased after NIR irradiation, while the spot width increased by a few tens of percent. The simultaneous behavior could be

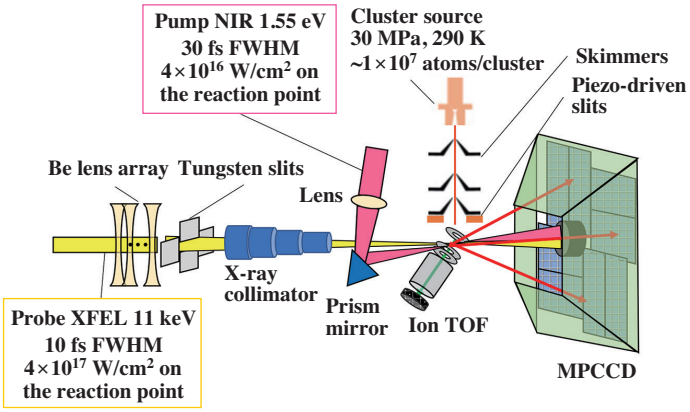

Fig. 1. Schematic of the time-resolved experiments at SACLA BL3. [5]

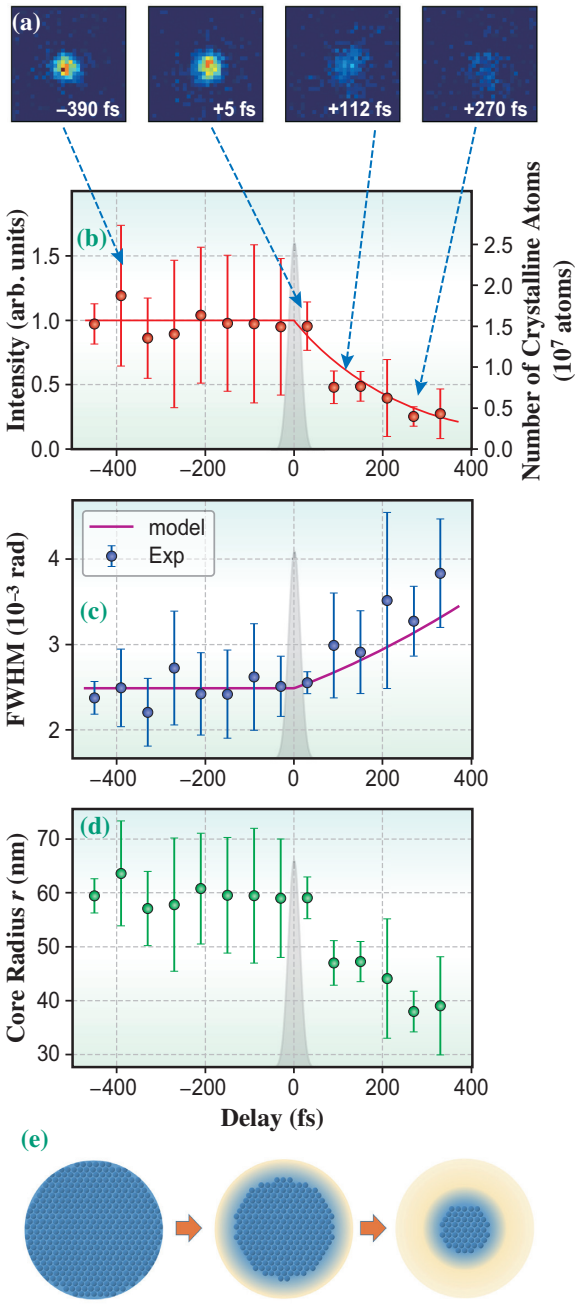

Fig. 2. Delay dependence of profiles of Bragg spots from fcc (111) reflection of xenon nanoparticles. **(a)** Characteristic spot images. **(b)** Temporal development of the spot intensity (marker). **(c)** Temporal development of the spot width (marker). **(d)** Temporal development of the radius of the crystalline core (marker). **(e)** Schematic of the crystal disordering consistent with the current experiments. [5]

reproduced by the model shown in Fig. 2(e), where the disordering of the crystalline structure proceeds from the surface (outer part) to the core (inner part) of the Xe nanocrystal.

Furthermore, the propagation speed of disordering, which was extracted from the temporal development of the radius of the crystalline core shown in Fig. 2(d), is close to the plasma sound speed estimated from the ion kinetic energy distributions. The present results can be interpreted as that the crystalline order of the core initially survives and is detectable even under an intense laser field, while local disordering on the nanoplasma proceeds from the surface towards the core with speed of the same order as the plasma sound speed.

In summary, ultrafast and atomic-scale structural changes in nanoplasma created under an intense NIR laser field were clarified by shot-by-shot time-resolved WAXS experiments at SACLA. Our findings provide a new insight into the structural dynamics in nanoplasma formation and its development on the atomic-scale spatial resolution and temporal resolution of several tens of femtoseconds.

T. N. Hiraki[a,b,*], Y. Kumagai[c,d], K. Nagaya[a,b] and K. Ueda[b,c]

[a] Department of Physics, Kyoto University
[b] RIKEN SPring-8 Center
[c] Institute of Multidisciplinary Research for Advanced Materials, Tohoku University
[d] Department of Applied Physics, Tokyo University of Agriculture and Technology

*Email: toshiyuki.nishiyama@riken.jp

References

[1] Th. Fennel *et al.*: Rev. Mod. Phys. **82** (2010) 1793.
[2] T. Ditmire *et al.*: Phys. Rev. A **53** (1996) 3379.
[3] T. Gorkhover *et al.*: Nat. Photonics **10** (2016) 93.
[4] R. Neutze *et al.*: Nature **406** (2000) 752.
[5] *T. Nishiyama, Y. Kumagai, A. Niozu, H. Fukuzawa, K. Motomura, M. Bucher, Y. Ito, T. Takanashi, K. Asa, Y. Sato, D. You, Y. Li, T. Ono, E. Kukk, C. Miron, L. Neagu, C. Callegari, M. Di Fraia, G. Rossi, D. E. Galli, T. Pincelli, A. Colombo, T. Kameshima, Y. Joti, T. Hatsui, S. Owada, T. Katayama, T. Togashi, K. Tono, M. Yabashi, K. Matsuda, C. Bostedt, K. Nagaya and K. Ueda: Phys. Rev. Lett.* ***123*** *(2019) 123201.*
[6] T. Katayama *et al.*: Struct. Dynam. **3** (2016) 034301.

Studying ultrafast dynamics of element-dependent magnetization dynamics in ferromagnetic Co/Pt multilayer thin films using femtosecond X-ray magneto-optical Kerr effect measurement

The increase in the amount of information that humans deal with has enhanced the importance of the development of high-density recording media. There are various recording methods using semiconductors and dielectrics, but recording media using magnetic materials are widely used because they are nonvolatile and economical. Materials with high magnetic anisotropy are important and are being developed for application to high-density recording media. On the other hand, the method of controlling the magnetization for writing information on such materials is equally important. Currently, heat-assisted magnetic recording (HAMR) and microwave assisted magnetic recording (MAMR), which facilitate magnetization reversal by the external magnetic field assisted by heat or microwaves, are becoming commercially available.

In recent years, optically induced spin dynamics of magnetic materials has been studied and novel phenomena, such as ultrafast demagnetization and magnetization reversal without an external magnetic field, were reported. All-optical switching (AOS) of magnetization has been reported in the ferrimagnetic materials such as GdFeCo and ferromagnetic materials such as FePt and CoPt. In particular, ferromagnetic FePt and CoPt thin films have high magnetic anisotropy and are expected to be used for high-density recording media. These phenomena are realized in an energy-efficient and ultrafast process, and are expected to be applied to recording media.

In the ferrimagnetic material GdFeCo, which is representative of materials showing AOS, the photoinduced magnetic dynamics was investigated by time-resolved X-ray magnetic circular dichroism (XMCD) [1]. It was found that the two magnetic moments of Gd and Fe change with different time constants, resulting in a transient ferromagnetic state via which a magnetic reversal is realized. On the other hand, there is a limited number of element-resolved observations of light-induced transient states in ferromagnetic 3*d*-5*d* alloys such as FePt and CoPt.

Time-resolved XMCD measurements have been performed on FePt at the Pt *L*-edge of the hard X-ray region at SACLA **BL3** [2]. The time scale of the photoinduced demagnetization of Pt was reported to be about 600 fs. However, since the absorption edge of the 3*d* element which gives a large magnetic signal does not exist in the hard X-ray region, measurements investigating 3*d* and 5*d* elements simultaneously have not been performed.

We have performed time-resolved measurements of the X-ray magneto-optical Kerr effect (XMOKE) on ferromagnetic Pt(1.7 nm)/[Co(0.4 nm)/Pt(0.7 nm)]$_3$/Co(0.4 nm) multilayers using SACLA **BL1**, which supplies X-rays in the VUV region [3]. Elementally resolved observations were carried out using X-rays of the Co M and Pt N edges. The schematic diagram of the experimental setup is shown in Fig. 1. Horizontally polarized X-ray pulses were incident on the sample along the same axis as the excitation laser. The reflected X-rays were measured using the rotational ellipsometry analyzer to determine the rotation of the polarization plane. The photoinduced dynamics were captured by the pump-probe method. With the use of a timing monitor to correct the jitter of the X-ray pulses, the time resolution reaches to ~50 fs [4].

Figure 2 shows the results of the static measurement of XMOKE. The reflectivity of multilayer mirror of the rotational ellipsometry analyzer depends on the relationship between the scattering plane and polarization of X-rays. Reflectivity curves are plotted as a function of the angle of ellipsometry analyzer. Those curves are shifted by the change in the direction of the magnetization field as a result of XMOKE. The Kerr rotation angle is obtained as the shift induced by the magnetic field. The Kerr rotation angles are 3 degrees at the Co *M*-edge and 1.5 degrees at the Pt *N*-edge.

Figure 3 shows the results of the time-resolved XMOKE measurements. The vertical axis is normalized by the Kerr rotation angle before laser irradiation. The demagnetization time scales for Co and Pt were evaluated by fitting exponential functions and determined as τ_{Co} = 80 ± 60 fs and τ_{Pt} = 640 ± 140 fs.

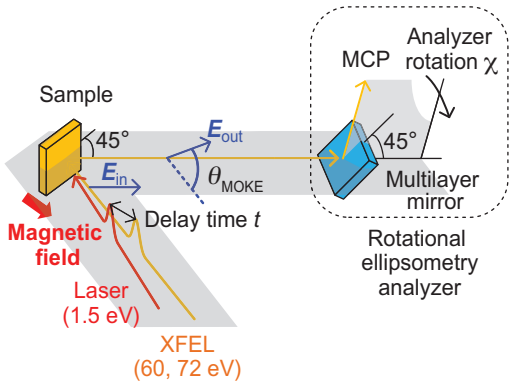

Fig. 1. Experimental setup for time-resolved XMOKE used in SACLA BL1.

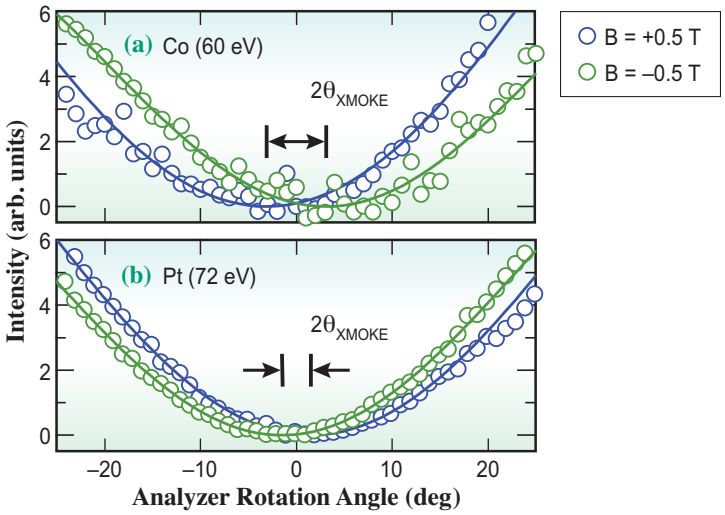

Fig. 2. Reflectivity intensities plotted as a function of polarization analyzer angle for Co M (60 eV) **(a)** and Pt N (72 eV) **(b)** edges.

We proposed an explanation for this difference on the basis of the electron transfer between Co and Pt layers described in our paper [3].

The results of our study show that there is a clear difference in demagnetization time for both Co/Pt superlattices, with the demagnetization time for the 3*d* elements Fe and Co being less than about 100 fs, and the demagnetization time for the 5*d* element Pt being about 600 fs. This is similar to the results of the time-resolved XMCD of GdFeCo, where the demagnetization time of Fe is about 100 fs and that of Gd, a 4*f* element, is about 400 fs. Thus, we suggest that we have obtained an important guiding principle that, for ultrafast spin manipulation such as laser-induced magnetization reversal, it may be important to combine two or more magnetic elements with different photoinduced magnetization time scales. We obtained, for the first time, element-dependent spin dynamics using time-resolved XMOKE in VUV XFEL. This approach will be useful for studying the ultrafast magnetization dynamics of advanced magnetic materials.

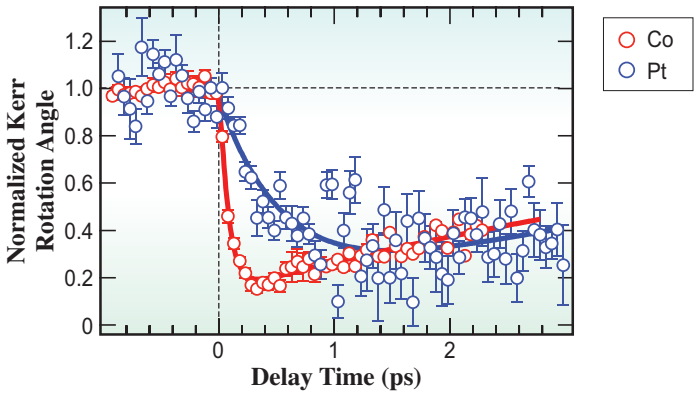

Fig. 3. Kerr rotation angles of Co and Pt edges. Kerr rotation angle is normalized to the initial value before photoexcitation. Solid lines indicate the results of fitting.

Kohei Yamamoto[a,*] and Hiroki Wadati[b]

[a] Institute for Molecular Science
[b] Graduate School of Material Science, University of Hyogo

*Email: yamako@ims.ac.jp

References

[1] I. Radu *et al.*: Nature **472** (2011) 205.
[2] K. Yamamoto *et al.*: New J. Phys. **21** (2019) 123010.
[3] *K. Yamamoto, S. El Moussaoui, Y. Hirata, S. Yamamoto, Y. Kubota, S. Owada, M. Yabashi, T. Seki, K. Takanashi, I. Matsuda and H. Wadati: Appl. Phys. Lett.* ***116*** *(2020) 172406.*
[4] S. Owada *et al.*: J. Synchrotron Rad. **26** (2019) 887.

Search for η′-meson bound nuclei using a GeV photon beam

In today's cold universe, two or three quarks are confined in a hadron such as a meson and a nucleon. The mass of a hadron composed of light quarks cannot be explained by the sum of bare quark masses, which are generated by the interaction of quarks with the Higgs field. For example, such a sum accounts for only about 1% of the nucleon mass. Thus, a dynamical mechanism of hadron-mass generation is widely believed in modern physics. In this mechanism, the quantum-mechanical vacuum changes its ground-state properties by the spontaneous breaking of chiral symmetry and interacts with quarks to provide a hadron mass, as the universe evolves from a high-temperature and high-density plasma of massless quarks, where all symmetries hold. Such a phenomenon is called the chiral phase transition, whose order parameter is the vacuum expectation value of quark condensates. This idea was proposed by Nambu, who was inspired by the theory of superconductivity. The generation of quark condensates and hadron masses correspond to the appearance of Cooper pairs and energy gaps.

Experimental efforts to prove mass generation by the spontaneous breaking of chiral symmetry have been actively attempted in the field of hadron physics. The partial restoration of the chiral symmetry is expected even inside the nucleus, which has an ultrahigh density of about 10^{14} g/cm^3, as a precursor phenomenon of the chiral phase transition. Therefore, the BGOegg experiment, running at SPring-8 **BL31LEP**, has searched for the signals of hadron-mass reduction inside a nucleus through the photoproduction of η′ mesons [1]. The η′ meson has attracted attention in recent years because its mass (958 MeV/c^2) is abnormally heavier than those of the other pseudoscalar mesons in the flavor SU(3) nonet owing to the $U_A(1)$ quantum anomaly. Studying the η′-meson properties in nuclei should provide a clue for exploring the relationship between the spontaneous breaking of chiral symmetry and the $U_A(1)$ anomaly, both of which should be taken into account at the Lagrangians of effective hadron models. Several models have predicted the η′-meson mass reduction at the nuclear density to be 40–150 MeV/c^2 [2].

The BGOegg experiment uses a photon beam produced at BL31LEP in the energy range of 1.3–2.4 GeV. A large acceptance electromagnetic calorimeter (Fig. 1) has been set up with several charged-particle detectors at the LEPS2 experimental building [3]. This calorimeter covers a polar angle range from 24° to 144° with 1320 $Bi_4Ge_3O_{12}$ (BGO) crystals, giving the world's best energy resolution of 1.3% for a 1 GeV γ-ray. For studies of the η′-meson mass in nuclei, a 20-mm-thick carbon target was adopted to search for nuclear bound states of η′ mesons by missing mass spectroscopy with forward high-momentum protons. If the η′ mass reduction is large, such a bound state can be formed with a corresponding attractive potential inside a nucleus [4].

A conceptual description of the experiment is shown in Fig. 2. The η′ bound nuclei were searched by detecting a forward proton at the resistive plate chamber (RPC) wall located 12.5 m downstream of the carbon target with a polar angle coverage up to 6.8°. The time of flight of a charged particle was measured with a time resolution of 60–90 ps to determine its momentum, assuming that the detected particle is a proton. If η′ bound signals exist, they must appear below the production threshold in the proton missing mass spectrum, which is calculated by solving the unknown mass of an η′ bound nucleus under the 4-momentum conservation of the $\gamma + {}^{12}\mathrm{C}$ reaction. Because there remains much background in such a spectrum, the BGOegg experiment has, for the first time, required the simultaneous detection of a conversion signal by the bound η′ meson and a spectator proton (**p**), namely, the reaction $\eta' p \to \eta p$, followed by the $\eta \to \gamma\gamma$ decay.

Black dots in Fig. 3 show the excitation energies $E_{ex} - E_0$ (missing masses relative to the η′ production threshold or the sum of boron-nucleus and η′-meson masses in a vacuum) and η emission angles cos(η) (polar angles in the Lab frame) of the real data events after the detection of an η meson, decaying into γγ, and a slow proton (p_s) at the calorimeter. Unfortunately,

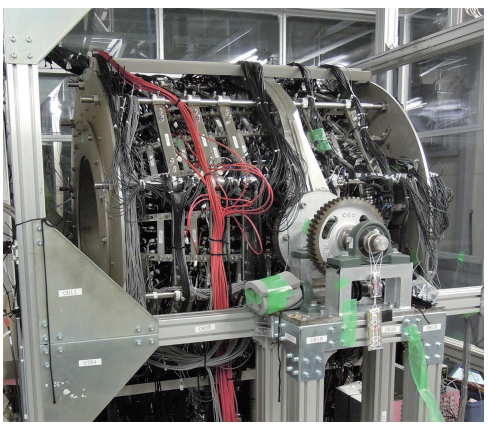

Fig.1. Photograph of the BGOegg calorimeter, assembled with 1320 BGO crystals.

this sample was still dominated by background mainly due to η photoproduction, where the secondary interactions of primary products generated additional slow protons. Therefore, we further developed kinematical conditions to select events with a back-to-back behavior of the η–p_s pair and to exclude events having boosted kinematics with a very forward production of either η or p_s. These conditions were optimized without examining the predetermined signal region, indicated by the red shaded area in Fig. 3. Finally, only events shown by blue circles survived after applying the kinematical conditions. No events were observed in the signal region. We obtained an upper limit for the production of η′ bound nuclei with η–p_s pairs of 2.2 nb/sr (90% confidence level) at the opening angles $\cos(\eta p_s) < -0.9$.

We compared this upper limit of the production cross section with the results of a theoretical calculation using the distorted wave impulse approximation (DWIA) and a few assumed optical-potential values [4]. In the comparison process, we normalized the theoretical calculation by the observed amount of quasi-free η′ photoproduction events, which were not affected by the mass reduction. This normalization was essential to remove ambiguities in the DWIA calculation. As a result, we have concluded that a branching fraction of the process where the one-nucleon (1N) absorption of the bound η′ meson occurs with conversion to a pair of an η meson and a nucleon is constrained to be lower than 24% (the 90% confidence level) in the case of optical potential $V_0 = -100$ MeV, indicating that such a large V_0 value or a large mass reduction is not favored.

In the BGOegg experiment, a complementary analysis to study the η′ mass at the nuclear density is carried out concurrently. In this method, the mass spectrum of η′ mesons decaying into γγ inside a nucleus is directly measured by reconstructing the invariant mass with the selection of low-momentum η′ mesons. This analysis mode has a higher sensitivity in the case of a smaller mass reduction. On the basis of the results of the above two analyses, we plan the second-phase experiment with an upgraded detector setup to observe firm evidence of the partial restoration of chiral symmetry in nuclei.

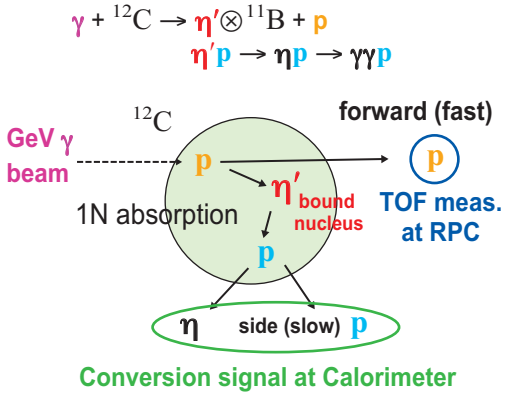

Fig. 2. Conceptual description of the search for η′-meson bound nuclei by the BGOegg experiment at BL31LEP.

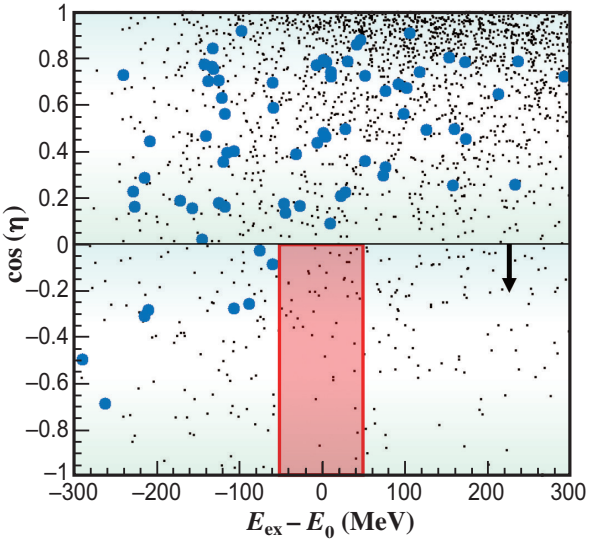

Fig. 3. Two-dimensional plot of the η polar angle versus the excitation energy for signal samples of the η′ bound nuclei search. The kinematical region of $\cos(\eta) < 0$ was selected to reduce background. The red shaded area indicates the signal search region.

Norihito Muramatsu[a,*] and Natsuki Tomida[b]

[a] Research Center for Electron Photon Science, Tohoku University
[b] Research Center for Nuclear Physics, Osaka University

*Email: mura@lns.tohoku.ac.jp

References

[1] *N. Tomida, N. Muramatsu, M. Niiyama, J.K. Ahn, W.C. Chang, J.Y. Chen, M.L. Chu, S. Daté, T. Gogami, H. Goto, H. Hamano, T. Hashimoto, Q.H. He, K. Hicks, T. Hiraiwa, Y. Honda, T. Hotta, H. Ikuno, Y. Inoue, T. Ishikawa, I. Jaegle, J.M. Jo, Y. Kasamatsu, H. Katsuragawa, S. Kido, Y. Kon, T. Maruyama, S. Masumoto, Y. Matsumura, M. Miyabe, K. Mizutani, H. Nagahiro, T. Nakamura, T. Nakano, T. Nam, T.N.T. Ngan, Y. Nozawa, Y. Ohashi, H. Ohnishi, T. Ohta, K. Ozawa, C. Rangacharyulu, S.Y. Ryu, Y. Sada, M. Sasagawa, T. Shibukawa, H. Shimizu, R. Shirai, K. Shiraishi, E.A. Strokovsky, Y. Sugaya, M. Sumihama, S. Suzuki, S. Tanaka, A. Tokiyasu, Y. Tsuchikawa, T. Ueda, H. Yamazaki, R. Yamazaki, Y. Yanai, T. Yorita, C. Yoshida, M. Yosoi: Phys. Rev. Lett.* ***124*** *(2020) 202501.*
[2] H. Nagahiro *et al.*: Phys. Rev. C **74** (2006) 045203; S. Sakai and D. Jido: Phys. Rev. C **88** (2013) 064906; S.D. Bass and A.W. Thomas: Phys. Lett. B **634** (2006) 368.
[3] N. Muramatsu *et al.*: Phys. Rev. C **100** (2019) 055202.
[4] H. Nagahiro: J. Phys. Soc. Jpn. Conf. Proc. **13** (2017) 010010.

Charge transfer transitions stemming from $6s^0$ and $6s^2$ charge degree of freedom in valence skipping Bi and Pb ions

Bi and Pb are main group elements but they have charge degrees of freedom that depend on the $6s^2$ (Bi^{3+}, Pb^{2+}) and $6s^0$ (Bi^{5+}, Pb^{4+}) electronic configurations. The $6s^1$ configuration is prohibited. Bi and Pb are therefore called valence skipping elements. Since the energy levels of Bi and Pb 6*s*, transition metal 3*d* and oxygen 2*p* are close to each other, intermetallic charge transfer is observed in perovskite oxides composed of these elements [1]. The composition-, temperature- and pressure-induced changes in local charge distributions were investigated comprehensively by synchrotron X-ray diffraction, total scattering and photoemission studies.

The perovskite $BiNiO_3$ has an unusual $Bi^{3+}_{0.5}Bi^{5+}_{0.5}Ni^{2+}O_3$ valence distribution at atmospheric pressure. Distinct Bi^{3+}/Bi^{5+} crystallographic sites exist in the $\sqrt{2}a \times \sqrt{2}a \times 2a$ unit cell, where *a* is the lattice parameter of a simple cubic perovskite. The simultaneous melting of charge disproportionation and charge transfer between Bi^{5+} and Ni^{2+} ions accompanied by a triclinic (*P*-1) to an orthorhombic $GdFeO_3$-type (*Pbnm*) structural transition occur under high-pressure conditions. This structural transition results in a contraction of the unit cell volume by ~3%, because of the shrinkage of the Ni–O bond owing to the oxidation of Ni from 2+ to 3+. Fe^{3+} substitution for Ni^{2+} stabilizes the $Bi^{3+}(Ni, Fe)^{3+}O_3$ phase, and a charge transfer transition accompanied by volume shrinkage occurs in $BiNi_{1-x}Fe_xO_3$ upon heating at atmospheric pressure [2]. This transition is of first order, but because large low-temperature (LT) triclinic and small high-temperature (HT) orthorhombic phases coexist and their fractions change upon heating, the weighted average unit cell volume linearly decreases, leading to negative thermal expansion (NTE). The crystal structure of the LT phase investigated by powder diffraction at SPring-8 **BL02B2** changed to the polar *R*3*c* $BiFeO_3$-type with a unique Bi site, shown in Fig. 1(d), at $x = 0.3$. On the other hand, hard X-ray photoemission spectroscopy at SPring-8 **BL09XU** indicated the presence of Bi^{3+} and Bi^{5+}, as shown in Fig. 1(a). The PDF analysis of total scattering data collected at SPring-8 **BL22XU** (Figs. 1(b) and 1(c)) revealed that the local structure had *R*3 symmetry with two Bi sites (Fig. 1(e)). These results mean that the ordering of Bi^{3+}/Bi^{5+} is short-ranged, probably because of the deviation from the 1:1 ratio. Since the Fe ion has a +3 charge, as confirmed by Mössbauer spectroscopy, the amounts of Bi^{5+} and Ni^{2+} contributing to the charge transfer transition decrease with increasing *x*. The amount of unit cell volume reduction during the NTE therefore decreases with *x*. However, the volume reductions of $BiNi_{1-x}Fe_xO_3$ with $x \geq 0.3$ are found to be independent of *x*, as shown in Fig. 2(a). It is well known that ferroelectric to the

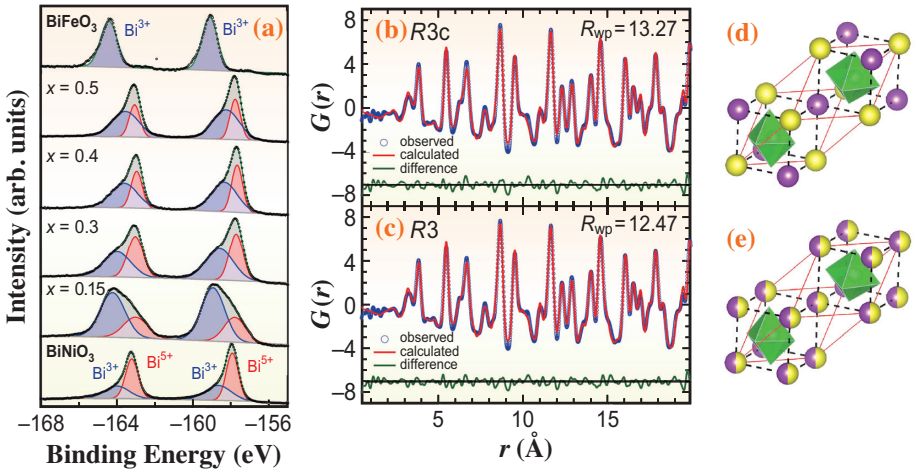

Fig. 1. **(a)** Observed hard X-ray photoemission spectroscopy (HAXPES) spectra (black points), fitting results (green line), Bi^{3+} components (blue) and Bi^{5+} components (red) for $BiNi_{1-x}Fe_xO_3$ measured at 300 K. Observed (blue points) and simulated (red line) pair distribution functions (PDFs) for $BiNi_{0.7}Fe_{0.3}O_3$ using **(b)** *R*3*c* and **(c)** *R*3 models. Lower green lines indicate the difference between the observed and simulated data. Average *R*3*c* **(d)** and local *R*3 (e) structures. [3]

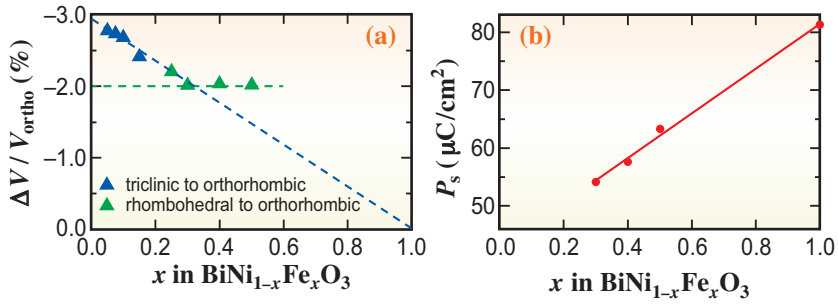

Fig. 2. Negative thermal expansion (NTE) induced by simultaneous charge transfer and polar–nonpolar transitions in $BiNi_{1-x}Fe_xO_3$. **(a)** Fe concentration dependence of the volume difference between low-temperature (LT) phases (triclinic or rhombohedral) and high-temperature (HT) orthorhombic phase. Blue and green triangles indicate transitions from triclinic to orthorhombic phases and from rhombohedral to orthorhombic phases, respectively. **(b)** Calculated P_S from structural parameters refined by Rietveld analyses of synchrotron X-ray diffraction (SXRD) patterns. [3]

paraelectric change in materials such as $PbTiO_3$ is accompanied by NTE. The spontaneous polarization of the polar rhombohedral LT phase of $BiNi_{1-x}Fe_xO_3$ increases with x (Fig. 2(b)). These indicate that the decrease in the amount of volume reduction due to charge transfer is compensated by the NTE induced by the polar–nonpolar transition [3].

$PbCoO_3$ prepared at 12 GPa has a $Pb^{2+}_{0.25}Pb^{4+}_{0.75}Co^{2+}_{0.5}Co^{3+}_{0.5}O_3$ charge distribution. Pb^{2+}/Pb^{4+} and Co^{2+}/Co^{3+} are respectively ordered at A- and B-sites of perovskite ABO_3, leading to the quadruple perovskite $Pb^{2+}Pb^{4+}{}_3Co^{2+}{}_2Co^{4+}{}_2O_{12}$ structure illustrated in Fig. 3(a) [4]. Similarly to $BiNiO_3$, a pressure-induced charge transfer transition leading to $Pb^{2+}{}_{0.5}Pb^{4+}{}_{0.5}Co^{3+}O_3$ is expected to occur. Synchrotron X-ray diffraction (SXRD) data collected at BL22XU indicated 1.76 and 1.12% reductions in unit cell volume at 20 and 24 GPa (Fig. 3(b)). An X-ray emission study at SPring-8 **BL12XU** revealed that the first reduction was due to the high-spin to low-spin transition of Co^{2+}. The second reduction was attributed to the charge transfer transition [5].

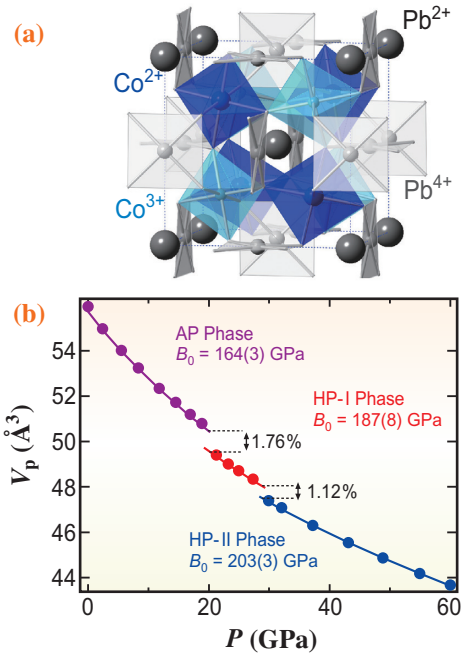

Fig. 3. **(a)** Crystal structure of $PbCoO_3$ with $Pb^{2+}Pb^{4+}{}_3Co^{2+}{}_2Co^{4+}{}_2O_{12}$ charge distribution. **(b)** Pressure evolution of unit cell volume of $PbCoO_3$. [5]

Masaki Azuma[a,b,*], Takumi Nishikubo[a] and Yuki Sakai[a,b]

[a] Laboratory for Materials and Structures, Tokyo Institute of Technology
[b] Kanagawa Institute of Industrial Science and Technology

*Email: mazuma@msl.titech.ac.jp

References

[1] M. Azuma *et al.*: Dalton Transactions **47** (2018) 1371.
[2] K. Nabetani *et al.*: Appl. Phys. Lett. **106** (2015) 061912.
[3] *T. Nishikubo, Y. Sakai, K. Oka, T. Watanuki, A. Machida, M. Mizumaki, K. Maebayashi, T. Imai, T. Ogata, K. Yokoyama, Y. Okimoto, S. Koshihara, H. Hojo, T. Mizokawa and M. Azuma: J. Am. Chem. Soc.* ***141*** *(2019) 19397.*
[4] Y. Sakai *et al.*: J. Am. Chem. Soc. **139** (2017) 4574.
[5] *Z. Liu, Y. Sakai, J. Yang, W. Li, Y. Liu, X. Ye, S. Qin, J. Chen, S. Agrestini, K. Chen, S.-C. Liao, S.-C. Haw, F. Baudelet, H. Ishii, T. Nishikubo, H. Ishizaki, T. Yamamoto, Z. Pan, M. Fukuda, K. Ohashi, K. Matsuno, A. Machida, T. Watanuki, S. I. Kawaguchi, A. M. Arevalo-Lopez, C. Jin, Z. Hu, J. P. Attfield, M. Azuma and Y. Long: J. Am. Chem. Soc.* ***142*** *(2020) 5731.*

Identification of Fe^{3+} single-atom sites for CO_2 conversion to CO using *operando* X-ray absorption spectroscopy

Efficiently converting carbon dioxide (CO_2) to carbon-based chemicals and fuels presents a promising catalytic approach to reduce the anthropogenic CO_2 emission. To achieve high energy efficiency and scalability, the electroreduction of CO_2 must occur rapidly and selectively at low overpotentials. To date, precious gold (Au) and silver (Ag) have been to be demonstrated the most efficient at low overpotentials, exhibiting a high Faradaic efficiency of carbon monoxide (CO) above 90%. Unfortunately, catalysts composed solely of Earth-abundant elements typically have low selectivity for CO production. Recently, many single-atom catalysts have been developed, in which numerous catalytic metal sites, especially iron (Fe), cobalt (Co) and nickel (Ni), were atomically dispersed and coordinated to the conductive carbon support. Although these non-precious metal catalysts show comparable Faradaic efficiency for CO to those of Au and Ag catalysts, much larger overpotentials are required to obtain the same partial current density (j_{CO}). Here, we report a catalyst with atomically dispersed Fe^{3+} sites with ultrahigh activity at low overpotentials for CO_2 electroreduction to CO.

The Fe catalyst (Fe^{3+}-N-C) was prepared through the pyrolysis of Fe-doped zinc (Zn) 2-methylimidazolate framework (ZIF-8) under nitrogen atmosphere at 900°C. To investigate the atomic structures and oxidation states of the as-prepared Fe^{3+}-N-C catalyst, we have conducted X-ray absorption experiments using SPring-8 **BL12B2** beamline [1]. The Fe *K*-edge X-ray absorption near-edge structure (XANES) spectrum of Fe^{3+}-N-C showed the binding and edge energies close to those of Fe_2O_3 and Fe^{3+}TPPCl (tetraphenylphosphonium chloride), indicating that the Fe ions in the catalyst were in the +3 oxidation state (Fig. 1(a)). Moreover, the Fe *K*-edge extended X-ray absorption fine structure (EXAFS) spectrum supported the atomic dispersion of Fe sites and their planar Fe-X_4 (X = N or C) structures in Fe^{3+}-N-C (Fig. 1(b)). The catalytic activity toward CO_2 electroreduction was then evaluated using a gas diffusion electrode in a flow cell. At –0.45 V versus reversible hydrogen electrode (RHE), the Fe^{3+}-N-C catalyst exhibited a high j_{CO} reaching 94 mA cm^{-2} with a Faradaic efficiency of CO above 90%. The j_{CO} for Fe^{3+}-N-C measured in an H-cell between –0.2 and –0.5 V versus RHE was also observed considerably high, which even overwhelmed that attained by other previously reported Fe single-atom catalysts. Notably, the performance of Fe^{3+}-N-C could be stable between –0.2 and –0.5 V versus RHE, although at potentials more negative than –0.5 V versus RHE, the activity became unstable, indicating some changes in the Fe^{3+}-N-C around –0.5 V versus RHE.

We further conducted *operando* XAS experiments using SPring-8 BL12B2, which enabled the precise monitoring of changes in the catalysts under working conditions. Fe *K*-edge spectra were obtained on dry samples and on samples that were loaded on glassy carbon electrodes and immersed in the electrolyte at various potentials. For Fe^{3+}-N-C catalyst (Fig. 2(a)), the Fe *K*-edge exhibited no obvious shift between the dry powder and the *in situ* sample at –0.4 V versus RHE, indicating that the Fe ions in Fe^{3+}-N-C remained in the +3 oxidation state during CO_2 electroreduction. When the applied potential was shifted further negative, the Fe-edge shifted to lower energies, showing the reduction of Fe^{3+} to Fe^{2+}. Such reduction process occurred at the same potential as the above-mentioned deactivation of Fe^{3+}-N-C, implying that Fe^{3+} sites were more active for generating CO. Moreover, the fitting of EXAFS spectra indicated that the reduction of Fe^{3+} sites was accompanied by a change in local structure, where the first shell coordination

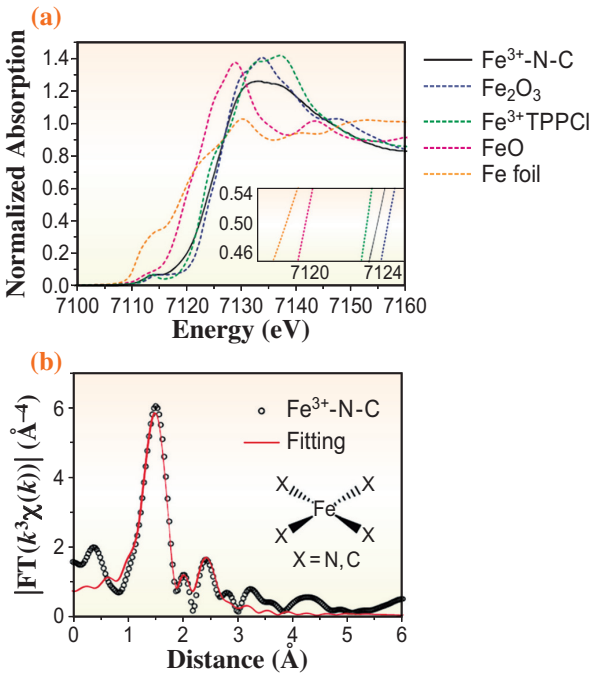

Fig. 1. **(a)** Fe *K*-edge XANES spectra of Fe^{3+}-N-C and reference samples. (Inset) Enlargement of the main edges. **(b)** R-space Fe *K*-edge EXAFS spectra of Fe^{3+}-N-C.

number of Fe was reduced from 4 to about 3. To investigate the origin of the improved activity of Fe^{3+}-N-C, we also measured the *in situ* Fe *K*-edge XANES of previously reported single-atom $Fe_{0.5}$d catalyst [2]. It was revealed a +2 rather than +3 oxidation state for the Fe sites under potentials between –0.2 and –0.5 V versus RHE, which might be due to different ligand environments with regard to the N atoms. For those previously reported Fe single-atom catalysts, Fe ions coordinated with four pyridinic N were proposed as the active sites [3]. By a sharp contrast, Fe^{3+}-N-C was observed to be coordinated to pyrrolic N, as demonstrated by the N *K*-edge XANES spectrum.

Furthermore, we directly compared the Fe^{3+}-N-C with an analogous Fe^{2+}-N-C catalyst in which the Fe ions were coordinated by pyridinic N atoms. Fe *K*-edge XANES spectra showed a considerable number of Fe^{3+} sites in the as-prepared sample of Fe^{2+}-N-C (Fig. 2(b)). Moreover, the *in situ* Fe *K*-edge exhibited that Fe^{3+} sites in the Fe^{2+}-N-C started to be reduced to Fe^{2+} at –0.1 to –0.2 V versus RHE, and at potentials more negative than –0.2 V versus RHE (CO_2 electroreduction), the energy of the Fe *K*-edge was slightly lower than that of FeO, suggesting that Fe^{2+}-N-C had an oxidation state of +2 or lower under reaction conditions. Correspondingly, the turnover frequency (TOF) of CO production of Fe^{2+}-N-C is more than one order of magnitude lower than that of Fe^{3+}-N-C under the same potential. The current density of Fe^{2+}-N-C decreased markedly during 2 h chronoamperometry tests, indicating its lower stability as compared with the Fe^{3+}-N-C catalyst. These data suggest that pyrrolic type ligands are significant to keep Fe sites in the +3 oxidation state during CO_2 electroreduction and consequently maintain the high activity and stability of Fe^{3+} sites.

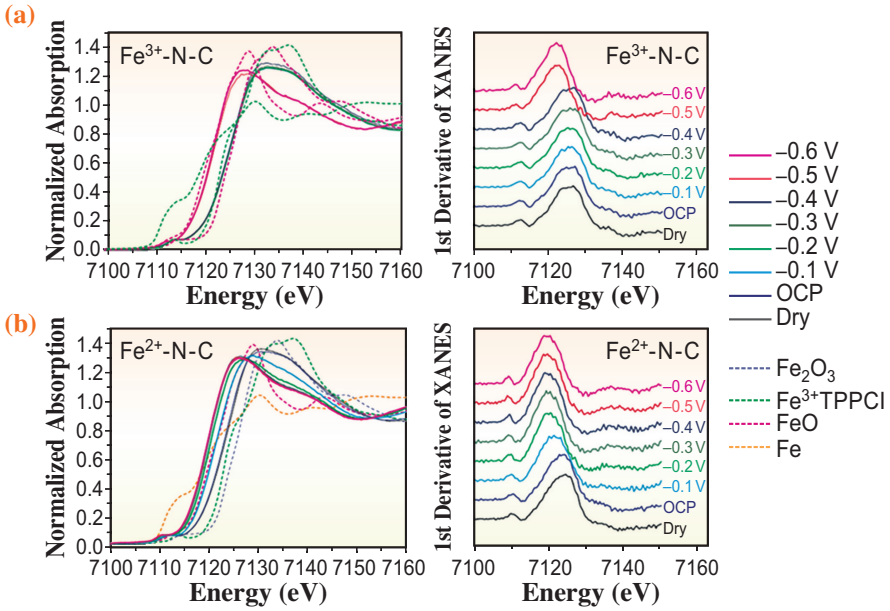

Fig. 2. *Operando* XAS characterization. **(a, b)** Fe *K*-edge XANES spectra (left) and the first derivative of the spectra (right) of (a) Fe^{3+}-N-C and (b) Fe^{2+}-N-C as dry powder and loaded on glassy carbon electrodes at various potentials.

J. Gu[a], C.-S. Hsu[b], H. M. Chen[b,*] and X. Hu[a]

[a] Institute of Chemical Sciences and Engineering, Ecole Polytechnique Fédérale de Lausanne, Switzerland
[b] Department of Chemistry, National Taiwan University, Taiwan

*Email: haomingchen@ntu.edu.tw

References

[1] *J. Gu, C.-S. Hsu, L. Bai, H.M. Chen, X. Hu: Science* ***364*** *(2019) 1091.*
[2] T.N. Huan *et al.*: ACS Catal. **7** (2017) 1520.
[3] W. Ju *et al.*: Nat. Commun. **8** (2017) 944.

Formation of Xe 4*d* double-core-hole states in intense EUV-FEL fields studied by multielectron-ion coincidence spectroscopy

The nonlinear optical response of materials in the extreme ultraviolet (EUV) and X-ray regions has attracted a great deal of attention for its importance in various applications of intense ultrashort free-electron lasers (FELs). Atoms and molecules in intense FEL fields have been studied as a benchmark for clarifying the underlying processes, which revealed that they typically undergo multiple ionization by multiphoton absorption [1].

In the multiple ionization process involving inner-shell electrons, Auger electron emission processes associated with the decay of the inner-shell hole compete with the subsequent multiphoton absorption process, resulting in the emission of many electrons as well as charged ions depending on the ionization pathway. To understand the nonlinear ionization mechanism involving such multiple pathways in detail, it is necessary to clarify the electronic states involved in each ionization process.

Electron spectroscopy is a powerful technique for this purpose since it allows the measurement of the energy of electrons emitted during ionization, from which intermediate and/or final electronic states can be identified. It has been applied to nonlinear ionization involving doubly excited states [2] and double-core-hole (DCH) states [3], but nonlinear signals are usually weak such that they are often smeared out by signals originating from strong one-photon (linear) processes.

In EUV and X-ray intense laser fields, highly charged ions tend to be generated in high-order nonlinear processes where a large number of photons are absorbed. This means that the ions can be used as "tags" for separating electron signals associated with a target nonlinear process from other dominant signals mainly produced by one-photon processes (Fig. 1). In this work, we introduced multielectron-ion coincidence spectroscopy to tag electrons with the counterpart ion produced by the ionization of a single atom. We incorporated this idea in the multiphoton ionization of Xe by EUV-FEL irradiation as a benchmark system. By relating electron signals to Xe^{4+} ions generated by the two-photon process, we successfully captured electron signals that are associated with the two-photon DCH formation of Xe 4*d* inner-shell states [4].

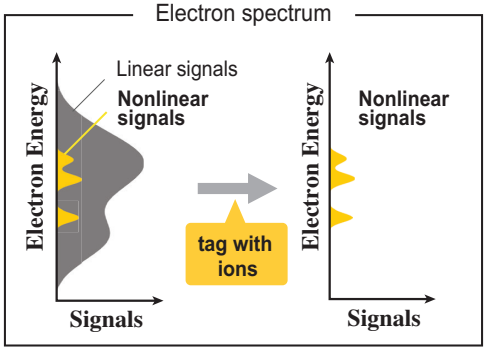

Fig.1. Schematics of electron spectra obtained by multielectron-ion coincidence spectroscopy.

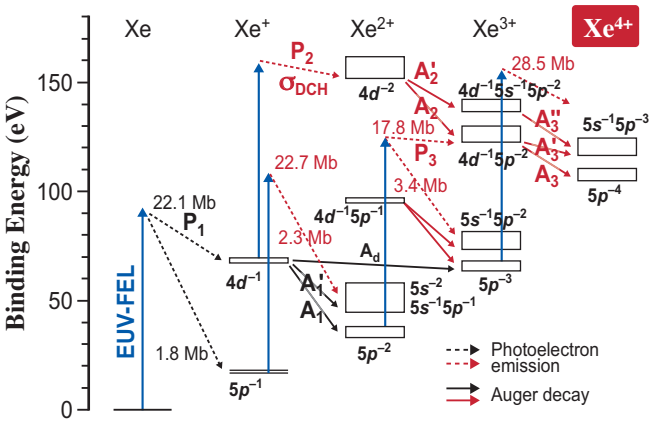

Fig.2. Energy diagram of relevant electronic states of neutral and ionic Xe atoms [4]. P and A stand for electron emissions by photoionization and Auger decays, respectively.

Experiments were conducted at the soft X-ray beamline, SACLA **BL1**. Intense EUV laser pulses were focused by a Kirkpatrick-Baez mirror onto the diffusive Xe gas introduced into the interaction region of a magnetic bottle-type electron spectrometer equipped with an ion detection unit. Electrons produced in the interaction region were guided to a microchannel plate (MCP) detector placed in one end of a time-of-flight (TOF) tube by magnetic fields formed by a permanent magnet and a solenoid coil, while the counterpart ions were introduced into the TOF tube by pulsed electric fields and detected with the same MCP. The chamber was kept under an ultrahigh-vacuum condition ($<5\times10^{-10}$ Torr), and coincidence measurements were carried out at a typical event rate of 0.25 events/shot to suppress false coincidence events to less than 20% of the total events.

Irradiation with EUV-FEL pulses (91 eV, 30 fs, 60 Hz, 1.6×10^{12} W/cm^2) produced Xe^{Z+} ions ($Z \leq 4$).

Xe^{Z+} ions with lower charge (Z=1–3) can be generated by single-photon ionization, while for the formation of Xe^{4+} ions, the absorption of more than two photons is required because of the FEL photon energy used (see Fig. 2).

Figure 3(a) shows a two-dimensional correlation map of electrons that are simultaneously detected with Xe^{2+} ions. The observed features are formed by electrons generated by the photoionization of Xe 4*d* inner-shell levels (4*d* photoelectron; P_1) and the ultrafast Auger decay to Xe^{2+} (Auger electron; A_1, A_1') [5]. These features are also identified in the electron map for Xe^{4+} ions (Fig. 3(b)), indicating that Xe^{4+} can be produced via the Xe^{2+} states by the absorption of another EUV photon. On the other hand, broad electron distributions that are not explained by the sequential photoionization process mentioned above are observed in the energy region of 26–38 eV. These electron energies agree well with the kinetic energies of Auger electrons (A_2) associated with the decay of $Xe^{2+}(4d^{-2})$ into $Xe^{3+}(4d^{-1}5p^{-2})$, suggesting that the two-photon formation of Xe 4*d* DCH states is involved in the generation of Xe^{4+} ions.

A quantitative analysis of the Auger electron intensities associated with these two pathways, (A_1, A_1') and (A_2, A_2'), revealed that the contribution of the Xe 4*d* DCH pathway is comparable to that of the sequential one [4]. This result indicates that the Xe 4*d* DCH states are efficiently formed from the transient $Xe^{+}(4d^{-1})$ states (lifetime of ~6 fs) even though the EUV-FEL pulses employed here have a rather long pulse duration of 30 fs. A numerical simulation based on coupled rate equations for two-photon absorption processes showed that the efficient two-photon formation of the Xe 4*d* DCH states becomes possible when the ionization cross section σ_{DCH} of $Xe^{+}(4d^{-1})$ states, $Xe^{+}(4d^{-1}) + h\nu \rightarrow Xe^{2+}(4d^{-2}) + e^{-}$, falls in the range between 27 and 64 Mb. The obtained results suggest that σ_{DCH} is considerably larger than the normal 4*d* cross sections (~20 Mb), which could be attributed to the resonance excitation from the $4d^{-1}$ to $4p^{-1}$ states in Xe [4].

The present work clearly demonstrates the power of multielectron-ion coincidence spectroscopy for gaining a deeper understanding of nonlinear phenomena induced by intense EUV and X-ray laser fields. This coincidence technique can be extended to molecular systems in which core holes can be created in different atomic sites. Since such DCH states are known to sensitively reflect the local environment of core-hole sites within a molecule [3], the present approach is expected to become a key technique for uncovering nonlinear reaction pathways for a novel X-ray chemical analysis.

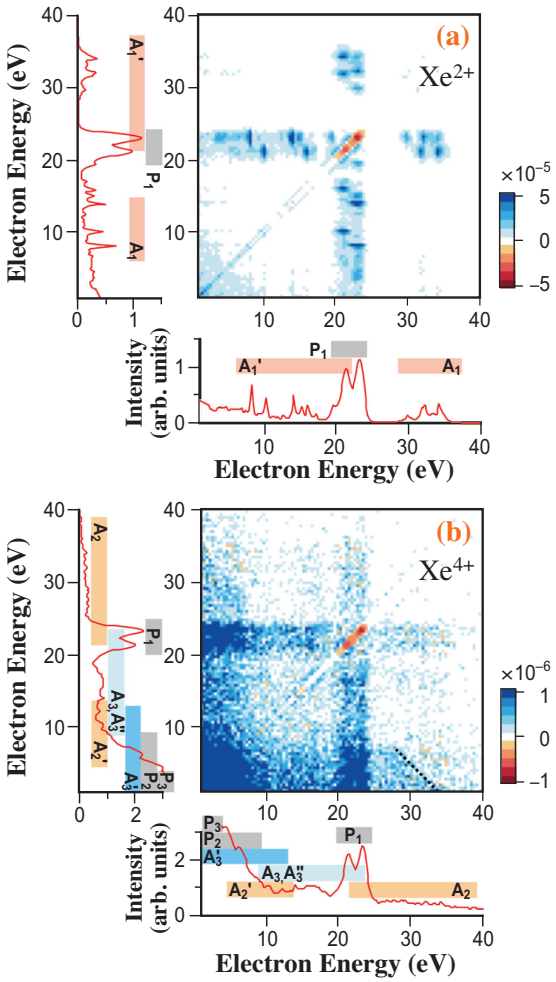

Fig.3. Two-dimensional map of electrons detected in coincidence with **(a)** Xe^{2+} and **(b)** Xe^{4+} ions, obtained by triple covariance analysis [4]. Electron energy regions observed in each process are indicated by color bars.

Mizuho Fushitani[a,*], Yasumasa Hikosaka[b] and Akiyoshi Hishikawa[a,c]

[a] Graduate School of Science, Nagoya University
[b] Institute of Liberal Arts and Sciences, University of Toyama
[c] Research Center for Materials Science, Nagoya University

*Email: fusitani@chem.nagoya-u.ac.jp

References

[1] M. Yabashi *et al.*: J. Phys. B **46** (2013) 164001.
[2] A. Hishikawa *et al.*: Phys. Rev. Lett. **107** (2011) 243003.
[3] P. Lablanquie *et al.*: J. Phys. B **49** (2016) 182002.
[4] *M. Fushitani, Y. Sasaki, A. Matsuda , H. Fujise , Y. Kawabe, K. Hashigaya, S. Owada, T. Togashi, K. Nakajima, M. Yabashi, Y. Hikosaka, and A. Hishikawa: Phys. Rev. Lett. **124** (2020) 193201.*
[5] M. Fushitani *et al.*: J. Electron Spectrosc. Relat. Phenom. **184** (2012) 561.

Femtosecond X-ray liquidography captures the birth of molecular vibrations mediating bond formation

Trajectories of wavepackets along reaction coordinates, which determine real-time atomic motions in molecules during reactions, are often drawn in calculated or imagined potential energy surfaces (PES). However, it is still challenging to experimentally determine the trajectories of wavepackets on multidimensional nuclear coordinates. In our recent work, we succeeded in achieving this goal using photoinduced bond formation of a gold trimer complex (GTC), $[Au(CN)_2^-]_3$, in an aqueous solution [1]. The equilibrium structure of GTC in the ground state (S_0) determines the position of the Franck-Condon (FC) region and the structure in the FC region, where the excited-state wavepacket is initially created, can be considered as the reactants (A+B+C) of the reaction. This wavepacket moves toward the equilibrium structure of T_1', which is the product (A-B-C) with two equivalent covalent Au–Au bonds. Regarding the bond formation process of GTC, the three candidate reaction mechanisms can be considered: (i) the concerted bond formation mechanism where two covalent bonds, A-B and B-C, are formed synchronously, and the asynchronous bond formation mechanism where (ii) A-B is formed first or (iii) B-C is formed first. To determine the reaction mechanism among the three candidate mechanisms, it is required to directly observe the initial motions of the wavepacket starting from the FC region on multidimensional PES.

To accomplish this task, we performed femtosecond time-resolved X-ray liquidography (TRXL) experiments [2] using X-ray free electron lasers (XFELs) at SACLA **BL3** [3] and the X-ray Scattering and Spectroscopy (XSS) beamline of PAL-XFEL [4]. Structural analyses were performed against the TRXL data, and the best fits shown in Fig. 1(a) were obtained when both of the ground and excited states, S_0 and T_1', were considered, indicating that wavepacket motions in PESs of both S_0 and T_1' contribute to the TRXL signal. Using the time-dependent changes of structural parameters, R_{AB}, R_{BC}, R_{AC}, and Au–Au–Au angle (θ), shown in Figs. 1(b)–1(c), we reconstructed the trajectories of the excited-state (Figs. 2(a) and 2(c)) and ground-state [1] wavepackets in multidimensional nuclear coordinates, R_{AB} vs R_{BC} vs θ.

As shown in Fig. 2(a), the excited-state wavepacket generated in the FC region (R_{AB} = 3.13 Å and R_{BC} = 3.38 Å, θ = 119°) moves on the PES of T_1' toward the equilibrium structure of T_1' (R_{AB} = 2.82 Å

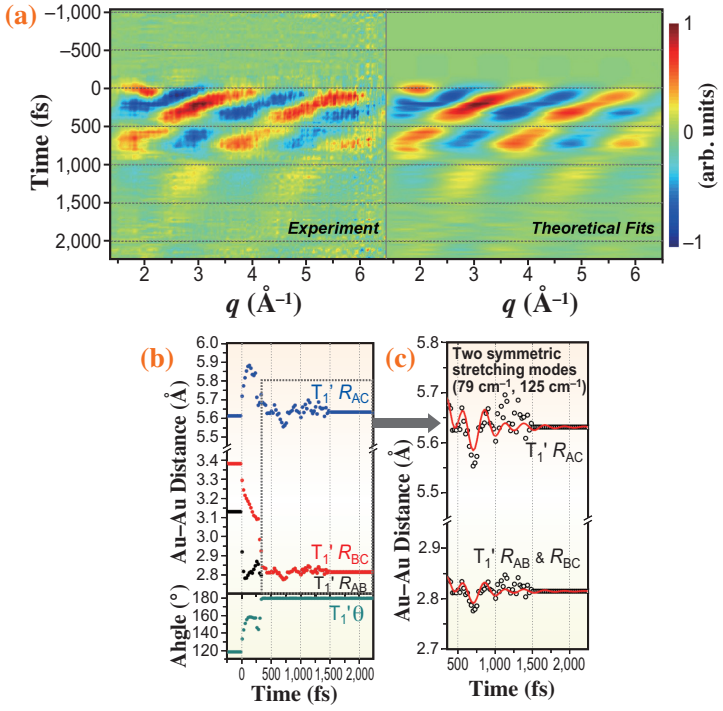

Fig. 1. **(a)** Experimental TRXL signal (left), and their theoretical fits (right) obtained from the structural analysis. **(b)** $R_{AB}(t)$, $R_{BC}(t)$, and $R_{AC}(t)$, and Au–Au–Au angle, θ, of T_1' are represented by black, red, blue, and cyan dots, respectively. **(c)** The Au–Au distances in the late time range (>360 fs) for T_1' are represented by black open circles with their fits by a sum of two damping cosine functions (red lines).

and R_{BC} = 2.82 Å, θ = 180°). Specifically, R_{AB} decreases rapidly down to the covalent Au–Au bond length of the equilibrium T_1' (2.82 Å) at 35 fs time delay and becomes even shorter at 60 fs to reach the minimum length along the entire trajectory, whereas R_{BC} is still much longer than the covalent bond length (2.82 Å) at those time delays, as shown in Fig. 2(a). The early-time trajectory reveals that the two covalent bonds are formed in an asynchronous manner, in which the covalent bond is formed earlier in the shorter Au–Au pair of the ground state. With respect to θ, the excited-state wavepacket starts from the FC region (θ = 119°) and reaches the equilibrium value of T_1' (θ = 180°) in 335 fs, giving the time scale of bent-to-linear transformation. After the initial motions, the wavepacket oscillates around their equilibrium structures in the late time range (> 360 fs), as can be seen in Fig. 1(c). The trajectory of the wavepacket in T_1' in the late time range (> 360 fs) is shown in Fig. 2(c). For T_1', a sum of two symmetric stretching modes with 79 cm^{-1} and 125 cm^{-1} frequencies give satisfactory fits (Fig. 1(c)), and for S_0, a symmetric stretching mode with 32 cm^{-1} frequency and an asymmetric stretching mode with 44 cm^{-1} frequency gives satisfactory fits [1].

In summary, the trajectories of nuclear wavepackets were visualized using femtosecond TRXL and unambiguously provides a direct view of the vibrational motion that drives an asynchronous bond formation. Femtosecond TRXL can be used as a fundamental tool to visualize atomic motions and reveal reaction pathways in many chemical reactions.

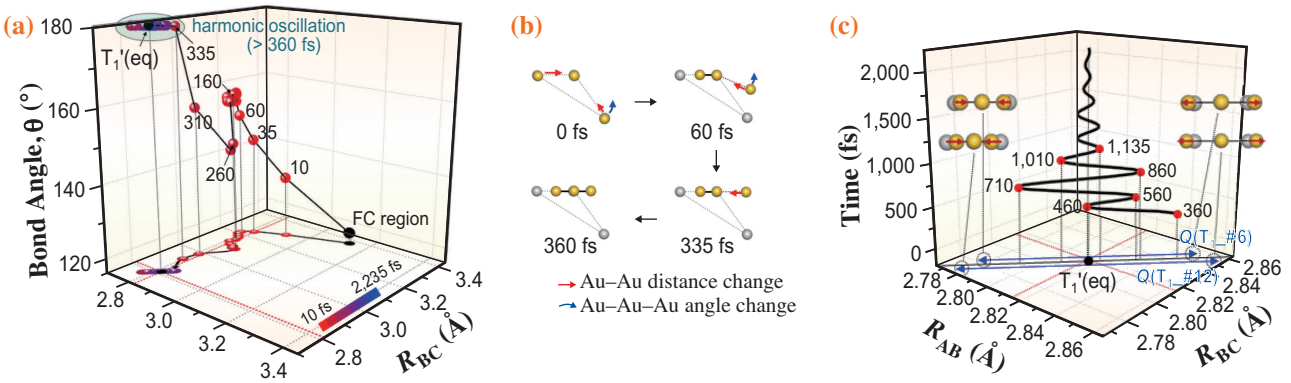

Fig. 2. **(a, c)** The trajectory of the wavepacket in T_1' in (a) the early time range (<360 fs) and (c) the late time range (>360 fs) is represented in the coordinates of R_{AB} versus R_{BC} versus θ and R_{AB} versus R_{BC}, respectively. In (a), the positions of the wavepacket at measured time delays are indicated by dots using a color scheme shown at the bottom of each panel. For several time delays, the time delays in femtoseconds units are shown. **(b)** Transient structures of T_1' at representative time delays. The Au atoms at each time delay are represented by yellow dots while the Au atoms in the FC region are represented by gray dots. Covalent bonds are indicated by black solid lines. The changes of interatomic distance and angle are indicated by red arrows and blue arrows, respectively. The trajectory of the wavepacket in S_0 is now shown due to space limitation. In (c), the wavepacket positions at several time delays are indicated by red dots, and the time delays in femtoseconds units are shown. The normal coordinates of the normal modes are indicated by blue arrows. At the end of each arrow, the representative structure with Au atoms as yellow spheres is shown to indicate displacements of three Au atoms according to the normal coordinate while the equilibrium structures are represented by gray spheres. The red arrows indicate the displacement vectors of Au atoms.

Jong Goo Kim[a,b,c], Shin-ichi Adachi[d,e] and Hyotcherl Ihee[a,b,c,*]

[a] Department of Chemistry, KAIST, Republic of Korea
[b] KI for the BioCentury, KAIST, Republic of Korea
[c] Center for Nanomaterials and Chemical Reactions, Institute for Basic Science (IBS), Republic of Korea
[d] Photon Factory, High Energy Accelerator Research Organization (KEK)
[e] Department of Materials Structure Science, The Graduate University for Advanced Studies

*Email: hyotcherl.ihee@kaist.ac.kr

References

[1] *J.G. Kim, S. Nozawa, H. Kim, E.H. Choi, T. Sato, T.W. Kim, K.H. Kim, H. Ki, J. Kim, M. Choi, Y. Lee, J. Heo, K.Y. Oang, K. Ichiyanagi, R. Fukaya, J.H. Lee, J. Park, I. Eom, S.H. Chun, S. Kim, M. Kim, T. Katayama, T. Togashi, S. Owada, M. Yabashi, S.J. Lee, S. Lee, C.W. Ahn, D.-S. Ahn, J. Moon, S. Choi, J. Kim, T. Joo, J. Kim, S. Adachi and H. Ihee: Nature* ***582*** *(2020) 520.*
[2] K.H. Kim *et al.*: Nature **518** (2015) 385.
[3] T. Ishikawa *et al.*: Nat. Photon. **6** (2012) 540.
[4] H.S. Kang *et al.*: Nat. Photon. **11** (2017) 708.

A novel porous molecular crystal that varies its color in response to the change in surrounding humidity

Sensors that detect the content of a certain molecule are of fundamental importance in many industrial processes. To ensure safety and reproducible operations, facilities often need to monitor the feed or drain gases. Along with organic or inorganic gases, water plays a crucial role in such chemical processes. Water molecules are ubiquitous in the environment, but they are not always preferable for chemical or physical processing, especially when delicate reactive compounds or substrates are treated.

An established way of monitoring the water content in the atmosphere is to use an electrical capacitor whose capacitance changes in response to the surrounding humidity. However, electricity and physically connected circuits are necessary for these types of electric sensor, which limits the applicable situations of these devices. Namely, these devices cannot be implanted in physically and electrically isolated chambers.

Colorimetric humidity sensors are advantageous in this context. Colorimetric sensors, or constituent hydrochromic compounds, alter their absorption color in response to the surrounding humidity. Although the color change is not easy to detect precisely, it is beneficial in various situations because of the setup simplicity and the electricity-free working mechanism. Cobalt complexes, for instance, change their absorption color from blue to pink upon the adsorption of humidity. Since the color change is readily visible and requires no additional equipment, these colorimetric compounds are frequently utilized in the food industry.

The color change of these compounds commonly relies on the adsorption of water molecules onto the constituent organic or inorganic molecules. Therefore, porous crystals featuring extremely large surface areas and uniform pore morphology are advantageous for enhancing the color change and response speed. However, organic porous crystals are unstable under humid conditions. Representative porous organic crystals, such as metal–organic frameworks (MOFs), covalent organic frameworks (COFs), or hydrogen-bonded organic frameworks (HOFs), are built up via coordination bonds, dynamic covalent bonds, or hydrogen bonds, which are all susceptible to water molecules. Elaborate and complex molecular design is necessary to make these materials tolerant to water.

A much simpler and straightforward way of circumventing this issue is to grow porous crystals with less-polar bonds such as van der Waals forces, π-π stacking, and C–H···X bonds [1,2]. The attractive nature of these less-polar bonds originates mostly from the dispersion forces, whose bonding strength is independent of the polarity of the surrounding medium. Therefore, porous crystals grow with these less-polar bonds (van der Waals porous molecular crystals, VPCs) survive even in highly polar solvents including water. However, the design strategy for porous molecular crystals has yet to be established because of the difficulty in predicting and controlling these weak bonds.

In this study, we newly synthesized a porous molecular crystal from a novel aromatic dendrimer and examined its hydrochromic behavior (Fig. 1) [3]. The constituent organic molecule **1** is a second-generation fully aromatic dendrimer featuring six carbazole (Cz) moieties at the periphery and a dibenzophenazine (DBPHZ) core (Fig. 1(a)). The carbazole dendron and dibenzophenazine act as an electron donating group and an electron accepting group, respectively, providing a charge transfer (CT) nature to **1**. The Lippert–Mataga plot, as well as the E_{30} plot, of **1** based on electronic absorption and photoluminescence spectra confirms the CT character of **1**.

Despite its sterically bulky morphology, **1** formed crystalline powder (**VPC-1**) upon thermal annealing in a binary mixture of $CHCl_3$ and MeOH. The N_2 adsorption isotherm of **VPC-1** measured at 77 K exhibits a marked uphill profile in the low relative pressure range, indicating that **VPC-1** is a microporous crystal. This finding itself is of fundamental importance because **VPC-1** is a molecular crystal sustained totally by weak van der Waals forces. Despite the weak intermolecular bonding network, **VPC-1** maintains its porous framework even after the evacuation of the crystallization solvent.

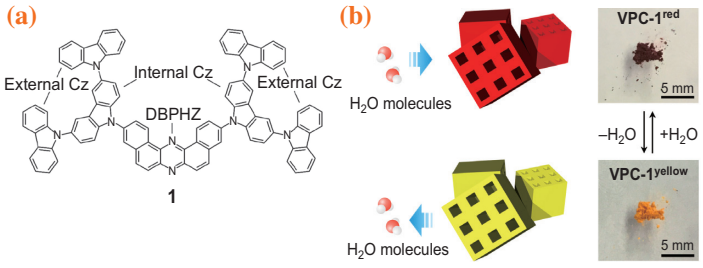

Fig.1. **(a)** Molecular structure of **1**. **(b)** Schematic representation of the hydrochromic behavior of **VPC-1** upon adsorption and desorption of H_2O molecules together with their photographs.

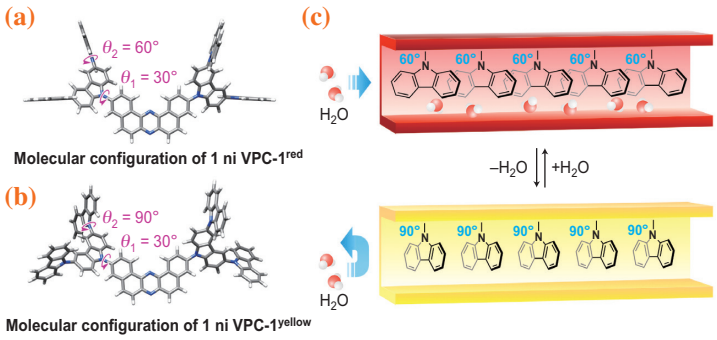

Fig. 2. **(a)** Computational models for **1** in **VPC-1**^{red} and **VPC-1**^{yellow}. **(b)** Schematic representation of the flipping of carbazole dendrons in **VPC-1** upon adsorption and desorption of H_2O molecules.

The powdery specimen of **VPC-1** exhibited a yellow color (**VPC-1**^{yellow}) just after drying under vacuum but became red (**VPC-1**^{red}) upon exposure to humid air. The color change was investigated in detail by means of IR (infrared), Raman, and diffuse reflection measurements under controlled humidity at SPring-8 **BL43IR**, where a series of spectroscopic or diffractometric apparatuses equipped with humidifier is available. These facilities can also enable us to investigate the molecular structure in detail when needed. Therein, microscopic measurements were also available and beneficial for the kinetic study of the hydration and dehydration processes.

This color change process is fully reversible upon decreasing the humidity. The K-M values of **VPC-1** at 570 nm plotted against the relative humidity (RH) of the surrounding atmosphere show a sigmoidal curve with a clear threshold at around 50 RH% without hysteresis.

The color change of **VPC-1** is attributed to the prompt uptake/removal of the H_2O molecules accompanied by the flipping of the outer carbazole moieties (Fig. 2). Molecular vibrational bands corresponding to C–N stretching, pyrrole breathing, C–H bending, and O–H stretching modes in the IR spectra exhibit analogous abrupt changes upon increasing or decreasing the surrounding humidity (Fig. 3). According to the results of our computational analysis, the IR spectral change indicates the rotational motion of carbazole. The H_2O adsorption isotherm measured at 20°C also shows a sigmoidal curve.

The heat of adsorption profile and computational analysis shed light on the possible molecular mechanism of how **VPC-1** responds to the humidity. At a low humidity, the carbazole dendrons of **1** have a lower affinity to H_2O molecule. When the surrounding humidity surpasses a certain threshold, the carbazole dendrons flip and undergo a dipole–dipole interaction with the guest H_2O and accelerates the adsorption of H_2O (Fig. 2(b)).

The sigmoidal H_2O adsorption and following color change of **VPC-1** are of practical value, especially for H_2O detection in an isolated chamber. Fundamentally, the thermal stability of **VPC-1** with the sigmoidal flipping of carbazole dendrons in response to H_2O is intriguing, since it combines seemingly incompatible features, namely, structural rigidity and flexibility.

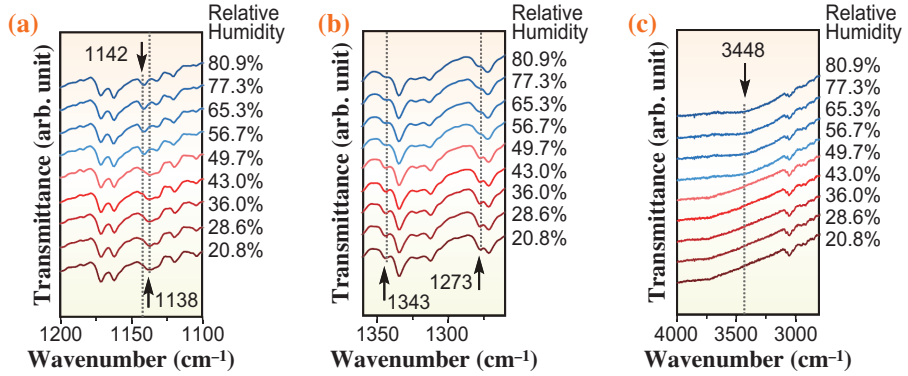

Fig. 3. Magnified IR spectra that correspond to the C–N stretching, pyrrole breathing, and C–H bending **(a, b)** and O–H stretching modes **(c)** of **1** in **VPC-1** upon increasing the surrounding humidity from 20.8 to 80.9%.

Hiroshi Yamagishi[a,b] and Yohei Yamamoto[a,b,*]

[a] Department of Materials Science, University of Tsukuba
[b] Tsukuba Research Center for Energy Materials Science (TREMS), University of Tsukuba

*Email: yamamoto@ims.tsukuba.ac.jp

References

[1] H. Yamagishi *et al.*: Science **361** (2018) 1242.
[2] A. Nakayama *et al.*: Chem. Commun. **56** (2020) 6937.
[3] *H. Yamagishi, S. Nakajima, J. Yoo, M. Okazaki, Y. Takeda, S. Minakata, K. Albrecht, K. Yamamoto, I. Badía-Domínguez, M.M. Oliva, M.C.R. Delgado, Y. Ikemoto, H. Sato, K. Imoto, K. Nakagawa, H. Tokoro, S. Ohkoshi and Y. Yamamoto: Commun. Chem.* ***3*** *(2020) 118.*

Structural characterization of acid-responsive hydrogen-bonded organic frameworks with permanent porosity

Hydrogen-bonded organic frameworks (HOFs) are porous molecular crystalline materials constructed through intermolecular hydrogen-bonding interactions [1]. Compared with other porous organic frameworks such as covalent organic frameworks (COFs), HOFs tend to give highly crystalline materials with a large single domain, enabling us to elucidate the structure-property relationship by single-crystalline X-ray diffraction analysis. Moreover, HOFs can show the ability to restore the original structures of frameworks by, for example, reannealing with solvents. These features originate from the reversible nature of hydrogen bond formation and destruction. However, this characteristic simultaneously results in the fragility of the frameworks and the difficulty in obtaining frameworks as designed; no rule-of-thumb for the design of rigid HOFs with permanent porosity had been established until recently.

To overcome the above-mentioned problems, we have hypothesized that building-block molecules possessing both a highly symmetric large π-conjugated planar moiety and highly directional H-bonding groups can provide predictable HOF structures with permanent porosity and rigidity. Indeed, we have demonstrated that a series of C_3-symmetric cyclic π-conjugated molecules possessing six carboxyphenyl groups in the periphery form predictable H-bonded hexagonal network (H-HexNet) structures that stack without interpenetration to give porous layered HOFs [2]. To provide further functionality to porous HOFs, we applied hexacarboxylic acid with a heteropolycyclic aromatic hydrocarbon moiety, namely, hexakis(carboxyphenyl) hexaazatrinaphthylene (CPHATN). Consequently, we demonstrated that CPHATN forms a rigid HOF exhibiting stimuli responsiveness toward strong acid species because of the nitrogen atoms incorporated in a large π-conjugated system (Fig. 1) [3,4].

The crystal structure of solvated HOF CPHATN-1(TCB), where TCB denotes 1,2,4-trichlorobenzene used as a recrystallization solvent, was characterized by single-crystalline X-ray diffraction analysis to have a layered structure of H-HexNet sheets (Fig. 2(a)). To activate the inner spaces of the frameworks, solvent molecules inside CPHATN-1(TCB) were removed by heating under a vacuum condition to give single crystals of the activated HOF CPHATN-1a, whose structure was analyzed at SPring-8 **BL38B1**.

CPHATN-1a has a very similar molecular packing to CPHATN-1(TCB), except for the conformation at one of the H-bonded carboxyphenyl dimers shown in the red square in Figs. 2(a,b). The conformational distortion causes a small shrinkage of the crystallographic cell by 200.7 Å^3 (Fig. 2(c)). The results of a N_2 sorption experiment at 77 K were used to calculate the BET surface area and pore size of the framework to be 379 m^2g^{-1} and 0.78 nm, respectively. Precise structural changes upon the sorption of hydrocarbons were analyzed at SPring-8 **BL02B2**. In PXRD patterns of CPHATN-1a recorded upon introducing benzene vapor (Fig. 2(d)), the 010 and 011 diffraction peaks shifted to the small-angle region upon vapor absorption, while the 001 peak remain at its original position during the sorption. Furthermore, when the benzene-filled CPHATN-1a was heated, the 010 and 011 peaks shifted to the large-angle region, indicating the shrinkage of the cell due to the release of benzene molecules (Fig. 2(e)). The observed structural changes to crystal structures of CPHATN-1(TCB) and CPHATN-1a indicate that the framework slightly changes its structure and volume of spaces upon the sorption of guest molecules.

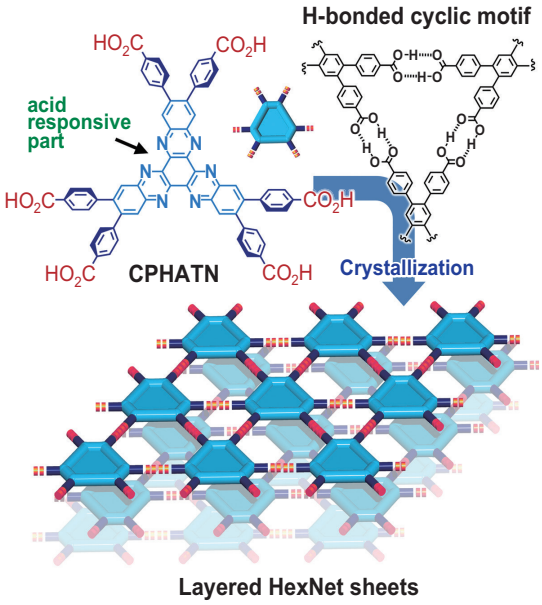

Fig. 1. Schematic representation for construction of porous HOF possessing layered HexNet structures of CPHATN. The HexNet structure is formed via a H-bonded cyclic motif.

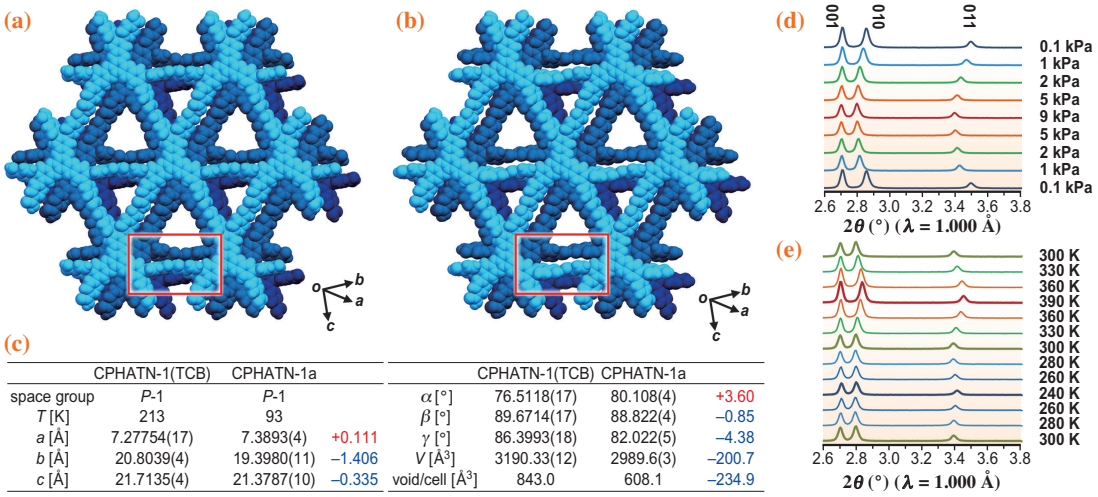

	CPHATN-1(TCB)	CPHATN-1a			CPHATN-1(TCB)	CPHATN-1a	
space group	*P*-1	*P*-1		α [°]	76.5118(17)	80.108(4)	+3.60
T [K]	213	93		β [°]	89.6714(17)	88.822(4)	–0.85
a [Å]	7.27754(17)	7.3893(4)	+0.111	γ [°]	86.3993(18)	82.022(5)	–4.38
b [Å]	20.8039(4)	19.3980(11)	–1.406	*V* [Å^3]	3190.33(12)	2989.6(3)	–200.7
c [Å]	21.7135(4)	21.3787(10)	–0.335	void/cell [Å^3]	843.0	608.1	–234.9

Fig. 2. Selected crystal structures of the **(a)** solvated HOF CPHATN-1(TCB) and **(b)** activated HOF CPHATN-1a. **(c)** Differences in cell parameters between CPHATN-1(TCB) and CPHATN-1a. **(d)** PXRD pattern changes of CPHATN-1a upon exposure to benzene vapor. **(e)** PXRD pattern changes of benzene-filled CPHATN-1a with temperature.

It is noteworthy that CPHATN-1a shows color changes upon exposure to HCl. Yellow crystalline bulk CPHATN-1a turned reddish-brown upon exposure to HCl atmosphere, and the original color was recovered by removing HCl from the framework (Fig. 3(a)). Similarly, the green fluorescence was quenched by HCl exposure and then recovered by HCl removal (Fig. 3(b)). These observations are consistent with spectroscopic results. When exposed to HCl, a new band at 500–600 nm appeared in the absorption spectrum (Fig. 3(c)) and the emission spectrum was strongly quenched (Fig. 3(d)). These results clearly indicate the sensitivity of this HOF to acid vapors, which is explained in terms of strong interactions of the protons of acid with the core of the fundamental unit.

In conclusion, we demonstrated, for the first time, that CPHATN can be a suitable building block for constructing acid-responsive porous crystalline materials. The crystal structure of CPHATN-1a and its dynamic behavior upon the sorption of guest molecules were precisely characterized by synchrotron X-ray radiation.

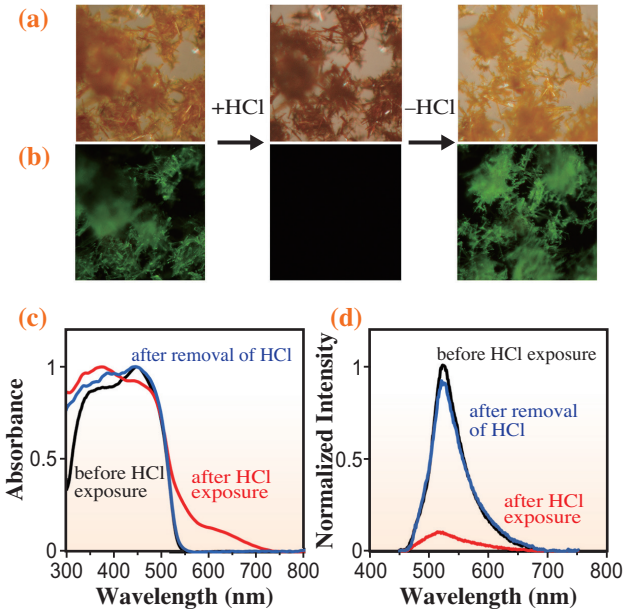

Fig. 3. HCl responsiveness of crystalline bulk of CPHATN-1a. Color changes of crystals upon exposure to HCl vapor under **(a)** ambient light and **(b)** UV light of 365 nm. **(c)** Absorption and **(d)** emission spectra of solid CPHATN-1a upon exposure to HCl atmosphere and after removal of HCl.

Ichiro Hisaki* and Yuto Suzuki

Graduate School of Engineering Science, Osaka University

*Email: hisaki@chem.es.osaka-u.ac.jp

References

[1] R.-B. Lin *et al.*: Chem. Soc Rev. **48** (2019) 1362.
[2] I. Hisaki *et al.*: J. Am. Chem. Soc. **138** (2016) 6617.
[3] I. Hisaki: J. Incl. Phenom. Macro. Chem. **96** (2020) 215.
[4] *I. Hisaki, Y. Suzuki, E. Gomez, Q. Ji, N. Tohnai, T. Nakamura, A. Douhal: J. Am. Chem. Soc.* ***141*** *(2019) 2111.*

Formation of large confined spherical space with small aperture using flexible hexa-substituted sumanene

As represented by Metal Organic Frameworks (MOFs) and Covalent Organic Framework (COFs), network compounds having pores are of great interest due to their high potential as functional materials in, for example, selective molecular sorption, separation, and catalytic reaction. Additionally, discrete caged materials are also of interest due to the unusual regioselectivity of the reactions within and the ability to trap large molecules such as proteins. In view of these properties, aperture (or open window) size of the pores or the cages strongly influence their utilizations. Especially, the ones with small aperture work as the useful molecular hosts to embed functional guests such as polyoxometalates, which eventually serve Lewis acidic heterogeneous catalytic ability. In addition, such porous materials with confined space are promising to protect the interactive species to enable unimolecular-analysis.

Sumanene (**1**) is one of the representative curved-π conjugated molecules, which possesses a partial structure of fullerene C_{60} (Fig. 1(a)) [1]. Its three-dimensionally curved structure has attracted the interest of many researchers and is also a promising building block for the preparation of porous materials. However, so far curved-π conjugated molecules exclusively formed non-porous layered network structures rather than with spherical pores despite their curved skeletons. This is strongly due to their intrinsic nature to easily stack each other. Meanwhile, **1** is known to show the dynamic bowl inversion, which requires the structural flexibility [2]. In addition, further structural flexibility at the peripheral moiety of sumanene skeleton is afforded by hexa-substitution of **1**, which also brings high structural symmetry [3]. Such properties of hexa-substituted sumanene give rise to the expectation that they will also meet the criteria for the formation of confined space by proper introduction of metal coordination.

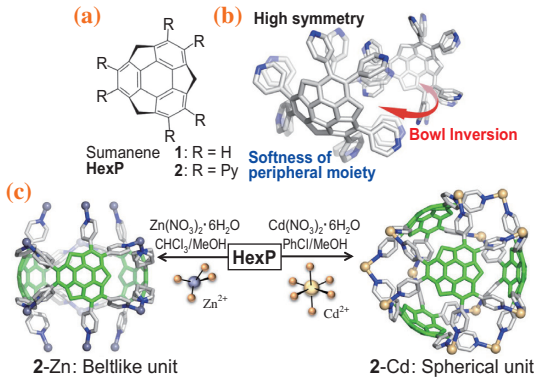

Fig. 1. **(a)** Molecular structures of sumanene **1** and **HexP 2**. **(b)** Structural features of hexa-substituted sumanene as the building block of spherical confined space. **(c)** Schematic models of the formation of **2**-Zn and **2**-Cd.

In this work, we show the preparation of porous coordination networks with effective use of the sumanene skeleton to form large confined space exclusively with small apertures (Fig. 1(b)) [4]. For the ligand, we used hexapyridylsumanene (**2**: **HexP**) having a γ-pyridyl group at the periphery of **1** [5]. The obtained network systems contained a belt-like trimer unit and a spherical tetramer unit, which beautifully reflected the curved structure of **1** skeleton, resulted in possessing large confined spaces with small open window.

Both of the single crystals of $[Zn_2\mathbf{2}Cl_2](NO_3^-)_n(solv)_m$ (**2**-Zn) and $[Cd_{1.5}\mathbf{2}(CH_3OH)(H_2O)_2](NO_3^-)_3(solv)_n$ (**2**-Cd) were prepared by layer diffusion method. X-ray diffraction data was obtained using SPring-8 **BL02B1** (for **2**-Zn) and **BL40XU** (for **2**-Cd). X-ray single crystal structure analysis revealed that **2**-Zn possessed a highly symmetrical packing pattern with a $P6_3/m$ space group reflecting the C_3 symmetric structure of **2**. All six pyridine moieties of the ligand **2** connected to Zn atoms having tetrahedral geometry with typical N-Zn^{2+} distances. The unique feature of this system is that large voids with the diameter of 10.3 Å, which can even hold C_{60}, were formed by the connection of three **HexP** moieties via total six Zn atoms forming the belt-like repeating units (Fig. 2(a)).

All Zn atoms had tetrahedral coordination geometry and the two bonds of the four were used for the formation of the belt-like repeating unit (Fig. 2(b)). The remaining two were used for the formation of Zn^{2+}-Cl bond and further connection among the belt-like units resulted in the three-dimensional network with the channels along the *c* axis, in which crystallin solvents and counter anions were severely disordered (Fig. 2(c)).

Meanwhile, highly symmetrical structure with $P4_2/n$ space group were confirmed for **2**-Cd crystal (Fig. 3). In the crystal structure, all six pyridine rings of **2** connected to Cd atom having octahedral geometry with typical N-Cd^{2+} distances. As a result of the combination of octahedral coordination environment of Cd^{2+} and the curved structure of **2**, the unique spherical repeating unit composed of four **HexP** ligands and 12 Cd atoms was formed instead of the belt-like unit found in **2**-Zn. The diameter of the spherical unit was 13.7 Å. The unit had two types of the open windows with different size of the apertures (Fig. 3(b), pink and light blue parts) and the inner space of the void was filled with severely disordered crystalline solvents as observed in **2**-Zn.

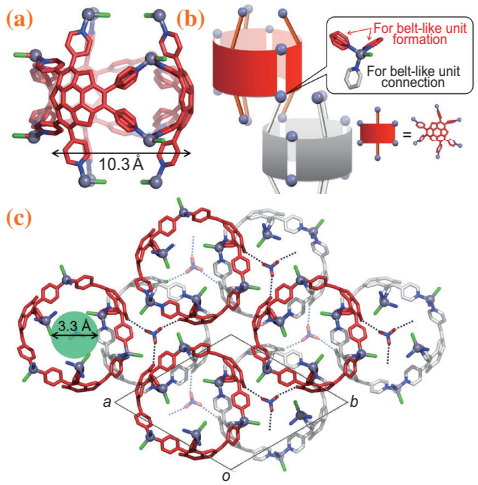

Fig. 2. **(a)** The belt-like trimer unit. **(b)** The schematic model of the connection mode between the two belt-like units in a unit cell viewed from the *a** axis. The red model is corresponding to the belt-like unit in figure (a). **(c)** the *c* axis projection of the packing pattern in **2**-Zn. The same colored units are in the same plane. Blue, N; pale blue, Zn; bright green, Cl. Hydrogen atoms and disordered molecules are omitted for clarity.

These apertures were covered by forming the packing structure to eventually construct 1D channel along the *c* axis with very small open window (2.1 Å×2.1 Å). This indicated that all the spherical units in the **2**-Cd network work as almost isolated spaces.

To Investigate the detailed structural information of **HexP** moiety in both of the networks, we focused on how the sumanene bowl structure changed and how the peripheral pyridine rings distorted (Fig. 4). In **2**-Zn, the sumanene bowl became deeper than the pristine one. On the other hand, sumanene bowl became shallower in **2**-Cd. In addition, the peripheral pyridine ring distortion in the networks were characteristic based on the packing structures. In **2**-Zn, two types of the tendencies were observed; the four pink-colored peripheral pyridine rings that contributed to the formation of the trimer unit distorted to the endo direction of the sumanene skeleton, while the remaining orange-colored peripheral pyridine rings involved in the formation of 1D channels went to the exo direction. Meanwhile, all the peripheral pyridine rings in **2**-Cd went to the exo direction of the sumanene bowl. These different structural parameters clearly indicated that **HexP** moiety in both of the porous networks provided high flexibility. Eventually, the central angles of the skeleton of **2** in **2**-Zn and **2**-Cd, which extends from the center of the hexagonal ring at the bottom of the sumanene skeleton to almost all the diagonal directions were nicely arranged to form 3D network structures with beautiful spherical components by coordinate both tetrahedral and octahedral metal ions (125.13°, 135.63° in **2**-Zn, 145.58°~149.26° in **2**-Cd).

These network materials having large confined spaces with small apertures might be useful to isolate the reactive species, which may facilitate the investigation of the properties of single molecule or the control of the assembled properties such as magnetism.

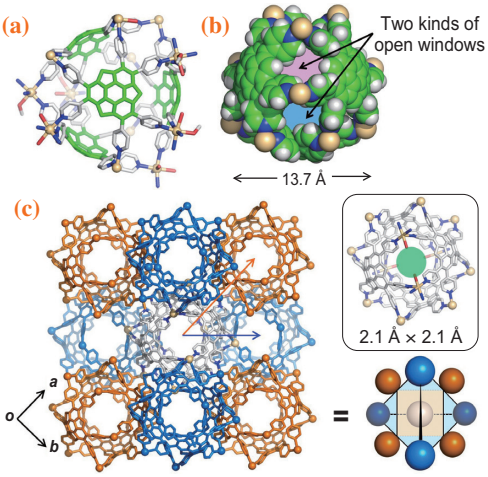

Fig. 3. **(a)** The spherical repeating unit. **(b)** Two types of open windows. Pink: surrounded by two Cd^{2+}s; Light blue: surrounded by three Cd^{2+}s. **(c)** The *c* axis projection of the packing structure in **2**-Cd. Marine blue and orange parts are corresponding to the same colored spheres in the inset model.

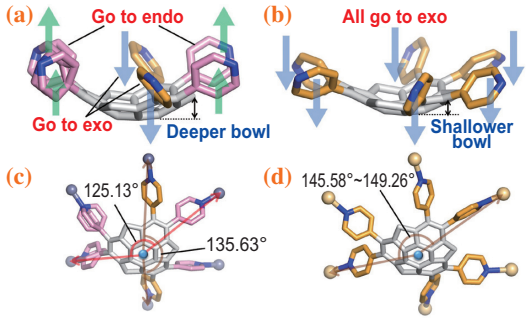

Fig. 4. **(a)** Peripheral distortion angles of the skeleton of **2** in **2**-Zn. **(b)** Peripheral distortion angles of the skeleton of **2** in **2**-Cd. **(c)** Central angles of the skeleton of **2** in **2**-Zn. **(d)** Central angles of the skeleton of **2** in **2**-Cd.

Yumi Yakiyama and Hidehiro Sakurai*

Graduate School of Engineering, Osaka University

*Email: hsakurai@chem.eng.osaka-u.ac.jp

References

[1] M. Saito *et al.*: Mater. Chem. Front. **2** (2018) 635.
[2] T. Amaya *et al.*: Chem. Commun. (2008) 765.
[3] I. Hisaki *et al.*: Angew. Chem. Int. Ed. **56** (2017) 15294.
[4] H. Toda *et al.*: Chem. Lett. **46** (2017) 1368.
[5] *Y. Yakiyama, T. Hasegawa, H. Sakurai: J. Am. Chem. Soc.* ***141*** *(2019) 18099.*

Tubular aggregate with hydrophilic interior formed by one-dimensional assembly of cyclic peptide amphiphile in nonpolar organic media

Peptide amphiphiles consisting of several amino acid residues and a long hydrocarbon chain have attracted much attention in biomedical applications, such as drug vehicles in drug delivery systems and scaffolds in tissue engineering, owing to the biological compatibility and properties endowed by self-assembled structures [1]. The self-assembled structures of peptide amphiphiles are generally determined by the sequences of amino acid residues, the corresponding secondary structures of the peptide chains, and the surrounding environment. In addition, if the molecular structure of a peptide amphiphile has a specific topology, e.g., a ring or branched structure, the self-assembled structure should reflect the molecular topology. Therefore, the unique self-assembled structure and related properties caused by topological features of peptide amphiphiles are of great interest.

Surfactin (SFNa), a cyclic peptide amphiphile produced by *Bacillus subtilis*, consists of a heptapeptide closed by a lactone bond with a β-hydroxy fatty acid (Fig. 1). It has been known that SFNa shows unique properties, e.g., the ability to decrease surface tension at extremely low concentrations of the order of 10^{-2} mM, monodisperse micelle formation, hemolytic activity, protease activity, antibacterial activity, and the ability to facilitate ion transport through lipid bilayer membranes [2]. These properties of SFNa are considered to originate from the cyclic topology of the peptide chain. For example, it has been found that the monodisperse *Platonic* micelle formation of SFNa is caused by the formation of regular polyhedra owing to the flat-on orientation of bulky peptide rings of SFNa at the hydrophobic-hydrophilic interface [3]. Among the unique properties of SFNa, the facilitation of ion transport through lipid bilayer membranes is of particular interest because of its potential application in functional membranes such as biomimetic ion transport membranes. The inner parts of lipid bilayer membranes are regarded as nonpolar hydrophobic media, and the self-assembly of SFNa in a nonpolar organic medium is the key to understanding the molecular mechanism of facilitated ion transport through such membranes. Thus, we investigated the self-assembled structures of SFNa in cyclohexane (CHx), which is a typical nonpolar organic solvent, to clarify the mechanism of this property of SFNa in a nonpolar organic medium.

In nonpolar organic media, the self-assembly of SFNa is driven by hydrogen bonds between peptide groups. Hydrogen bonds in SFNa are formed between different peptide rings owing to the restriction of the peptide rings of SFNa. Inevitably, SFNa assembles into fiber-like aggregates with unimolecular width owing to a one-dimensional arrangement through inter-ring hydrogen bonds. We observed thermo-reversible gelation in CHx solution of SFNa as a result of the formation of nanofibers (Fig. 2). Surprisingly, the SFNa gel and sol can dissolve a certain amount of water, although CHx negligibly dissolves water. This means that SFNa nanofibers include water. Because the ionic groups of SFNa are lipophobic, they are directed toward the inside of SFNa nanofibers to avoid contact with CHx. Therefore, SFNa nanofibers should form water channels. To elucidate the inside structure of the SFNa nanofibers, small-angle X-ray scattering (SAXS) measurements are performed. Figure 3(a) shows SAXS profiles of the SFNa gel and sol obtained at SPring-8 **BL40B2**. $I(q)$ exhibits q^{-1} dependence in the low q region assigned to nanofibers, where q is the magnitude of the scattering vector corresponding to the scattering angle. The solid lines in Fig. 3(a) were calculated using a core-shell cylinder model with the cross-sectional electron density profile shown in Fig. 3(b). Since the electron density inside the SFNa nanofiber is much lower than that of the outer shell, SFNa nanofibers are regarded as nanotubes. As mentioned above, ionic groups on SFNa rings are oriented toward the inside of nanotubes. This means that SFNa nanotubes have hydrophilic interiors. The added water therefore forms a channel through the SFNa nanotube shown in Fig. 3(c). The existence of the water channel in the SFNa nanotube is confirmed

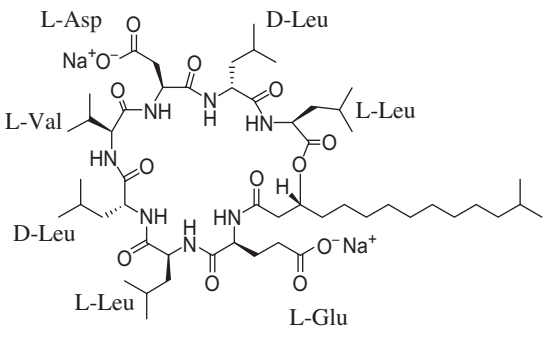

M. W. = 1080 g/mol

Fig. 1. Chemical structure of surfactin (SFNa).

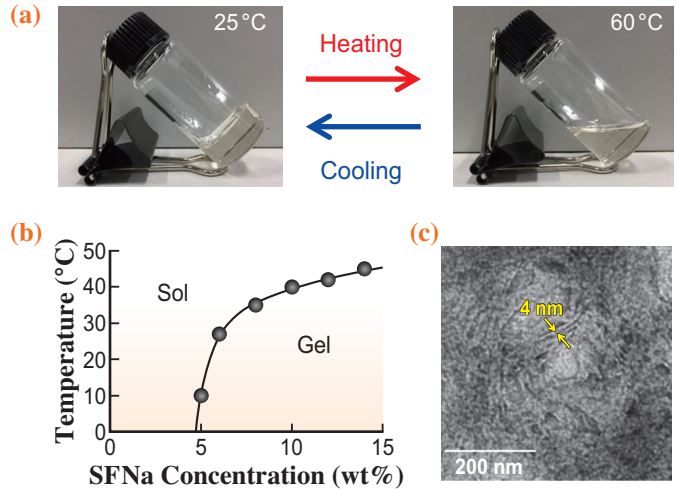

Fig. 2. Thermoreversible organogelation of SFNa in CHx: **(a)** photographs of CHx solution of SFNa at a concentration of 5.0 wt% at 25°C (left) and 60°C (right); **(b)** gel-to-sol transition temperature of SFNa gel; **(c)** TEM image of dried SFNa gel.

by the results of SAXS and small-angle neutron scattering. It has been known that SFNa enhances ion transport through lipid bilayer membranes. The inner parts of the lipid bilayer membranes are regarded as a nonpolar hydrophobic medium. SFNa should therefore form nanotubes with hydrophilic interiors in lipid membranes. The SFNa nanotubes penetrating the lipid membrane should act as ion channels and thus enhance ion transport through the membranes. Such an enhancement of ion transport through the lipid membranes as a result of the formation of ion channels is reminiscent of the relationship of actual biological phenomena. Therefore, we hope that this achievement will lead to the clarification of unsolved biological phenomena and the creation of novel biomimetic materials.

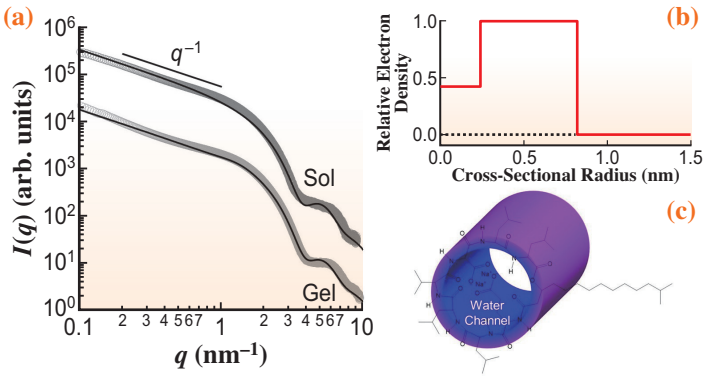

Fig. 3. Structural analysis of SFNa nanofiber: **(a)** SAXS profiles of SFNa sol and gel; **(b)** cross-sectional electron density profile of SFNa nanofiber; **(c)** schematic representation of SFNa nanotube with water channel.

Satoshi Kanazawa and Isamu Akiba*

Department of Chemistry and Biochemistry,
The University of Kitakyushu

*Email: akiba@kitakyu-u.ac.jp

References

[1] J.D. Hartgerink *et al.*: Science **294** (2001) 1684.
[2] *S. Kanazawa, K. Morimoto, E. Tabata, A. Okura, Y. Ikemoto, K. Yamamoto, L. de Campo, I. Akiba: Langmuir* ***36*** *(2020) 7627.*
[3] S. Fujii *et al.*: Sci. Rep. **7** (2017) 44494.

Unravelling the "transition-state" of the respiratory function

Ever since the end of the 19th century, light has been used to mimic and probe the detachment and rebinding of ligands to the Iron atom of the porphyrin in haem proteins, such as haemoglobin (Hb) and myoglobin (Mb). Haemoglobin is a tetramer (Fig. 1(a)) of four myoglobin-like (Fig. 1(b)) units. The most important ligand for respiration is of course molecular oxygen, but Mb and Hb can also bind small ligands such as CO, NO, H_2O, CN, etc., which confer them different biological functions. For example, NO is well-known for neurotransmission, regulation of vasodilatation, platelet aggregation, and immune response in our organism.

The process of ligand binding and release is accompanied by a significant structural and electronic change of the haem porphyrin. It is well established since the works of Pauling *et al.*, that when the ligand is bound, the porphyrin (Fig. 1(c)) is in a low spin (LS) state (Fig. 1(d)) and is planar, while without ligand (the so-called deoxy form), the porphyrin is in a high spin (HS) state and is domed with the Fe atom moving out of the porphyrin plane on the proximal side (Fig. 1(c)). This in-and-out motion of the Fe atom is the trigger of large-scale motions of the entire protein, which lead to the so-called tense (S) and relaxed (R) state of haemoglobin that is essential in respiration.

With the birth of femtosecond (fs) spectroscopy in the 1980s, the first systems to be investigated were actually haem proteins with the aim to describe in "real-time" the process of ligand detachment and possibly, its recombination to the haem [1]. The methods used were pump-probe spectroscopy in the infrared and visible range [2], or time-resolved resonance Raman spectroscopy [3]. More recently, picosecond [4] and fs [5] X-ray absorption spectroscopy (XAS) were also implemented. The focus of these studies was the initial events after excitation of the haem (into the π-π^* transitions of the porphyrin) and ligand detachment, and how the system reaches the HS deoxy state. After nearly thirty years of experiments, two main interpretations have prevailed: a) formation of the HS state goes via a cascade through different electronic states [6] or; b) the excited system decays directly into the HS ground state of the deoxy form, which then undergoes vibrational cooling [2]. The first hypothesis does not exclude vibrational relaxation within the electronic states. The main difficulty in this debate stems from the fact that none of the used optical spectroscopic probes is sensitive to the electronic structure.

In order to solve this issue, we implemented femtosecond Fe K_α and K_β X-ray emission

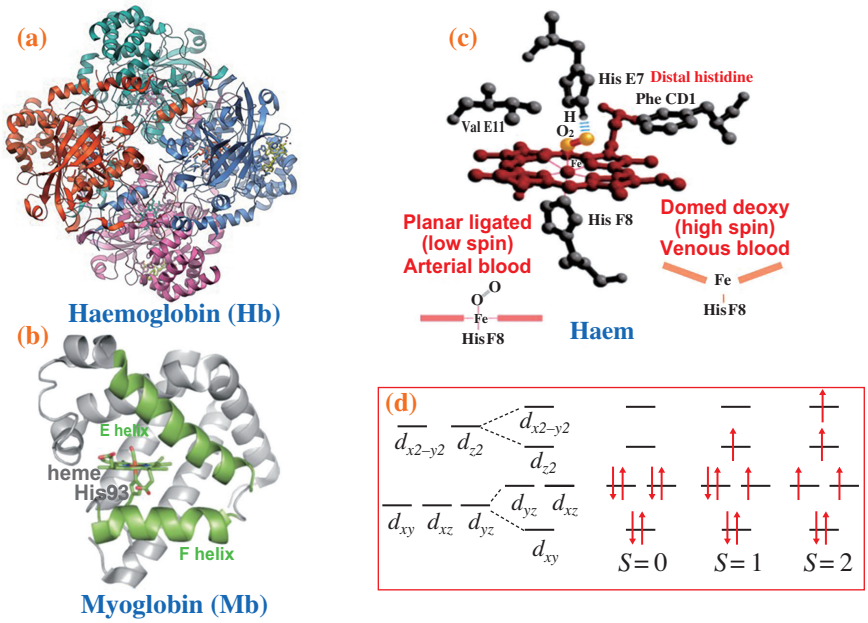

Fig. 1. **(a)** Haemoglobin with its four myoglobin-like **(b)** units. **(c)** Haem Iron-porphyrin with a ligand on the distal side and a histidine (His93, see also (b)) on the proximal side, which anchors the haem to the rest of the protein scaffold via the F-helix. **(d)** Occupancy of Fe 3*d*-orbitals that are split by the ligand-field between bonding (d_{xy}, d_{yz}, d_{xz}) and antibonding (d_{x2-y2}, d_{z2}) orbitals, for the different spin states of a ferrous haem.

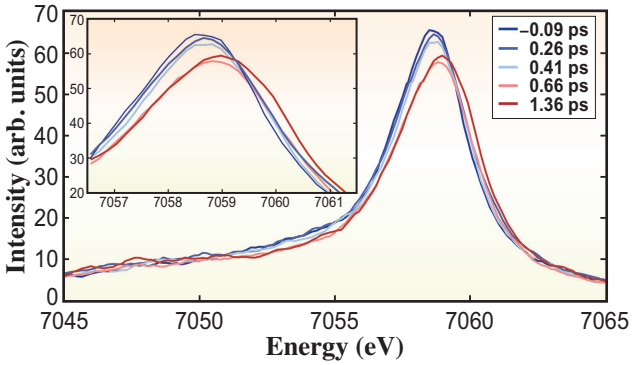

Fig. 2. Laser-off (unpumped) and Laser-on (pumped) K_β XES spectra of MbNO at different time delays between –0.09 and 1.36 ps (from blue to red) showing a blue shift of the $K_{\beta1,3}$ line and an intensity decrease. The inset zooms into the region of the maximum of $K_{\beta1,3}$ XES line showing peak shifts smaller than the energy resolution (~0.5 eV) of our experiment.

spectroscopy (fs-XES) and fs-XAS in the study of myoglobin-NO (MbNO). The choice of fs-XES is motivated by its well-established sensitivity to spin states, and the choice of MbNO is motivated by the fact that the detachment-recombination cycle takes place in ~200 ps, while all other Myoglobins have either very long (MbCO) or very short (MbCN, MbH_2O, MbO_2) cycles. Fs-XAS helps probe the structural changes [7]. Figure 2 shows a series of laser-off and laser-on K_β XES spectra at various time delays. The shift of these lines reflects the changes undergone by the system between its LS planar form and its HS domed form. The temporal evolution of the K_β line shift and the K_α line width reflects the same processes and shows a rise time of ~700 fs, followed by a biexponential decay of 30 ps and >1 ns [8]. These time scales reflect changes in the spin state of the system and cannot be attributed to thermal effects, which do not affect the XES lines. Combining these data, with our previous ultrafast optical [9], ps XAS [4] studies and the resonance Raman studies by Kruglik *et al.* [3], we deduce the scheme that is shown in Fig. 3: a) upon photoexcitation of the haem, NO dissociation is prompt and simultaneous to the passage into an intermediate spin state ($S = 1$). This first event occurs in <100 fs; b) it is followed by a relaxation to the HS ($S = 2$) state in ~600–800 fs, which leads to formation of a deoxyMb ground state; c) the rebinding of NO takes places in a bimodal mode of a few ps (for ligands in the haem pocket) and 150–200 ps for ligands that have escaped the pocket. Contrary to other ligands, NO can bind to deoxyMb and the subsequent relaxation back to a planar LS MbNO takes place in ~30 ps. Thus, the whole cycle from ligand detachment to its rebinding and reformation of a planar MbNO is a sequence of spin cross-over (SCO) and reverse SCO. It should be stressed that steps (a) and (b) are common to all Mb's undergoing ligand detachment. Only step (c) is ligand specific. Because the initial events of ligand detachment and relaxation to the deoxy form are crucial for the subsequent processes they can be considered the "transition state" of the respiratory function. However, a recent study on ferric Cytochrome c [10] shows that such spin transitions also occur in non-respiratory proteins, which calls for elucidation of their role in such systems. This work was performed at SACLA **BL3**.

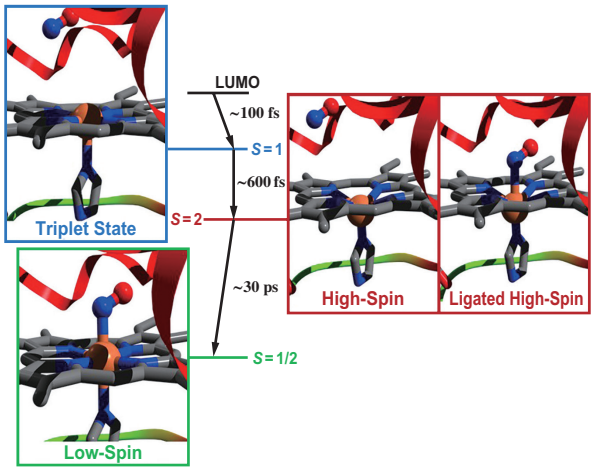

Fig. 3. Photocycle of MbNO as deduced for Ref. 8. Excitation of the Q-band of the porphyrin (π-π^* transition) leads to a prompt dissociation of NO and formation of the intermediate $S=1$ state of the deoxyMb pentacoordinated haem. This state then decays to the high spin $S=2$ state, which returns to the initial low spin state in ~30 ps after rebinding the NO ligand.

Majed Chergui

Lausanne Centre for Ultrafast Science (LACUS), EPF-Lausanne, Switzerland

Email: Majed.Chergui@epfl.ch

References

[1] J.L. Martin & M.H. Vos: Ann. Rev. Biophys. and Biomol. Struct. **21** (1992) 199.
[2] X. Ye *et al.*: J. Phys. Chem. A **107** (2003) 8156.
[3] S.G. Kruglik *et al.*: Proc. Natl. Acad. Sci. USA **107** (2010) 13678.
[4] M. Silatani *et al.*: Proc. Natl. Acad. Sci. USA **112** (2015) 12922.
[5] M. Levantino *et al.*: Struct. Dynamics 2 (2015) 041713.
[6] J.W. Petrich *et al.*: Biochemistry **27** (1988) 4049.
[7] C. Bacellar *et al.*: Faraday Discuss. (2021) doi:10.1039/D0FD00131G.
[8] D. Kinschel *et al.*: Nat. Commun. **11** (2020) 4145.
[9] O. Bräm *et al.*: J. Phys. Chem. A **123** (2019) 1461.
[10] C. Bacellar *et al.*: Proc. Natl. Acad. Sci. USA **117** (2020) 21914.

Mechanistic investigation of chromium-chloride-promoted formation of dioxins by *in situ* XAFS

Ever since the discovery of polychlorinated dibenzo-p-dioxins and dibenzofurans (PCDD/F), or, in brief dioxins, in emissions from municipal solid waste incineration (MSWI), numerous endeavors have been launched for determining their mechanisms of formation. The catalytic formation of PCDD/F requires specific metal ions as catalysts [1]. Chromium is widely contained in municipal solid wastes and is commonly used in MSWI superheater metal alloys. Although present in fly ash in concentrations comparable to that of the strongest catalyst, copper, chromium has been less investigated regarding its influence and role during dioxin formation. X-ray absorption fine structure (XAFS) spectroscopy is one of the best-known techniques for determining the chemical forms of the target element. *In situ* XAFS spectroscopy enables the measurements of XAFS spectra of target elements only during the thermochemical reaction process without altering the original conditions of the test. A combination of both *in situ* and *ex situ* XAFS techniques has been applied to elucidating the formation mechanisms of chlorinated aromatics from MSWI model fly ash (MFA) catalyzed by the metals Cu, Fe, Zn and Pb [1-4]. In this study, the *in situ* XAFS technique was used to investigate the reaction mechanisms of PCDD/F formation promoted by Cr compounds [5].

Firstly, model fly ash (MFA_1) doped with chromium chloride ($CrCl_3·6H_2O$, 0.2wt% Cr; activated carbon, 3wt%; NaCl, 10wt% Cl; SiO_2, remainder) was heated over a wide range of temperatures to confirm the effects of $CrCl_3$ on PCDD/F formation (Fig. 1). MFA_1 was heated in a tubular furnace for 60 min at each temperature except for 120 min at 250°C in a gas stream of 10% O_2 + 90% N_2 and the resulting PCDD/F were collected and analyzed. A blank MFA_1 without the addition of $CrCl_3·6H_2O$ was also tested at 350°C. Both PCDD and PCDF yields were highest at 350°C, being 16.4 ng PCDD/g and 217 ng PCDF/g, attaining factors of 9.7 (PCDD) and 17.9 (PCDF) compared with those of the blank MFA_1. This result confirmed the appreciable promoting effect of $CrCl_3$ on the formation of PCDD/F.

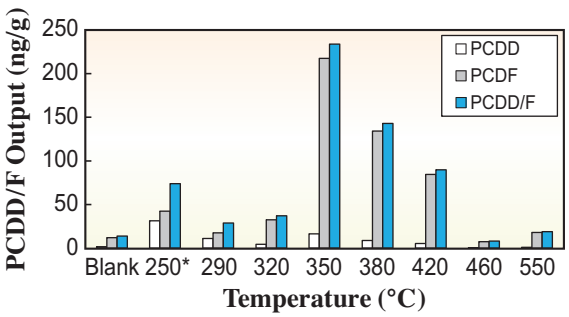

Fig. 1. Formation of PCDD, PCDF, and PCDD/F (ng/g) as a function of temperature at 10% oxygen. *MFA_1 at 250°C was heated for 120 min.

The dynamic changes in the chemical states of chromium and chlorine were detected by *in situ* Cr *K*-edge XAFS at SPring-8 **BL01B1** and *in situ* Cl *K*-edge X-ray absorption near edge structure (XANES) at BL-9A in Photon Factory, respectively. The MFA used for XAFS measurements (MFA_2) consisted of activated carbon, $CrCl_3·6H_2O$, and boron nitride (BN), with BN constituting 80% and the remaining 20% being composed of activated carbon and $CrCl_3·6H_2O$ in the same weight ratio as in MFA_1. MFA_2 was heated in an *in situ* cell in a gas stream with 10% O_2 (+90% N_2 for Cr-XAFS; +90% He for Cl-XANES) from room temperature (RT) to 550°C at a rate of 5°C/min. During heating, the temperature was successively sustained at eight stages (250, 290, 320, 350, 380, 420, 460 and 550°C) for measuring Cr-XAFS and Cl-XANES spectra.

As the temperature increased from RT to 550°C, most changes in the Cr *K*-edge XANES spectra were observed in the pre-edge region (–3 to 9 eV from the Cr *K*-edge position at 5989 eV Fig. 2(a)). The pre-edge region of the spectrum at RT featured only one weak peak at ~5989 eV, similar to the spectrum of the $CrCl_3·6H_2O$ standard. A second peak at around 5992 eV emerged at 250°C, grew with increasing temperature, slightly decreased at 350°C, peaked at 380°C, and then rapidly declined, finally to the level of Cr_2O_3 (Fig. 2(a)). The appearance of this peak suggests that the $CrCl_3$ in MFA_2 was oxidized to Cr_2O_3 and even to Cr(VI)-O during heating. The fraction of Cr(VI) in Cr was estimated by peak fitting in the pre-edge region (Fig. 2(a)). The analysis of Cr *K*-edge EXAFS data (Fig. 2(b)) further confirms the results of Cr-XANES. The peak at ~1.6 Å (denoted as Peak 1) is mainly attributed to the Cr(III)-O bond, while the second peak at ~2.5 Å (denoted as Peak 2) arises from Cr–Cr scattering. As temperature increased, Peak 1 initially dropped owing to the dehydration of chromium chloride hydrate and subsequently increased owing to oxidation to Cr_2O_3. With increasing temperature, Peak 2 exhibited an increasing trend, providing further proof of the gradual formation of Cr_2O_3.

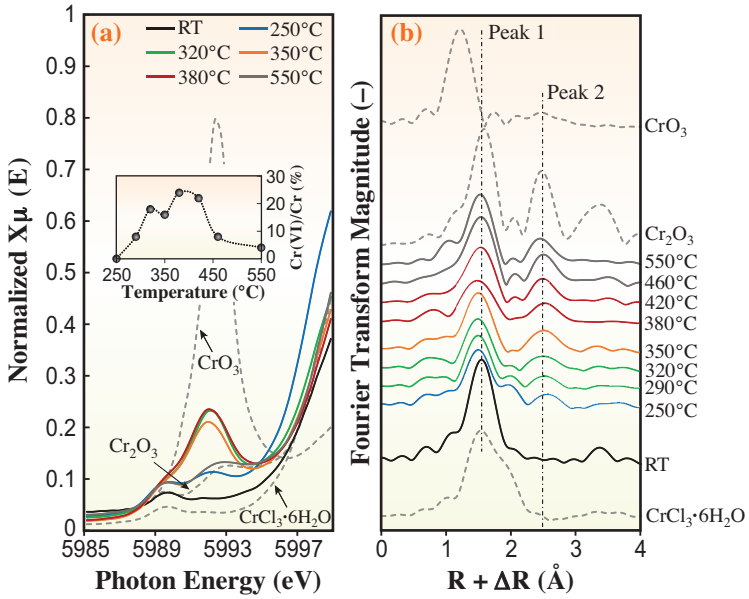

Fig. 2. Pre-edge region of Cr *K*-edge XANES spectra of MFA_2 during the temperature increase and of reference standards **(a)**. Fourier transform of k^3-weighted Cr *K*-edge EXAFS spectra as a function of temperature **(b)**.

The dynamic changes of chlorine species were observed in *in situ* Cl *K*-edge XANES spectra (only RT to 350°C owing to the indiscernibility of higher-temperature spectra) and an *ex situ* spectrum measured from MFA_2 heated at 460°C for 60 min (Fig. 3). As temperature increased a peak at around 2821 eV, a typical feature of chlorine connected to carbon (Cl to aliphatic carbon, aliphatic-Cl: 2820.6 eV; Cl to aromatic carbon, aromatic-Cl: 2821.1–2821.3 eV), occurred and gradually increased. Ratios of different Cl species (%) in MFA_2 were estimated by linear combination fitting. The conversion of Cl in $CrCl_3$ to that bound to carbon (Fig. 3) occurred simultaneously with the oxidation of $CrCl_3$ (Fig. 2), providing direct evidence for carbon chlorination through $CrCl_3$ oxidation and dechlorination.

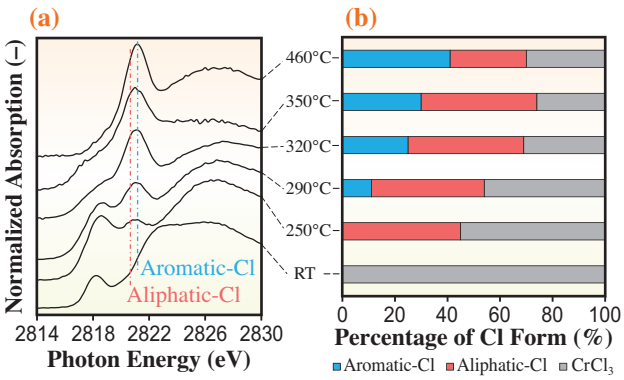

Fig. 3. Cl *K*-edge XANES spectra of MFA_2 during the temperature increase **(a)** and the percentage of Cl species as a function of temperature **(b)**.

Overall, chromium compounds play two key roles during dioxin formation: the chlorination of carbon by the chlorine derived from the oxidation of $CrCl_3$ to Cr_2O_3 and to Cr(VI)-O, and facilitating the oxidative destruction of the carbon matrix by the reduction of Cr(VI)-O as well as the end-product Cr_2O_3. As a result, chloro-aromatic compounds including PCDD/F are generated. The XAFS technique provides visual evidence of the invisible chemical reactions and proves to be a very useful tool for understanding the mechanistic aspects in various thermochemical processes.

Mengmei Zhang, Takashi Fujimori* and Masaki Takaoka

Department of Environmental Engineering,
Kyoto University

*Email: fujimori.takashi.3e@kyoto-u.ac.jp

References

[1] M. Takaoka *et al.*: Environ. Sci. Technol. **39** (2005) 5878.
[2] T. Fujimori *et al.*: Environ. Sci. Technol. **44** (2010) 1974.
[3] T. Fujimori *et al.*: Environ. Sci. Technol. **45** (2011) 7678.
[4] T. Fujimori *et al.*: Environ. Sci. Technol. **47** (2013) 2169.
[5] *M. Zhang, T. Fujimori, K. Shiota, A. Buekens, K. Mukai, Y. Niwa, X. Li, M. Takaoka: J. Hazard. Mater. (2020) 122064.*

Characterization of two types of cesium-bearing microparticle (CsMP) emitted from the Fukushima nuclear power plant accident using multiple synchrotron radiation analyses

On March 11, 2011, a great earthquake hit the eastern part of mainland Japan and triggered several gigantic tsunami waves that attacked the six-unit Fukushima Daiichi Nuclear Power Plant (FDNPP). The tsunamis damaged the electric functions to cool reactor cores and rapidly increased the temperature in the primary containment vessels, finally resulting in accidents in Units 1–3. As a result, large amounts of radionuclides in the nuclear reactors of FDNPP were released into the environment [1]. Ten years after the accident, the internal conditions of these units are still unknown.

Some of the radiocesium (Cs) emitted by the Fukushima nuclear accident was incorporated in Cs-bearing microparticles (CsMPs) mainly consisting of silica (SiO_2) [2]. There have been mainly two types of CsMP found thus far. One is called Type-A CsMP, which is spherical with a diameter of ~0.1–10 μm and ~10^{-2}–10^{2} Bq ^{137}Cs radioactivity per particle, and was emitted from Unit 2 or 3 of FDNPP. In contrast, Type-B CsMP has various shapes of 50–400 μm diameter and 10^{1}–10^{4} ^{137}Cs (Bq/particle), and was emitted from Unit 1. The chemical properties of these radioactive particles have been reported in detail, but in the previous studies, only a small number of particles were investigated especially in the case of Type-B CsMPs. In this study, we endeavored to understand the radioactive particles systematically by analyzing a large number of particles [3]. In particular, micro-X-ray computed tomography (X-ray μ-CT) combined with X-ray fluorescence (XRF) analysis played an important role in analyzing these samples because of the presence of many voids and an iron (Fe)-rich part within the Type-B CsMPs [3].

As for CsMPs, road dust samples and other materials were collected at more than 100 sites within 50 km of FDNPP during 2011-2012. Sixty-seven CsMP samples were isolated in three steps [3]. First, the spatial distribution of radioactive Cs in the samples was measured by autoradiography with imaging plates to identify CsMPs. Second, the wet separation method [4-6] was employed to isolate CsMPs from the samples containing CsMPs. After the isolation, the CsMP in water used for the separation was carefully dropped on Kapton tape and air-dried for scanning electron microscopy (SEM) with energy-dispersive spectrometer (EDS) analysis to finally identify CsMPs on the basis of shape and elemental composition. For Type-B CsMPs, X-ray μ-CT analysis was conducted at SPring-8 **BL37XU** [3]. We could acquire projection images at different angles that included information on the inner structure. Element maps were also generated by observing the difference between the pre-edge and post-edge energies of the element. In this study, projections below and above Fe and zinc (Zn) *K*-edges were recorded to obtain Fe and Zn maps. For the Type-B CsMPs, 2D μ-XRF measurement for various elements was conducted at BL-4A of the Photon Factory, KEK.

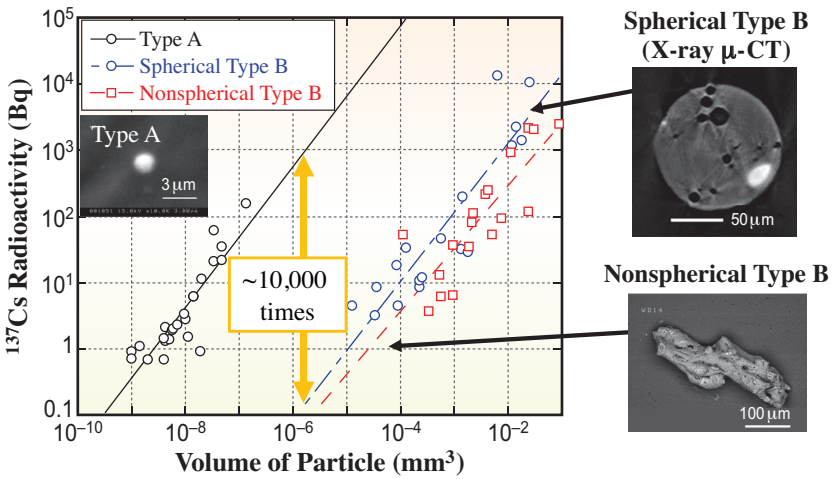

Fig. 1. Relationship between ^{137}Cs radioactivity and volume of each CsMP with X-ray μ-CT image for spherical Type-B CsMP.

X-ray μ-CT results for Type-B CsMPs show a number of voids in their structures possibly related to gas release during their cooling processes. A CT image for one sample of Type-B CsMP is shown in Fig. 1. White areas in the CT image absorbed X-rays to a greater degree than the matrix area, reflecting the presence of heavy elements in Type-B CsMPs. Although it is difficult to determine the volume of Type-B CsMPs from the external shape, X-ray μ-CT analysis enabled us to accurately calculate the volume of internal voids. On the other hand, the volume of Type-A CsMPs was calculated from the apparent diameter, since we can assume a spherical shape on the basis of transmission electron microscopy (TEM) observations reported thus far [2]. Figure 1 shows the relationship between ^{137}Cs radioactivity and volume for Types-A and -B CsMPs. As a result, the ^{137}Cs concentration per volume (Bq/mm^3) of Type-A CsMPs was ~10,000 times higher than that of Type-B CsMPs. Among the Type-B CsMPs, the spherical ones had higher concentrations of volatile elements such as ^{137}Cs than the nonspherical ones. These differences suggest that Type-A CsMPs were formed through gas condensation, whereas Type-B CsMPs were formed through melt solidification. It is expected that (i) the ^{137}Cs concentration per volume of Type-A CsMP will be higher than that of Type-B CsMP, and (ii) that of spherical Type-B CsMP will be higher than that of nonspherical Type-B CsMP, since ^{137}Cs in Type-B CsMP is diluted by structural materials to a greater degree, particularly in nonspherical Type-B CsMP. These differences reflect the genetic processes of Type-A and two types of Type-B CsMPs.

To support the hypothesis, μ-XRF analysis was conducted particularly for rubidium (Rb) and strontium (Sr), since their X-ray fluorescence lines (Rb, Kα_1: 13.4 keV; Sr, Kα_1: 14.1 keV) were at high energies, which are not subject to the self-absorption effect. Since the matrix of CsMPs is SiO_2, the attenuation length was larger than 500 μm at X-ray energies above 13 keV. Therefore, Rb and Sr with high-energy XRF, which also represented volatile and refractory elements, respectively, were selected for the analysis. As expected from the volatility of these elements, spherical Type-B CsMPs had a higher Rb/Sr ratio than nonspherical Type-B CsMPs (Fig. 2). The Rb/Sr ratio in the spherical Type-B CsMPs increased with ^{137}Cs concentration, showing that spherical Type-B CsMPs have a higher concentration of volatile elements, including Cs, than nonspherical Type-B CsMPs. Similar results were also found for antimony-125 (^{125}Sb), another volatile radionuclide emitted from FDNPP.

Consequently, this study provided chemical and morphological characteristics of 67 CsMPs, the number of which is larger than in previous CsMP studies, which usually dealt with less than 10 particles. In addition, systematic variations found in the relationships of ^{137}Cs radioactivity with the (i) volume of CsMPs, (ii) porosity, (iii) Rb/Sr ratio, and (iv) ^{125}Sb activity allowed us to present some ideas regarding the formation and emission of CsMPs: (i) the condensation of gaseous species and melt solidification are the main processes for Types-A and -B CsMPs, respectively, and (ii) spherical particles had higher ^{137}Cs and ^{125}Sb concentrations and Rb/Sr ratios than nonspherical particles, possibly owing to the rapid cooling process, which inhibits the loss of volatile species during cooling.

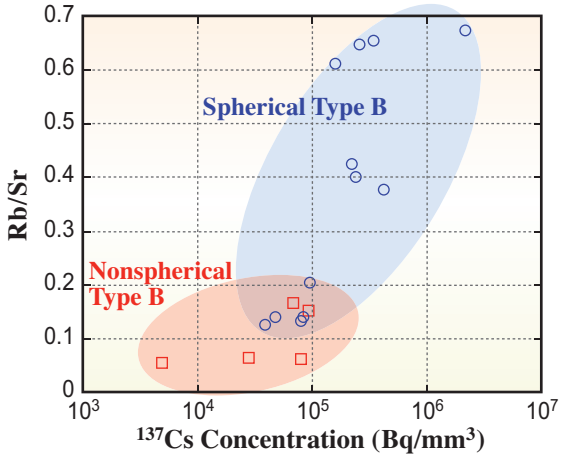

Fig. 2. Relationship between ^{137}Cs concentration and XRF intensity ratio of Rb/Sr for each CsMP.

Hikaru Miura[a] and Yoshio Takahashi[b,*]

[a] Atmospheric and Marine Environmental Sector, Central Research Institute of Electric Power Industry
[b] Department of Earth and Planetary Science, The University of Tokyo

*Email: ytakaha@eps.s.u-tokyo.ac.jp

References

[1] N. Yoshida and Y. Takahashi: Elements **8** (2012) 201.
[2] Y. Igarashi *et al.*: J. Environ. Radioactivity **205** (2019) 101.
[3] *H. Miura, Y. Kurihara, M. Yamamoto, A. Sakaguchi, N. Yamaguchi, O. Sekizawa, K. Nitta, S. Higaki, D. Tsumune, T. Itai and Y. Takahashi: Sci. Rep.* ***10*** *(2020) 11421.*
[4] H. Miura *et al.*: Geochem. J. **52** (2018) 145.
[5] Y. Kurihara *et al.*: Sci. Rep. **10** (2020) 3181.
[6] H. Miura *et al.*: Sci. Rep. **11** (2021) 5664.

Equation of state of liquid iron under extreme conditions

Iron is the sixth most abundant element in the universe and the main component of metallic cores of planets including Earth, Mars, Mercury, and likely some terrestrial planets outside of our solar system (so-called super-Earths). The Earth's core is considered to be composed mainly of iron but includes substantial amounts of lighter elements, particularly in its liquid outer part. The identification of core light elements is of great importance because it has wide implications, for example, for the Earth's building blocks, core formation process, thermal structure, and mechanism of core convection and geodynamo that generates the Earth's magnetic field. Since the properties of the liquid outer core that can be directly determined are the density ρ and longitudinal sound velocity V_P (equivalent to the bulk sound velocity V_Φ in a liquid), which are derived from seismic observations, laboratory measurements of these properties at high pressures are necessary to understand Earth's and other planets' core composition and behavior.

Although the density of crystalline materials under high pressure and temperature (P–T) conditions has been extensively studied experimentally by *in situ* X-ray diffraction (XRD), such study is still challenging for disordered materials. Although XRD can potentially be applied up to 100 GPa and high temperature, analytical methods for extracting ρ from a diffuse XRD signal, which is characteristic of a disordered material, have not been well established. In particular, no density measurement for liquid pure iron under static compression has been performed because of experimental difficulties arising from its high melting temperature at high pressures. V_P is also a key property in understanding the liquid behavior at high pressures as it is related to properties such as compressibility, thermal expansivity, and the Grüneisen parameter γ. Although V_P of liquid iron was previously determined up to 5.8 GPa by ultrasonic measurements in a Kawai-type multi-anvil apparatus, this is much lower than the pressure conditions of the Earth's core. Furthermore, the structure of liquid iron may possibly be different above 6 GPa. Thus, measurements at higher pressures are required to understand the nature of the core. Although only shock-wave compression experiments previously yielded measurements of ρ and V_P of liquid iron at high pressures between 278 and 397 GPa [1,2], it is impossible to conduct experiments on liquid iron at lower pressures via shock experiments, since the shock compression can generate high P–T only along the Hugoniot path which crosses the melting curve of iron at 270 GPa.

In this study, we measured ρ of liquid pure iron at high pressures for the first time via static compression using laser-heated diamond-anvil cell (LH-DAC) techniques [3]. The measurements were performed up to 116 GPa and 4350 K. This is close to conditions in the top region of the Earth's core. We measured angle-dispersive X-ray diffraction (XRD) spectra using a highly focused, brilliant X-ray beam at SPring-8 **BL10XU**. Strong diffuse scattering signals from liquid iron were found in the XRD spectra obtained at about 100–400 K above its melting point. After background subtraction, the result was converted into the structure factor $S(Q)$, where Q is the momentum transfer. Fourier transform of $S(Q)$ yielded the reduced pair distribution function $F(r)$ and the pair distribution function $g(r)$ (r, radial distance) (Fig. 1). The density of the liquid can, in principle, be determined from the slope of $F(r)$ for r smaller than the interatomic spacing. However, it has been considered that the conventional technique of analyzing the diffuse signals gives a liquid density with uncertainty exceeding 10%. To overcome this problem, we developed a new analytical method for deriving ρ from the diffuse X-ray scattering signal, in which the observed $S(Q)$ is extended beyond Q_{max} (the maximum Q in experimental data) so that the corresponding $g(r)$ is physically reasonable; no atom exists within the distance between the nearest-neighbor atoms. This is the key to the precise determination of liquid density under pressure. We

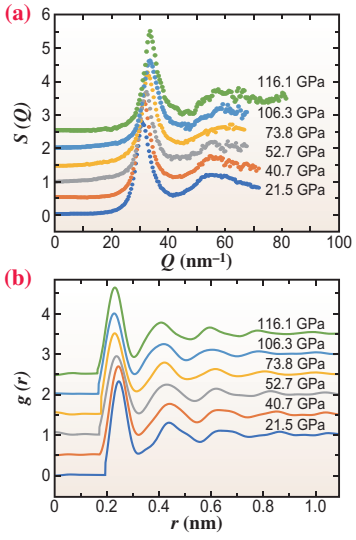

Fig. 1. **(a)** Structure factor $S(Q)$ of liquid iron up to 116.1 GPa. **(b)** Corresponding radial distribution function $g(r)$ determined in this study.

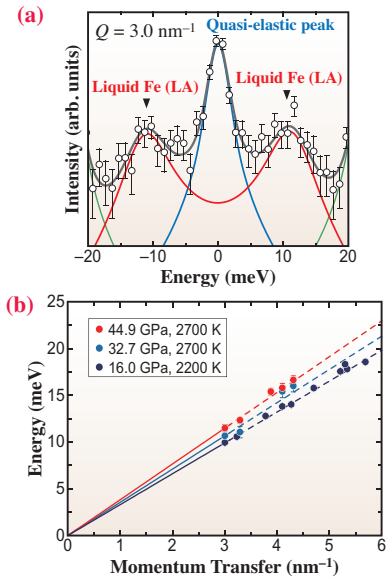

Fig. 2. **(a)** Typical IXS spectrum of liquid iron collected at 44.9 GPa and 2700 K at momentum transfer $Q = 3.0$ nm^{-1}. **(b)** Longitudinal acoustic phonon dispersion of liquid iron at pressures from 16.0 to 44.9 GPa.

verified the new method by analyzing 1) the XRD data previously collected for a Ce-based metallic glass ($Ce_{70}Al_{10}Ni_{10}Cu_{10}$) and 2) a synthetic XRD pattern, and found that the new analytical method is universally applicable to density determinations of amorphous materials.

We also determined V_P of liquid iron up to 45 GPa by inelastic X-ray scattering (IXS) measurements in the LH-DAC at SPring-8 **BL43LXU**. The experimental temperature was determined from the thermal radiation from the sample, as in the XRD experiments. The IXS spectra of liquid iron included three peaks in the present scanned energy range: Stokes and anti-Stokes components of the longitudinal acoustic phonon mode from the sample, and a quasi-elastic contribution near zero energy transfer (Fig. 2). V_P of liquid iron was determined using dispersion relations.

Now we have both P–T–ρ and P–T–V_P data for liquid iron from the present experiments, in addition to the P–ρ–V_P–γ relation (γ, Grüneisen parameter) from previous shock experiments [1,2]. From these data, we obtain the P–T–ρ–V_P–γ relation for the Earth's entire outer core conditions (136–330 GPa and 4000–5400 K) using the Mie-Grüneisen equation of state (EoS). To compare the liquid iron properties with seismological observations [4], we calculated the isentropic T profiles considering three different model temperatures at the liquid/solid core boundary (inner core boundary, ICB) (T_{ICB} = 5000 K, 5400 K, and 5800 K) (Fig. 3). Compared with ρ and V_P of liquid iron calculated along the isentrope with T_{ICB} = 5400 K, the Earth's liquid outer core exhibits ρ lower by 0.99–0.81 g/cm^3 (7.5–7.6%) and V_P higher by 0.43–0.29 km/s (4.3–3.7%). Our results also show that liquid iron is less dense than solid hexagonal-close-packed (hcp) iron by $\Delta\rho_{melting} = 0.32$ g/cm^3 at 330 GPa and its melting point of 6230 K [5]. This is only half of the seismologically observed density difference between the liquid outer and solid inner cores at the ICB, indicating a compositional difference between the outer and inner cores. With the knowledge of the phase diagrams of iron alloys, our results show that the oxygen concentration in the outer core is limited to 1.6–3.8 wt%, although it has been repeatedly suggested to be the main core light element, indicating that the core should include other impurity elements.

We determined the EoS of liquid iron that is applicable to all core conditions. This will serve as an important baseline for understanding the composition and behavior of the Earth's core.

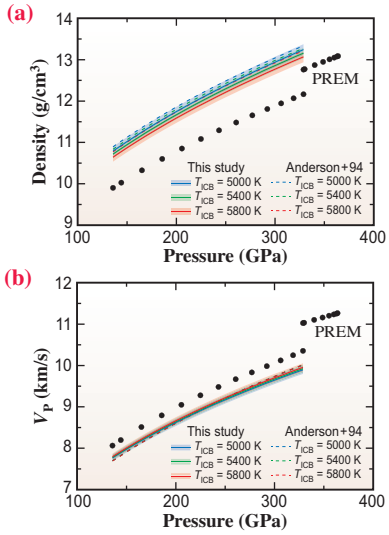

Fig. 3. Seismic observations (black circles, PREM [4]) and ρ, V_P, and K_S of liquid Fe under core pressures along the isentropic temperature profiles with T_{ICB} = 5800 K (red), 5400 K (green), and 5000 K (blue).

Yasuhiro Kuwayama[a,*] and Kei Hirose[a,b]

[a] Department of Earth and Planetary Science, The University of Tokyo
[b] Earth-Life Science Institute, Tokyo Institute of Technology

*Email: kuwayama@eps.s.u-tokyo.ac.jp

References

[1] J.M. Brown and G. McQueen: J. Geophys. Res. **91** (1986) 7485.
[2] W.W. Anderson and T.J. Ahrens: J. Geophys. Res. Solid Earth **99** (1994) 4273.
[3] *Y. Kuwayama, G. Morard, Y. Nakajima, K. Hirose, A. Q.R. Baron, S.I. Kawaguchi, T. Tsuchiya, D. Ishikawa, N. Hirao and Y. Ohishi: Phys. Rev. Lett.* ***124*** *(2020) 165701.*
[4] A.M. Dziewonski and D.L. Anderson: Phys. Earth Planet. Inter. **25** (1981) 297.
[5] S. Anzellini *et al.*: Science **340** (2013) 464.

Viscosity measurement of silicate melts under mantle conditions infers the primordial structure of Earth's silicate mantle

Owing to massive energy released by a giant Moon-forming impact, the early Earth is believed to experience large-scale melting, which forms a deep or even whole-mantle magma ocean (MO) [1]. The present-day mantle is evolved from the primordial mantle after the solidification of MO. Whether the primordial mantle is chemical-layered or not depends on the solidification type (fractional or equilibrium), which in turn depends on the suspension of crystals in a convecting MO. If the crystals can be suspended, equilibrium solidification should occur, resulting in a homogeneous primordial mantle. If the crystals can't be suspended, fractional solidification should occur, resulting in a layered primordial mantle. The solidification type of MO is therefore vital to constrain the evolutional scheme of the mantle. Although the solidification type was investigated by geodynamic modeling, poorly constrained physical parameters prevent the geodynamic modeling from giving a definitive conclusion.

Besides the heat flux (a flow of energy per unit of area per unit of time) of MO surface, viscosity is a key parameter for geodynamic investigations [2]. The viscosity of a fluid is a measure of its resistance to deformation at a given rate. For example, honey has higher viscosity than water. *In situ* falling sphere viscometry is the best method to directly measure viscosity under high-pressure conditions. Based on the Stoke's law (Eq. 1), the viscosity of melt is evaluated from the vertical velocity of the sphere, which is monitored through sequential radiographic images (Fig. 1).

$$\eta = \frac{2gr_s^2(\rho_s - \rho_m)}{9v_s} \qquad (1)$$

where v_s, r_s, ρ_s, ρ_m and g are the terminal velocity, sphere radius, sphere density, melt density, and gravity acceleration, respectively.

Unfortunately, the viscosity measurement of silicate melts was limited to ~13 GPa (upper mantle) for more than 10 years due to technique difficulties (Fig. 1(b)). Major limitations encountered in previous works of the same type were (i) lack of X-ray transparent heating element to generate ultrahigh temperatures (more than ~2500 K) required to melt the silicate phases entirely and (ii) the extremely low viscosity of silicate melts at high pressure, requiring very fast radiographic measurements. Being refractory and highly X-ray transparent, recently developed boron-doped diamond heater [3] is a perfect heater to extend the pressure range of viscosity data. By combining

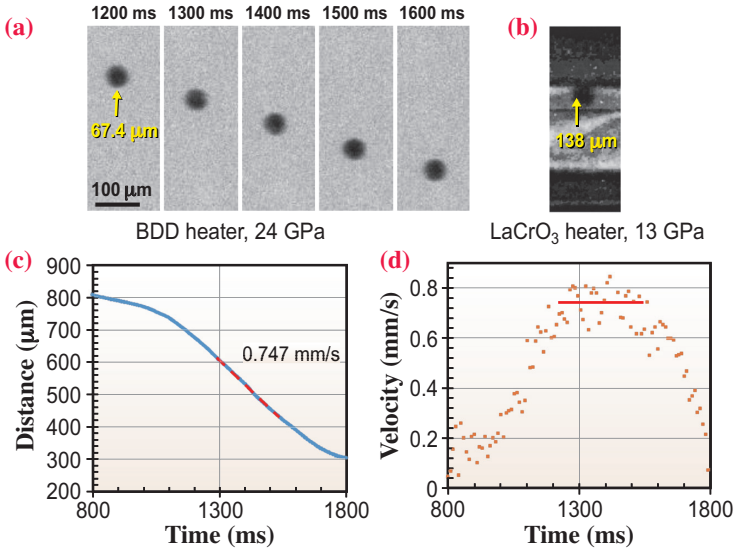

Fig. 1. Example falling path and terminal velocity of a probe sphere. **(a)** Selected radiographic image of a probe sphere falling in liquid forsterite taken with a frame rate of 1000 frame/s. **(b)** Radiographic image of a probe sphere in $LaCrO_3$ heater for comparison [5]. **(c)** Position of the sphere as a function of time according to radiographic images. The sphere position was fitted by a Gaussian function in each X-ray radiographic image (blue symbol). The melt viscosity can be calculated from the terminal velocity (red dashed line). **(d)** Corresponding velocity/time plot of the sphere, using a sampling time of 10 ms. The red dashed line is a best fit through the data points located on the "velocity plateau" corresponding to the terminal velocity.

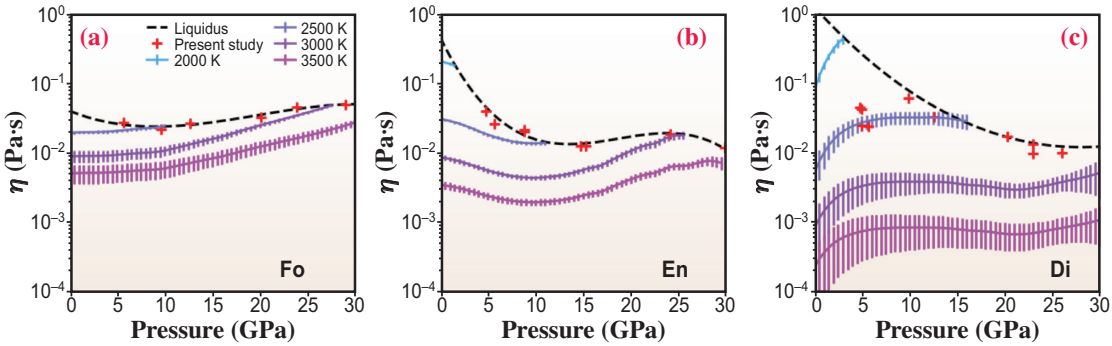

Fig. 2. Viscosities of silicate melts under pressure. **(a**, **b**, **c)** Fo, En and Di composition, respectively. Dashed black lines are viscosities along liquidus. Colored lines are viscosities recalculated along isotherms with one standard deviation using an Arrhenius equation.

the boron-doped diamond heater and an ultra-fast camera (frame rate reaches 1000 f/s), we succeeded to extend the pressure range of *in situ* falling sphere viscometry to 30 GPa at SPring-8 **BL04B1** (Japan) and PSICHE, SOLEIL (France) [4].

We investigated the viscosity of melts with compositions similar to major mantle minerals, namely forsterite (Mg_2SiO_4, Fo), enstatite ($MgSiO_3$, En) and diopside ($CaMgSi_2O_6$, Di). The viscosity of silicate melts in mantle conditions is found very low, in the order of 0.01 Pa·s, which is comparable to water (Fig. 2). Then, we applied the new viscosity data set to constrain the crystallization processes of the MO in the early Earth. We concluded that a bridgmanite-enriched layer forms at the top lower-mantle during the cooling of magma ocean (Fig. 3).

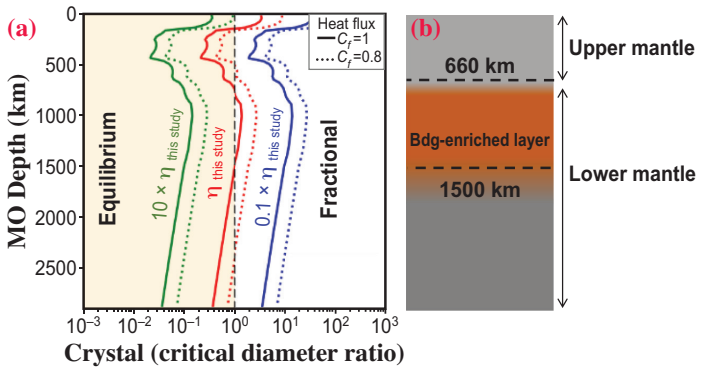

Fig. 3. Crystal/critical diameter ratio and solidification type during MO cooling. **(a)** Crystal/critical diameter ratio (Rcc) as a function of MO depth. Critical diameter is the largest grain size of crystal that can be suspended in a convecting MO. Crystal diameter is the grain size in the MO. Fractional or equilibrium solidification should occur when Rcc is large or smaller than 1, respectively. The heat flux of MO is affected by the atmosphere. When we ignore the blanketing effect of atmosphere (C_f = 1), MO has the highest heat flux, resulting in the smallest Rcc value (solid lines). When we consider the blanketing effect (e.g., 20%, i.e., C_f = 0.8), MO has a lower heat flux, resulting in a larger Rcc value (dotted lines). In order to show the effect of viscosity on Rcc value, Rcc calculated with 10 and 1/10 times viscosity are also plotted. Even with the highest heat flux, fractional solidification (Rcc > 1) should occur at depth of ~1000 km. **(b)** A conceptual drawing of mantle after magma ocean solidification. Bdg: bridgmanite.

Longjian Xie[a,b,c,*] and Akira Yoneda[a,d]

[a] Institute for Planetary Materials, Okayama University
[b] Earth and Planetary Laboratory, Carnegie Institute for Science, USA
[c] Bayrisches Geoinstitut, University of Bayreuth, Germany
[d] Graduate School of Science, Osaka University

*Email: Longjian.Xie@uni-bayreuth.de

References

[1] W.B. Tonks and H.J. Melosh: J. Geophys. Res. Planets **98** (1993) 5319.
[2] V. Solomatov: Treatise Geophys. Second Ed. **9** (2015) 81.
[3] L. Xie *et al.*: Rev. Sci. Instrum. **88** (2017) 093904.
[4] *L. Xie, A. Yoneda, D. Yamazaki, G. Manthilake, Y. Higo, Y. Tange, N. Guignot, A. King, M. Scheel and D. Andrault.: Nat. Commun.* ***11*** *(2020) 548.*
[5] J.E. Reid *et al.*: Phys. Earth Planet. Inter. **139** (2003) 45.

Phase transition of aluminium hydroxide at extremely high pressure

Hydrogen is the most abundant element in the universe. In the Earth, hydrogen is transported into deep mantle regions as a hydrous mineral via the subduction of oceanic plates. To better understand the global hydrogen circulation in the Earth's mantle, a number of high-pressure experiments were conducted on the stability of hydrous phases under lower mantle conditions. The results of recent experimental and theoretical studies indicated that hydrous phases may deliver a certain amount of water to the bottom of the Earth's mantle (~130 GPa) [1,2]. Despite its ubiquity and the profound effects of hydrogen on our Earth, there have been few studies on the stabilities of hydrous minerals on other planets. We consider that there is a possibility that water is present in hydrous phases in such planetary interiors, because a mixture of anhydrous minerals and H_2O phases has been used to discuss the interior structure of icy planets. There have also been reports of the existence of extrasolar planets having a few times the Earth's mass, where hydrous phases may play important roles as hosts of water in the deep interior of those planets.

An *ab initio* calculation predicted that a new high-pressure form of AlOOH, which has a pyrite-type structure, would be stabilized at pressures >170 GPa [3]. Furthermore, in a recent theoretical study, it was proposed that the transformation of δ-AlOOH to a new orthorhombic phase at ~160 GPa would occur prior to the transformation to pyrite-type AlOOH [4]. Thus, mineralogy based on theoretical calculations implies the potential stability of hydrous phases under extreme conditions. In this study, we conduct high pressure–temperature (P–T) experiments on the stability of pure AlOOH and its solid solutions with FeOOH using laser-heated diamond anvil cell (DAC) techniques and first-principles density-functional calculations for a range of pressures up to 270 GPa [5].

In situ X-ray diffraction (XRD) measurements were performed at SPring-8 **BL10XU**. High P–T conditions were achieved using a laser-heated DAC technique and the instrument was equipped with beveled anvils with 50 and 90 μm culets. We used $CaCl_2$-type hydroxide powders with compositions of AlOOH and $(Fe_{0.75}Al_{0.25})OOH$ as starting materials. They were synthesized at ~20 GPa and 1,000 K in a multianvil apparatus prior to DAC experiments. Samples were coated with a sputtered gold (Au) film on both sides to serve as an internal pressure standard and laser absorber. AlOOH and $(Fe_{0.75}Al_{0.25})OOH$ were loaded into ~20 μm holes in a pre-indented rhenium gasket, together with insulation layers of AlOOH and SiO_2 glass powders, respectively. Heating was performed from both sides of the samples using two 100 W single-mode fiber lasers. Angle-dispersive XRD patterns at high P–T were collected with an imaging plate (IP, Rigaku) and an X-ray flat-panel (FP) detector

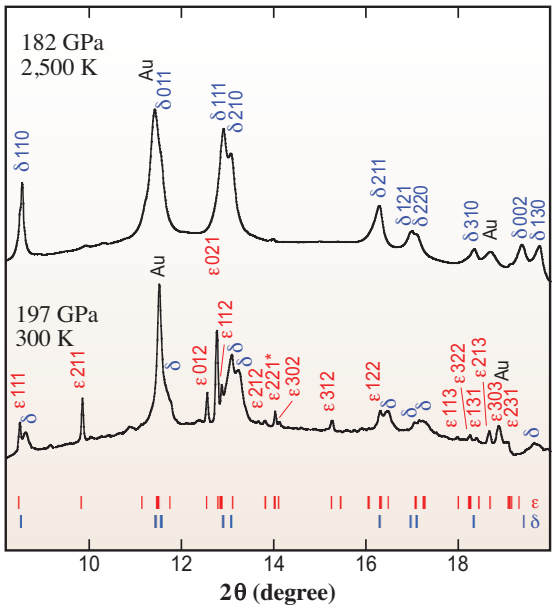

Fig. 1. *In situ* XRD patterns of ε-AlOOH formed from δ-AlOOH under various P–T conditions. The XRD pattern at 195 GPa and 300 K, after heating at 204 GPa and 2,500 K, shows the formation of ε-AlOOH. δ, δ-AlOOH; ε, ε-AlOOH; Au, gold.

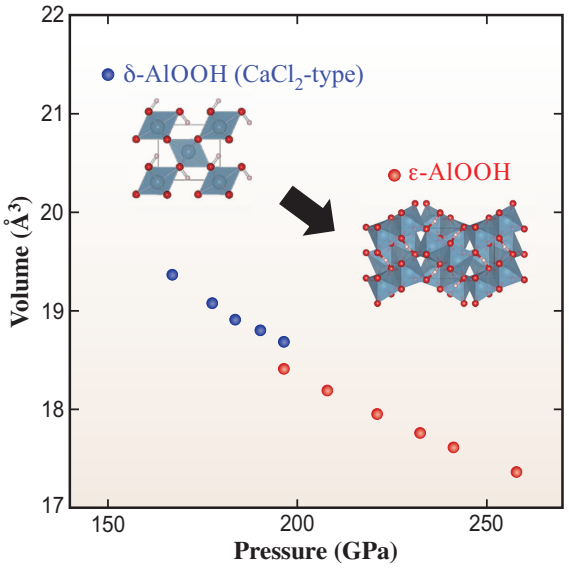

Fig. 2. Cell volumes (V/Z) of hydroxides as a function of pressure. Pressure and volume errors are smaller than the symbol size.

(Perkin Elmer) with typical exposure times of 30 s and 1 s, respectively.

We observed that XRD patterns of δ-AlOOH changed at 190 GPa and ~2500 K, where additional diffraction peaks corresponding to the new high-pressure form (hereafter, ε-AlOOH) appeared (Fig. 1). All of these new peaks were reasonably indexed with an orthorhombic symmetry phase, as predicted by a recent theoretical study [4]. Furthermore, the observed cell parameters (a = 8.311(8), b = 4.145(2), c = 4.275(2) Å, and V = 18.43(5) Å^3/AlOOH at 197 GPa and 300 K; Table 1) were close to those of the theoretically predicted orthorhombic phase of AlOOH (a = 8.354 Å, b = 4.191, c = 4.314 Å, and V = 18.88 Å^3/AlOOH at 180 GPa and 0 K). Formation of ε-AlOOH was reproduced in an additional experiment using AlOOH boehmite powder up to 271 GPa and 2,500 K. Experimentally determined cell volumes of δ-AlOOH and ε-AlOOH up to 258 GPa are shown in Fig. 2. Our experimental results show a density reduction of ~1.8% during the δ-AlOOH to ε-AlOOH transition at 197 GPa, in good agreement with the *ab initio* calculation.

In the structural and compositional models of ice giants such as Uranus and Neptune, H_2O is a dominant component stored mainly as mantle water or ice overlying the central rocky core. Our experimental results show that the high-pressure forms of hydroxides have wide stability fields, up to at least ~270 GPa, far beyond the pressures found in the Earth's mantle. If hydrous phases are stable even in other major chemical compositions at extreme high pressures, hydrous phases may be present in the rocky cores of some icy planets with sizes smaller than Neptune.

Terrestrial exoplanets that are a few times Earth's mass (super-Earths), have been discovered in extra-solar systems. Deep water transport via the hydrous phase, as suggested in the Earth's interior, may be applicable to those super-Earths that feature plate tectonics (Fig. 3). Although further studies on the dehydration temperatures of ε-AlOOH, pyrite-type hydroxides and their potential high-pressure forms are required, we conclude that water may be stored in hydroxides in the deep interior of some terrestrial super-Earths and the rocky cores of ice giants.

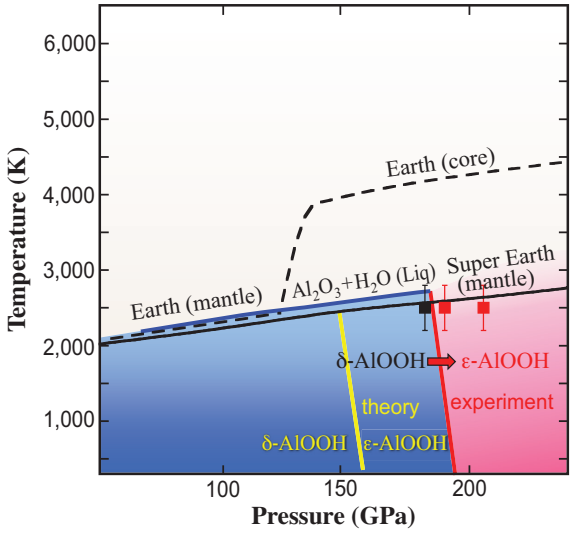

Fig. 3. High P–T phase diagram of AlOOH. The thick red solid line indicates the phase boundary estimated by combining the transition pressure of the present experiment with the previous ab initio calculation of the Clapeyron slope [3,4]. The thick blue line indicates the dehydration melting temperature of δ-AlOOH. Colored areas represent the regions where water is retained in AlOOH. The P–T conditions of Earth and super-Earth having a mass several times that of Earth are shown as black solid and dashed lines, respectively. Note that the dehydration temperatures of the ε-AlOOH phases were not clarified.

Masayuki Nishi

Department of Earth and Space Science, Osaka University

Email: nishimasa@ess.sci.osaka-u.ac.jp

References

[1] M. Nishi *et al.*: Nat. Geosci. **7** (2014) 224.
[2] M. Nishi *et al.*: Nature **547** (2017) 205.
[3] J. Tsuchiya and T. Tsuchiya: Phys. Rev. B **83** (2011) 054115.
[4] A.K. Verma *et al.*: Am. Miner. **103** (2018) 1906.
[5] *M. Nishi, Y. Kuwayama, J. Tuchiya: Icarus **338** (2020) 113539.*

What happened after the meteoroid impact at the end of the Cretaceous Period? - Paleoenvironmental reconstruction based on synchrotron XRF images

Biodiversity has not been constant throughout Earth's history. Declines in biodiversity within a short period of geologic time, roughly 10^5 years or less, can be observed in fossil records and are known as mass extinctions. Although varying degrees of mass extinctions have occurred, "Big Five" mass extinctions were the five most severe events. One of these severe mass extinctions occurred at the Cretaceous-Paleogene (K–Pg) boundary (66 million years ago). The K–Pg mass extinction is considered to have been triggered by the impact of a 10-km-diameter meteoroid. In the sedimentary record, this boundary is characterized by a thin clay layer, called K–Pg boundary clay, which contains materials derived from the impact, such as fragments of the meteoroid and impacted target rocks and condensates from impact-induced vapor. The K–Pg boundary clay contains anomalously high concentrations of siderophile elements that favorably concentrate in the metallic phase and are therefore depleted in the Earth's crust and mantle. The elemental ratios of these siderophile elements in the K–Pg boundary clay are very similar to those of carbonaceous chondrites [1,2], indicating that a meteoroid impact triggered the K–Pg mass extinction.

The K–Pg boundary clay contains high concentrations of chalcophile elements, which preferentially concentrate in sulfides, as well as siderophile elements. As the ratios of chalcophile to siderophile elements, such as Zn/Ir, As/Ir, and Sb/Ir, are one to two orders of magnitude larger than those of chondrites [3], the chalcophile elements in the K–Pg boundary clay were likely derived from surface processes rather than the meteoroid. Such processes might be related to environmental perturbations that directly induced the K–Pg mass extinction. As mentioned above, the extinction was triggered by the meteoroid impact, but was directly caused by environmental perturbations that occurred following the K–Pg meteoroid impact. Sunlight shielding, global wildfires, global warming, acid rain, ultraviolet exposure, and ozone toxicity have been proposed as environmental perturbations [4]; however, it is unclear which of these perturbations actually occurred and most severely affected biota at the end of the Cretaceous Period. This is because the necessary time-resolved information (annual to millennial scale) is absent from the sedimentary record. To determine which processes occurred immediately after the K–Pg meteoroid impact, the chemical compositions of major and trace elements in the K–Pg boundary clay from Stevns Klint, Denmark, were analyzed [5].

The concentrations of major and trace elements, including chalcophile and siderophile elements, of the K–Pg boundary clay varied among the samples analyzed herein, even between the samples collected from neighboring outcrops. The concentrations of some chalcophile elements such as Cu, Ag, and Pb were correlated with those of iridium, all of which in the K–Pg boundary clay were derived from the meteoroid (Figs. 1(a–c)). Therefore, these chalcophile elements might have been enriched during the period after iridium was supplied by the meteoroid impact and before iridium was removed from oceans. Synchrotron X-ray fluorescence (SXRF) microscopic images obtained using SPring-8 **BL37XU** showed that Cu and Ag were present as trace elements in pyrite (FeS_2) grains and as discrete 1–10 μm phases enriched in Cu or Ag [5] (Fig. 2). The pyrite grains also contained

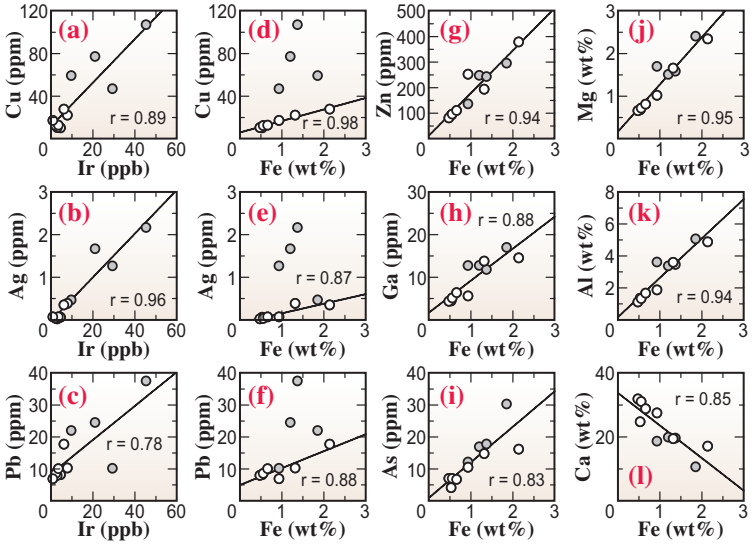

Fig. 1. Concentrations of trace and major elements of **(a)** Cu, **(b)** Ag, and **(c)** Pb compared with Ir, and of **(d)** Cu, **(e)** Ag, **(f)** Pb **(g)** Zn, **(h)** Ga, **(i)** As, **(j)** Mg, **(k)** Al, and **(l)** Ca compared with Fe. Solid lines in **(d)**–**(l)** are regression lines based on the data shown by open circles for samples in which Cu concentrations correlated with Fe concentrations. [5]

chalcophile elements (Zn, Ga, As, and Pb) other than Cu and Ag, whereas the discrete grains consisted mainly of Cu or Ag. The concentrations of some chalcophile elements (Zn, Ga, and As) were positively correlated with those of Fe, whereas correlations for the concentrations of Cu, Ag, and Pb with those of Fe were observed only in some of the data (closed circles in Figs. 1(d–i)). This implies that the concentrations of Ag, Cu, and possibly Pb can be explained by the mixing of two components for chalcophile elements: one component related to pyrite and containing other chalcophile elements in addition to Ag, Cu, and Pb, and a component especially enriched in Cu, Ag, and Pb. The SXRF images (Figs. 2(a,b)) also support two-component mixing for Ag and Cu. The two proposed components might accompany iridium; therefore, both components may have been supplied to the oceans immediately after the meteoroid impact.

Although iron is present in the form of pyrite (FeS_2) in the Stevns Klint K–Pg boundary clay, Fe might have been supplied to the oceans as high-temperature condensates of iron oxide, as indicated by the correlations between Mg and Al concentrations and those of Fe (Figs. 1(j,k)). This is because Mg and Al oxides were supplied to the oceans as condensates from the impact-induced vapor (Figs. 3(a,b)). Iron oxide on the seafloor can be reduced to Fe^{2+}, which could react with hydrogen sulfide produced by sulfate-reducing bacteria and be converted into pyrite containing chalcophile elements.

The component unrelated to pyrite was enriched especially in Ag, Cu, and Pb, which is typically present in acid-soluble sulfides, such as chalcocite, sphalerite, and galena. Thus, these elements might have been supplied to the oceans via leaching caused by highly acidic rain that occurred immediately following the K–Pg meteoroid impact (see references in [4]). In summary, the presence of two components related to chalcophile enrichments in the K–Pg boundary clay may reflect environmental perturbations such as impact heating and highly acidic rain immediately following the meteoroid impact (Fig. 3).

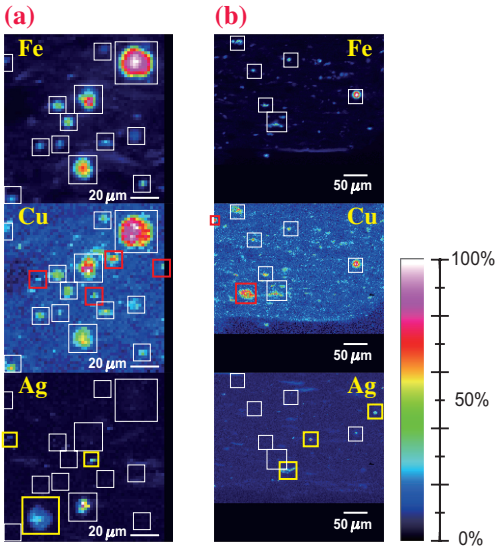

Fig. 2. Synchrotron-XRF images of Fe, Cu, and Ag in two regions **(a)** and **(b)** of a thin section from the Setvns Klint K–Pg boundary clay. The intensities were normalized using the maximum intensities in the field of view. White squares indicate the locations of typical pyrite grains. Red and yellow squares indicate the locations of Cu- and Ag-enriched grains, respectively. [5]

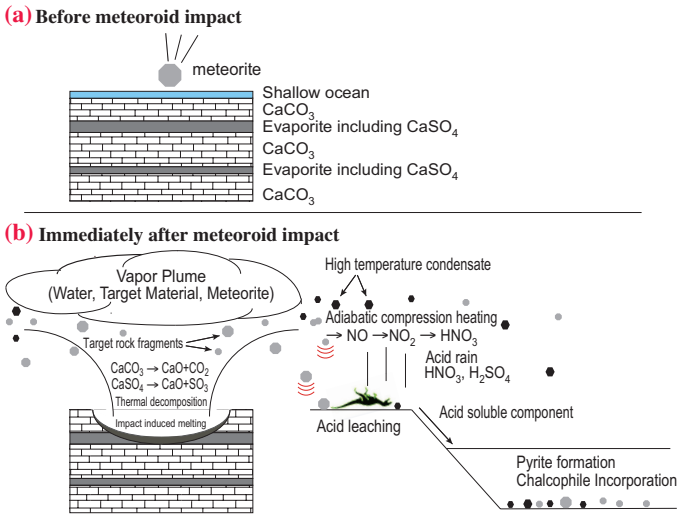

Fig. 3. Schematic drawing depicting the K–Pg meteoroid impact: **(a)** prior to the impact and **(b)** immediately after the impact. A vapor plume incorporating vaporized target rock and meteoroid materials might have been produced by the impact, from which high-temperature condensates (including Mg, Al, and Fe oxides) might have been produced. At the seafloor, Fe oxide may have been converted to pyrite containing chalcophile elements. The adiabatic compression of air by falling target rock fragments may have produced nitrogen oxide, which could have produced nitric acid rain. The thermal decomposition of $CaSO_4$ in the target rock may have released SO_3, which could have produced sulfuric acid rain.

Teruyuki Maruoka

Faculty of Life and Environmental Sciences,
University of Tsukuba

Email: maruoka.teruyuki.fu@u.tsukuba.ac.jp

References

[1] L.W. Alvarez *et al.*: Science **208**(1980) 1095.
[2] R. Ganapathy: Science **209** (1980) 921.
[3] I. Gilmour and E. Anders: Geochim. Cosmochim Acta **53** (1989) 503.
[4] T. Maruoka: Astrobiology (ed. A. Yamagishi *et al.*) (2019) 303.
[5] *T. Maruoka, Y. Nishio, T. Kogiso, K. Suzuki, T. Osawa, Y. Hatsukawa and Y. Terada: GSA Bulletin* ***132*** *(2020) 2055.*

In situ preservation of nitrogen-bearing organic matter in carbonates from ancient Mars

Mars was once warm enough to maintain persistent liquid water around 4-billion-years ago (Ga), where by the surface environment would have been favorable to sustain life [1]. Thus, the question of "life on Mars" has driven intensive studies of the Red Planet. In the late 1970s, NASA's Viking lander reported organic matter for the first time. More recently, in the 2010s, NASA's Curiosity rover detected various C- and S-bearing molecules from 3.5 Ga mudstones at Gale crater. Such findings strongly indicate the importance of organic matter in Martian near-surface systems. However, little is known about its origin, distribution, preservation and evolution, as well as its possible relationship to biological activity. The international Mars science community has set a long-term goal toward achieving Mars sample return (MSR) to search for biosignatures/biomarkers. Yet, the success of MSR must be awaited until the mid-2030s. Along with planetary explorations, laboratory analyses of Martian meteorites also provide important insights. In particular, a unique Martian meteorite named Allan Hills (ALH) 84001 is known to contain carbonate minerals that precipitated from aqueous fluid at 4 Ga Mars. In our latest study [2], we found that these carbonates preserved indigenous nitrogen-bearing organic matter, thanks to our recently developed analytical technique for high-spatial-resolution *in situ* nitrogen speciation.

Nitrogen (N) is one of the essential elements for life on Earth. In addition, N is a useful geochemical tracer to reveal the co-evolution process of the atmosphere–hydrosphere–lithosphere–biosphere of the planets. On Mars, chemical/isotopic signatures of N are not well understood because of analytical difficulties. Most previous studies relied on destructive analyses of bulk rock of Martian meteorites, whereby severe contamination from the environments is a serious possibility.

We conducted an *in situ* N *K*-edge micro-X-ray absorption near-edge structure (μ-XANES) analysis at SPring-8 **BL27SU**, which enabled the near-contamination-free measurement of micrometer-scale N species in the carbonates from ALH 84001 [2]. Since the target carbonate grains are small (≤~100 μm in diameter; Fig. 1), the X-ray beam was focused using a polycapillary lens to a final spot of 25 μm diameter or cut by closing slits 10 μm (V) × 30 μm (H). Furthermore, to reduce experimental contamination, we did not use any conventional preparation tool (e.g., epoxy resin or polishing paste). The surfaces of the carbonates were sputtered to ~1 μm in depth using a FIB-SEM Ga ion beam at Extraterrestrial Sample Curation Center, JAXA.

Nitrogen XANES spectra present two prominent absorption peaks at 398.9 and 399.9 eV with a broader absorption peak at around 408 eV (Fig. 1). Several smaller peaks are also seen between 400.7 and 402 eV. Such spectral shapes do not match XANES spectra of dinitrogen (N_2), sodium nitrate ($NaNO_3$), or ammonium chloride (NH_4Cl). On the other hand, they are consistent with the absorptions of organic imino and nitrile groups. Pyridinic N-heterocyclic groups also have peaks in a similar energy range. The peaks between 400.7 and 402 eV may correspond to pyrrolic N-heterocyclic, amide, and/or amino groups. Our XANES data indicate that the carbonates in ALH 84001 contain various N-bearing organic components. The plausible groups are the imino, nitrile, N-heterocyclic, amide, and/or amino groups. The contributions from inorganic N (e.g., N_2, nitrate, or ammonium salt) are negligible.

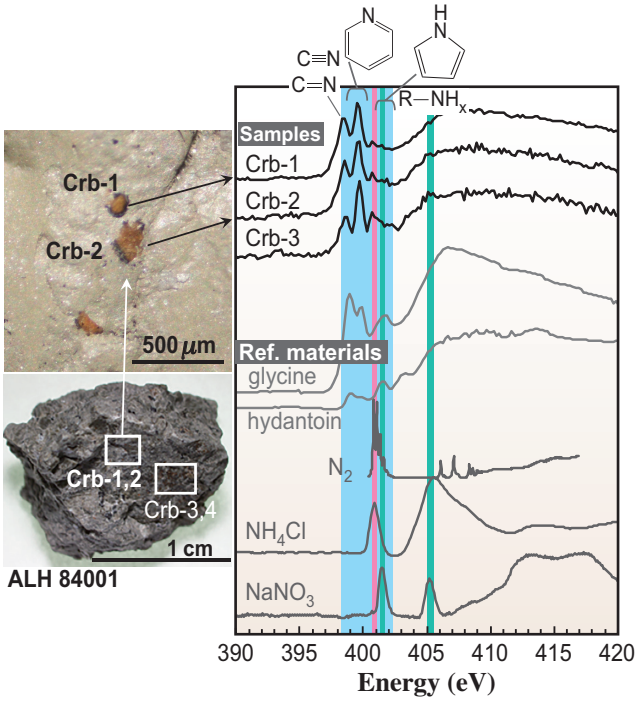

Fig. 1. Nitrogen *K*-edge XANES spectra (right) of the carbonate grains (upper left) acquired from the host rock of ALH 84001 (lower left) along with the XANES spectra of the selected reference N-bearing compounds. The significant absorption energies for N_2 (400.8 eV; magenta), $NaNO_3$ (401.4 and 405.2 eV; green), and N-bearing organics (398–402.5 eV; light blue) are highlighted. Images modified after [2].

The N-bearing organics found in the ALH 84001 carbonates are expected to have survived in the Martian near-surface system since 4 Ga. The 4-Ga aqueous fluid, from which these carbonates precipitated, must have provided nondestructive environments for the organics (i.e., moderate conditions of pH, oxidation-reduction potential (Eh), UV, and cosmic-ray irradiation). Strong oxidants, such as chlorine oxides (ClO_x) and nitrogen oxides (NO_x), are known to exist in the current Martian near-surface system and to degrade its organics. In contrast, our N-XANES results suggest the absence of nitrogen oxides of the ALH 84001 carbonates. Our on-going sulfur *K*-edge study of the same samples proposes moderate oxidation to a neutral condition for the 4-Ga Martian fluid (pH = 6–9 and Eh = –0.25–0 V). The coexisting N in that fluid should be in the form of N_2 (aq) and/or NH_4^+. It is inferred that early Mars had a less oxidizing surface than that of today, at least locally and temporally. Our finding further implies that the organic matter could have survived in the carbonates (and other alteration minerals) on Mars over a long geological time.

Possible origins of the Martian organics are (1) *in situ* synthesis and/or (2) meteoritic supply (Fig. 2). In Case 1, chemically inert atmospheric N_2 should first be fixed into accessible forms. NO_x could have been produced on early Mars via thermal shock by volcanic lightning, meteorite impacts, and/or solar/cosmic X-ray irradiations. Moreover, reduced N (e.g., ammonia and hydrogen cyanide) has not been identified on Mars. However, several abiotic paths for the formation of reduced N species are proposed for ancient Earth's environment, such as the reduction of NO_x by metallic iron and/or aqueous solutions, as well as the photochemical reduction of atmospheric N_2. Similar processes could have occurred on early Mars. In Case 2, the meteoritic supply of organic compounds is also a plausible source. Carbonaceous chondrites are known to contain various insoluble and soluble N-bearing organic groups at sub-ppm to 10^2-order ppm levels. Interplanetary dust particles and comets also contain various components. The previous detection of organic matter in a much younger Martian meteorite may reflect such an extra-Martian origin.

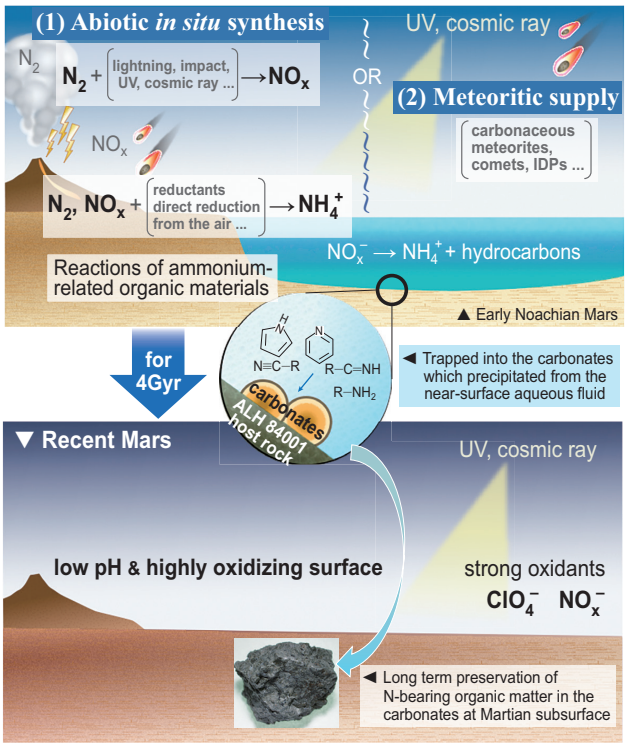

Fig. 2. Schematic image of the 4 Ga and current Martian near-surface systems. The ancient N-bearing organics were trapped and preserved in the carbonates over geological time scales. Images modified after [2].

Whatever the origin, the organic and reduced forms of N in ancient Mars indicate the presence of a "Martian N-cycle." If considerable amounts and variations of organic compounds were produced, delivered, and preserved in the Martian near-surface system over geological time scales, they may have had a chance to evolve into more complex forms. It is expected that additional hidden records of the Martian N-cycle will be acquired by future investigations, including a sample return mission from the Martian moons (Martian Moons eXploration; MMX) [3], MSR missions [4], and exploration of the Martian subsurface, as well as further advanced studies of Martian meteorites.

Mizuho Koike[a,b,*], Ryoichi Nakada[c] and Tomohiro Usui[b]

[a] Earth and Planetary Systems Science Program, Hiroshima University
[b] Institute of Space and Astronomical Science, Japan Aerospace Exploration Agency
[c] Kochi Institute for Core Sample Research, Japan Agency for Marine-Earth Science and Technology (JAMSTEC)

*Email: mizuhokoike@hiroshima-u.ac.jp

References

[1] B.L. Ehlmann *et al.*: J. Geophys. Res. **121** (2016) 1927.
[2] *M. Koike, R. Nakada, I. Kajitani, T. Usui, Y. Tamenori, H. Sugahara and A. Kobayashi: Nat. Comm.* ***11*** *(2020) 1988.*
[3] T. Usui *et al.*: Space Sci. Rev. **216** (2020) 49.
[4] D.W. Beaty *et al.*: Metorit. Planet. Sci. **54** (2019) S3-S152.

Microscopic 3-dimensional stress distribution inside crystalline grains of bulk steel under plastic deformation measured by scanning 3-dimensional X-ray diffraction microscopy

Assuring the reliability of smaller, lighter, and more functional components is becoming an increasingly important issue in transportation industries. One of the key properties in reliability analysis is mechanical stress, which is categorized into three types. Type I stresses are macroscopic stresses that can be measured using commercial X-ray diffraction equipment and are widely used in mechanical designing and computer-aided engineering. Type II stresses are grain-averaged stresses, which represent individual grains; therefore, the value differs from grain to grain. On the other hand, type III stresses are intragranular stresses, i.e., local stresses inside a grain, which have a distribution within the grain. The measurement of type III stresses is important because the life and strength of a component are considered to depend on the type III stresses that affect the microscopic crack propagation behavior. Although measuring the 3-dimensional microscopic distribution of stress is necessary for improving the reliability of components, conventional techniques are not capable of accomplishing it nondestructively. Synchrotron X-ray-based techniques, such as 3-dimensional X-ray diffraction (3DXRD) [1–3], have been realized in nondestructive measurements using high-energy and super-brilliant X-rays. In this research [4], we developed a scanning 3DXRD microscopic methodology that combines a highly transmissive synchrotron X-ray microbeam with techniques of extracting the internal information of single grains.

The schematic of the scanning 3DXRD measurement system constructed at SPring-8 **BL33XU** [5] is shown in Fig. 1. The size of the incident synchrotron X-ray microbeam is 1×1 μm^2 at the measurement volume in the specimen. To detect diffracted beams from only the measurement volume, a conical slit was placed between the specimen and area detector. The conical unit of concentric slits blocks the diffraction from the outside of the measurement volume. Diffraction images were obtained every 0.6° while the specimen was rotated for 180° around the vertical axis. The stresses at the measurement point can be analyzed from the diffraction images. The 3-dimensional distribution of the stresses was obtained by scanning the specimen at intervals of 1.2 μm. The measured specimen is low-carbon steel with a tensile strength of σ_{TS} = 330 MPa. The sample has a cross-sectional size of 1×1 μm^2 with a mean grain size of 20 μm. Scanning 3DXRD measurements were conducted while the specimen was plastically deformed by 5.1% under tensile loading.

We succeeded in nondestructively measuring the 3-dimensional distribution of type III stresses inside the grains of bulk polycrystalline steel under tensile deformation using a 1 μm X-ray beam, as shown in Fig. 2. The macroscopic type I stress, calculated as the average for all voxels, was 240 MPa, which approximately agrees with the applied tensile load. The type II stresses in the cubic area were not more than the tensile strength of σ_{TS} = 330 MPa. On the

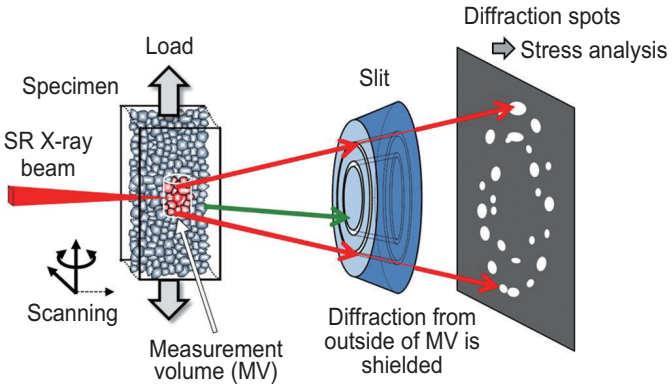

Fig. 1. Schematic of internal stress measurement by scanning 3DXRD microscopy with a conical slit at BL33XU.

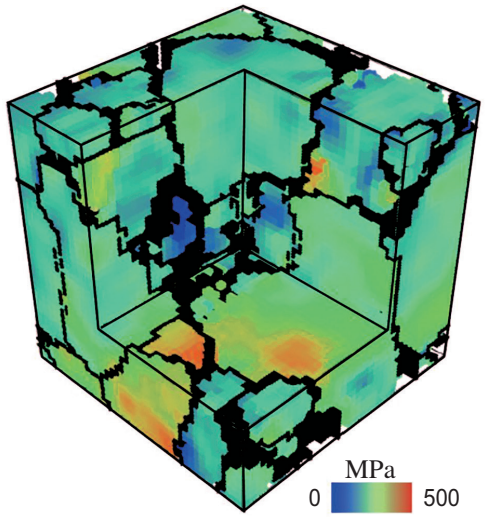

Fig. 2. Measured 3-dimensional distribution of type III stresses in the vertical direction. The size of the cube is 44.4 × 44.4 × 44.4 μm^3.

other hand, the type III stresses exceeded σ_{TS} and reached 500 MPa after the 5.1% elongation.

An internal 2-dimensional map of type III stresses on a plane normal to the tensile direction is shown in Fig. 3(a). The distribution of microscopic stresses is shown in Fig. 3(b) along line A in (a). Since the type II stresses are independent of position in each grain, they are represented by a constant value indicated by the blue line. The type III stresses have the distribution shown by red dots. Error bars were evaluated using the deviations of forces from equilibrium. The type III stress inside the grain exceeds σ_{TS} = 330 MPa and reaches 520 ± 160 MPa. The results show that the local stresses greatly deviate from the average stresses measured by conventional methods.

The developed technique will enable the extraction of weak points inside components and the identification of their degradation and deformation mechanisms. This should contribute to the development of even more reliable components and manufacturing processes for vehicles, home appliances, and information/communications equipment. Since this technique enables the nondestructive measurement of stresses from the microscopic to the macroscopic scale, it should also facilitate the development of multiscale material modeling that expresses both fractures and deformation, as well as simulations that predict the life of components.

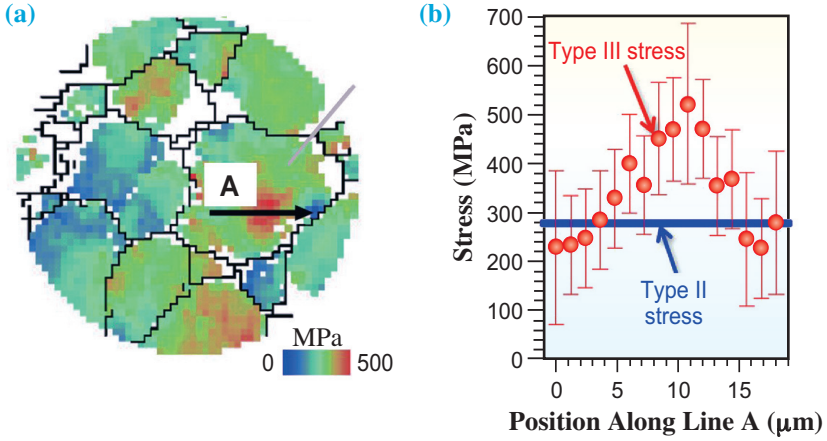

Fig. 3. **(a)** Internal 2-dimensional map of type III stresses on a plane normal to tensile direction. **(b)** Distribution of type III stresses along line A in (a) markedly deviated from that of type II stresses.

Yujiro Hayashi†, Daigo Setoyama and Hidehiko Kimura*

Quantum Beam Analysis Laboratory,
Toyota Central R&D Labs., Inc.

† Present address : RIKEN SPring-8 Center

*Email: hdkimura@mosk.tytlabs.co.jp

References

[1] L. Margulies *et al.*: Science **291** (2001) 2392.
[2] S. Schmidt *et al.*: Science **305** (2004) 229.
[3] H.F. Poulsen: J. Appl. Cryst. **45** (2012) 1084.
[4] *Y. Hayashi, D. Setoyama, Y. Hirose, T. Yoshida, H. Kimura: Science* ***366*** *(2019) 1492.*
[5] T. Nonaka *et al.*: AIP Conf. Proc. **1741** (2016) 030043.

Interpenetration of polymer chains on particle surfaces in latex films determined by small-angle X-ray scattering

Polymeric latex films play important roles in industrial coatings, paintings, and adhesives. Water-borne latex films are particularly interesting in this context, as they are obtained by evaporating water from aqueous dispersions of polymeric latex particles, and thus reduce/circumvent the use of volatile organic compounds (VOCs) during film formation. To prepare water-born latex films, the glass-transition temperature T_g of the particles should ideally be lower than the drying temperature, i.e., the hydrophobic particles should be allowed to interpenetrate each other after the evaporation of water (Fig. 1(a)). However, water-borne latex films usually show poor mechanical strength as is usually the case with latex polymers with a low T_g [1,2]. Thus, tremendous efforts have been devoted to the structural analysis and the understanding of the toughness of latex films. Nevertheless, a method for the quantitative analysis of the interpenetration between polymer chains on particles remains elusive. In this study, small-angle X-ray scattering (SAXS) was applied to characterize latex films.

Here, the latex films were prepared with three types of particle synthesized by mini-emulsion polymerization under the same conditions. The tested particles are rotaxane crosslinked (RC), chemically crosslinked (CC), and non-crosslinked (NC) particles, respectively (Fig. 1(b)). The rotaxane crosslinking points affect the flexibility of the polymers in the particles (the so-called 'stress relaxation'). In addition, annealing increased the fracture energy of the latex films used in this study and was more effective for latex films composed of RC particles than for those composed of NC and CC particles [1,2]. Accordingly, chemically 'clean' latex-film systems were suited as models for the evaluation of the interpenetration of polymer chains.

The latex films were examined at 25°C under vacuum by SAXS using synchrotron X-rays sourced at SPring-8 **BL03XU**. The SAXS profiles of dry RC, CC, and NC films are displayed in Fig. 2(a). For all films, peaks were observed in the range of the measured scattering vector (q). These peaks seem to reflect the ordered structure of the particles in the films and are the Bragg peaks derived from face-centered cubic colloidal crystals. However, detailed information on the interpenetration of near-surface polymer chains on these microspheres remains unclear.

To quantitatively analyze the interpenetration degree of polymer chains on the particles in these latex films, we used SAXS analyses to determine the thickness of the domain boundaries in the block copolymers [3]. For those cases, a model for the trapezoidal electron-density variation for the domain structure was developed, where the block copolymer forms the domain structure (the so-called 'pseudo-two-phase system'). In brief, this method examines the SAXS intensity in the high-q region. According to Ruland's theory for two-phase materials with diffuse boundaries, the domain boundary thickness can be determined using Porod's law by analyzing the deviation of the scattering curves in the high-q region, where the intensity is expressed by $I(q) = Cq^{-4}\exp(-\sigma^2 q^2)$, with C being a constant and σ the diffuseness of the boundary. Consequently, a plot of $\ln[q^4 I(q)]$ as a function of q^2 affords a straight line, wherein the slope affords the parameter σ.

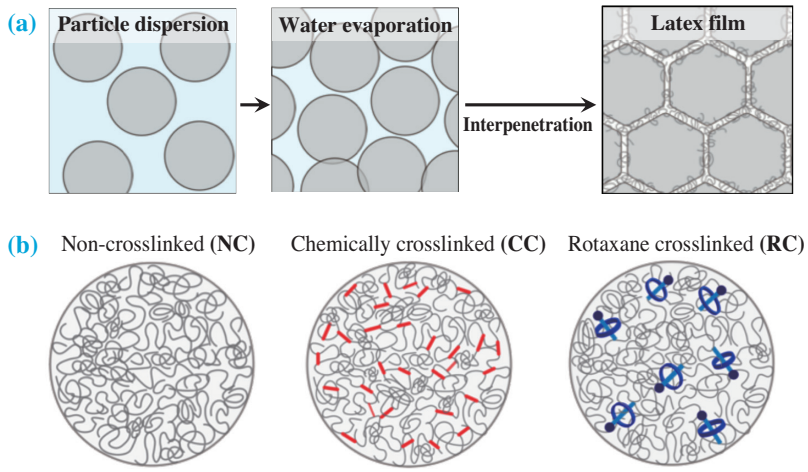

Fig. 1. **(a)** Scheme of latex film formation and **(b)** illustrations of the tested non-crosslinked (NC), chemically crosslinked (CC), and rotaxane-crosslinked (RC) particles. [4]

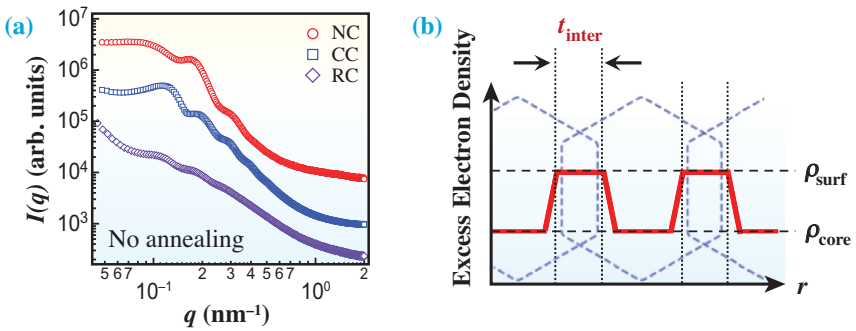

Fig. 2. **(a)** SAXS intensities of NC, CC, and RC latex films obtained at SPring-8 BL03XU. The data are reprinted from Ref. 4. **(b)** Model of trapezoidal electron-density variation (red line) for the packed structure of the particles (blue dashed line).

Here, the domain boundary thickness (t_{inter}) is given by $t_{inter} = (2\pi)^{1/2}\sigma$. In the latex films, we assumed the pseudo-two-phase system that consists of a low-density particle core (ρ_{core}) and a high-density interphase between the particle surfaces (ρ_{surf}) (Fig. 2(b)). Thus, t_{interr} can be regarded as the characteristic interfacial thickness and/or the degree of interpenetration of the polymer chain on the particles.

The obtained t_{inter} exhibited the annealing time dependence (Fig. 3(a)). Without annealing (0 h), t_{inter} decreases in the order of NC (3.3 nm) > RC (3.1 nm) > CC (2.5 nm), which indicates that NC particles exhibit high deformability and flexibility due to the lack of crosslinking. Moreover, the difference between RC and CC particles may be due to the fact that the rotaxane crosslinking points endow the polymer chains in the individual particles with mobility during the formation of the films. On the other hand, the interpenetration of polymer chains on CC microspheres may be suppressed owing to the increased rigidity of the individual particles.

Furthermore, t_{inter} of latex films strongly affects their toughness, i.e., fracture energy (Fig. 3(b)). In particular, the increments of both t_{inter} and the fracture energy of the RC latex film are higher than those of the NC films, resulting in a relatively steep slope. The rotaxane crosslinker thus enhances the interpenetration with and without annealing. Therefore, the rotaxane crosslinker provides synergetic effects in the film in terms of both polymer interpenetration on the particle surface and stress relaxation [4]. We are convinced that the proposed method represents a universally applicable strategy to quantitatively analyze microscopic interdiffusion in latex films and, potentially, in other colloidal crystals [5].

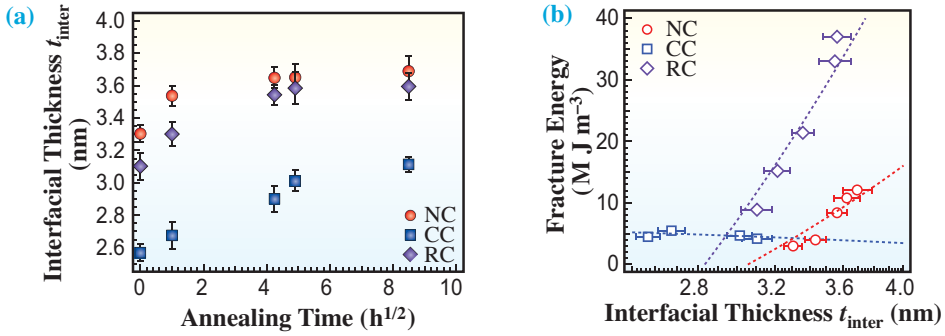

Fig. 3. **(a)** Interfacial thickness (t_{inter}) of the tested latex films. **(b)** Relationship between t_{inter} and the fracture energy of NC, CC, and RC latex films. [4]

Takuma Kureha

Department of Frontier Materials Chemistry,
Hirosaki University

Email: t-kureha@hirosaki-u.ac.jp

References

[1] S. Hiroshige *et al.*: Chem.-Eur. J. **23** (2017) 8405.
[2] S. Hiroshige *et al.*: J. Soc. Rheol. Jpn. **47** (2019) 051.
[3] M. Shibayama and T. Hashimoto: Macromolecules **19** (1986) 740.
[4] *T. Kureha, S. Hiroshige, D. Suzuki, J. Sawada, D. Aoki, T. Takata, M. Shibayama: Langmuir* ***36*** *(2020) 4855.*
[5] S. Hiroshige *et al.*: Polymer J. **53** (2021) 345.

Accelerators & Beamlines Frontiers

SPring-8 Beam Performance

Recent update on accelerators

The user time operation of SPring-8 with full-energy direct beam injection from the linear accelerator of SACLA to the SPring-8 storage ring started in 2020. Some user experiments require the ratio of the number of electrons in the satellite bunches to that in the main bunch, that is the bunch purity, to be as small as 10^{-8} or less. Here, we define the main bunches as those that are expected to fill specific RF buckets in the filling patterns for the operation modes. In the traditional SPring-8 operation with beam injection from the booster synchrotron, undesired electrons in the satellite bunches are removed using the RF knock-out system in the booster synchrotron to deliver storage ring users high-purity isolated bunches. However, once we started the beam injection from the SACLA linac, it was no longer possible to remove the undesired electrons in the booster. Experiments of beam injection from SACLA have revealed that unwilling electrons can be injected into several RF buckets coming after the main bunches. That will not be tolerated in some user experiments such as nuclear resonant scattering experiments.

We have developed a bunch cleaner system to remove spurious satellite bunches inside the storage ring. As long as spurious bunch cleaning is carried out in a storage ring, it is crucial not to disturb the main bunches in the several filling patterns for the user operation modes. The bunch cleaner system developed is composed of a signal-generating digital processor, amplifiers, and a stripline kicker. The digital processor generates a time-gated signal to kick out spurious bunches. The output signal of the processor is amplified and fed to a stripline kicker so as to kick the spurious bunches vertically. The stripline kicker is installed in cell 30 of the storage ring. The signal fed to the kicker is modulated at a frequency equal to the product of a fractional vertical betatron tune and the revolution frequency of the ring. The spurious bunches are resonantly excited to oscillate, and they are lost at a beam scraper in cell 48, limiting the vertical aperture of the ring.

The performance of the bunch cleaner of the storage ring is shown in Fig. 1 by an example of the bunch purity history during the user time. The filling pattern is the H mode, which includes one isolated bunch, and the bunch purities of the 12 satellite bunches after the main bunch are also illustrated. The beam refill on 9 February at 10 a.m. and the following continuous top-up operation were carried out with beam injection from SACLA. In the SACLA linac, the spurious bunch sweeping system is available to eliminate impure electrons that appear out as satellite bunches in the storage ring. The bunch sweeping system was in operation and the impure electrons were being substantially eliminated in the SACLA linac. Undesired electrons were nonetheless accumulated in the storage ring through the top-up injection from SACLA and significantly detected as satellite bunches in certain RF buckets after the main bunch. The operation of the bunch cleaner in the storage ring started on 12 February at 4 p.m., and it was activated once every eight hours aiming at clearing the fourth and the following RF buckets after the main bunch. After starting the operation of the bunch cleaner in the storage ring, the targeted spurious bunches were successfully cleared and an ultimate bunch purity better than 10^{-10} was realized, except for the first two satellite bunches behind the main bunch.

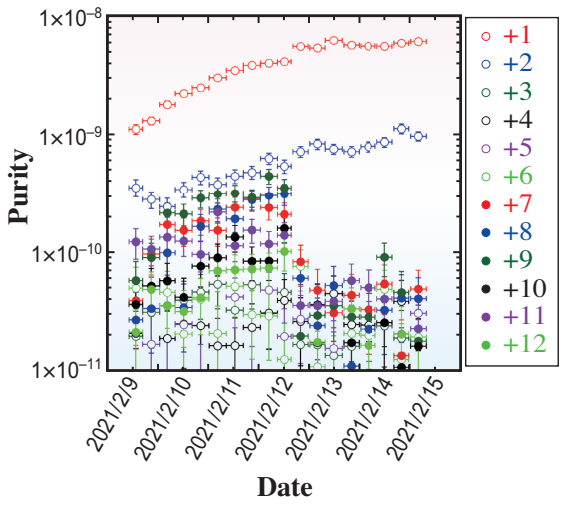

Fig. 1. Example of bunch purity history during the user time with injection from SACLA. The bunch purities of the 12 satellite bunches after the main bunch are illustrated for the H mode. The beam was refilled on February 9 at 10 a.m. followed by continuous top-up injections. The operation of the bunch cleaner started on February 12 at 4 p.m., and it was activated once every eight hours.

Shiro Takano and Takahiro Watanabe*

Japan Synchrotron Radiation Research Institute (JASRI)

*Email: twatanabe@spring8.or.jp

Development of X-ray imaging detector for 200 keV X-ray microtomography

High-energy X-ray microtomography is a promising tool for observing inner fine structures of metallic samples and large rocks containing fossils in three dimensions without the need to cut them into small pieces. A synchrotron-radiation-based high-energy X-ray beam with plentiful flux and a relatively high degree of spatial coherence can be better serve for high-spatial-resolution X-ray microtomography compared with laboratory-based computed tomography systems. Recently, 200 keV high-energy X-ray microtomography using a white beam from a bending magnet source has become available at SPring-8 **BL28B2**. The high-energy X-ray spectrum at around 200 keV can be extracted by using an absorber composed of heavy metal plates: a tungsten plate with a thickness of 0.5 mm and a lead plate with a thickness of 2 mm [1]. The 200 keV high-energy X-ray microtomography has been applied to the observation of, for example, metallic cultural heritages and fossils.

Because of the high penetration power of a high-energy X-ray beam, large objects filled with dense materials are the primary targets of high-energy and high-spatial-resolution X-ray microtomography. A dedicated X-ray imaging detector, which allows a wide field of view (FOV) observation, was developed for using these applications. In addition, a high-definition CMOS camera was introduced to realize high-spatial-resolution X-ray microtomography while keeping the wide FOV [2].

An X-ray imaging detector employing a lens-coupled visible-light conversion-type system to allow for the flexibility to change the effective pixel size and FOV has been developed [3]. Photographs of this detector are shown in Fig. 1. A large-format camera lens (Planar 135/3.5, Carl Zeiss) was used as the first lens to enable wide-FOV imaging without vignetting. The focal length, which is almost equal to the distance from the scintillator to the lens, is 135 mm, and the *F* number is 3.5. The first lens is moved along the optical axis of visible light by a linear actuator to adjust the focus of the image. This system employs an "L-shaped" configuration in the horizontal plane to reduce the X-ray scattering from the prism mirror caused by high-energy X-rays passing through the scintillator. A high-definition industrial CMOS camera, C13949-50U (4096 (H) × 3008 (V) pixel format, 3.45 μm/pixel, dynamic range of 4565:1, full-well capacity of 10,500 e^-, Hamamatsu Photonics), was used to achieve a wide FOV with a smaller effective pixel size. The second lens, which had a focal length of 35 mm (Al Nikkor 35 mm f/1.4 S, Nikon), was set just in front of the CMOS camera. In this case, the effective pixel size was 12.98 μm.

In high-energy X-ray imaging, selecting an optimal scintillator is an important issue to realize efficient and high-spatial-resolution measurements. This is because high-energy X-rays of around 200 keV are easily transmitted through even thick scintillators. Although a thick scintillator provides a high conversion efficiency from X-rays to visible light, the achievable spatial resolution in the thick scintillator becomes lower than that in a thin scintillator. By evaluating several scintillators in terms of their efficiency and imaging property using the modulation transfer function, a $Lu_3Al_5O_{12}:Ce^+$ (LuAG) ceramic of 500 μm thickness is found to be a good candidate for 200 keV high-energy X-ray microtomography when the effective pixel size is 12.98 μm.

As a demonstration of high-energy X-ray microtomography using the developed detector, an

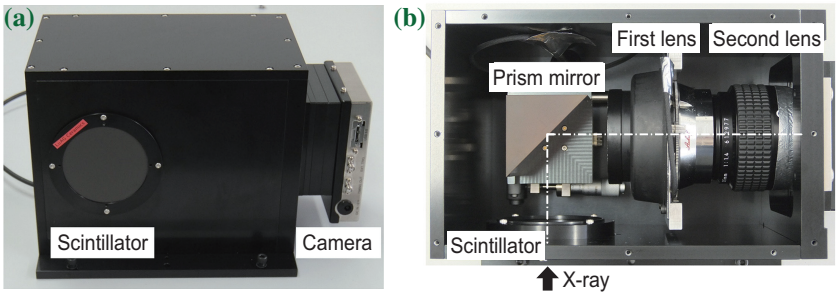

Fig. 1. Photographs of the developed X-ray imaging detector. **(a)** Exterior view and **(b)** top view showing the interior.

elliptical nodule containing a fossil was observed. A photograph of the nodule is shown in Fig. 2(a). The propagation distance from the nodule to the X-ray imaging detector was set to 3 m. Then, the effective pixel size was 12.15 μm, which is slightly smaller than the pixel size shown above. This is because the projection image was slightly magnified by the relatively long propagation distance. In this case, the horizontal FOV in the image was calculated to be 49.8 mm. Since the effective beam size along the vertical direction in the 200 keV region was approximately 1.5 mm at the sample position, the nodule was scanned along the vertical direction at 1.42 mm per step to observe the whole shape. Cross-sectional images in three orthogonal directions are shown in Figs. 2(b)–2(d). The inside of the nodule was clearly observed. The three-dimensional view of the fossil of a shell at the center of the nodule is shown in Fig. 2(e). The fine structure of the nodule as well as the fossil inclusion could be clearly observed with the developed X-ray imaging detector.

As a merit of the lens-coupled X-ray imaging detector, the effective pixel size and FOV can be easily changed by replacing the second lens. In this detector, the effective pixel size of a few microns can also be achieved by using a second lens with a large focal length. The high-spatial-resolution observation of the local fine structure in a large object will be an outstanding feature of synchrotron-radiation-based high-energy X-ray microtomography. The optimal measurement conditions will be explored in future work.

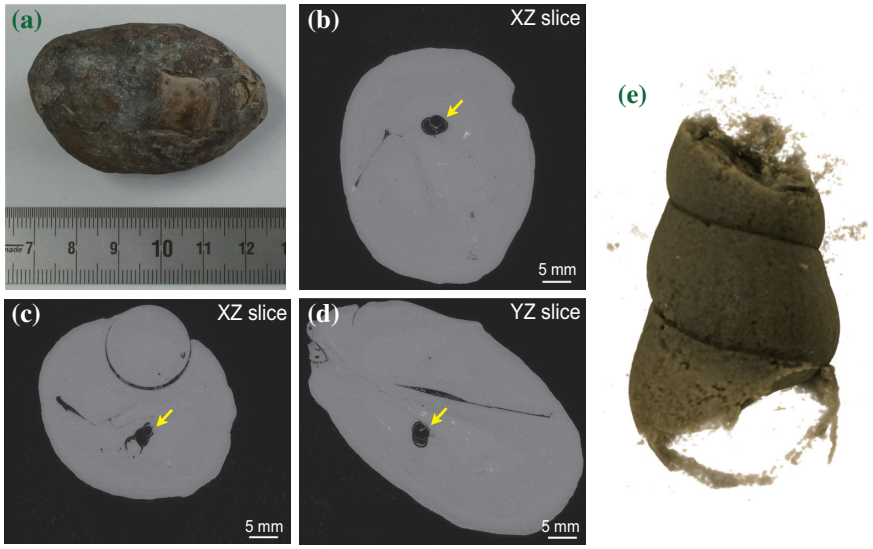

Fig. 2. **(a)** Photograph of the nodule. Cross-sectional images of the nodule in the **(b)** XY, **(c)** XZ and **(d)** YZ planes. Here, the XY plane is normal to the rotational axis in the tomographic measurements. Number of projections: 7200. Exposure time: 25 ms. Thirty tomographic scans were required to observe the whole shape. **(e)** Three-dimensional view of the shell indicated by arrows in the cross-sectional images.

Masato Hoshino*, Kentaro Uesugi and Naoto Yagi

Japan Synchrotron Radiation Research Institute (JASRI)

*Email: hoshino@spring8.or.jp

References

[1] M. Hoshino *et al.*: AIP Advances **7** (2017) 105122.
[2] *M. Hoshino, K. Uesugi and N. Yagi: J. Synchrotron Rad. **27** (2020) 934.*
[3] K. Uesugi *et al.*: J. Synchrotron Rad. **18** (2011) 217.

A high-efficiency X-ray emission spectrometer of SPring-8 BL39XU beamline

X-ray spectroscopy is a useful tool for studying the element-selective electronic states of functional materials. In particular, X-ray emission spectroscopy (XES) can obtain detailed information about electronic states, such as valence, spin, and coordination states [1-3]. However, an accurate XES spectrum of trace elements may take a long time to acquire because their emission signals are generally weak. To overcome this problem, a high-efficiency XES spectrometer equipped with multiple analyzer crystals has been developed at synchrotron radiation facilities worldwide. Such an XES spectrometer was desired for the public beamline of SPring-8. Thus, a new high-efficiency XES spectrometer was installed at SPring-8 **BL39XU** for the main purpose of high-energy resolution X-ray absorption spectroscopy.

The specifications of the spectrometer are summarized in Table 1. The sample, analyzer crystals, and detector are located on the Rowland circle of 820 mm diameter, as shown in Fig. 1(a). The spectrometer consists of three towers each with an assembly of five analyzer crystals, so that a maximum of fifteen analyzer crystals can be mounted on the spectrometer (Fig. 1 (b)). The X-ray path for the emission X-rays, including the analyzer crystals, is vacuumized, except at the sample position corresponding to the X-ray emission point and at the detector position corresponding to the focal point. The vacuum chamber provides the emission intensity that is the collection of the emission intensities of 15 analyzer crystals and suppresses X-ray absorption through air and window materials (Kapton film) so that the efficiency of XES measurements is improved.

It is important to be able to freely select target elements and/or fluorescence (emission) lines for X-ray spectroscopy. Figure 2 shows the types of analyzer crystal and the emission energy range available for the XES spectrometer. Emitted X-rays with a wide energy range of 4.4–16 keV are available with little energy loss, so that important elements of the functional materials, such as 3*d*/5*d* transition metals, 4*f* lanthanide elements, and 5*f* actinide elements, are covered. The energy resolution of the spectrometer is estimated to be 1×10^{-4} in an incident photon energy range of 4.9–18 keV. Currently, 15 analyzer crystals of Ge (111) plane and those of Ge (220) plane can be used for XES measurement. For the other analyzers, mostly five crystals can be used for the measurements. To adjust the emission X-ray energy, an automatic alignment system for the

Table 1. Specification of the X-ray emission spectrometer installed at BL39XU.

Emission energy range (keV)	4.41 – 16.0
Energy resolution (eV)	0.5 – 1.5 ($\Delta E/E = 10^{-4}$)
Rowland radius of spectrometer (mm)	820
Available Bragg angle (degrees)	70 – 83
Motion range of analyzer crystal (degrees)	75 ± 10 (horizontal, θ_B) / 0 ± 10 (vertical, χ)
Scattering angle (degrees)	30 – 150
Photon flux @ sample (phs/s)	10^{11} – 10^{13} (horizontal, vertical, and circular polarizations)
Beam size @ sample (μm)	300 (vertical) × 120 (horizontal), or 2 (vertical) × 9 (horizontal)*
Detectors	PILATUS 100K (sensor: Si, pixel size: 172 μm), PiXirad-2 (sensor: CdTe, pixel size: 60 μm (honeycomb array)), SOPHIAS-L (sensor: Si, pixel size: 30 μm)
Sample environment	Pulse-tube type cryostat (3 – 300 K), Helium-flowing type cryostat (10 – 330 K), Permanent magnet (1.15 T in gap 10 mm), High-pressure cell (Diamond-Anvil-Cell, A.P.–50 GPa)

* using Kirkpatric-Baez mirror

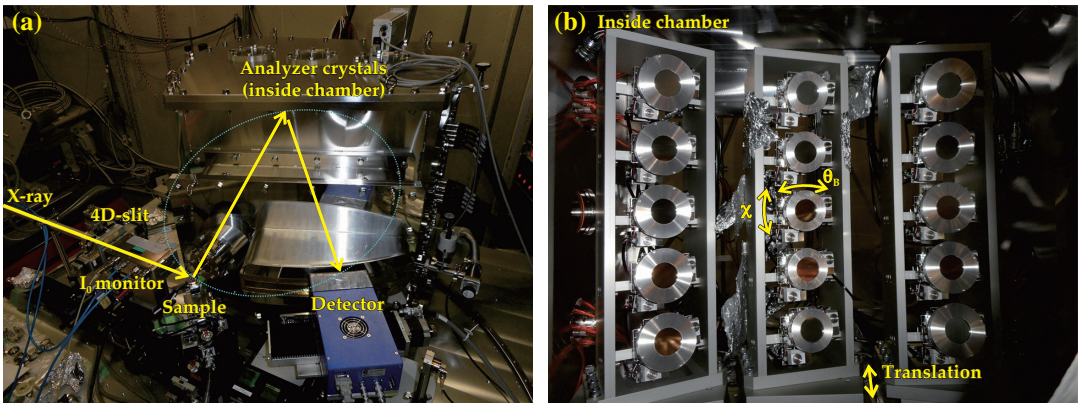

Fig. 1. **(a)** New vacuum chamber of the X-ray emission spectrometer with 15 analyzer crystals. The emission point (sample) and focal point (detector) are located outside the chamber. **(b)** Three towers, each of which can mount a set of five analyzer crystals, are installed inside the chamber.

analyzer crystals is currently under development. This system provides a collection of emitted X-rays from the sample to the same focal point by adjusting the five analyzer crystals in each tower. The system will allow users to change the analyzer crystals in accordance with the target elements/emission lines on their own.

The number of users of XES spectroscopy has gradually increased, and about 50% of beamtime is occupied. The research fields have expanded to strongly correlated electron systems, chemical analysis, and earth/environment science. This wider range of research field necessitates a certain degree of freedom in selecting elements and/or emission lines. We also have a plan to amplify different types of analyzer crystal to facilitate the widening of the X-ray energy range.

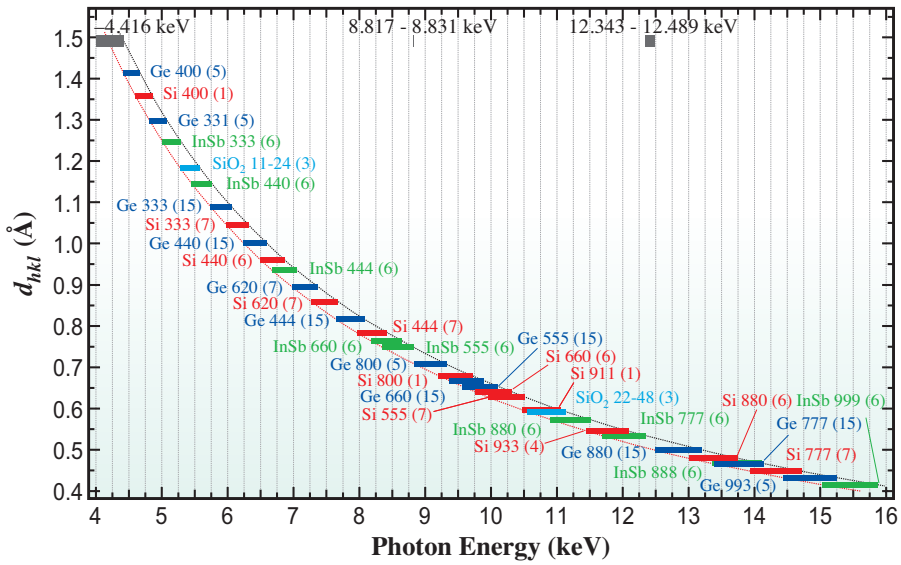

Fig. 2. Analyzer crystals available for the XES spectrometer. The number in parentheses ( ) represents the quantity of crystals. Black and red dotted lines denote the conditions of Bragg angles of 70 and 83 degrees, respectively. Gray thick lines denote the unavailable energy range.

Naomi Kawamura

Japan Synchrotron Radiation Research Institute (JASRI)

Email: naochan@spring8.or.jp

References

[1] A. Kotani and S. Shin: Rev. Mod. Phys. **73** (2001) 203.
[2] J.P. Rueff and A. Shukla: Rev. Mod. Phys. **82** (2010) 847.
[3] P. Glatzel *et al.*: J. Electr. Spectrosc. Relat. Phenom. **188** (2013) 17.

SACLA Beam Performance

During the period from April 2020 to the summer shutdown in August 2020, SACLA user experiments were severely affected by the global outbreak of COVID-19. Many of the experiments were cancelled not only by overseas users but also by domestic users. Even during this period, SACLA and SPring-8 accelerators were kept in operation to deliver X-rays to specially permitted experiments and R&D, contributing to a victory in the battle against the coronavirus pandemic. The above period was efficiently utilized for finalizing SACLA injection (beam injection from the SACLA to the storage ring) at a level applicable for user operations. After the long summer shutdown period, we continued test use of SACLA injection in regular user operations to confirm the stability of the performance over a long period of time.

At this point, there were still two major problems remaining. The first major problem is the purity deterioration of isolated bunches used for precise measurements of the time spectra. The purity deterioration is caused by dust electrons that are injected a few ns to tens of ns later than the main injection beam. We have investigated how the dust electrons are formed after the main beam and identified the following mechanism. Part of the electron beam is decelerated by a L-band APS cavity at the end of the buncher section and runs back towards the electron gun. Some of these electrons are captured by the upstream RF cavities and accelerated again with a distributed time delay from the main beam, forming dust electrons. A special dust electron sweeper was thus installed between the L-band correction and APS cavities to clean up the injection beam by kicking off the back-running electrons. This dust electron sweeper was able to efficiently purify the injection beam. Furthermore, in combination with the bunch cleaning system installed in the ring, highly purified isolated bunches have been constantly delivered to user experiments. Figure 1 illustrates the dust electron sweeper installed in the SACLA buncher section.

The second major problem is how to constantly deliver high-performance XFEL to experimental users by multi-beamline operations keeping top-up beam injections to the ring. During top-up operations, we can neither stop SACLA linac operations nor perform destructive measurements of beam profiles and RF phases, which severely restricts accelerator tuning.

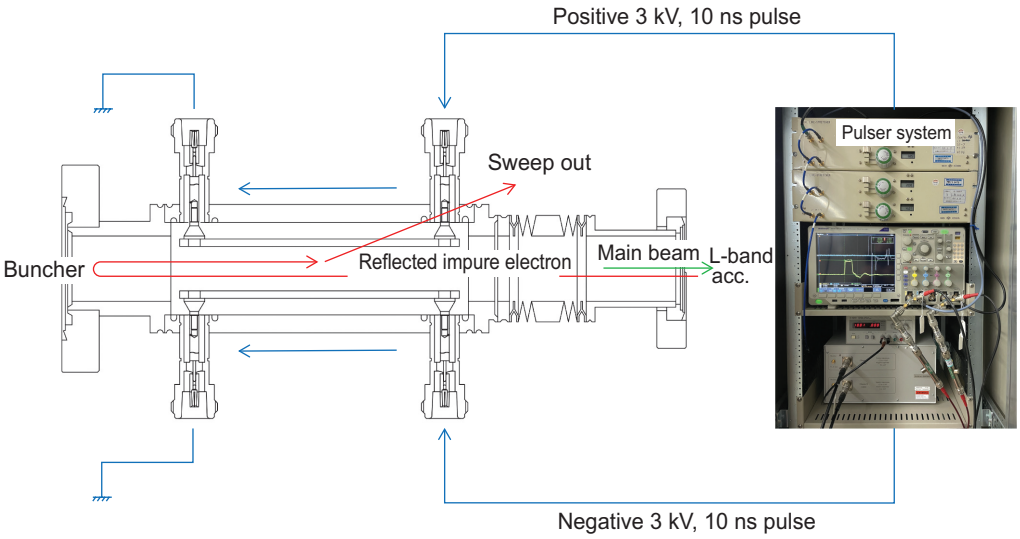

Fig. 1. Schematic of the dust electron sweeper installed in the SACLA buncher section.

To solve this problem, we should markedly improve the efficiency and transparency of accelerator tuning. As a first step towards highly efficient accelerator tuning to reproduce the XFEL performance, we have developed a model-free tuning tool using a Gaussian process regression (GPR) optimizer. To clearly define the target XFEL performance as a numerical value, several XFEL characteristics such as pulse energy, spectral bandwidth, and laser profile are numerated and linearly combined with arbitral weights to form an objective function. We have also built a shot-by-shot data acquisition system that collects the necessary data from the photon beam diagnostic system, so that the GPR optimizer utilizes shot-by-shot data representing XFEL characteristics. The developed tuning tool is now in daily accelerator operations. As shown in Fig. 2, the developed optimizer can reproduce XFEL efficiently.

The performance of SXFEL at BL1 has been at a low level owing to the serious demagnetization of three undulators by electron bombardment. Although it is difficult to apply drastic measures in a short period of time, we plan to implement the following measures in March 2021. The two old in-vacuum undulators of the three will be removed, and one in-vacuum undulator will be moved from each of BL2 and BL3. The field distribution of the undulator not to be replaced will be adjusted on the basis of the SAFARI measurement result to reduce the phase error. With this improvement, we expect to be able to recover the pulse energy of SXFEL to about 50 μJ at a photon energy of 100 eV.

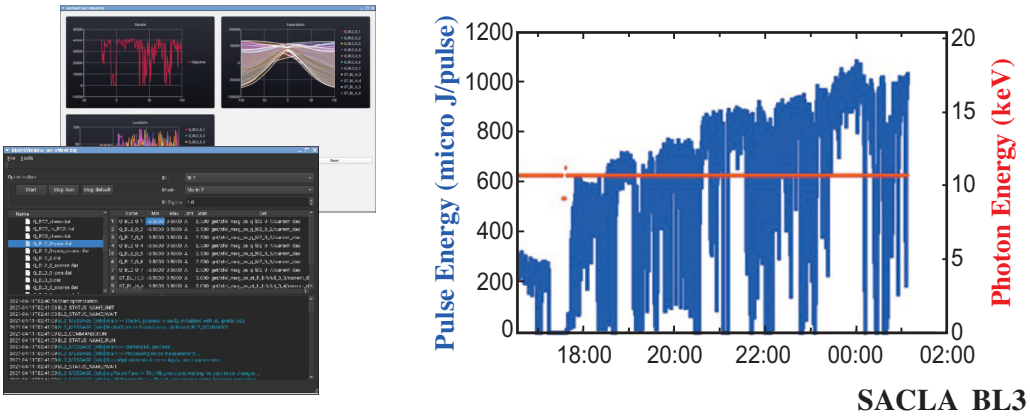

Fig. 2. Progress of pulse energy with the GPR optimizer during the startup period (right) and displays of the developed GPR tool kit.

Hitoshi Tanaka

RIKEN SPring-8 Center

Email: tanaka@spring8.or.jp

FACILITY STATUS

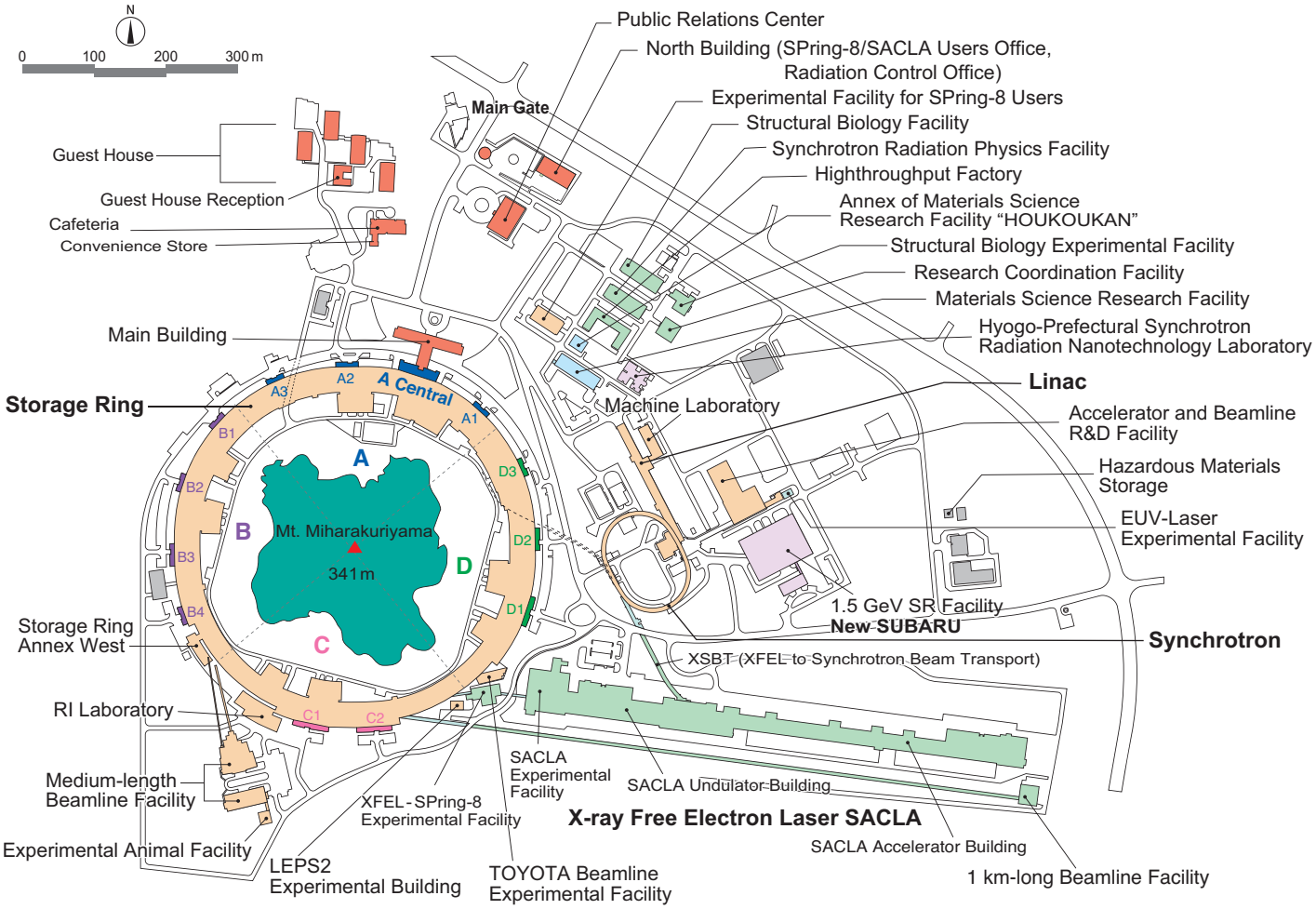

SPring-8

I. Introduction

SPring-8 was stably operated throughout FY2020 with the total operation time of the accelerator complex and the total user beam time of 5284.6 h and 4309.0 h, respectively, and a total downtime of 7.4 h. SPring-8 had to complete all its operations by the middle of February 2021. (Because of the rapid spread of COVID-19, user operations at SPring-8/SACLA had been suspended from 11th April to 15th June 2020.)

Concerning the contract beamlines, there were two interim reviews conducted for Hyogo BM (BL08B2, Hyogo Prefecture) and Hyogo ID (BL24XU, Hyogo Prefecture), and the project was authorized to continue. Upon the expiration of their contract terms, reviews were also conducted for Laser-Electron Photon (BL31LEP, Research Center for Nuclear Physics, Osaka University), and RISING II BL28XU, Kyoto University), and their proposals for the next term were approved. On the other hand, Laser-Electron Photon (BL33LEP, Research Center for Nuclear Physics, Osaka University) was recommended to be terminated.

At present, the number of SPring-8 users is as high as 13,000, all of whom are members of the SPring-8 User Community (SPRUC).

It is important for SPring-8 to jointly organize scientific events with SPRUC, such as the SPring-8 Symposium, to facilitate dialogue between users and the facility staff. In 2020, the SPring-8 Symposium was held online on September 18 owing to COVID-19, with a participant number of 391. SPring-8 also facilitates communication between users and industry. The Joint Conference on Industrial Applications of SPring-8 was held in Hyogo Prefecture on September 3–4, 2020, with 232 participants (126 online participants). As part of its continuous effort towards fostering human resources in synchrotron sciences, SPring-8 organized the 20th SPring-8 Summer School with 32 students of graduate schools nationwide, in cooperation with University of Hyogo, Kwansei Gakuin University, the University of Tokyo, Okayama University, Osaka University, Japan Atomic Energy Agency, National Institutes for Quantum and Radiological Science and Technology, and RIKEN. Furthermore, SPring-8 and SPRUC organized the 4th SPring-8 Autumn School with 47 participants, which included university students and corporate researchers.

II. Machine Operation

In FY2020, the SPring-8 operation of beam injection from the SACLA linac to the storage ring was started. The total operation time of the entire SPring-8 accelerator complex was 5284.6 h. The operation time of the storage ring was 5274.8 h, 81.7% of which (4309.0 h) was devoted to SR experiments. Most of the user time was taken up by beam accumulation and topping-up by beam injection from the SACLA linac. There was no serious machine trouble in the storage ring that might have led to interruptions of user time for more than two hours. The total downtime caused by failures amounted to 7.4 h, which accounted for 0.17% of the total user time. The considerably shorter downtime than in previous years has led to an excellent storage ring availability of 99.7%. The availability this year was calculated by excluding, from the planned user time, a certain period when normal user operation was not available owing to the COVID-19 state of emergency. For 99.4% of the user time in FY2020, the stored beam current was maintained at 100 mA by the top-up operation wherein the stored beam was filled up on demand at any time. Extreme stability of better than 0.1% in the light source intensity was achieved by the top-up operation. The operation statistics of SPring-8 for the last five fiscal years are shown in Fig. 1.

The large variety of operation modes for the SR experiments is one of the characteristics of SPring-8. The operation modes are classified into two types: the several-bunch and hybrid-filling modes. The several-bunch mode consists of equally spaced bunches or trains of bunches, for example, 203 bunches or 29 trains of 11 bunches. The hybrid-filling mode is composed of a long train of bunches and isolated single bunches. The operation modes of SPring-8 are listed in Table 1 with the share of each operation mode in FY2020. In the operation with beam injection from the SACLA linac, the spurious bunch sweeping system in the SACLA linac and the bunch cleaning system in the storage ring are activated to maintain a sufficient isolated bunch purity. Table 2 shows the beam parameters of the storage ring.

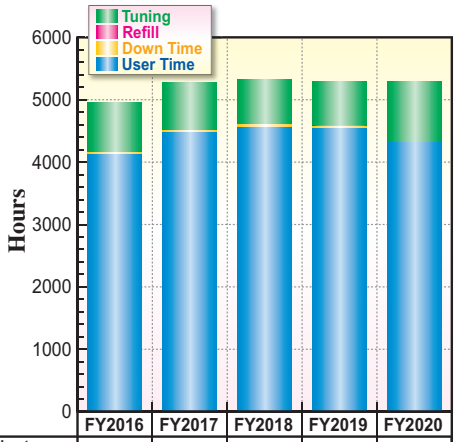

	FY2016	FY2017	FY2018	FY2019	FY2020
Accelerator Operation Time	4951.7	5281.6	5329.8	5285.7	5284.6
Storage Ring Operation Time	4941.1	5270.4	5316.7	5271.2	5274.8
Tuning & Study (Acc. & BL)	803.1	769.6	721.8	701.7	964.6
Refill	3.4	4.6	5.3	5.6	3.6
Down Time	23.1	28.7	43.1	40.5	7.4
Mean Time Between Failures	229.2	194.7	168.9	206.3	718.2
Achieved User Time	4125.5	4478.7	4559.6	4537.9	4309.0
Planned User Time	4152.0	4512.0	4608.0	4584.0	4464.0
Availability (%)	99.4	99.3	98.9	99.0	99.7

Fig. 1. Operation statistics for last five fiscal years.

Table 1. Operation modes in FY2020

	Single bunch current (mA)	Share of operation time (%)
203 bunches		32.6
4 bunch-train × 84		14.0
11 bunch-train × 29		14.6
1/7-filling + 5 single bunches	3	20.8
2/29-filling + 26 single bunches	1.4	5.1
1/14-filling + 12 single bunches	1.6	0
4/58-filling + 53 single bunches	1.0	0
11/29-filling + 1 single bunch	5	12.9

Table 2. Beam parameters of SPring-8 storage ring

Energy [GeV]	8
Number of buckets	2436
Tunes (ν_x / ν_y)	41.14 / 19.34
Current [mA]:	
single bunch	12
multi bunch	100
Bunch length (σ) [psec]	13
Horizontal emittance [nm·rad]	2.4*
Vertical emittance [pm·rad]	4.8*
Coupling [%]	0.2
RF Voltage [MV]	14.4** ~ 16
Momentum acceptance [%]	3.2 (~256 MeV)
Beam size (σ_x / σ_y)* [μm]	
Long ID section	333 / 7
ID section	316 / 5
BM1 section	94 / 12
BM2 section	100 / 12
Beam divergence (σ_x' / σ_y')* [μrad]	
Long ID section	8 / 0.7
ID section	9 / 1.0
BM1 section	58 / 0.5
BM2 section	68 / 0.5
Operational chromaticities (ξ_x / ξ_y)	+2 / +2***
Lifetime [hr]:	
100 mA (multi bunch)	~250
1 mA (single bunch)	~30
Horizontal dispersion [m]:	
Long ID section	0.153
ID section	0.146
BM1 section	0.039
BM2 section	0.059
Fast orbit stability (0.1 – 200 Hz) [μm]:	
horizontal (rms)	~4
vertical (rms)	~1

* Assuming 0.2% coupling
** Power saving mode
*** With bunch-by-bunch feedback

III. Beamlines

The SPring-8 storage ring can accommodate up to 62 beamlines: 34 insertion devices, 4 long undulators, and 24 bending magnets. At present, 57 beamlines are in operation, covering a wide variety of research fields involving synchrotron radiation science and technology. The beamlines are classified into the following three types.

(1) Public Beamlines (26 beamlines operating),
(2) Contract Beamlines (17 beamlines operating), and
(3) RIKEN Beamlines (13 beamlines operating).

There are now 26 public beamlines in full operation. The beamlines that have been proposed and constructed by external organizations, such as universities, research institutes, private companies and consortiums, are called contract beamlines and are used exclusively by the contractors for their own research purposes. At present, 17 contract beamlines are in operation. The beamlines constructed by RIKEN or transferred to RIKEN, except for public beamlines, are called RIKEN beamlines and are mainly used for RIKEN's own research activities, with partial availability for public use. RIKEN is now operating 13 beamlines. To illustrate the beamline portfolio of SPring-8, a beamline map is shown in Fig. 2 together with the beamline classification. The research fields of each beamline are presented in Table 3.

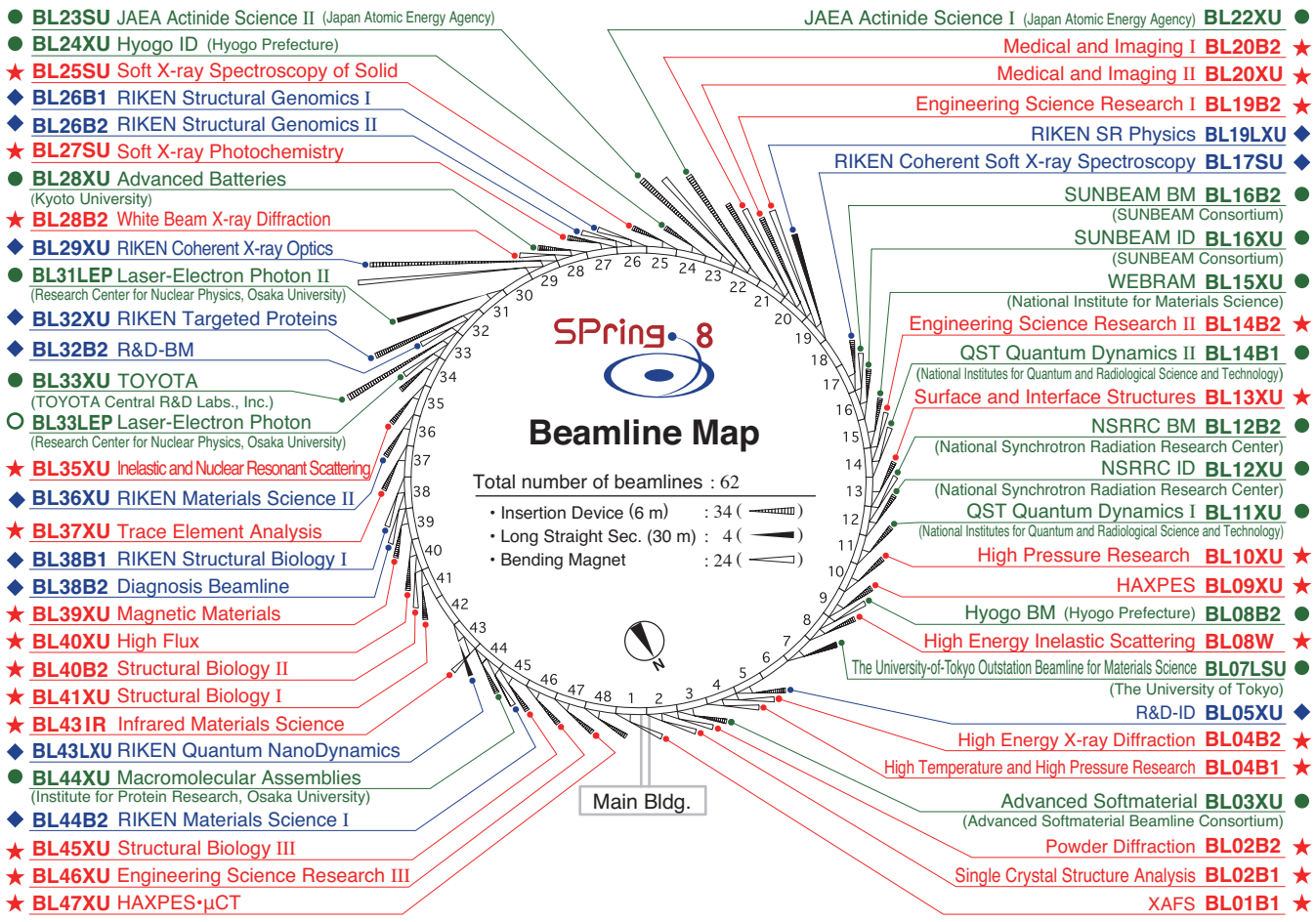

BL: Beamline
B1, B2: Bending Magnets
XU: X-ray Undulator
SU: Soft X-ray Undulator
W: Wiggler

IR: Infrared Radiation
LEP: Laser-Electron Photon
LXU: Long-length X-ray Undulator
LSU: Long-length Soft X-ray Undulator

★ : Public Beamlines
● : Contract Beamlines
◆ : RIKEN Beamlines

○ : Under removal work

WEBRAM: Wide Energy Range Beamline for Research in Advanced Materials
NSRRC: National Synchrotron Radiation Research Center, Taiwan
RISING: Research & Development Initiative for Scientific Innovation of New Generation Batteries

Fig. 2. Beamline map.

Table 3. List of beamlines

BL #	Beamline Name	(Public Use) or (First Beam)	Areas of Research and Available Techniques
★ Public Beamlines as of April 2021			
BL01B1	XAFS	(Oct. 1997)	XAFS in wide energy region (3.8 to 113 keV). XAFS of dilute systems and thin films. Quick XAFS with a time resolution of seconds to tens of seconds.
BL02B1	Single Crystal Structure Analysis	(Oct. 1997)	Charge density study and crystal structure analysis from single crystal X-ray diffraction. (X-ray energy range: 8 – 115 keV)
BL02B2	Powder Diffraction	(Sept. 1999)	Crystal structure study by Rietveld method, and *in situ* powder diffraction experiment under various conditions. (X-ray energy range: 12 – 37 keV)
BL04B1	High Temperature and High Pressure Research	(Oct. 1997)	High temperature and high pressure research with the multi-anvil press by powder X-ray diffraction, radiography and ultrasonic measurement.
BL04B2	High Energy X-ray Diffraction	(Sept. 1999)	Pair distribution function analysis for glass, liquid, and amorphous materials. High-energy X-ray total scattering. Containerless levitation.
BL08W	High Energy Inelastic Scattering	(Oct. 1997)	Magnetic Compton scattering. High-resolution Compton scattering. High-energy Bragg scattering. High-energy fluorescent X-ray analysis.
BL09XU	HAXPES	(Oct. 1997)	Hard X-ray photoelectron spectroscopy (HAXPES). Electronic state analysis with tunable energy (resonant HAXPES) and high energy resolution. Depth analysis of angle resolved HAXPES with wide acceptance lens.
BL10XU	High Pressure Research	(Oct. 1997)	Structure analysis and phase transitions under ultrahigh pressure (DAC experiment). Earth and planetary science.
BL13XU	Surface and Interface Structures	(Sept. 2001)	Atomic-scale structural analysis of surfaces and interfaces of crystalline materials, ultrathin films, and nanostructures. Surface X-ray diffraction (SXRD). Microbeam diffraction.
BL14B2	Engineering Science Research II	(Sept. 2007)	X-ray Imaging. XAFS in wide energy region (3.8 to 72 keV). XAFS of dilute systems and thin films.
BL19B2	Engineering Science Research I	(Nov. 2001)	Residual stress measurement. Structural analysis of thin film, surface, interface. Powder diffraction. X-ray topography. Ultrasmall angle X-ray scattering.
BL20XU	Medical and Imaging II	(Sept. 2001)	Microimaging. Micro-/nano-tomography, phase-contrast microtomography, X-ray diffraction tomography (XRD-CT), hard X-ray microbeam/scanning microscopy, imaging microscopy, coherent X-ray optics, and other experiments on X-ray optics and developments of optical elements. Refraction-enhanced imaging. Ultrasmall angle scattering.
BL20B2	Medical and Imaging I	(Sept. 1999)	Microimaging: microtomography, phase-contrast microtomography with grating interferometer for biological specimen and other kinds of specimen. Evaluation and development of various kinds of optical elements for novel imaging techniques. Large field X-ray topography.
BL25SU	Soft X-ray Spectroscopy of Solid	(Apr. 1998)	Study of electronic state of solids by soft X-ray photoemission spectroscopy (PES) including angle-resolved PES (ARPES). Atomic arrangement analysis of surfaces by photoelectron diffraction (PED) technique using two-dimensional photoemission analyzer. Magnetic state analysis by magnetic circular dichroism (MCD) of soft X-ray absorption and its element-specific magnetization curve measurements.
BL27SU	Soft X-ray Photochemistry	(May 1998)	Ambient atmospheric pressure soft X-ray photoabsorption spectroscopy. Chemical state analysis of light elements in dilute samples (NEXAFS). Elemental and chemical mapping using micro soft X-ray beam. Soft-X-ray emission spectroscopy.
BL28B2	White Beam X-ray Diffraction	(Sept. 1999)	White X-ray diffraction and topography. Time-resolved energy-dispersive XAFS (DXAFS) for studies of chemical and/or physical reaction process. Biomedical imaging and radiation biology studies. High energy X-ray microtomography.
BL35XU	Inelastic and Nuclear Resonant Scattering	(Sept. 2001)	Phonons in solids and atomic dynamics in disordered materials by inelastic X-ray scattering. Atomic and molecular dynamics by nuclear resonant inelastic scattering and quasi-elastic scattering. Synchrotron-radiation-based Mössbauer spectroscopy. Nuclear excitation.
BL37XU	Trace Element Analysis	(Nov. 2002)	X-ray spectrochemical analysis using micro/nano beam: Scanning X-ray microspectroscopy. X-ray spectroscopic imaging: Projection type spectroscopic tomography and imaging type spectroscopic tomography. Ultra trace element analysis. High energy X-ray fluorescence analysis.
BL39XU	Magnetic Materials	(Oct. 1997)	X-ray magnetic circular dichroism (XMCD) spectroscopy and element-specific magnetometry under multiple-extreme conditions. XMCD/XAS using a 100 nm focused X-ray beam. X-ray emission spectroscopy.
BL40XU	High Flux	(Apr. 2000)	Time-resolved diffraction and scattering experiments. Microbeam X-ray diffraction and scattering experiments. X-ray photon correlation spectroscopy. Fluorescence analysis. Quick XAFS. Submicrometer-scale single crystal structure analysis with high flux and zone plate focused X-ray beam. Single shot imaging with X-ray choppers. Laser pump-X-ray probe experiment.
BL40B2	Structural Biology II	(Sept. 1999)	Noncrystalline small and wide angle X-ray scattering.
BL41XU	Structural Biology I	(Oct. 1997)	Structural biology. Macromolecular crystallography. Microcrystallography. High resolution data collection.
BL43IR	Infrared Materials Science	(Apr. 2000)	Infrared microspectroscopy.
BL45XU	Structural Biology III	(Apr. 2019)	Structural biology. Macromolecular crystallography. Automation & High throughput data collection. Microcrystallography.
BL46XU	Engineering Science Research III	(Nov. 2000)	Structural characterization of thin films by X-ray diffraction and X-ray reflectivity measurement. Residual stress measurement. Time resolved X-ray diffraction measurement. Hard X-ray Photoemission Spectroscopy. X-ray Imaging.
BL47XU	HAXPES·μCT	(Oct. 1997)	Hard X-ray photoelectron spectroscopy (HAXPES). Depth analysis of angle resolved HAXPES with wide acceptance lens. Projection type microtomography. Imaging type microtomography. Hard X-ray microbeam/scanning microscopy.

BL #	Beamline Name	(Public Use) or (First Beam)	Areas of Research and Available Techniques
	● Contract Beamlines as of April 2021		
BL03XU	**Advanced Softmaterial** (Advanced Softmaterial Beamline Consortium)	(Nov. 2009)	Structural characterization of softmaterials using small- and wide-angle X-ray scattering. Grazing-incidence small- and wide-angle X-ray scattering for thin films.
BL07LSU	**The University-of-Tokyo Outstation Beamline for Materials Science** (The University of Tokyo)	(Oct. 2009)	Ambient pressure photoemission spectroscopy, nano-beam photoemission spectroscopy, high-resolution soft X-ray emission spectroscopy, and any methods requiring the highly brilliant soft X-ray beam.
BL08B2	**Hyogo BM** (Hyogo Prefecture)	(Jun. 2005)	XAFS in a wide energy region. Small angle X-ray scattering. X-ray topography. Imaging. X-ray diffraction for multipurpose.
BL11XU	**QST Quantum Dynamics I** (National Institutes for Quantum & Radiological Science & Technology)	(Oct. 1998)	Nuclear resonant scattering. Surface and interface structure with MBE. Resonant inelastic X-ray scattering. X-ray emission spectroscopy.
BL12B2	**NSRRC BM** (National Synchrotron Rad. Res. Center)	(Oct. 2000)	X-ray absorption spectroscopy. Powder X-ray diffraction. High resolution X-ray scattering. Protein crystallography.
BL12XU	**NSRRC ID** (National Synchrotron Rad. Res. Center)	(Dec. 2001)	Non-resonant or resonant inelastic X-ray scattering. Hard X-ray photoemission spectroscopy.
BL14B1	**QST Quantum Dynamics II** (National Institutes for Quantum & Radiological Science & Technology)	(Dec. 1997)	Materials science at high pressure. XAFS. Time-resolved energy-dispersive XAFS (DXAFS).
BL15XU	**WEBRAM** (National Institute for Materials Science)	(Jan. 2000)	Under preparations
BL16B2	**SUNBEAM BM** (SUNBEAM Consortium)	(Oct. 1998)	Characterization of secondary battery related materials, semiconductors, fuel cells, catalysts, and several industrial materials with using X-ray absorption fine structure measurements, X-ray diffraction (including X-ray reflectivity technique), X-ray topography and computed tomography/laminography.
BL16XU	**SUNBEAM ID** (SUNBEAM Consortium)	(Oct. 1998)	Characterization of secondary battery related materials, semiconductors, fuel cells, catalysts, and structural materials using X-ray diffraction, X-ray microbeam based evaluation techniques (including X-ray magnetic circular dichroism), hard X-ray photoelectron spectroscopy and fluorescence X-ray analysis.
BL22XU	**JAEA Actinide Science I** (Japan Atomic Energy Agency)	(May 2002)	HAXPES. XAFS. Residual stress/strain distribution analysis. Materials science under high-pressure. Coherent X-ray diffraction. Surface X-ray diffraction. High-energy X-ray diffraction.
BL23SU	**JAEA Actinide Science II** (Japan Atomic Energy Agency)	(Feb. 1998)	Surface chemistry with supersonic molecular beam. Photoelectron spectroscopy. Magnetic circular dichroism. STXM.
BL24XU	**Hyogo ID** (Hyogo Prefecture)	(May. 1998)	Microbeam small- and wide-angle X-ray scattering for local structure analysis. Scanning and imaging microscope, micro-tomography, coherent diffraction. Microbeam X-ray diffraction and bright field X-ray topography for electronic device materials. Near-ambient pressure hard X-ray photoelectron spectroscopy.
BL28XU	**Advanced Batteries** (Kyoto University)	(Apr. 2012)	Characterization of rechargeable battery reactions and battery related materials by resonance X-ray diffraction, X-ray absorption spectroscopy (XAS), X-ray diffraction spectroscopy (XDS), and hard X-ray photoemission spectroscopy (HAXPES).
BL31LEP	**Laser-Electron Photon II** (RCNP, Osaka University)	(Oct. 2013)	Production of high intensity GeV photon beam by laser-backward Compton scattering. Hadron physics via photonucleon and photonuclear reactions. Test and calibration of detectors with GeV gamma-ray and converted electrons/positrons.
BL33LEP	**Laser-Electron Photon** (RCNP, Osaka University)	(Jun. 1999)	Under removal work
BL33XU	**TOYOTA** (TOYOTA Central R&D Labs., Inc.)	(Apr. 2009)	Time-resolved XAFS. 3DXRD. Characterization of industrial materials and devices (e.g. catalysts, lightweight bodies, secondary batteries, fuel cells, and power modules).
BL44XU	**Macromolecular Assemblies** (IPR, Osaka University)	(May 1999)	Crystal structure analysis of biological macromolecular assemblies (e.g., membrane protein complexes, protein complexes, protein-nucleic acid complexes, and viruses).
	◆ RIKEN Beamlines as of April 2021		
BL05XU	**R&D-ID**	(Mar. 2004)	Structural and dynamical research using small and wide angle scattering, R&D of SR instruments.
BL17SU	**RIKEN Coherent Soft X-ray Spectroscopy**	(Sept. 2003)	High resolution photoemission spectroscopy. Soft X-ray emission spectroscopy. Soft X-ray diffraction spectroscopy. Soft X-ray microspectroscopy.
BL19LXU	**RIKEN SR Physics**	(Oct. 2000)	SR science with highly brilliant X-ray beam.
BL26B1	**RIKEN Structural Genomics I**	(Apr. 2002)	Structural biology research based on single crystal X-ray diffraction.
BL26B2	**RIKEN Structural Genomics II**	(Apr. 2002)	Structural biology research based on single crystal X-ray diffraction.
BL29XU	**RIKEN Coherent X-ray Optics**	(Dec. 1998)	X-ray optics, especially coherent X-ray optics.
BL32XU	**RIKEN Targeted Proteins**	(Oct. 2009)	Protein microcrystallography.
BL32B2	**R&D-BM**	(May 2002)	X-ray computed tomography, X-ray diffraction, X-ray absorption fine structure, R&D of SR instruments.
BL36XU	**RIKEN Materials Science II**	(Jan. 2013)	Time resolved XAFS and X-ray diffraction, 2D/3D scanning XAFS imaging, 3D computed tomography/laminography XAFS imaging, X-ray emission spectroscopy, ambient pressure hard X-ray photoelectron spectroscopy, pink beam experiment.
BL38B1	**RIKEN Structural Biology I**	(Oct. 2000)	Structure study of non-crystalline biological materials using small-angle scattering and diffraction techniques.
BL38B2	**Diagnosis Beamline**	(Sept. 1999)	Accelerator beam diagnostics.
BL43LXU	**RIKEN Quantum NanoDynamics**	(Oct. 2011)	High resolution inelastic X-ray scattering for investigating atomic and electronic dynamics.
BL44B2	**RIKEN Materials Science I**	(Feb. 1998)	Structural materials science research using powder X-ray diffraction.

IV. User Program and Statistics

SPring-8 calls for public use proposals twice a year, in principle. However, proposals were not called for 2020B because of the COVID-19 pandemic. The submitted proposals are reviewed by the SPring-8 Proposal Review Committee (SPring-8 PRC). Since 1997, SPring-8 has accepted a variety of proposals. For the promotion of research on industrial applications at SPring-8, the Industrial Application Division was established in 2005, with consultation support for industrial users being provided by the division's coordinators. Currently, Industrial Application Proposals account for approximately 16%–18% of the total number of proposals conducted at the public beamlines. There always exist those companies and research institutes that find it difficult to retain specialized staff and to accommodate the need for quick access to SPring-8. To appropriately respond to this circumstance, the SPring-8 Measurement Service has been established. In this framework of service, JASRI staff members perform measurements on behalf of users. It is up to the users whether to come to SPring-8 and be present during the measurements or to simply send their samples to SPring-8. As far as the formalization of the proposal system is concerned, applications for this service are treated as proprietary, and, therefore, are subject to the conditions applied to proprietary beamtime and the user beamtime fee for Time-Designated Proposals (calculated in two-hour increments), as mentioned in the previous section. Currently, the Industrial Application Division of JASRI is carrying out XAFS measurements on behalf of users at BL14B2. Since 2009B, the purview of the SPring-8 Measurement Service has been expanded by including Mail-in Protein Crystallography Data Collection at BL38B1 and Powder X-ray Diffraction at BL19B2. In addition, the Feasibility Study Proposal for Industrial Application was introduced in 2018A. The Feasibility Study Proposal for Industrial Application is designed to provide a simple procedure for beamtime application to SPring-8 for users who are interested in the use of SPring-8 or considering an application to SPring-8. Feasibility Study Proposals for Industrial Applications are considered a form of proprietary proposals and are subject to the proprietary beamtime fee and user fee applicable to “Proprietary Time-Designated Proposals.” All three Engineering Science Research Beamlines (BL14B2, BL19B2 and BL46XU) as well as measurement techniques at these beamlines are available to this proposal. The staff of the Industrial Application Division of the Japan Synchrotron Radiation Research Institute (JASRI) will perform measurements at SPring-8 on behalf of users, in common with Measurement Services. Therefore, users can choose whether to come to SPring-8 and be present during the measurements or to simply send their samples to SPring-8. Protein Crystallography Automatic Data Collection was introduced in 2019B; users need only to send samples to SPring-8 to obtain data (no visit required).

SPring-8 has been consistently providing ~4,500 h of user beamtime per year. Since the start of its operation in 1997, SPring-8 has succeeded in providing users with

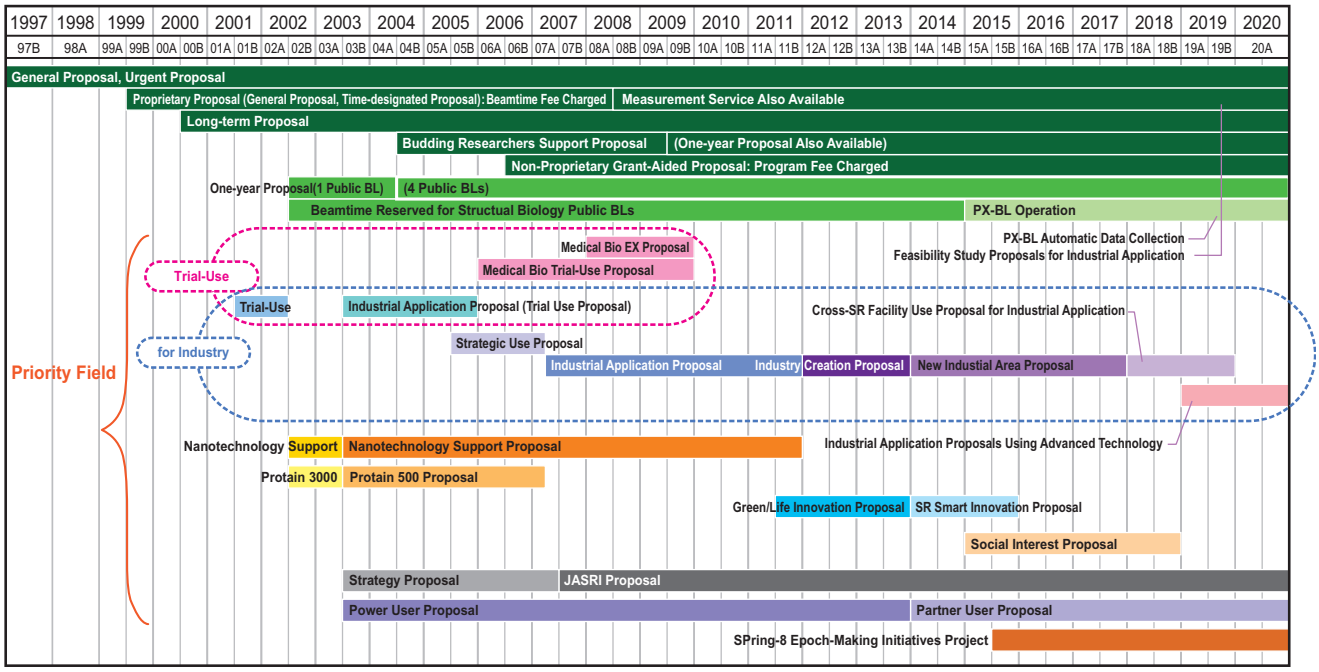

Fig. 3. Categories of proposals for the public beamlines.

a total beamtime of 91,859 h. The beamtime available to users, the number of experiments conducted, and the number of user visits at the public and contract beamlines are summarized in Fig. 3. Part of the proposals are for proprietary use, for which refereed reports are not required. Figures 4 to 13 show the information on user programs.

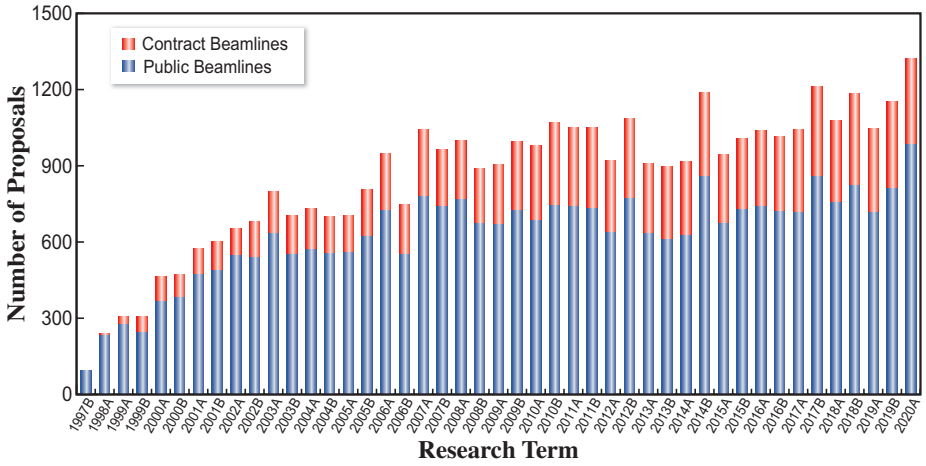

Fig. 4. Numbers of conducted experiments.

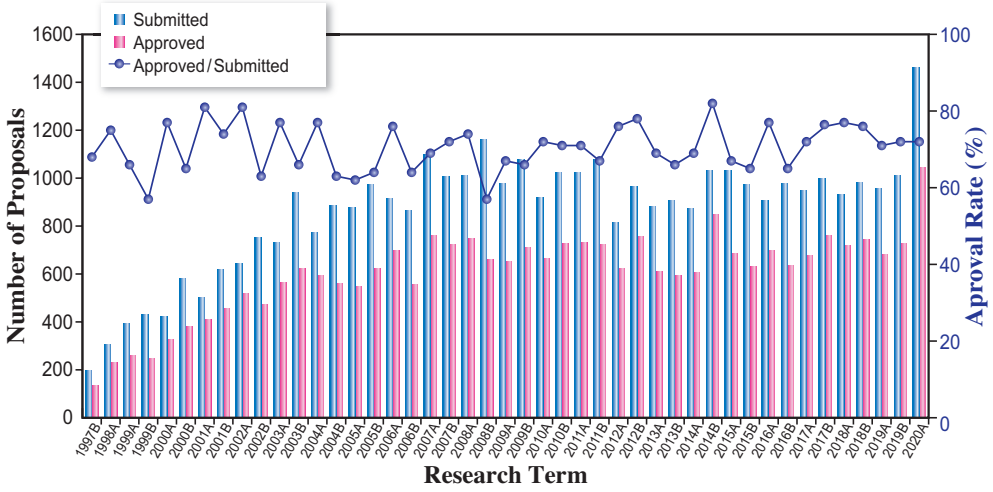

Fig. 5. Numbers of submitted proposals and approved proposals by research term (public beamlines).

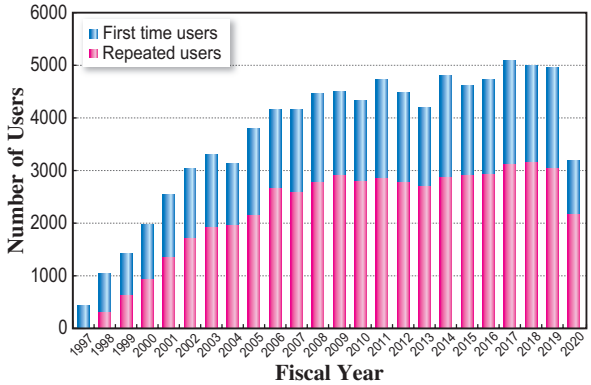

Fig. 6. Numbers of users by fiscal year.

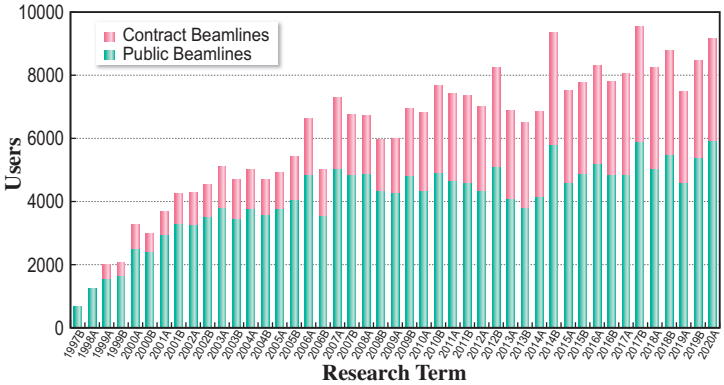

Fig. 7. Numbers of users visits by research term.

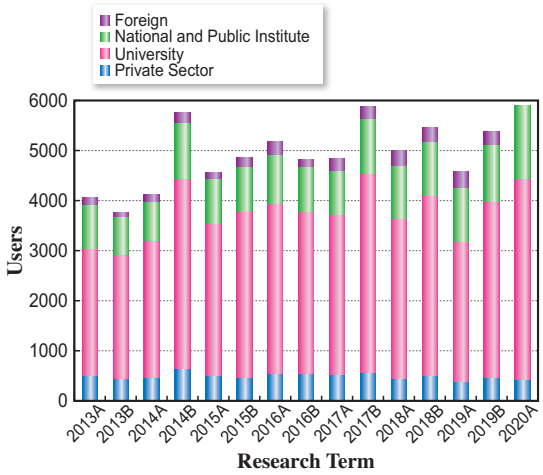

Fig. 8. Numbers of users by affiliation categories (public beamlines).

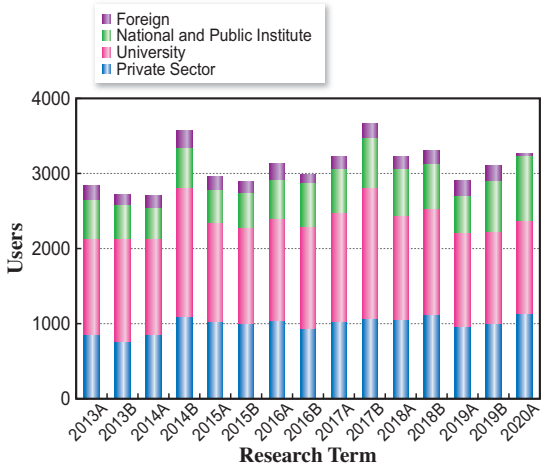

Fig. 9. Numbers of users by affiliation categories (contract beamlines).

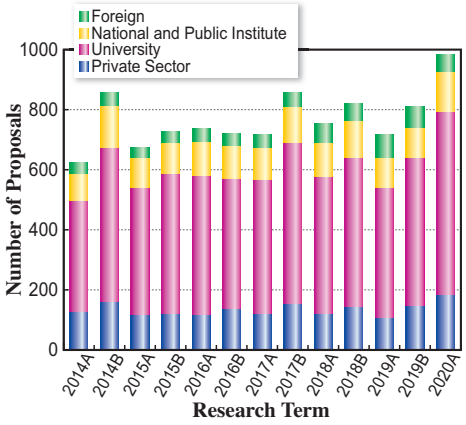

Fig. 10. Numbers of conducted proposals by affiliation (public beamlines).

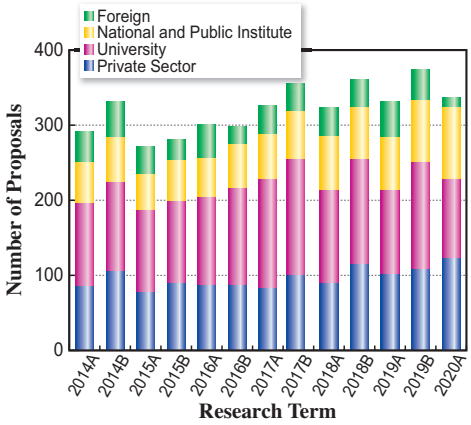

Fig. 11. Numbers of conducted proposals by affiliation categories (contract beamlines).

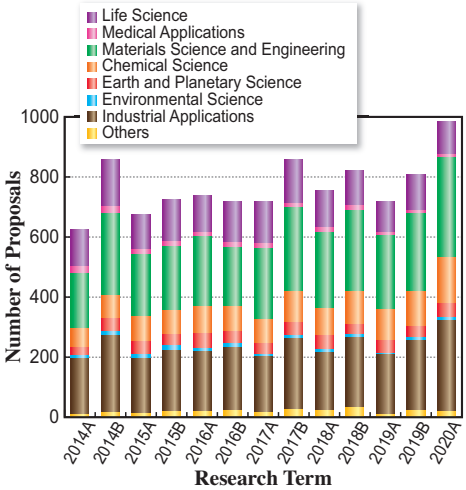

Fig. 12. Numbers of conducted proposals by research area (public beamlines).

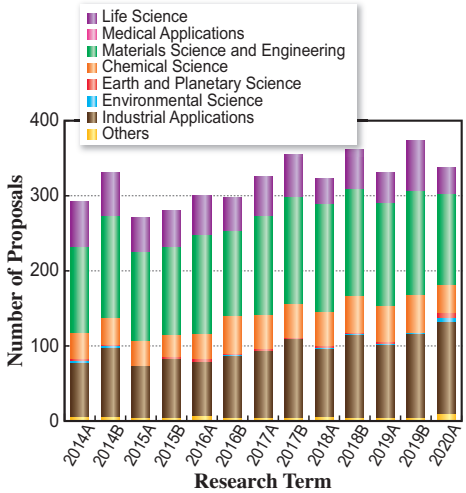

Fig. 13. Numbers of conducted proposals by research area (contract beamlines).

V. Research Outcome

As of March 2021, the total number of registered refereed papers from SPring-8 was 18,398. Figure14 shows the annual statistics of refereed papers.

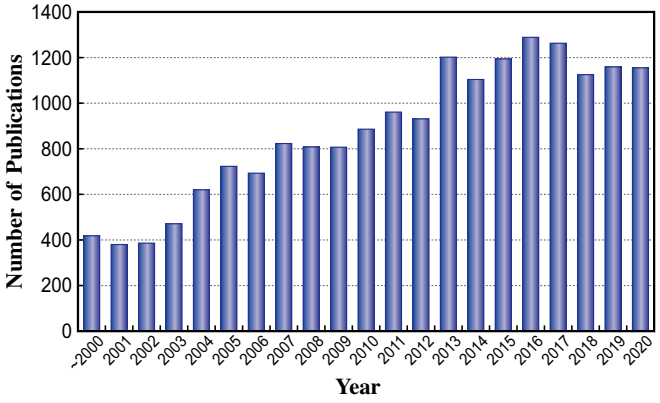

Fig. 14. Number of refereed publications.

VI. Budget and Personnel

When SPring-8 started operation in 1997, it was jointly managed by RIKEN, JAERI (now JAEA), and JASRI. However, JAERI withdrew from the management of SPring-8 on September 30, 2005. SPring-8 is currently administered by RIKEN and JASRI collaboratively.

The total budget for the operation of SPring-8 in FY2020 was about 9.1 billion yen. As of October 2020, the total number of RIKEN and JASRI staff members is 446. Figure 15 shows the annual budget allocated to the operation, maintenance, and promotion of SPring-8. Figure 16 shows the manpower of RIKEN and JASRI.

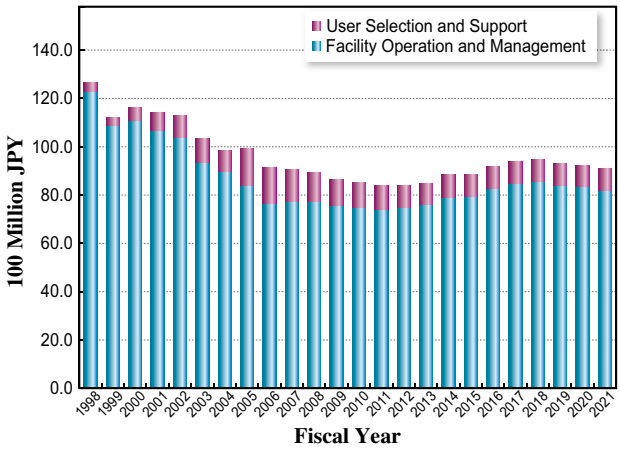

Fig. 15. SPring-8 budget.

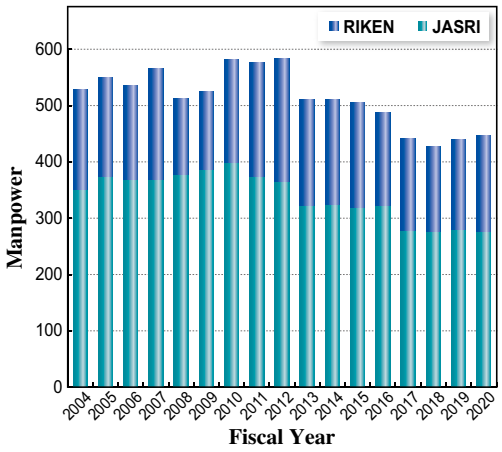

Fig. 16. Personnel at SPring-8: JASRI and RIKEN.

VII. Research Complex

The facilities of SPring-8, SACLA, and NewSUBARU form the Center of Excellence (COE) at the SPring-8 campus where JASRI, public beamline users, the contractors of contract beamlines, RIKEN, and the University of Hyogo work in close cooperation, forming a research complex where each member has their own role in delivering high-quality results to the field of synchrotron radiation science and technology. The organizational charts of RIKEN and JASRI, which are at the center of this research complex, are shown in Fig. 17 and Fig. 18, respectively.

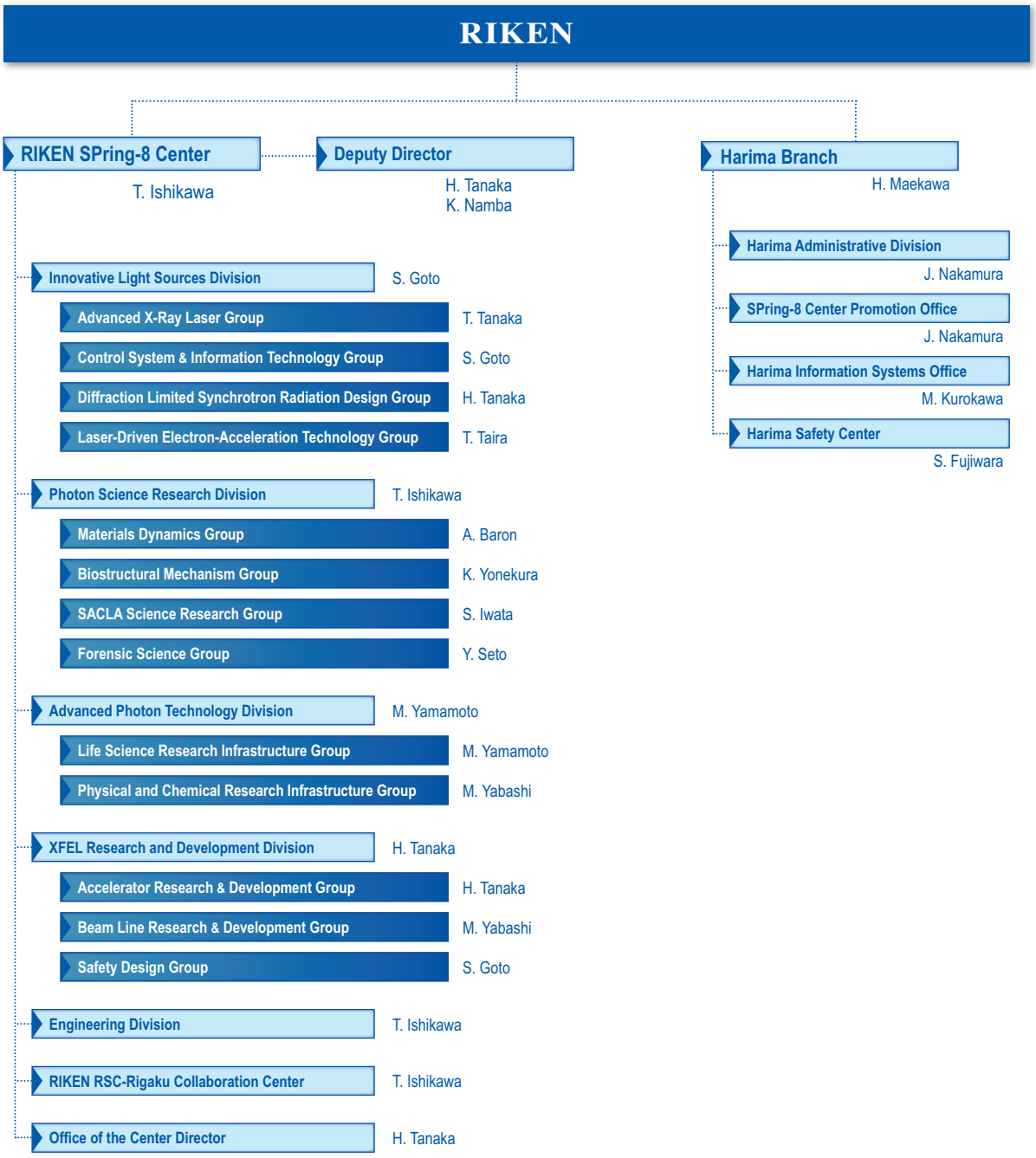

Fig. 17. RIKEN Harima Campus chart as of April 2021.

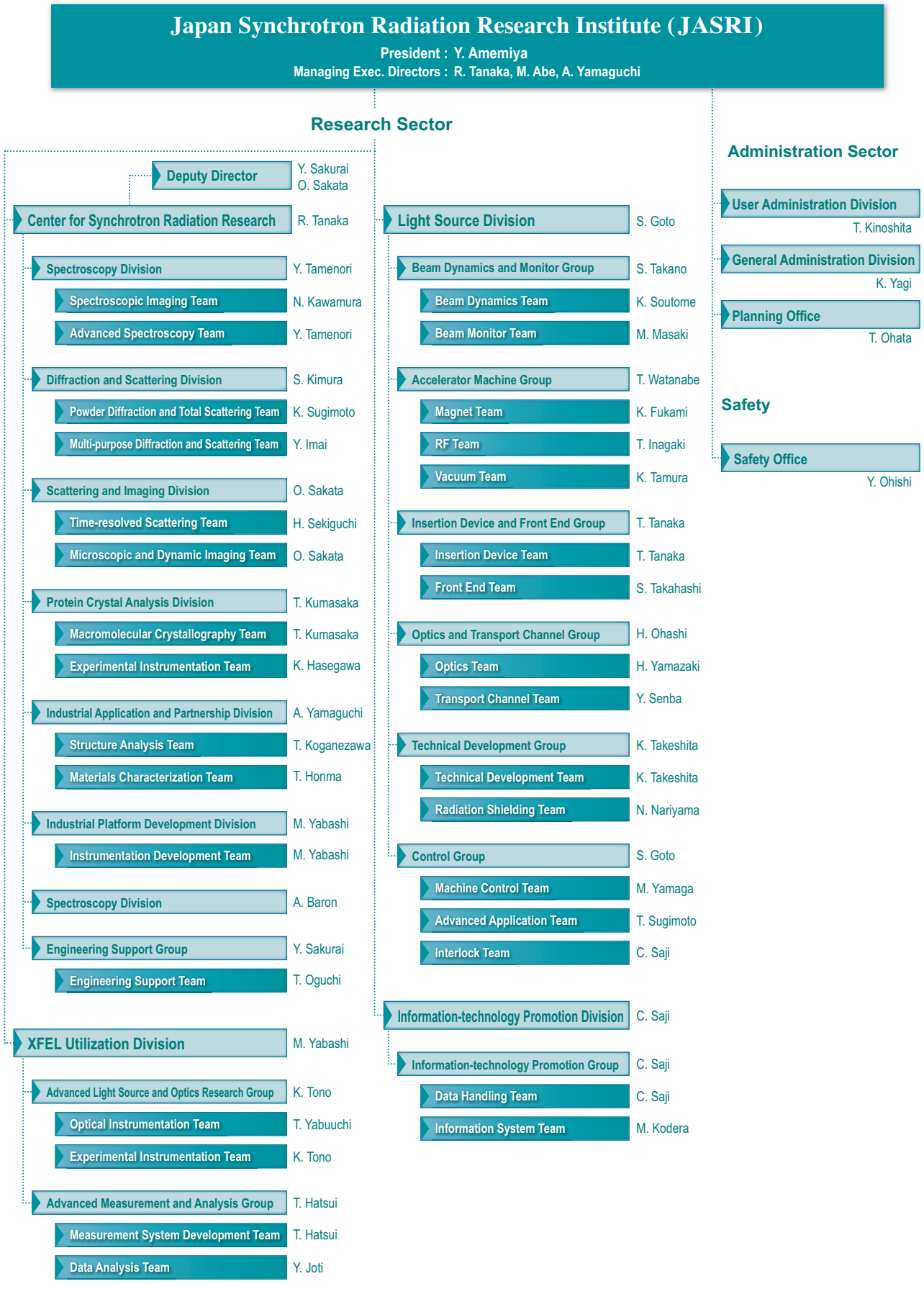

Fig. 18. JASRI chart as of April 2021.

VIII. SPring-8 Users Community (SPRUC)

Prof. A. Kimura
Hiroshima University
SPRUC Chairman FY2020

The SPring-8 Users Community (SPRUC) is a user society that consists of all users of SPring-8/SACLA. In addition to individuals, representative organizations comprising 26 institutes (principal universities, national/international research institutes, industries, beamline consortiums) participate in SPRUC to discuss further promotion of the utilization of SPring-8 from strategic and perspective viewpoints. Prof. Akio Kimura, Hiroshima University, has been serving as the president of SPRUC since FY2020.

As one of the key activities of SPRUC, the SPring-8 Symposium is held annually at the site of one of the representing organizations jointly with RIKEN and JASRI. SPring-8 Symposium 2020 had been scheduled to be held on September 18 and 19 at the International Congress Center EPOCAL TSUKUBA. However, owing to the COVID-19 pandemic, the plan was forced to be changed. SPring-8 Symposium 2020 with the theme "Use of SPring-8 in the Post-CORONA era" was held on September 18 with a hybrid style of on-site and online presentations. As indicated by the theme, the major issue of the symposium was to discuss how to promote remote experiments and automation of experimental processes. Demands and supplies concerning future perspectives, including Digital Transformation technology information transportation, were shared between users and facility. The ceremony to present the SPRUC 2020 Young Scientist Award, which was conferred on Dr. Taito Osaka, RIKEN, and Dr. Longjian Xie, University of Bayreuth, was also held. The decision on how to hold SPring-8 Symposium 2021, jointly hosted by SPRUC, RIKEN, JASRI, is to be made on the basis of the status of the COVID-19 pandemic.

SPRUC cohosted the third beamline upgrade workshop on March 5–6 with RIKEN and JASRI. The workshop was planned to enrich the information exchange between members of SPRUC and the facility. The workshop was also held as a hybrid style of on-site and online presentations. The workshop focused mainly on mutual consensus about the beamline reorganization of the hard X-ray photoemission, non-resonant inelastic X-ray scattering and nuclear resonant scattering experiments. The facility presented the latest situation of their reorganization, future prospect and related problems, and the members discussed demands and suggestions for beamline upgrades.

SPRUC2020 Young Scientist Award
Dr. T. Osaka, Dr. L. Xie, and Prof. A. Kimura

The fifth-term SPRUC research groups were voluntarily organized in each research field, and the research groups actively conducted research meetings. Each SPRUC research group has been collecting ideas and needs for beamline reorganization and innovative experimental techniques toward SPring-8 II, and has presented opinions and demands obtained through discussion in each field.

SPRUC supported the "SPring-8 Summer School" for the enhancement of user's research competency, and also hosted the "SPring-8 Autumn School" with JASRI for acquiring new users and human resources development. For the Autumn School, the SPRUC research groups contributed to planning of lectures. Although the number of participants was greatly reduced compared with previous years and the Autumn School was postponed to December owing to the COVID-19 pandemic, both schools were successfully held.

Finally, SPRUC continues to consider, as part of the SPring-8 utilization committee, how the Science Promotion Board, which was established with the purpose of making practical plans to realize cutting-edge science at SPring-8, should be actuated to promote the creation of new multidisciplinary research fields.

IX. Outreach Activities

To reach out to new users in unexplored fields of application, SPring-8 holds various serialized seminars named "Workshop on Advanced Techniques and Applications at SPring-8". This year, most of the workshops are being held as video conferences because of COVID-19. Here are some representatives.

- 54th: Automatic and Remote Measurement in the Protein Beamlines at SPring-8
  November 27, 2020 • Video conference
- 56th: Research for Advanced Devices
  March 3, 2021 • Video conference
- 59th: Current Status and Future Prospects of Protein Structural Biology Research at SPring-8
  March 23, 2021 • Video conference

Also taking advantage of video conferencing, we have been holding a "Seminar on Advanced Techniques and Applications at SPring-8" every Tuesday evening since January 2021. The participants of these seminars number over 500 in total for the first 9 seminars.

SACLA

I. Machine Operation & Beamlines

Our ninth year of operations proceeded without any significant issues. Operation statistics are summarized in Table 1. The ratio of downtime to user time was kept below 4%, a reasonably low rate for linac-based light sources.

Table 1. Operation Statistics for FY2020

		Time (h)
Total operation time		5798
User time		
	BL1	840
	BL2	1044
	BL3	1368
Facility tuning time		948
Downtime		109.1

In 2012, two beamlines, BL3 for XFEL and BL1 for broadband spontaneous light, were opened for users, while all experiments were conducted at BL3. As the newest beamline, construction of BL2 was completed during the summer shutdown of 2014, and first laser amplification was achieved on October 21. An upgraded beamline for soft X-ray FEL, BL1, which combines the prototype accelerator of SACLA (SCSS), started operation in 2016. Parallel user operation of BL2 and BL3 started in 2018.

II. User Program and Statistics

SACLA normally calls for public user proposals twice per year. However, due to the COVID-19 situation, the 2020A term was extended to March 2021. Most of the user experiments were rescheduled for the second half of FY2020. Some new proposals were additionally approved for the extension period.

In FY2016, JASRI introduced the proprietary research of General Proposals and the Proprietary Time-Designated Proposals. The project leaders of these proprietary proposals are not required to publish their research results, but required to pay each beamtime fee. In addition, to apply for the proprietary research the project leaders should be affiliated with a corporate enterprise located and registered in Japan.

Figures 1 and 2, and Table 2 provide statistics on proposals, users, and beamtime.

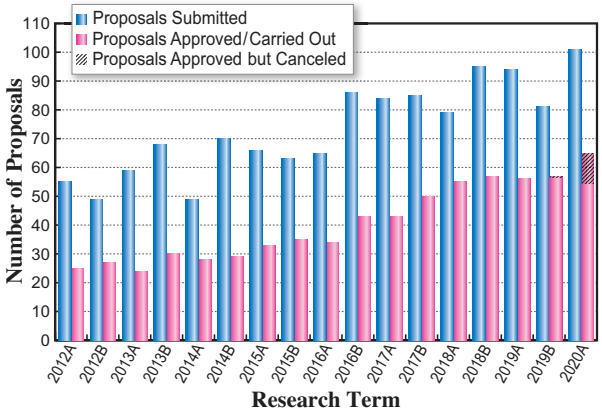

Fig. 1

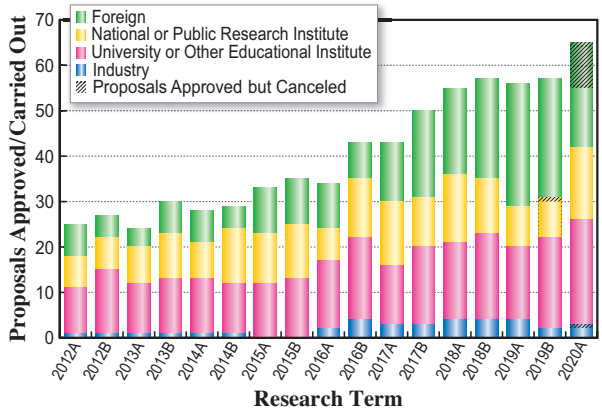

Fig. 2

Table 2. Number of proposals submitted, proposals approved/carried out, cumulative users, and beamtime available by research term

Half-year Research Term	Proposals Submitted	Proposals Approved / Carried Out					Cumulative Users	Beamtime Carried Out (Shifts)
			Priority Strategy Proposals	Non-proprietary	Proprietary			
				General Proposals	General Proposals	Time-Designated Proposals		
2012A	55	25	(12)	(13)	–	–	297	126
2012B	49	27	(19)	(8)	–	–	461	154
2013A	59	24	(15)	(9)	–	–	268	117
2013B	68	30	(19)	(11)	–	–	410	139
2014A	49	28	(20)	(8)	–	–	400	147
2014B	70	29	(17)	(12)	–	–	430	140
2015A	66	33	(23)	(10)	–	–	527	144
2015B	63	35	(23)	(12)	–	–	552	152
2016A	65	34	(21)	(12)	(1)	–	538	158
2016B	86	43	(21)	(20)	(1)	(1)	650	197
2017A	84	43	–	(43)	(0)	(0)	577	210
2017B	85	50	–	(50)	(0)	(0)	642	244
2018A	79	55	–	(55)	(0)	(0)	643	257
2018B	95	57	–	(56)	(0)	(1)	653	264
2019A	94	56	–	(55)	(0)	(1)	564	259
2019B	81	57	–	(56)	(0)	(0)	650	266
2020A	101	65	–	(54)	(0)	(0)	461	276

One shift = 12 hours at SACLA beamlines

Editor
Naoto Yagi
Japan Synchrotron Radiation Research Institute (JASRI)

Editing, Design & Layout
Marcia M. Obuti-Daté
Japan Synchrotron Radiation Research Institute (JASRI)

Printing
Hokuoh Printing Co.

JASRI
Information & Outreach Section
Users Administration Division

1-1-1 Kouto, Sayo-cho, Sayo-gun
Hyogo 679-5198 • JAPAN
Tel: +81-(0)791-58-2785 Fax: +81-(0)791-58-1869

Email: frontiers@spring8.or.jp
http://www.spring8.or.jp/

August 2021

SPring-8 SACLA

http://www.spring8.or.jp

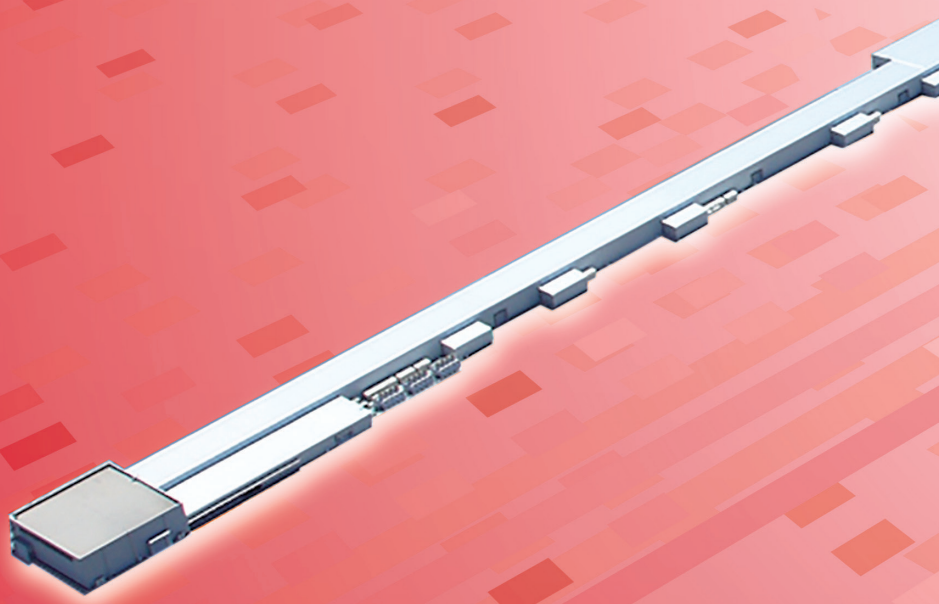

Japan Synchrotron Radiation Research Institute (JASRI)
1-1-1 Kouto, Sayo-cho, Sayo-gun, Hyogo 679-5198, Japan